João Filipe Rodrigues Antunes

Mestre em Engenharia Física Integrada

Design, implementation, and performance of a distributed and scalable sensor system for critical distance measurements in the CMS detector at LHC.

Dissertação para obtenção do Grau de Doutor em
Engenharia Física

Orientadores : Teresa Rodrigo Anoro, [Profª. Catedrático], IFCA (CSIC-Universidad de Cantabria), Espanha
Pedro Manuel Cardoso Vieira, [Prof. Auxiliar], Universidade Nova de Lisboa, Portugal

Júri:

Presidente:	Professora Adelaide Jesus da Universidade Nova de Lisboa
Arguentes:	Investigador Principal Rui Coelho
	Professor João Seixas
Vogal:	Professora Amélia Maio

FACULDADE DE CIÊNCIAS E TECNOLOGIA
UNIVERSIDADE NOVA DE LISBOA

Dezembro, 2014

Design, implementation, and performance of a distributed and scalable sensor system for critical distance measurements in the CMS detector at LHC.

Á família, amigos e orientadores.

Acknowledgements

Professor Teresa Rodrigo Anoro for her guidance, encouragement, her exceptional supervision and her trust in the work in which I have been engaged.

Dr. Andromachi Tsirou for the support and dedication to the project.

Professor Pedro Manuel Cardoso Vieira to be possible to do the Phd, supervision, encouragement.

Dr Patrice Siegrist for making it possible to do the Phd at CERN.

Dr. Piero Verdini for his support and wisdom.

I want to acknowledge all the help received from the Technical Coordination team during the many hours we spent together in SX5!.

All my close friends and family.

And last, but not least important, my loving parents Eduardo Moreira Antunes and Olga de Oliveira Rodrigues Antunes, for always being there, for their encouragement and support throughout these years.

Abstract

The "CMS Safety Closing Sensors System" (SCSS, or CSS for brevity) is a remote monitoring system design to control safety clearance and tight mechanical movements of parts of the CMS detector, especially during CMS assembly phases. We present the different systems that makes SCSS: its sensor technologies, the readout system, the data acquisition and control software. We also report on calibration and installation details, which determine the resolution and limits of the system.
We present as well our experience from the operation of the system and the analysis of the data collected since 2008. Special emphasis is given to study positioning reproducibility during detector assembly and understanding how the magnetic fields influence the detector structure.

Keywords: Keywords: CMS, remote monitoring system, safety clearance, position reproducibility, magnetic effects

Resumo

O "Sistema de sensores de segurança para o fecho do CMS" (SCSS ou abreviadamente CSS) é um sistema monitorização remota que fornece medidas de distâncias críticas, que monitoriza pequenos movimentos de partes mecânicas especialmente, durante o fecho e abertura do detector CMS. Apresentamos os vários subsistemas que constituem o SCSS: as tecnologias de sensores, o sistema de medida e o software de aquisição e controlo. Apresentaremos também os detalhes da calibração e instalação que determinam a resolução e limites do sistema.
Falaremos também da experiência das medições durante o fecho e abertura que ocorreu nos vários anos da operação do sistema. É dado especial ênfase ao estudo na reprodutibilidade da posição após os ciclos de abertura e fecho e na apresentação dos dados relativos aos efeitos dos campos magnéticos na estrutura do detector.

Palavras-chave: Palavras-chave: CMS, sistema monitorização remoto, margem de segurança, remoto, efeitos magnéticos

List of Acronyms

ALARA As Low As Reasonably Achievable
ADC Analog-to-Digital Converter
API Application Programming Interface
ATLAS A Toroidal LHC ApparatuS
B magnetic induction
BCM Beam Conditions Monitor
BP Beampipe
CAD Computer Aided Design
CAN bus/CANBUS Controller Area Network bus
CASTOR Centauro And Strange Object Research
CERN European Organization for Nuclear Research / Conseil Européen pour la Recherche Nucléaire
CMS Compact Muon Solenoid
COTS Commercial Off-The-Shelf
CSC Cathode Strip Chamber
CSS or **CS** Closing Sensors System
CSV Comma-Separated Values
CR Central Region
Ctrl Control Managers
DAC Digital-to-Analog Converter
DBM Data Base Manager
DC Direct current
DCS Detector Control Systems
DIN Deutsches Institut für Normung
DIP Data Interchange Protocol
Dist Distribution Manager
DT Drift Tube chamber

EB Electromagnetic Barrel calorimeter
ECAL Electromagnetic Calorimeter
EE Electromagnetic calorimeter end caps
ELMB Embedded Local Monitoring Box
ES Preshower detectors
EVM The Event Manager
FSM Finite State Machine
GEM Gas Electron Multiplier
GND ground
GUI Graphical User Interface
HB Hadronic Barrel calorimeter
HCAL Hadron Calorimeter
HE Hadron calorimeter
HEP High Energy Physics
HF Hadron Forward calorimeter
HO Hadron Outer Calorimeter
ICS Industrial Control System
INFN Istituto Nazionale di Fisica Nucleare
IP Interaction Point
IR infrared
IT/CO Information Technology COntrols Group
JCOP Joint Controls Project
LED Light Emitting Diode
LHC Large Hadron Collider
MTCC Magnet Test and Cosmic Challenge
Non IP Opposite side to Interaction Point
OPC Open Process Control
PCB Printed Circuit Board
POT Potentiometer
PP1 first patch panels inside the vacuum tank
PVSS Process Visualization and Steering System
RP Roman Pot
RPC Resistive Plate Chamber
RS Rotating Shielding
SCADA Supervisory Control and Data Acquisition
SMD Surface-Mount Device
SR Seal Ring
TOTEM TOTal Elastic and diffractive cross section Measurement
TP Transfer Plate
T1 Telescopes T1
T2 Telescopes T2

UIM User Interface Managers
US UltraSound
VT Vacuum Tank
YB0 Central Yoke Barrel 0^{st} wheel
YB+n Yoke Barrel n(1,2) wheel, positive side
YB-n Yoke Barrel n(1,2) wheel, negative side
YE+n Yoke Endcap n(1,2,3) disk, positive side
YE-n Yoke Endcap n(1,2,3) disk, negative side
YN Yoke Nose Endcap disk

Contents

List of Figures

List of Tables

Introduction

Particle physics or High Energy physics is the discipline of physics in charge of the study of the basic elements of matter and the forces acting among them. Accelerators and particle detectors are tools employed for their study. The best description of the nature, up to the energies probed today, is the Standard Model (SM) of particle physics, a quantum field theory that incorporates the fundamental particles, quarks and leptons, and the interactions among them, the strong, the weak and the electromagnetic interactions. During the last 50 years the SM has been tested in particle accelerators with great success and a very high degree of accuracy. At the moment there are no experimental results that contradict this theory. The discovery of the Higgs boson in 2012 has been the last big achievement in the field and the first outstanding scientific output from the Large Hadron Collider (LHC).

The work presented here has been carried out at CERN, at one of the large LHC experiments, the Compact Muon Solenoid (CMS) experiment. CERN (European Organization for Nuclear Research) is an intergovernmental organization with 20 members states. It has its seat in Geneva but straddles the Swiss-French border. Its objective is to provide a collaboration among European States in the field of High Energy Physics (HEP) research and for this pursuit designs, constructs and runs the necessary particle accelerators and the associate areas of experiments. Most of the activities at CERN are currently directed towards the Large Hadron Collider and associated experiments.

The LHC is the last accelerator built at CERN, it represents a large-scale world wide scientific cooperation project. The LHC tunnel is located 100 metres underground, in the region between the Geneva airport and the nearby Jura mountains. It uses a 27 km circumference circular tunnel, previously occupied by the Large Electron Positron Collider (LEP), which was closed down in November 2000. LHC is a proton-proton (p-p) and a lead-ion collider built at CERN. The assembly period was from 1994 to 2008 during which the project successfully overcame the several technical difficulties associated to the LHC stringent requirements. The first (p-p) collisions took place in November 2009.

Six experiments (CMS, ATLAS, LHCb, TOTEM, LHCf, and ALICE) are running on the collider, each of them has the task to study particle collisions under a different point of view, and with different technologies. The products of the collisions generate vast quantities of computer data, which CERN stream to laboratories around the world for distributed processing making use of a specialized World wide LHC Computing Grid infrastructure.

CMS is one of the two general purpose detectors at the LHC. It is a modular detector composed of big structures, instrumented with precise active elements. The weight of the structures varies from approx. 200 to 3,000 tonnes. It has a cylindrical symmetry around the collision point. The overall dimensions of the CMS detector are a length of 21.6 m, a diameter of 14.6 m and a total weight of 14,000 tonnes. The detector consists of different sub-detectors, each one with a well defined characteristics to measure a given physical property of the particles emerging from the collision. An overview of the LHC project and a detailed description of the CMS experiment and its sub-detectors is given in Chapter 1. The purpose of this chapter is to describe the experimental framework and environmental conditions under which the work described here has been developed. CMS must be fully assembled during data-taking periods, while the maintenance and upgrade of the detector requires the regular opening of structures and sub-systems involving delicate operations that must be precisely monitored. To fulfil this task a dedicated monitoring system, the Closing Sensor System (CSS), consisting of more than 200 sensors has been built and integrated into CMS. The different aspects of the work carried out by the author in the definition, implementation and exploitation of this monitoring system are the subject of this document.

From mechanical and integration point of view, CMS is characterized by its modularity and compactness. When closing the detector, the nominal distances between structures - and from them to the beam pipe tube - is optimized and safety clearances are minimized in order to preserve as much as possible the hermeticity of the detector. To ensure the detector's integrity and inform on the correct positioning of the different elements, the Closing Sensor System must guarantee that tight tolerances are respected during the assembly operations; it should provide positioning precision at the level of mm and mrad. Critical areas where tight tolerances must be satisfied are well identified in the different parts of the detector. The instrumentation of the CSS is distributed along the "central" and "forward" CMS regions, with special emphasis to the critical safety areas. An overview of the CSS, together with a discussion on the constraints imposed to the CSS instrumentation due to its specific environmental conditions, is presented in Chapter 2.

CSS devices have to survey reliably distances ranging from few mm up to few tens of cm. These numbers indicate the required dynamic range of the CSS's sensors. In terms of precision, a moderate intrinsic measurement resolution, approx. 0.5 mm, complies with

the system requirements. Both conditions are largely achieved with standard commercial devices. Nevertheless, during the operation of the detector, CSS sensors will be exposed to strong magnetic fields from the CMS solenoid, and high irradiation from the LHC collisions. Immunity to magnetic field or radiation tolerance requirements are difficult to meet by standard commercial products. However, taking into account scalability and maintenance scenarios, the decision to use Commercial Off-The-Shelf (COTS) items as far as possible was considered most appropriated. Following their degradation in performance, a regular replacement of the sensors is foreseen. A short presentation of the main characteristics of the three sensor technologies used by the CSS system, is given in Chapter 3.

All CSS's sensors were characterized prior to installation in the detector using dedicated calibration stands. Given the essential differences between the three technologies, as well as the different performance tests required for specific detector locations, various configurations of the experimental setup and acquisition system were deployed during the calibration campaigns. The different calibration benches are described in Chapter 4. Following the systematics uncertainties affecting the measurements provided by each technology, the aim of the performance studies were different for the chosen devices. In each case, the calibration tried to reproduce as much as possible the real operation conditions. Tests as thorough as possible were also performed to understand the expected lifetime and behaviour of the sensors under intense magnetic fields. The possible degradation of the devices under radiation is being followed in-situ during the operation of the system in CMS. A summary of the most relevant aspects and results obtained during the different calibration campaigns is presented in Chapter 5. In Chapter 6 a detailed description of the implementation of CSS sensors in the detector is given. Details on functionality, geometrical distribution, type of sensor technology as well as its accessibility are given. Considerations on the procedure to be followed during the detector assembly operations are also discussed.

The choice of the readout electronics and the layout of the CSS readout and control system is presented in Chapter 7. To optimize operation and maintenance, the design of the readout system was driven to make the best use of the existing infrastructure matching at the same time the requirements and restrictions imposed by LHC and CMS safety rules. Because of the harsh detector environment, special electronic boards in radiation tolerant format and immunity to magnetic field were developed for all LHC experiments to be used as readout/control electronic devices. They are part of a system known as ELMB (Embedded Local Monitor Board). CSS's sensor signals are collected and digitized using these ELMB cards as front-end electronics, situated next to the detector. Ad-hoc devices were developed to adapt the sensor signal such that they can be processed by the ELMB modules and to ensure the power distribution to the sensors, which also takes place close to the detector.

A complete Data Acquisition and Control (DAC) software pack was developed for the Closing Sensor System. The CSS DAC's program was defined following the standards recommend for the LHC experiments. It uses the software platform supervisory control and data acquisition (SCADA) using a Process Visualization and Steering System (PVSS II) (WinCC nowadays) with the Joint Controls Project (JCOP) a framework developed at CERN. The program performs the control of the system readout sequence, provides the display of the information, and allows the storage of the data. Different panels were defined to allow a quick and easy representation of results needed for an interactive response with the technical team conducting the mechanical operations in CMS. A set of warnings and alarms were introduced to guide the actions to be taken by the operators in charge of the different tasks. As described in Chapter 8 the CSS software has been continuously upgraded and adapted in order to cope with the always evolving CMS detector control requirements.

Chapters 9 and 10 report on the analysis of the measurements performed by the CSS system during an extended period of time, from 2008 to 2013. The data are grouped into three categories: a) measurements related with the closing and opening of the detector structures; b) measurements monitoring the powering cycles of the magnet, and finally; c) the data collected during the regular operation of the detector. The two first sets of measurements are critical to ensure the integrity of the detector. Special care has to be taken by the online monitoring during the complex processes involved in these operations. CSS was intensively used during the opening and closing campaigns, and at the different occasions the CMS solenoid is powered on and off. First measurements were performed during the initial assembly of the CMS in 2008 at the collision cavern, and later on, during the regular maintenance periods and magnet cycles. When the 3.8 T CMS solenoid is powered the strong magnetic forces generated in the detector induce large motions or deformations of the detector elements which are recorded. The size and reproducibility of this motion has been studied with the CSS data. During the first magnet cycles, in 2008, independent measurements were also performed by the CERN Metrology Group using standard survey and/or photogrammetry techniques. The comparison of the two sets of data allowed an independent validation of the CSS output. Finally, the set of data collected during the normal operation of the detector informs on the mechanical stability of the whole detector. Any unknown instability could influence the quality of the data taken by CMS and therefore the subsequent scientific production. If this occurs CSS can help to understand and fix the problem. This is mainly relevant for forward detectors where CSS provides the unique active monitoring in this region.

The last Chapter summarize the work done on the design, construction, implementation in the detector, and operation of the Closing Sensor System, as well as the main conclusions obtained from the analysis of the data provided by the

system.

The personal and original contribution of the author to the work reported here expands from the initial studies that resulted in the definition of the system, as described in Chapter 2, to the final analysis of the data collected by the Closing Sensor System. This is the first time that an online monitoring system of this kind is implemented in a particle physics detector. The work has been developed within the CMS Technical Coordination team. The group covers a wide range of activities related with the completion, integration, installation, maintenance and upgrade of the CMS detector, as well as the aspects related with safety, infrastructure and services of the experimental area. The author has been the main responsible in the development of the Closing Sensor System. He has been in charge of the selection and calibration of the system instrumentation, the construction of the readout electronics, and the development of the CSS DAC software. Working closely with a team of engineers and technicians he was in charge of the implementation of the system in CMS. Since 2008, the author has been also in charge of the operation, maintenance and upgrade of the system following the evolving CMS demands. The monitoring system has been working almost in a continuous mode during this long period of time with no major or unforeseen problems. The data collected by the system informs on the final global position parameters of CMS, the reproducibility of the motion of the different elements and on the stability of the detector mechanics during normal CMS data taking conditions.

1

The LHC, the CMS detector, and the TOTEM experiment

1.1 The Large Hadron Collider

The 27 km roughly circular Large Hadron Collider (LHC) [1] is a proton-proton (p-p) and lead-ions (Pb-Pb) collider built at CERN. It is an underground installation between two territories French and Swiss, placed between the Jura Mountains and the Lake Léman. It uses the tunnel of the previous (e+ e-) Large Electron–Positron Collider (LEP). The two crucial design parameters, for a particle accelerator in physics, are: the maximum energy and luminosity that it can provide.
The LHC contains two beam pipes in the interior where the protons or ions are accelerated in opposite directions and collisions take place in the centre of the detectors, at four interaction regions, that are more known as the interaction points (IP).
The tunnel is located at a depth between 70 to 175 meters underground, with 3 m of diameter and concrete-lined. It is installed underground for safety and environmental reasons, when in operation, high level of radiation is produced during of the particles collisions. The experimental detectors underground also benefits of the attenuation from background noise of the universe. The operational parameters of the LHC are listed in Table 1.1.

The goals of the LHC are the comprehension of the Standard Model in the TeV energy range, the search for the Higgs boson and discovery of new physics signatures. The discovery of the Higgs boson in 2012 is the first important scientific achievement. Hadron

Table 1.1: LHC parameters

Large Hadron Collider	
Circumference perimeter, (m)	26,659
Depth, (m)	70 - 175
Total number of magnets	9,593
Number of main dipoles	1,232
Number of quadrupoles	392
Temperature of the liquid helium on the dipole, (K)	1.9
Total beam current per beam (p-p), (A)	0.56
Particles per bunch (p-p)	1.1 x 10^{11}
Typical RMS beam size in the ring (p-p), (μmm)	200-300
Fraction of energy lost in synchr.rad. per turn (p-p)	10^{-9}
Total power radiated in synchr.rad. (p-p), (MW)	0.0078
Total energy stored in each beam (p-p), (MJ)	362
Total energy stored in the magnet system (p-p), (GJ)	10
Liquid nitrogen (LHC), (tonnes)	10,080
Liquid helium (LHC), (tonnes)	120
Beam vacuum pressure, (mbar)	10^{-10}
Ion pumps	780
Vacuum safety valves	303
Nominal p energy, (TeV)	7
centre-of-mass energy (p-p), (TeV)	14
Designed luminosity (p-p), ($cm^{-2}s^{-1}$) (design)	10^{34}
centre-of-mass energy (Pb-Pb), (TeV)	2.76
Designed luminosity (Pb-Pb), ($cm^{-2}s^{-1}$)	10^{27}
Bunches per proton beam	2,808
Turns per second	11,245
Collisions per second	600 million
Length of each dipole, (m)	15
Weight of each dipole, (tonnes)	35
Dipole field, (T)	8.33

colliders are the optimal type of collider, because the collisions cover a wide energy range. The construction period of the LHC was from 1994 to 2008, during which the project had suffered several technical difficulties in order to fill stringent requirements. It was switched on, for the first time, on the 10^{th} September 2008 ,but after 9 days running, a magnet quench incident halt the LHC for more 14 months. The LHC restarted the collisions (p-p) on 23^{rd} November 2009 with the energy injection of 450 GeV ,but the first collisions of (p-p) at 7 TeV only took place on the 30^{th} March 2010. The first collisions with 8 TeV energy (p-p) were on 5^{th} April 2012.

Figure 1.1: Diagram of the LHC with the respective chain of particle accelerators and injectors

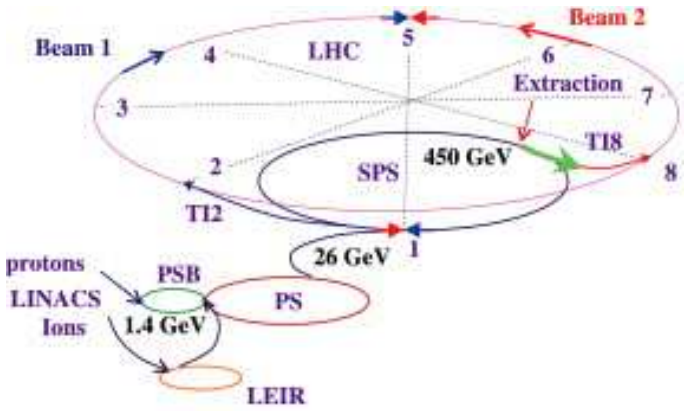

The LHC is the last piece of a complex of particle accelerators, where the particles reach the highest energy. To be feasible, there are two different accelerator chains for protons and lead ions, each chain consists of an injector and particles accelerators. Fig. 1.1 shows the map of the CERN accelerator complex. The chain of accelerators used, before the proton enters in the LHC, follows a sequence starting with Linac2, which is a linear accelerator, Proton Synchrotron Booster (PSB), the Proton Synchrotron (PS) and at last the Super Proton Synchrotron (SPS). The chain of accelerators used before the lead ion enters on the LHC, follows a sequence starting with Linac3, which is also a linear accelerator, then the Low Energy Ion Ring (LEIR), the Proton Synchrotron (PS) and at last the Super Proton Synchrotron (SPS). To supply Linac2 a machine called duoplasmatron that is connected to a bottle of hydrogen gas and strips from this gas its electrons is used, making a plasma of protons, electrons and molecular ions. Extraction electrodes are used to force the plasma expansion. As a result, a proton beam is created and ready to be injected on Linac2 to be accelerated up to 50 MeV. The PSB contains four superimposed rings with a radius of 25 meters in which, the particles are accelerated up to 1.2 GeV. On the PS there is a circular particle accelerator with a circumference of 628.3 m, in which the particles are accelerated up to 25 GeV. The SPS, a circular particle accelerator with almost 7 km in circumference, can accelerate up to a maximum energy of 450 GeV before the protons bunches are injected into the LHC.

Lead ions are produced from a small sample of isotopically pure solid lead - 208 by an electron-cyclotron-resonance ion source. To convert the metal into a beam of lead ions there is a process with the following steps: first the metal is heated for vapour of lead atoms; after that the lead vapour is ionized to form a plasma, and then the lead ions are extracted from the plasma and accelerated on Linac3, that can accelerate a bunch of lead ions up to 4.2 MeV. The LEIR can accelerate bunches of lead ions, in groups of two, from 4.2 MeV to 72 MeV.
The beam of particles travels in the interior of LHC with ultra-high vacuum UHV, and the magnets system cools down at 1.9 K. The beam pipe vacuum can reach 10^{-10} mbar. The vacuum system consists of 780 ion pumps, 303 vacuum safety valves using a complex interlocking system which makes them operate.

The LHC accelerator consists of thousands of magnets in order to guide the beams and focus, it uses different types of magnets as dipoles, quadrupoles, sextupoles, decapoles, etc. The majority of magnets on the LHC are dipoles and quadrupoles. The dipoles provide uniform magnetic field over their length with an intensity of 8.33 T. The high magnetic field is generated using special materials, as niobium-titanium (Nb-Ti) that has superconductivity properties when cooled down to 1.9 K. The largest cryogenic system of the world, using the liquid helium as fluid, is needed to cool down all magnets of the LHC. The cooling process has different stages: first the magnets are filled with liquid helium at 4.5 K and only after the refrigeration system brings down the temperature to 1.9 K. The magnet, when is cooled down, has a typical resistance on the nano ohm level, that can be supplied with a current up to 12 kA. The energy stored in a single dipole at full field is 7.2 MJ, meaning that a sector is able to store 1.1 GJ, and all LHC around 10 GJ. The fig. 1.2 shows the schematic cross-section of the LHC dipole magnet cryostat with the two independent vacuum chambers, magnet coils around the two vacuum chambers and common infrastructure for powering and cooling the magnet coils.
The magnets can suffer quenches, by increasing the temperature the magnet can pass from a super conductor to a normal one in a small area of a few millimetres, thus increasing the resistance and voltage. In order to detect this, the LHC magnets are instrumented with the Quench Protection System (QPS), that consists of a voltmeter detecting any variation larger than 100 mV over a period of at least 10 ms, which indicates a clear signal of a quench. When the quench is detected, the system will trigger the discharge of the capacitors into resistors in the magnet, the “quench-heaters” will warm-up the magnet up to 10 K in 25 ms. The second safety measure is to discharge the magnet and provide a bypass for the current of the other magnets, that are powered in series with the quenched magnet, to avoid more energy deposition on it.

Radio frequency (RF) cavities are used to accelerate the particle beams and to keep the bunches tightly bunched. The beams use the superconducting single cell cavities, that attenuates the effects of periodic transient beam load. In the design, it was planned to use

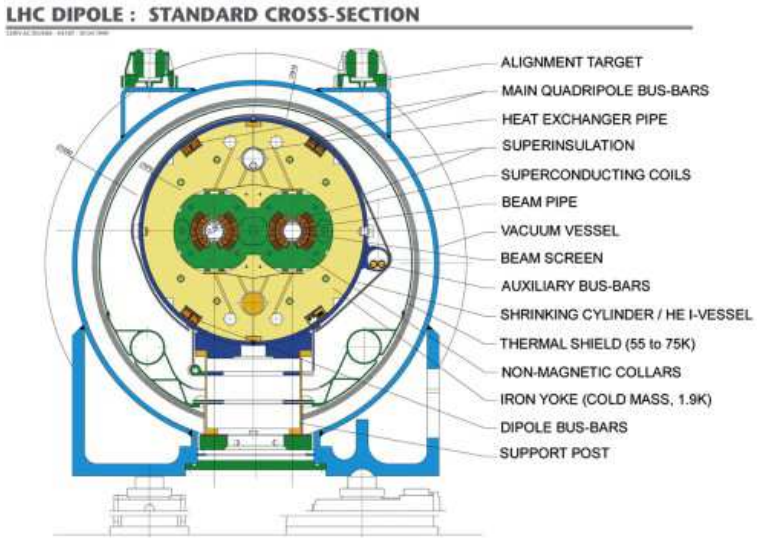

Figure 1.2: Schematic cross-section of the LHC dipole magnet cryostat with the two independent vacuum chambers, magnet coils around the two vacuum chambers and common infrastructure for powering and cooling the magnet coils.

8 cavities per beam, each one capable of delivering 2 MV (5 MV/m accelerating field) with a frequency of 400 MHz.

The designed maximum beam intensity is 3.23 x 10^{14} protons at 7 TeV, corresponding to a total energy of 362 MJ, that could heat and melt 517 kg of copper (1 kg of copper needs 0.7 MJ). The LHC is protected by a fast beam loss system. The beam loss system is installed on several thousand points on the ring. The threshold to trigger a beam abort is bellow the beam loss that could cause a quench on the magnets.The beams can be extracted from LHC by the beam dump system located at point 6 (see fig. 1.3). The full beam could be extracted in one single turn. This is possible due to a fast ($< 3\ \mu$s rise time) kickers magnets. The beams are stopped in about 8 m long graphite core of the beam dump absorber, which is made of concrete and iron located at 700 m downstream from point 6. The halo collimation also known as the main betatron, is installed far from the experiments on the point 7. It is a complex setup that allows removing halo particles in a continuous operation, in order to decrease the risk of damage, quenches in the superconducting equipment, to attenuate the impact of radiation and radioactive activation.

The experiments installed on the LHC collider, in alphabetic order, are: 'A Large Ion Collider Experiment'(ALICE) [2],'A Toroidal LHC Apparatus' (ATLAS) [3], 'Compact Muon Solenoid' (CMS) [4], 'Large Hadron Collider beauty' (LHCb) [5], 'Large Hadron Collider forward' (LHCf) [6] and 'ToTal Elastic and diffractive cross section Measurement' (TOTEM) [7].
The two general purpose experiments for high luminosity are ATLAS and CMS detectors,

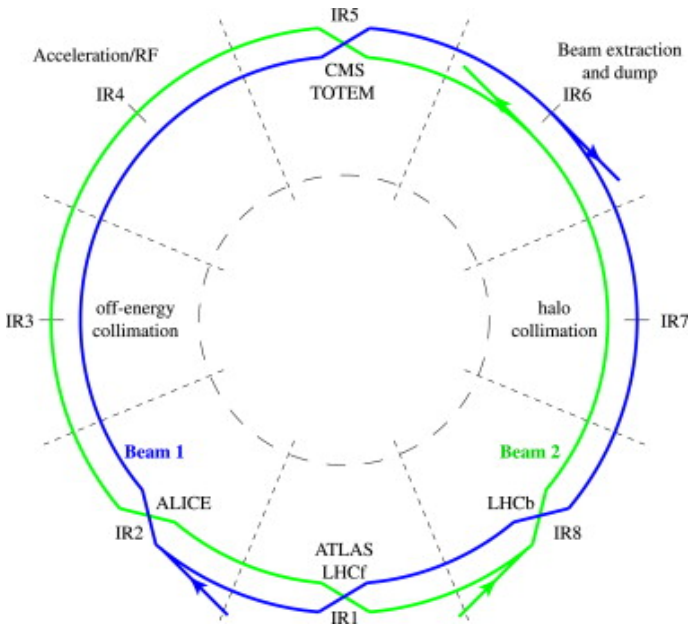

Figure 1.3: Schematic layout of the LHC installations and experiments on the different points.

that can use proton-proton collisions up to luminosities of $L \geq 10^{34}$ cm^{-2}s^{-1}. One B-meson experiment LHCb (up to $L \propto 10^{32}$ cm^{-2}s^{-1}) and one orientated experiment for ion collisions ALICE using lower luminosities ($L \propto 10^{29}$ cm^{-2}s^{-1}) for proton beam energy. The four detectors ALICE, ATLAS, CMS and LHCb have their own caverns built underground in the different points displayed in fig. 1.3. The LHCf is installed at a distance of 140 m from the ATLAS detector, and the TOTEM consists of three detectors the T1, T2 and Roman Pots, with the two first located in the forward region of CMS, and the Roman Pots installed on LHC tunnel.

1.2 The Compact Muon Solenoid Detector

The CMS experiment is a collaboration of more than 3600 scientists from 183 institutions over 41 countries, the detector is situated in Cessy village, at the point 5 of LHC complex. The CMS detector is one of the two detectors designed to operate at high luminosity and to explore the whole range of physics at the LHC. With LHC design luminosity the detectors will observe an event rate approximately of 1 billion interactions per second. With the high rate of interactions per second, good spacial and time resolution detectors are needed. This results in millions of readout electronic channels demanding a precise synchronization. The large flux of particles scattered in the interior of the detector will produce high radiation levels, which demands radiation-hard electronics and materials.

An important mark on the design and layout of the detector was the selection of a

strong magnetic field configuration for the precise measurement of the momentum of muons and in general of all charged particles produced in the collisions. The fig. 1.4 shows the exploded view of the CMS detector. The overall dimensions of the CMS magnet are 13 m long, and 5.9 m inner diameter, it can deliver a maximum of 4 T. With the high magnetic field over a large volume it allows a robust detection over the entire geometrical coverage. Outside the coil, interleaved in the return yoke, there are 4 muon "stations". Inside the magnet coil there are the inner tracker and the calorimeters subsystems that will be briefly described in the following sections.

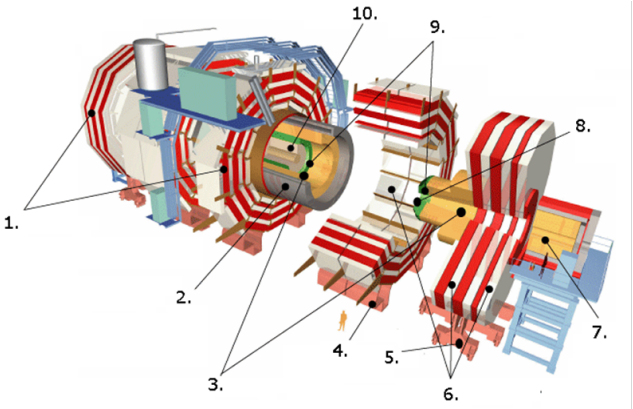

Fig. Num.	
1	Return Yoke
2	Superconducting magnet
3	Hadron Calorimeter (HCAL)
4	Muon Barrel (YB's)
5	Muon Endcap (YE's)
6	Muon Chambers (CSC) and (RPC)
7	Forward Calorimeter (HF)
8	Preshower (ES)
9	Electromagnetic Calorimeter (ECAL)
10	Tracker (TK)

Figure 1.4: Exploded view of the CMS detector

The magnet main parameters are listed in Table 1.2. It consists of a superconducting 5 coil modules embedded within a Vac tank, supported and surrounded by a return iron yoke with 15 m of diameter. The magnet conductors are made of reinforced niobium titanium (NbTi). Twenty conductors were produced with a continuous length of 2.65 km and there four conductors per each coil modules were used. The power supply can deliver to the magnet coil a maximum current of 19.5 kA (at 4 T) at a maximum ramping voltage of 16 V. Nevertheless, during the commissioning of the system, it was decided to operate the magnet at 3.8 T (18,164 kA) to extend, as much as possible, the magnet lifetime. The ramping up process can be controlled with setting different rates of currents per second that could determinate different time periods. The slow ramp down could be programmed or could be a result of fault on the magnet power supply, a problem on the cooling system, other auxiliary systems or external commands coming from LHC and have the duration period of approximately, three hours. In case of emergency, a fast discharge in a 50 MW resistor bank can be used. The time constant of the current decay is then 280 s. From the design a pre-cooler, fed with 500 l/h of liquid nitrogen, provides additional refrigeration power for the cool-down which is expected to last approximately 30 days from room temperature.

The recovery from a magnet fast-discharge takes 3 days from a temperature of 50 K to a temperature of TCS = 6.5 K that is the current sharing temperature. Other mechanical parameters are available on Tab. 1.3.

Table 1.2: Magnet Characteristics

Magnetic induction at interaction point, (T)	4
Magnetomotive force, (MAt)	42.28
Conductor peak magnetic field, (T)	4.6
Winding overall current density, (A/mm^2)	12.68
Stored energy, (GJ)	2.69
Magnetic radial pressure, (MPa)	6.4
Axial compressive force at mid plane, (MN)	148
Operating current, (kA)	19.5
Inductance, (H)	14.15
Total number of turns	2168
Turns per layer	542
Dump resistor, (MW)	50
Dump voltage, (V)	1000
Dump time constant, (s)	283

Table 1.3: Overall geometrical parameters

Magnetic length, (m)	12.4
External diameter (without cooling tubes), (m)	6.976
Internal diameter, (m)	6.36
Overall radial thickness, (mm)	308
Winding thickness, (mm)	296
Quench tube thickness, (mm)	12
Total mass (without supports), (tonnes)	220

The coordinate system adopted by CMS has its origin at the interaction point (IP) on the centre of the CMS detector. The Y axis is pointing vertically upward and the X axis is pointing inward towards the centre of the LHC. The Z axis points along the beam line and with the B field direction, towards the Jura Mountains. The azimuthal angle ø is measured from the X axis in the X-Y plane, the polar angle θ is measured from the z axis. The pseudorapidity η, as defined as $\eta = -\ln\ tan\left(\frac{\theta}{2}\right)$. The momentum and energy of a particle is measured transversely to the beam direction, p_T and E_T, are computed from the x and y components. A sector of CMS is shown in fig. 1.5. The various components displayed in the figure are described in the following sections.

1.2.1 The CMS Tracker

The CMS tracking [8] is located inside the coil, and it is the first detector surrounding the interaction point. It is designed to allow a precise reconstruction of the trajectory of the charged particles produced in the collisions. The active envelope (see fig. 1.6) extends to a

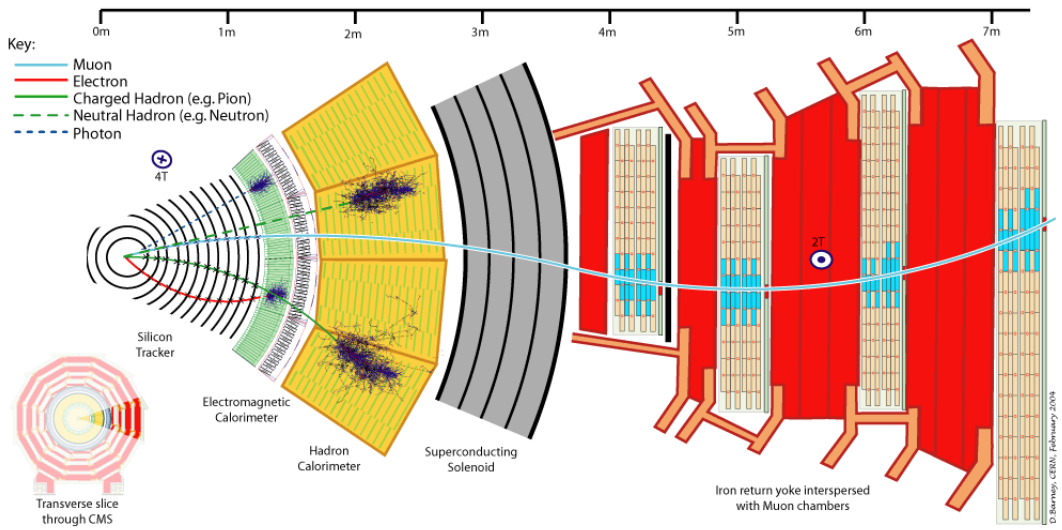

Figure 1.5: A sector, in the X-Y plane, of the CMS detector. The different systems, from the centre of the CMS detector to the outside are shown. The trajectories of the different particles are also displayed.

radii of 115 cm, over a length of approximately 270 cm on each side of the interaction point, with a total sensitive surface of around 200 m^2. At the nominal LHC luminosity, every 25 ns typically 20 proton-proton collisions occur, producing around 1,000 particles crossing the tracker volume. The flux of particles equates to have a high hit rate of 100 MHz/cm^2 at the innermost detector layer, decreasing to 300 kHz/cm^2 at the outermost. This imposes stringent conditions on the detector and readout electronics. To satisfy them the detector technology must provide high granularity combined with a fast readout, and be able to operate in this harsh environment for a expected lifetime of approximately 10 years.

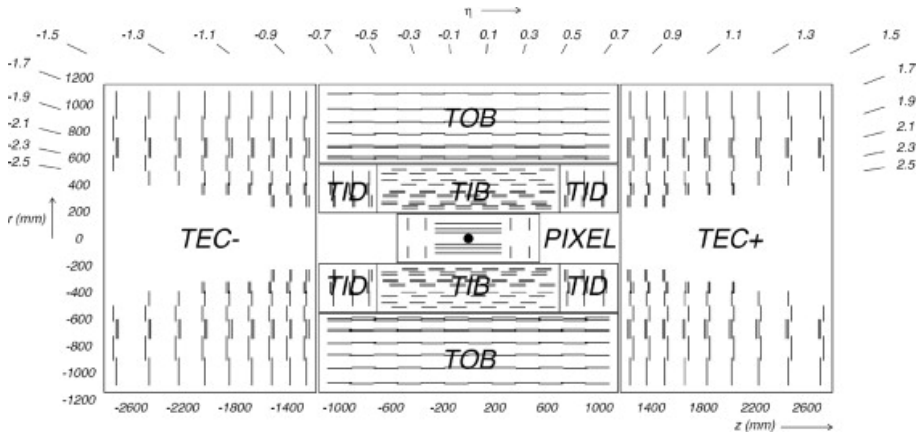

Figure 1.6: Layout of the CMS Tracker detector

The CMS tracker consist of two parts instrumented with two technologies: Pixel detectors and Silicon Strips. The Pixel system is the first element after the collision point.

The detector consists of two sub-detectors - the Barrel (BPIX) and Forward (FPIX). The BPIX is made of three layer detector with 53 cm long with layers at mean radius of 4, 7 and 11 cm. The FPIX has two layers at |z| = 34.5 and 46.5 cm with a radial coverage between 6 and 15 cm. The detector has more than 66 million readout channels, the sensitive area is of 1 m^2 of pixels with a unit size of 100 x 150 μm^2.

The Silicon Strip Tracker is formed of 15,148 detector modules mounted on the four different subsystems: Tracker Inner Barrel and Disk (TIB/TID), Tracker Outer Barrel (TOB) and Tracker End Caps (TEC). Each is assembled on an independent mechanical light support structure. The TIB is a group of 4 layers and covers up to $|z| < 65$ cm, using silicon sensors geometry with a thickness of 320 μm and strip pitch between 80 and 120 μm. The TIB is the loser part to the interaction point and is exposed to a high dose of radiation. The two first layers of TIB have two modules back-to-back with a stereo angle of 100 mrad in order to have a single-point resolution between 23-34 μm on r-ø direction and 23 μm in the z direction.
The TOB is a group of 6 layers with a half-length of $|z| < 110$ cm. The radiation level of TOB when compared to the TIB is lower. The geometry can be different with thicker silicon sensors of 500 μm which can be used to maintain a good signal-to-noise ratio for longer strip length and wider pitch between 120 to 180 μm. Also the two first layers of TOB have two modules back-to-back with a stereo angle of 100 mrad in order to have a single-point resolution between 35-52 μm in the r-ø direction and 52 μm in the z direction. The outer endcap TEC is composed of 9 disks that are between the 120 cm and 280 cm in Z axis. The two first and the fifth rings of TEC also have two modules mounted back-to-back in order to increase the resolution. The inner endcap TID is composed of 3 small disks filling the gap between the TIB and the TEC. In order to increase the resolution the TID also has two modules mounted back-to-back on the first two rings. The TEC and TID modules are organized in rings, centred on the beam line.

The Silicon Strip tracker has around 9.3 millions of strips with 200 m^2 of active sensing area. It can provide a minimum of 10 measurement points in the radial projection along a particle track for pseudorapidities up to a maximum of η=2.5.

The structure for the different parts of the silicon strip tracker is made of carbon fibre in order to reduce the budget material, high mechanical strength and low dilation coefficient. The cooling circuits have to allow the silicon strip tracker to operate with a temperature bellow -10 ^{o}C in order to reduce the thermal runaway and anti-annealing processes during the LHC collisions. During the shutdown periods it should be at $0\,^\circ$ C, once significant dose has been accumulated dose.

1.2.2 The CMS Electromagnetic Calorimeter

The CMS Electromagnetic Calorimeter [9] detector is a layer surrounding the CMS Tracker which function is to measure the energies from the electrons and photons. The main driver for the design of the ECAL was the search of the Higgs boson in the mass region below 130 GeV, by measuring the decay H$\rightarrow \gamma\gamma$ signature.

The ECAL consists of 76,000 lead tungstate $PbWO_4$ crystals with a density of 8.28 g/cm^3, a 3D view is shown in fig. 1.7. The detector volume is centred on the interaction point with a length 7.9 m and a 3.6 m in diameter with an approximated crystal mass of 90 tonnes. It is composed of a Barrel (EB) with a pseudorapidity range $|\eta|<1.479$ that is made of two halves, each of them divided into 18 ø-sectors called 'Supermodules' housing 1,700 crystals. The two Endcaps (EE) with a pseudorapidity range $1.479<|\eta|<3$ are composed of two 'Dees' divided vertically, each one formed by groups of 25 crystals mostly called 'Supercrystals' making a total of 3675 crystals per 'Dee'. On the front of the EE towards the interactions point the Preshower (ES) is installed with a pseudorapidity range $1.653<|\eta|<2.6$.

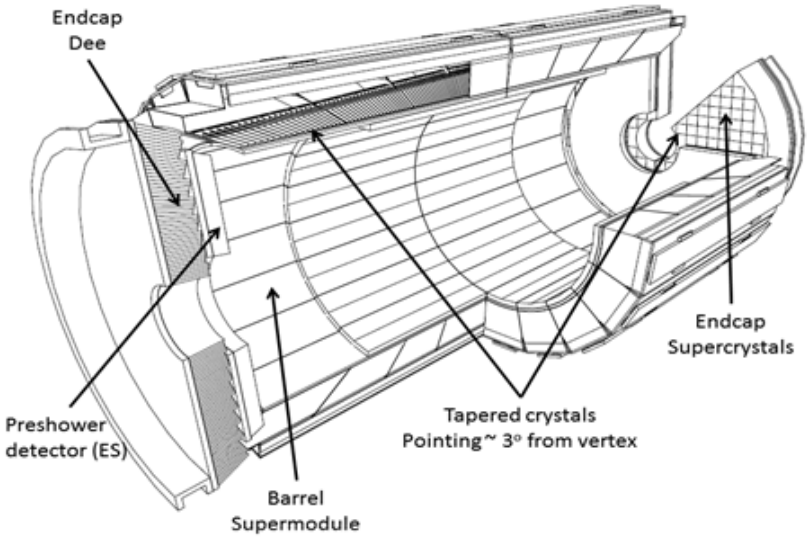

Figure 1.7: 3D view of the CMS ECAL

The crystals are tapered and distributed over the Barrel and Endcap's with the tip oriented approximately 3^o away from the main interaction point, to attenuate the effect of intercrystal gaps. The lead tungstate has the properties of having a short radiation length of 0.89 cm, related to the energy loss of high energy, electromagnetic-interacting particles with it. The small Molière radius of 2.19 cm allows containing approximately 90% of the shower energy deposited. The scintillation emission is sufficiently fast to emit 80% of the light in a period of 25 ns with a wavelength on the blue region at 425 nm. The crystals will deteriorate with the radiation creating colour centres and a self-anneal, depending on the temperature and time causing a variation on the energy measurement. In order to make

an accurate measurement a very precise system for monitoring the crystal transparency was installed.
Two different technologies of photo-detectors have been used, one on the Barrel and the other one on the Endcaps. Avalanche Photodiodes (APDs) were used on the Barrel, specially developed by the Hamamatsu Photonics for CMS ECAL. The endcaps use Vacuum Photo-Triodes (VPTs) developed by the manufacturer RIE in St Petersburg. The ECAL detector has to work under a magnetic field of around 3.8 T, resistant to radiation and have a lifetime around 10 years and up to doses of 4 kGy and 2x10^{13} n/cm^2 in the Barrel region and up to 50 times higher in the endcaps.

A Preshower detector is installed in the forward regions. Its main function is to identify two photons with a small distance between them, that are produced from a π decay in order to exclude them from single photon with high momentum measured on the ECAL crystal, that are indistinguishable. The Preshower is a sandwich made of two lead absorbers and two orthogonal layers of silicon strip sensors having the Pb absorber – Si strip sensor – Pb absorber – Si strip sensor sequence. The active sensing area of the ES detector is over a silicon base with a thickness of 320 μm with an area of 61 x 61 mm^2, glued on a ceramic support, containing 32 strips with a pitch of 1.9 mm. It is composed of 4300 detectors providing a total of 1.4x10^5 detector channels, covering an area of 16.5 m^2.

1.2.3 The CMS Hadronic Calorimeter

The CMS Hadronic Calorimeter (HCAL) [10] was designed to measure hadrons, as protons, pions or kaons produced by the LHC collisions. A longitudinal view of half of CMS is shown in fig. 1.8 where the location of all HCAL components are indicated. From the measurements of the hadrons it is possible to do an indirect measurement of the existence of non-interacting particles that do not leave any record when they cross the CMS detector, using as indirect measurement the imbalance momentum or a missing energy. To make this possible the hadronic calorimeter has to be hermetic. This means that it has to contain all the particle energy inside the hadronic calorimeter. In order to be the most hermetic as possible the HCAL was designed with two barrels HB and HO, two endcaps (HE) and two forward (HF) detectors.

The hadronic calorimeter also demands a design with the adequate granularity and mass resolution. The segmented design in towers with a granularity of $\Delta\eta$ x $\Delta\phi$ = 0.087 x 0.087 is adequate for good direct mass resolution. The working concept is based on a sequence of absorber and tiles of fluorescent scintillator material. The HCAL is made of around 10 k individual tiles. To simplify the construction it was assembled in megatiles that have a segmentation of 16(η) x 1(ϕ) or a segmentation of 16(η) x 2(ϕ). Brass was chosen as absorber as it has short interaction length, is non-magnetic and easy to machine. In order to measure the total of the high energy particles inside of the hadron

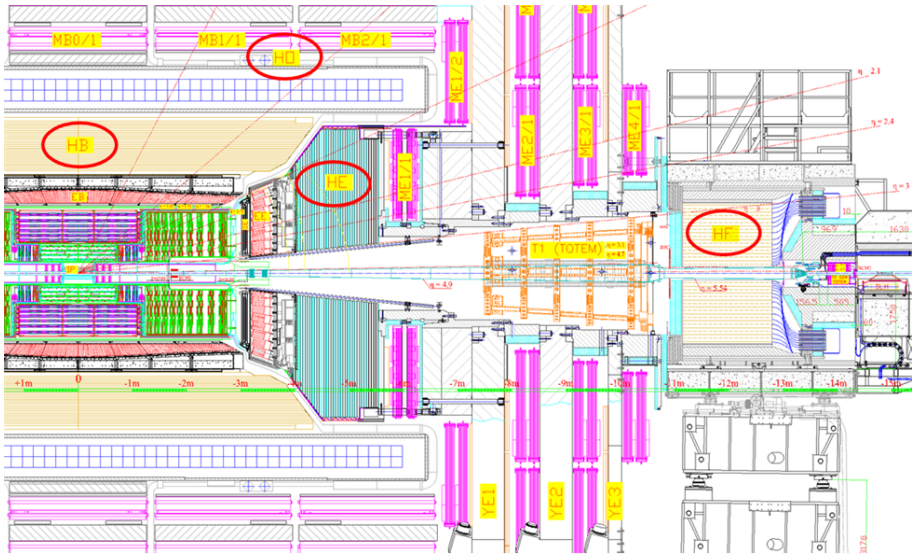

Figure 1.8: Longitudinal 2D view of the CMS detector with all HCAL calorimeters

calorimeter, it is necessary to maximize the amount of absorber; this leaves few space for the scintillating tiles. The concept used was tiles with embedded wavelength-shifting (WLS) fibres that are the optimal solution for the space available. The sensor technology used to measure the light from the fibres was hybrid photomultiplier (HPMT).

The barrel HB is built in two half's and is installed between the ECAL and the magnet (1.77 m $\leq$ R $\leq$ 2.95 m). Each half barrel is made of 18 barrel wedges with 26 tonnes each, with 17 layers - the first fifteen layers of the absorber are made of brass and the last 2 are made of stainless steel for structural reinforcement. The HB has a pseudorapidity range of $0 < |\eta| < 1.4$. A barrel HO or "Tail Catcher" is placed outside the magnet coil in the barrels with a few more two additional layers to measure all the energy that was deposited on the HB without escaping any energy to the outside. The thickness of the scintillators in this barrel is around 10 mm. This HO provides an additional 4 λ at $\eta = 0$. The HO has a pseudorapidity range of $0 < |\eta| < 1.3$ and a segmentation of $\Delta\eta$ x $\Delta\text{ø}$ =0.087 x 0.087.

The Hadronic Endcap modules (HE) are placed behind the ECAL endcap on the muon endcap disks. Each module has 18 wedges with 14 tonnes each, with 19 layers of absorber and with a pseudorapidity range of $1.4 < |\eta| < 3.0$. The HE has geometry with a inner radius of 0.4 m and a outer radius about 3 m with a thickness of 1.8 m. The HF calorimeter is placed on both sides of the detector at 11.1 m away from the interaction point. The HF has a pseudorapidity range of $3.0 < |\eta| < 5.0$. The materials could not be the same, used on the HB/HO and HE due to the high levels of the radiation on the region. The selected absorber on the HF calorimeter was iron. The active material used was quartz fibres embedded on the iron, absorbers installed parallel to the beam pipe. The quartz fibres has a fast response around 10 ns.

1.2.4 The CMS Muon System

The CMS Muon System [11] has the function of efficiently identifying muons and measuring their momenta, with a measuring range from a few GeV up to TeV and triggering. The muons detected during the LHC collisions can be a result from interesting particle decays that can prove theoretical models in study, as the Higgs boson, or measurements of W and Z sources that demand a large rapidity interval. The muon detector is one of the largest ever built, having a muon position resolution in ranges between 50 and 200 μm. The area covered by the muon chambers is around 2,000 m^2 for the barrel detector and an area of 1,500 m^2 for the endcaps. The layout of the muon system is shown in fig. 1.9. The muon detector can provide a measurement of the transverse momentum with a resolution around $(\Delta p_t/p_t) = 10\%$. On both ends of the magnet coil, there are 3 endcaps. The detector should be hermetic in order to measure precise signatures of the decays of the particles in study. The muon detectors were built with three different detector technologies based on gas technology: drift tubes (DT) chambers installed on the barrels, cathode strip chambers (CSC) installed on the endcaps and the resistive plate chambers (RPC) on both barrels and endcaps. The muon system has, in total, an active detection area of 25,000 m^2 in the different layers of the chambers and nearly 1 million channels.

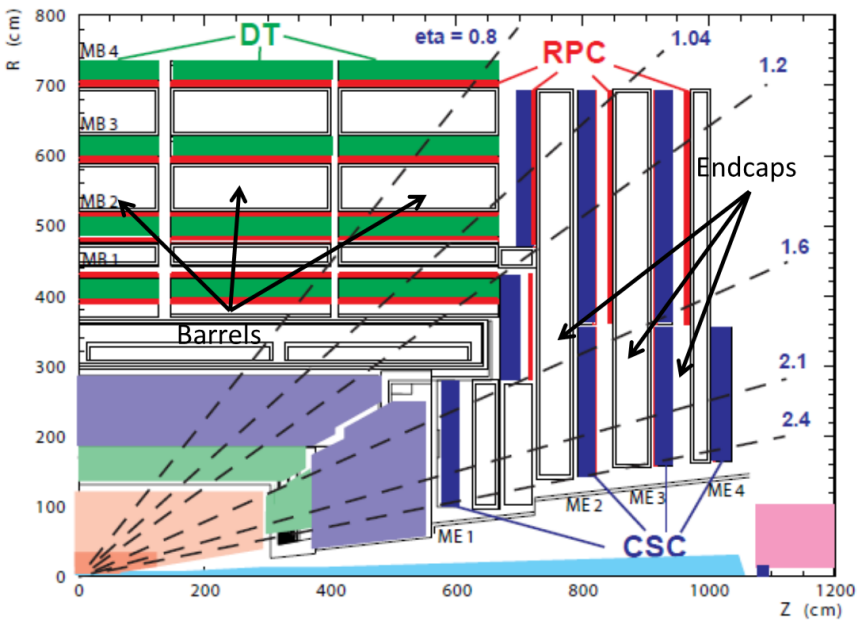

Figure 1.9: Longitudinal 2D layout of a quarter of CMS detector with the different types of muon chambers distribution

The combination of the different technologies according to the background rates and magnetic field ensures an excellent performance of muon detection and efficient triggering in the pseudorapidity range $0 < \eta < 2.4$.

For a neutron background (muon signal) in the range 1-10 (1) Hz/cm^2 the DT is the technology that was selected. In the region where the neutron background is higher 1000 (200) Hz/cm^2, with a higher magnetic field than in the barrels region, it was used the CSC. Both technologies have self-trigger capabilities that are used to measure the momentum and the time of crossing of the muon. The RPC chambers are used in the barrels and endcaps due to their rapidity and accuracy, with a resolution of 1 ns to do the identification of the crossing bunch.

The geometry of the muon barrels (MB) detector consists of 5 cylindrical barrels with 15 m of outer diameter and 2.5 m long. Each barrel is divided into 12 sectors of 30^o azimuthal angle each, and with 4 layers. They are made with rectangular DTs and RPCs parallel to the beam pipe see fig. 1.9 and fig. 1.10. The muon system installed in the barrels can provide a muon vector in space with a precision of ø~100 μm, θ~150 μm and ~ mrad in direction. Each muon chambers installed in the barrel wheels have 12 layers of drift tubes grouped in 3 independent units called SuperLayers (SL). The SL is made of drift cells with a spacial resolution of 250 μm, which has a rectangular shape and a maximum drift length of 2.1 cm, operating at a selected voltage that can determine 400 ns maximum drift time. The gas used on the drift tubes is a mixture of Ar(85%)+CO_2(15%).

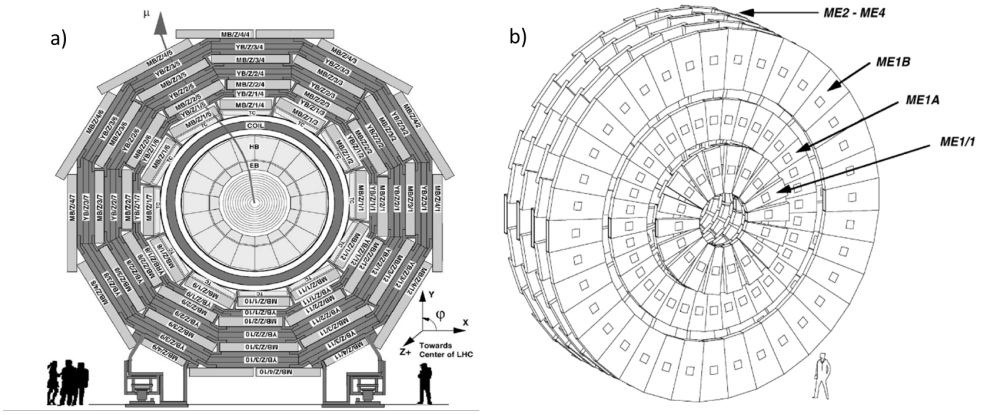

Figure 1.10: a) Transverse view of the CMS detector with an example of one muon crossing the detector and b) Encap Muon detector disks.

The muon endcap (ME) regions have the chambers with the trapezoidal shape organized in series of concentric rings around the beam pipe, as shown in b) fig. 1.10. The total ME consists of four layers. The system consists of 468 CSCs installed on two endcaps. The distribution of the CSCs is made in three chambers rings. Each ring contains 36 chambers. In the second and third rings chambers are overlapped in phi to avoid gaps that could reduce the detector performance. The CSCs use the technology of the multiwire proportional chamber, having 6 anode wires separated with 7 cathode panels with milled strips on them. The strip on the cathode panels runs radially in accordance with the CMS coordinate system. The precision achieved on the ø localization is between 75 μm in the

inner ring chamber and the worst precision is 150 μm The angular resolution ø obtained is around 10 mrad. The fast signal provided by the wires can deliver a precise time resolution (4.5 ns) with a poor spatial resolution between 16 mm and 54 mm. The nominal voltage of operation is 3.6 kV and the gas mixture used is Ar(30%)+CO_2(50%)+CH_4(20%) with a gas volume of 50 m^3 with the sensitive planes of all chambers is around 5000 m^2.

Finally, RPC chambers are used on both endcaps and barrels for trigger purpose. The chambers have double gaps design assembled with two Bakelite sheets of 2 mm thickness interspaced with 2 mm gas gap. In the centre of the gap a plane of readout strips is installed. The two gaps are filled with a gas mixture $C_2H_2F_4$(96.2%)+i-C_4H_{10}(3.5%)+SF_6(0.3%). The mode of operation is in avalanche mode, which can work efficiently with rates up to 10 kHz/cm^2.

The accuracy required in the position of the DT and CSC chambers is determined by the resolution demanded in the reconstruction of the momentum of high energy muons. CMS is designed to achieve a combined (Tracker and Muon system) transverse momentum resolution of 0.5-1% for $P_t \approx$ 10 GeV, 1.5-5% for $P_t \approx$ 100 GeV and 5-20% for $P_t \approx$ 1 TeV. The required accuracy demands the knowledge of the position of the chambers with an accuracy comparable to their resolution. To achieve this, after strict chamber construction specifications, CMS combines precise survey and photogrammetry measurements during detector assembly and installation and an on-line Alignment System [12] which allows a continuous measurement of the position of the chambers. The alignment system monitors large changes in the position due to magnet forces affecting the return yoke, and long-term mechanical instabilities due to thermal effects. The system combines local monitoring of the inner tracker detector and the muon system, and a link system that allows to relate the position of the muon system with respect to the inner tracker detector.

1.2.5 The CASTOR calorimeter

CASTOR (Centauro And Strange Object Research) [13] is one of the two forward calorimeters of the CMS experiment. CASTOR covers a pseudorapidity range from $5.10 < \eta < 6.57$. During the LHC heavy ion collisions this pseudorapidity range is very sensitive for observation and studies of the so-called centauro and strangelet objects, which were initially observed in cosmic ray induced showers [13]. Studies of energy flow in such forward region done for proton-proton, proton-ion and ion-ion collisions are also of high interest for tuning of cosmic ray showers Monte-Carlo generators. Under low luminosity proton-proton collisions CASTOR measurements are valuable for low-x and the diffractive QCD studies [14].

The CASTOR calorimeter is located at 14.37 m away from the interaction point. The dimension of the detector is about 1.5 m in length and 36 cm in diameter. A sketch of the detector is shown in fig. 1.11. Each halves of the detector weighs around 1 tonne. CASTOR is exposed to a residual magnetic field between 0.1 T and 0.16 T with a radiation level between 2 kGy and 20 kGy.

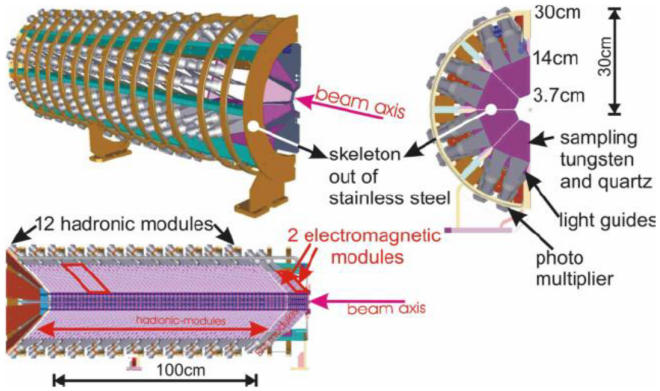

Figure 1.11: Sketch of the CASTOR structure

The detector is longitudinally segmented in 14 modules. The azimuthal segmentation provides 16 sectors. Each module consists of five alternating layers of tungstate and quartz glass (radiation hard fused silica). The layers are installed with an angle of 45^o with respect to the beam axis to provide efficient collection of the Cerenkov light produced by the shower particles in quartz plates. The first two front modules form the electromagnetic (EM) part of the CASTOR are made of 5 mm tungstate and 2 mm thick quartz plates, and provide X_0 = 20.12 g.cm^2 capable of absorbing all electromagnetic shower (originating from electrons or gammas). The next 12 modules are the so-called hadronic (HAD) part, consist of two thicker layers (10 mm tungstate and 4 mm quartz). Each hadronic modules corresponds to an interaction length of λ = 0.77 g.cm^{-2}; together with electromagnetic modules results in λ = 10 g.cm^{-2} for the total CASTOR length. Cerenkov light produced in the quartz plates during shower development are transported with air-core light-guides and to HAMAMATSU R5505 photomultiplier tubes. This type of photomultipliers can work under a magnetic field of up to 0.5 T, with the field lines doing a $\pm 45^o$ angle in relation with the PMT-axis.

1.3 The TOTEM Experiment

The TOTEM experiment [15] is a small experiment when compared to the major LHC experiments and is installed in point 5 together with the CMS detector. TOTEM stands for TOTal cross section, Elastic scattering and diffraction dissociation Measurement. The experiment is focused on the measurement of the proton-proton cross-section, and to the study of elastic and diffractive scattering. The experiment is composed of two tracking

telescopes, T1 centred at z = 9 m and T2 centred at z = 13.5 m installed on both sides of the CMS interaction point (see top part of fig. 1.12). T2 was installed in 2009 on both sides of the detector, while T1 was installed later, in the 2010 winter shutdown. T1 detector is located between the conical surface of the beam pipe and the innermost conical of the CMS endcaps. T2 is between a cylindrical beam pipe with a diameter around 56 mm and the inner shield of the HF calorimeter. The Roman Pot (RP) stations are located outside CMS, at distances of 147 m and 220 m from the CMS interaction point (see bottom part of fig. 1.12).

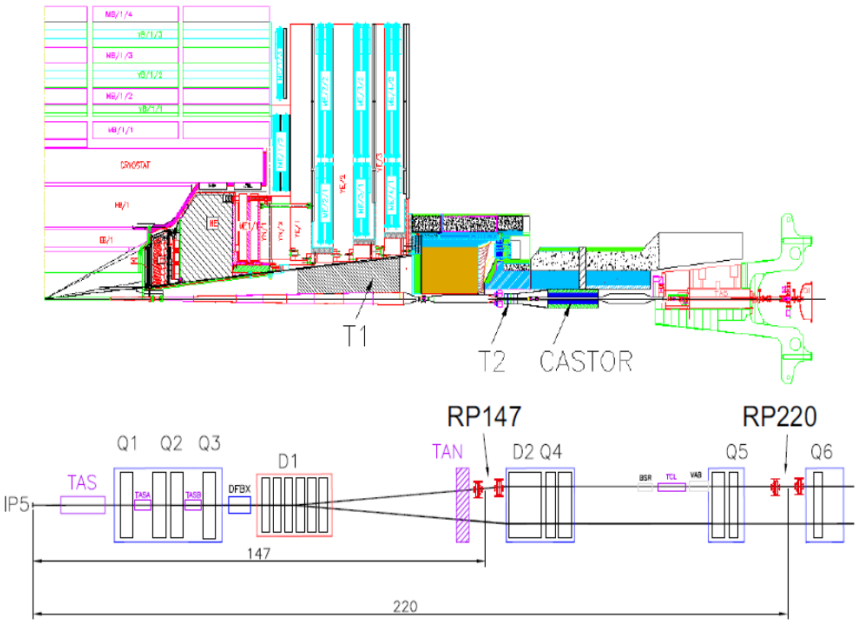

Figure 1.12: Top figure: The T1 and T2 telescopes and CASTOR calorimeter installed on CMS experiment. Bottom figure: The Roman Pots mounted on the LHC beam line.

The technology used for the T1 chambers is the same as for the Cathode Strip Chambers. T2 was made of triple Gas Electron Multipliers (GEM). The T1 telescope consists of four arms and each arm has five planes made of six CSC chambers. The geometry of T2 is shown in fig. 1.13. The T2 telescope uses the GEMs chambers are gas-filled detectors. This technology combines a good spatial resolution with a very high rate capability and a good resistance to radiation. The detector also consists of two arms, each arm has 5 perpendicular planes to the arm with an almost semicircular shape, with an entry for the beam pipe to be centred on the detector with a nominal distance of 9 mm. To guarantee no losses of the detector, the boundaries are overlapped when the detector is closed.

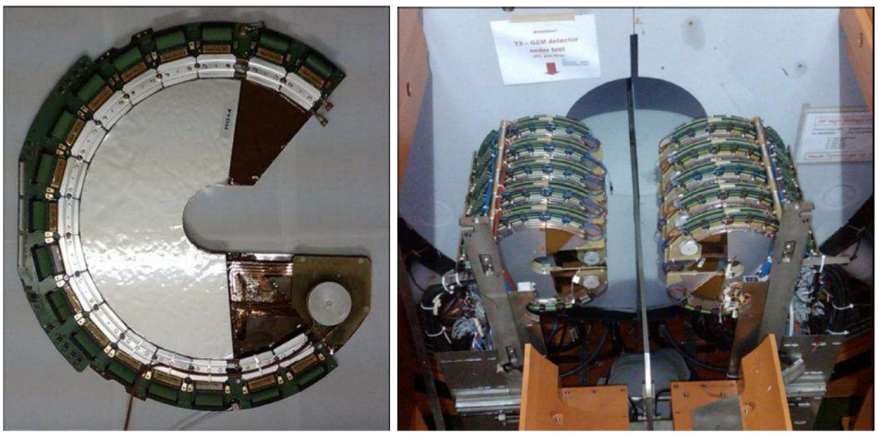

Figure 1.13: Left picture: T2 GEM chamber. Right picture: T2 detector on the floor open position before the insertion on CMS HF calorimeter.

2

The Closing Sensors System

From a mechanical and integration point of view CMS is characterized by its modularity and compactness. The detector is composed of 11 main independent structures that must be fully assembled to allow the operation and disassembled for maintenance or upgrade purposes. The assembly of the structures is usually named "closing" the detector. When closing the detector the nominal distance between the different structures - and from them to the beam pipe tube - must be respected to recover the CMS global position parameters and guarantee detector hermeticity. Tight tolerances should be carefully monitored in order to avoid unwanted collisions among, sometimes delicate, elements and preserve detector integrity. To accomplish this task a dedicated monitoring system, the Closing Sensor System (CSS) has been developed and implemented in CMS. This system constitute the main subject of this thesis. It consists of more than 200 sensors distributed over the whole detector. Built with the main purpose of supervising the closing of CMS and provide an automatic response to the technical team in charge of the mechanical operations, its functionality has been extended and it is now a fully integrated monitoring and control system running in a continuous mode during the periods of detector maintenance and regular operation.

An overview of the Closing Sensors System and the more relevant detector critical safety clearances are presented in this chapter. The designed monitoring system should provide positioning precision at the level of mm and mrad. Critical areas, where tight safety clearances should be satisfied at the assembly phase, were identified by the engineering and integration group at the different parts of the detector. The instrumentation of CSS is distributed along the "central" and "forward" CMS regions. In the following, we will briefly describe the special features for each region. A discussion

of the constraints imposed on the CSS by the LHC and CMS operational conditions is presented at the end of the chapter. A more detailed description of the CSS characteristics and its implementation will be given in the following chapters.

2.1 The Central region

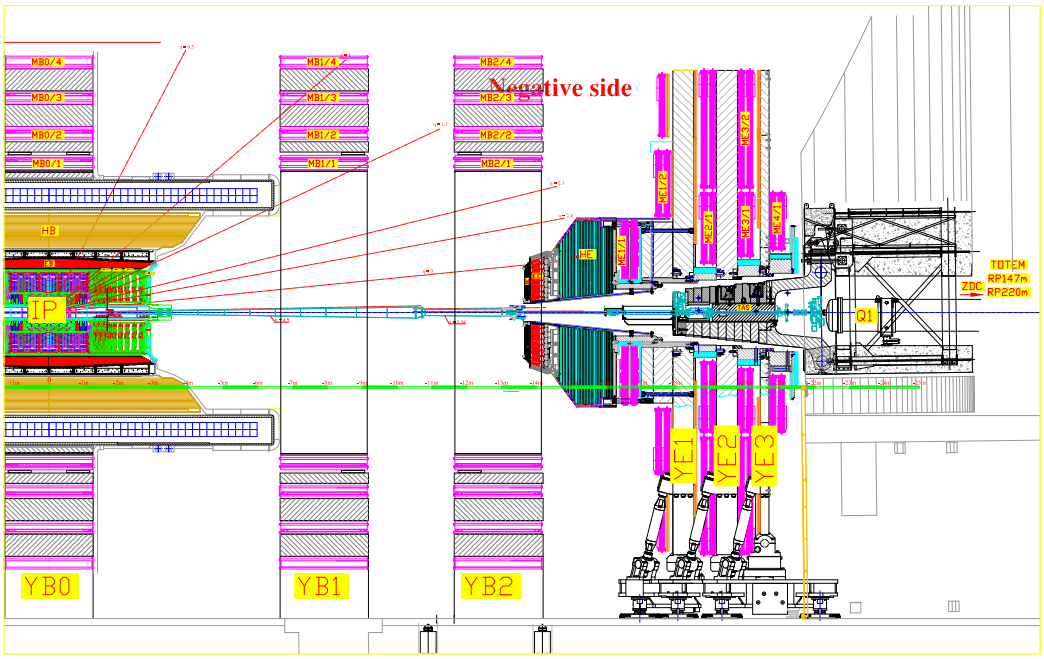

Figure 2.1: Layout of the CMS on the negative side of the main region open

For the purpose of this project, the CMS Central region is defined as consisting of the mechanical structures, services, and sub-detectors systems integrated into the YB0, YB+/-1, 2 and YE+/-1 yoke structures. YB and YE stands for Yoke of the Barrel and Yoke of the Endcap, respectively. While YB0, the central barrel wheel, is located at a fixed position at the centre of the collision cavern, YB+/-1,2 and YE+/-1,2,3 are movable structures. Fig. 2.1 shows these structures, for the minus detector side, in open position, and fig. 2.2 shows the same picture but with the detector closed.

The most critical area in this central region is the so called “53 degrees service crack” shown in fig. 2.3. In the figure, the cone is shown already inserted in the Vac tank (VT). This area, characterized by very tight tolerances once the detector is closed, runs along the end flange boundaries of the Tracker, Electromagnetic Barrel calorimeter (EB) and Hadronic Barrel calorimeter (HB). All cables, services and extra ancillary from those detectors exit from the inside VT volume though a tight path at approximately 53 degrees in polar angle. The operation that allows the insertion of the YE+/-1 nose, where the

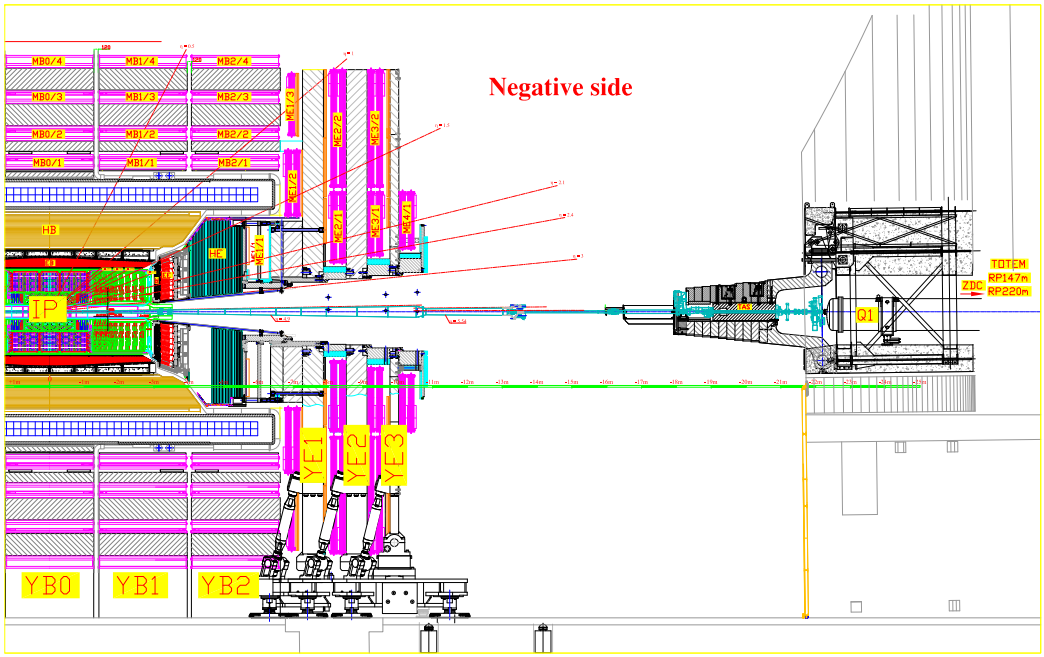

Figure 2.2: Layout of the CMS on the negative side of the main region close

Endcap calorimeters - Electromagnetic (EE), Hadronic (HE), and Endcap Preshower (ES)- sit, into the vacuum tank is a very delicate task. The gap between the two elements is in the order of a few centimetres. The special shape of YE-1 makes, difficult to obtain a smooth and controlled motion of the structure, during the process. Moreover, while the element slides along the beam pipe, the tolerance between the inner boundary of the ES cone on YE-1 (ES-cone sensors group) and the beam pipe also becomes critical.
The CSS instrumentation in this region has the goal to survey that the nominal safety clearances are respected during the closing of YE-1. In order to control the insertion, several sensors were installed along the "53 degrees service crack" and at four positions along the azimuthal angle (phi), to monitor the distance between ES (ES sensors group), EE (EE sensors group), HE (HE1 sensors group) and the patch panels (PP1) (YE-nose sensors group), housing the cables and services from the inner detectors sitting inside the VT. These sensors start measuring when, during the assembly process, YE-1 passes from being supported on "air pads" to stand on the final "grease pads". This transition is especially critical. To keep the beam pipe always, at a safe tolerance, the ES cone was instrumented with radial sensors (ES-cone sensors group) that allows monitoring radial tolerances of the YE-1 with respect to the beam pipe. They are also important to survey the very end of the closing step, when the thermal screen enters inside the ES-cone, at that point, the tolerances are around 3 cm.
After the first closing tests, two more groups of sensors were added to the VT area. A first group, of radial sensors surveys the clearance between the Seal Ring (SR) and the

cylindrical volume of the YE nose (HE2 sensors group). The second group of sensors also mounted, on the seal ring, surveys the closing of YE-1, measuring the distance in the Z coordinate between the seal ring and the YE-1 front face (SR sensors group). These two sets of extra sensors, monitors the distance required for an optimal performance of the sealing ring.

Still in the CMS Central region although less critical from a safety point of view is the region between the inner boundary of the movable barrel wheels (YB+/-1, and 2) and the outside boundary of the VT. The gap between elements has a few centimetres. During the closing/opening process, the movable barrel wheels slide along the periphery of the VT, in particular YB+/-1 travels more than 5 m on top of the VT. A survey of this motion prevents possible local collisions between elements that could damage the services in the muon and coil system. This monitoring also helps to achieve the needed final positioning of the muon detectors. Several sensors are distributed along the inner boundary of YB+/-1,2, as illustrated in fig. 2.4.

Table 2.1 shows the different groups of sensors installed in the CMS central region in the different sub-detectors.

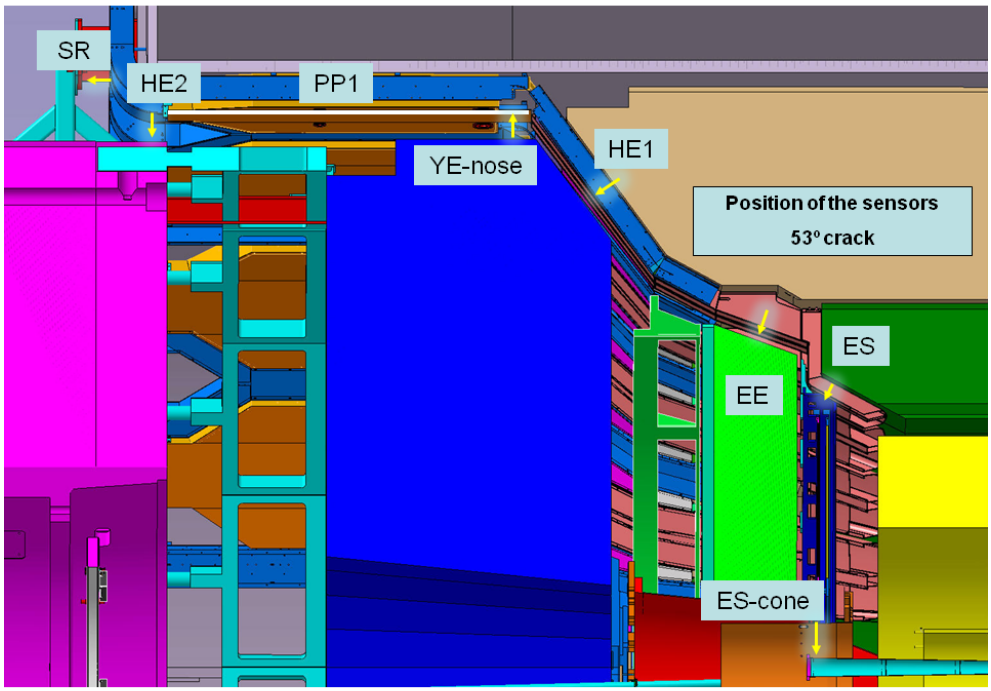

Figure 2.3: 3D engineering drawing of the “53 degree service crack” region, showing the points surveyed by the sensors, here indicated by the yellow arrows in the drawing

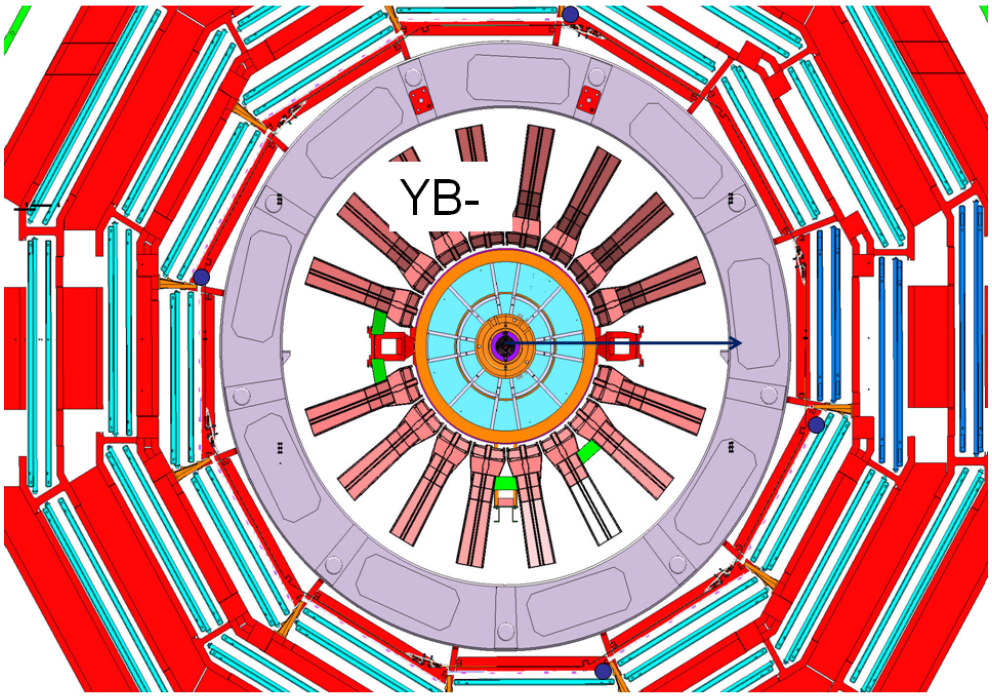

Figure 2.4: Transvese view of one movable barrel wheel in its final position. The distribution of monitoring sensors, in this view, are indicated with blue dots.

2.2 The Forward region

The CMS forward region houses several sub-detectors (see fig. 2.5): the Hadronic Forward calorimeter (HF), the CASTOR calorimeter, and the TOTEM detector composed of two modules called T1 and T2. All these detectors have been described in the previous chapter. In this region there are also dedicated mechanical structures holding the sub-detectors. For instance, the raiser system for HF, the extension platform or green balcony where the CASTOR table sits, the heavy mechanics shielding the detector from machine background and closing the magnetic field, as i.e. the Collar and Rotating shielding, etc.
This area also corresponds, to the most sensitive zone of the beam pipe (CT2), the entry point of the beam pipe to the CMS collision cavern. This zone of the beam pipe corresponds to a diameter around 5.2 cm, and a 0.8 mm wall thickness of the beam pipe in the CASTOR and T2 region. The above sub-detectors are very closely placed around the beam pipe with a minimum nominal distance of 9 mm, making this area the most critical in terms of mechanical tolerance and integrity/safety related issues.
The CSS is intensively used in this region during the processes of sub-detector installation and closing, and to control the detector motions during the powering of the solenoid. The strong magnetic forces induce large motion of the detectors and the associated mechanical structures.
The HF is instrumented with sensors, to monitor the motion along the beam pipe, as

well as with radial distance sensors to monitor the tolerance with respect to the beam pipe. Sensors are installed in the internal and external boundaries of CASTOR and TOTEM detectors, to monitor its position with respect to the beam pipe as well as towards the Rotating Shielding. Finally, other distance devices are used to monitor mechanical structures as the Collar or the CASTOR table. An overview of the region is shown in fig. 2.5.

Table 2.2 shows the different groups of sensors installed in the CMS forward region on the different sub-detectors and other auxiliary mechanical structures. The entries with undefined (nan, not-a-number) nominal distance correspond to measurements done in order to have a reference during the closing process and/or the powering of the magnet, but they are not considered critical from a safety point of view. The beam pipe is a delicate piece, shared by the whole LHC project, damaging it will stop the whole project for a long period of time.

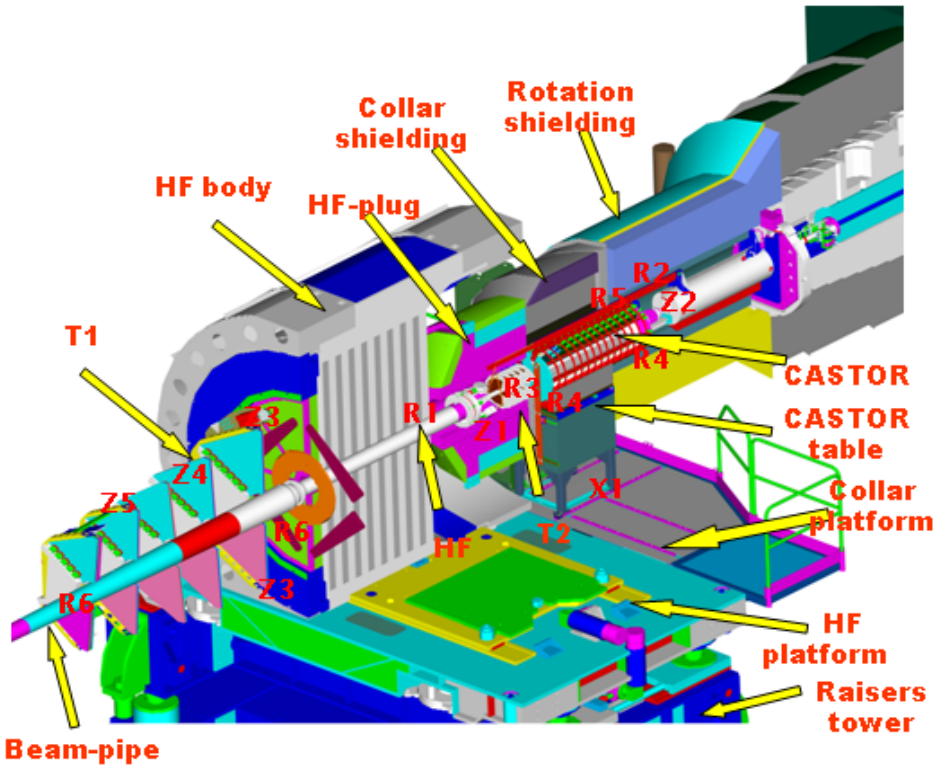

Figure 2.5: Detail of the forward region of the CMS detector. In the drawing the HF, CASTOR and TOTEM T2 are shown, together with details of their mechanical supports. Details of the beam pipe instrumentation are also shown.

Tables 2.1 and 2.2 summarize the surveyed regions in CMS, indicating the nominal distance to be monitored and the current CSS instrumentation. A more detailed description of the present implementation in the detector is given in Chapter 6. Special attention is given to the safety clearance with respect to the beam pipe.

Table 2.1: Sensors distribution in the CMS Central Region (CR)

CMS Central Region				
Location in CMS	Nominal distance (mm)	Number of measuring devices	Sensor distribution	Sensor technology
"53 degrees service crack" Distance from YB0 to ES, EE, HE(HE1)	10	32	3 meas. along η x 4 in ϕ x 2 (Z) sides	Non contact
ES-cone /BP(ES-cone)	50	8	4 in ϕ x 2 (Z) sides	Non contact
movable barrel wheels /outer VT thermal screen (YB-/+1,2)	50	32	4 in ϕ x 2 in Z x 2 wheels (YB+/-1, YB+/-2) x 2 (Z) sides	Non contact
YE+/-1-nose / VT(YE-nose)	40-50	8	4 in ϕ x 2 (Z) sides	Non contact
YE+/-1-nose /Seal Ring(SR)	nan	8	4 in ϕ x 2 (Z) sides	Non contact
End coil / YE+/-1 Seal Ring(HE2)	nan	8	4 in ϕ x 2 (Z) sides	Non contact

2.3 Magnetic field environment

CMS structures experience strong magnetic forces and sizeable deformations when the 4 T solenoid magnet is powered on. Finite element analysis was performed [16] to evaluate the field map as well as the forces generated on the ferromagnetic elements of the detector. The magnetic forces are very large compared to the gravitational forces, such that the later can be neglected. Taking advantage of the cylindrical symmetry around Z and the transverse symmetry in the plane Z = 0, fig. 2.6 from ref [16] shows a quarter of the domain RZ of the detector with the typical flux distribution and the magnetic forces acting on the individual elements of the iron yoke.

The forces generated in the barrel layers and transmitted from ring to ring are substantial, the main component being in the axial direction and pointing inward. They result in compressive axial forces equivalent to about 2,800 tonnes in the second layer, and 3,000 tonnes in the third layer. This requires attention during the design to ensure the stability of the barrel ring construction in the Z direction. The forces developed in the endcap disks are also substantial as can be seen in Table 2.3. They run an equivalent from 4,915 tonnes in the first disk YE+/-1 to 153 tonnes in the third, YE+/-3, disk. Note that the YNose (YN) attached to YE+/-1, has the smaller value since it is inside the magnet coil. The effect of the forces in the yoke were fully analysed and considered in their construction specifications.

The actual magnetic field map was extensively studied with data provided by different

Table 2.2: Sensors distribution in the CMS Forward Region (HF)

CMS Forward Region				
Location in CMS	Nominal distance (mm)	Number of measuring devices	Sensor distribution	Sensor technology
HF / BP	21.0	8	4 in ϕ x 2 (Z) sides	Contact
T2 / BP	9.0	32	3 in ϕ + 1 in entry x 2 half x 2 (Z) sides	Non contact
CASTOR Table / Beam pipe support	nan	8	1 in Z x 2 (Z) side	Non contact
CASTOR Cradle/HF-plug	nan	1	1 in Z x 1 (Z) side	Contact
CASTOR / BP	10.5	10	4 in ϕ(IP) + 6 in ϕ (Non IP) x 1 (Z) sides	Non contact
CASTOR / BP support	nan	5	1 in X + 1 in Y + 1 in Z x 2 (Z) sides	Contact
CASTOR / Rotating Shielding	20.0	6	3 in ϕ x 2 (Z) sides	Non contact
Collar / CASTOR rails	nan	4	2 in X x 2 (Z) sides	Contact
T1 / BP	23.0	12	3 in ϕ x 2 half x 2 (Z) sides	Contact
T1 / YE+/-1	nan	2	1 in Z x 2 (Z) sides	Contact
T1 / YE+/-2	nan	2	1 in Z x 2 (Z) sides	Contact
T1 / YE+/-3	nan	4	2 in Z x 2 (Z) sides	Contact

Table 2.3: Magnetic effects on the YE's

Iron element	YE+/-1	YN	YE+/-2	YE+/-3	Total (tonnes)
Mass of element (tonnes)	706	164	701	347	1,918
Magnetic force equivalent (tonnes)	4,915	1,300	1,700	153	8,068
Mass elem./Mag. force eq.	0.14	0.13	0.41	2.27	0.24

sources [17] including the CSS system. The behaviour under magnetic forces of the various CMS elements in the central region (barrel and endcap structures) predicted by simulation was rather well confirmed with the data. Instead, the field map and magnetic forces in the forward region (detectors and ancillary components) were much more difficult to simulate and only crude estimations were available. Using the data collected during the first powering cycles of the magnet an improved description [18] was possible. The comparison between old and new magnetic field flux distributions is shown in fig. 2.7. The new distribution shows that the magnetic flux is less confined in the barrel region and goes out to the Forward region of the detector, thus having a big impact on the designed mechanics for the forward components.

The instrumentation of the CSS system will be exposed to different magnetic field values depending on its location in the detector. Tables 2.4 and 2.5 list the location and the

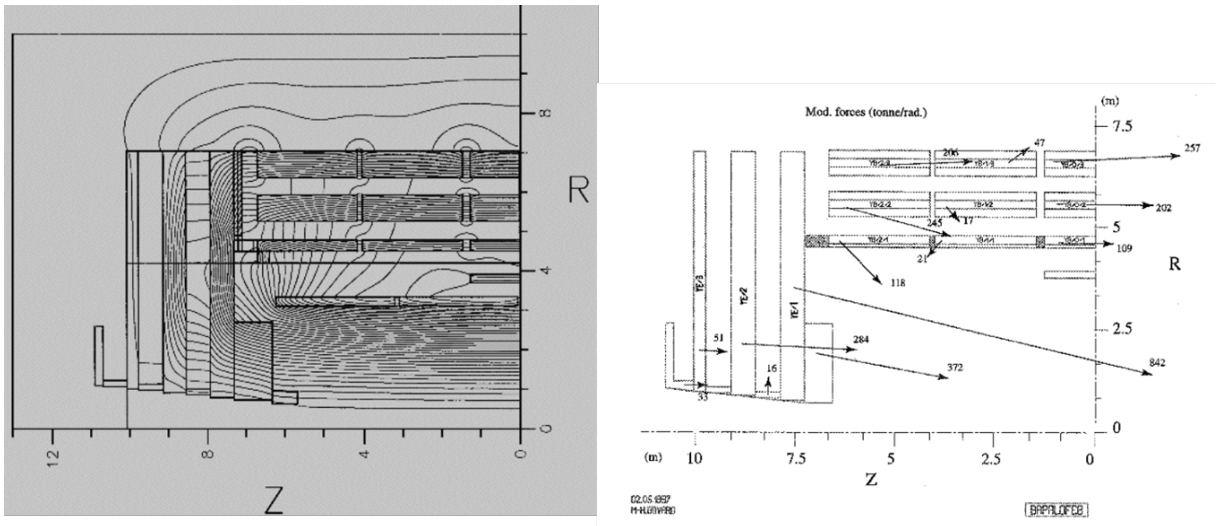

Figure 2.6: (Left) Magnetic flux line distribution; (right) Magnetic forces in tones/rd over elements of the iron yoke.

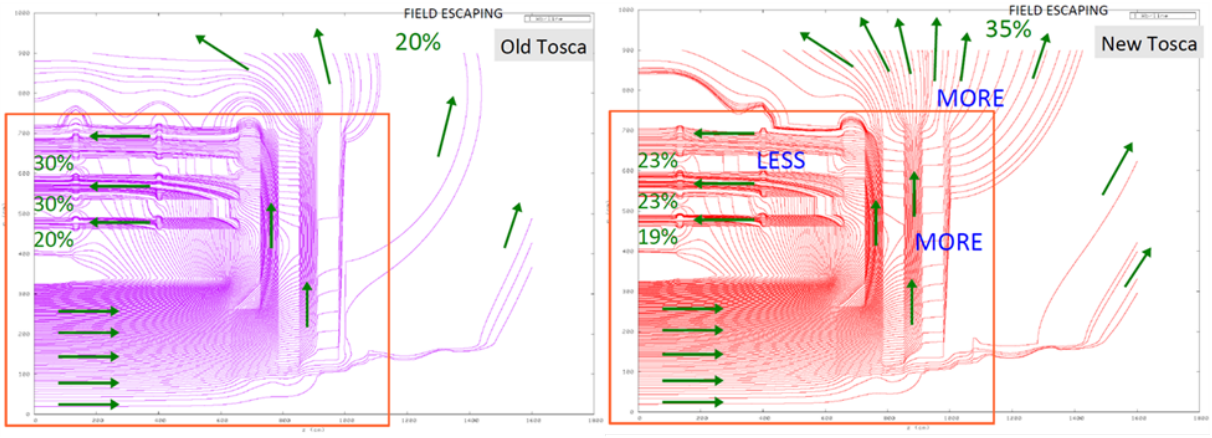

Figure 2.7: Initial (left) and improved (right) magnetic flux distributions

field value for the different sensors (details will be explained in the next chapters) in the central and forward regions of the detector. Making use of the symmetry of the detector, only the regions on the positive Z detector side are given, the same information is valid for the minus detector side changing appropriately the sign of the field components.

Table 2.4: Magnetic field values corresponding to the location of the CSS sensors on the positive side of the Central region of the detector (CMS coordinates in cm)

Central region	Z CMS	R CMS	Bx_plus (T)	By_plus (T)	Bz_plus (T)
ES-CONE	300.0	31.0	0.02049	-0,00016	3.63163
YE-NOSE	468.6	270.9	0.34544	-0,00013	3.51228
ES	299.6	137.7	0.08756	-0,00015	3.66076
EE	336.9	170.9	0.12722	-0,00014	3.62853
HE1	415.3	230.6	0.22988	-0,00014	3.55213
HE2	661.5	277.5	0.65290	-0,00012	1.11726
SR	657.2	284.3	0.69901	-0,00008	1.21047
IP YB+/-1	151.4	405.0	-0.02311	0,00030	-0.22673
NonIP YB+/-1	382.6	405.0	0.26872	0.00134	-0.16938
IP YB+/-2	420.5	405.0	0.28116	0.00187	-0.18873
NonIP YB+/-2	562.7	405.0	0.66806	0.00441	-0.14821

Table 2.5: Magnetic field values corresponding to the location of the CSS sensors on the positive side of the Forward region of the detector (CMS coordinates in cm)

Forward Region	Z CMS	X CMS	Bx_plus (T)	By_plus (T)	Bz_plus (T)
HF RADIAL POT	562.7	12.8	0.04594	-0,00019	2.86033
Z CASTOR BP FLANGE	1340.1	19.7	-0,00002	0	0,00029
T2-IP SIDE	1384.0	4.1	0,00005	0	0.00174
T2-NonIP SIDE	1423.3	4.1	-0.00574	0	0.02164
T1-YE+/-1 POT	797.5	85.0	-0.29680	0,00016	0.98837
T1-YE+/-2 POT	923.0	95.0	-0.02031	0,0001	0.09000
T1-YE+/-3 POT	1013.5	104.0	-0.01335	0,00015	0.00319
T1-LAYER1	755.4	13.7	0.01486	-0,00021	0.73168
T1-LAYER5	1019.4	18.7	0.00389	-0,00011	0.06883
CASTOR IR IP	1442.5	4.1	0.00169	0	0.04237
CASTOR IR NonIP	1582.7	5.3	0.00282	0	0.01121
CASTOR X/Y/Z	1598.2	4.0	0,00079	0	0.00613
CASTOR RS	1580.5	29.3	0.00452	0	0.00557
HF EXT PLUG POT	1434.0	56.0	-0.05682	0	0.20015
CASTOR CRADLE POT	1437.9	-18.1	-0.00785	0	0.07660
Collar	1478.9	173.0	0.03470	0,00058	0.06172

2.4 Radiation environment

The LHC project was designed to reach a nominal luminosity of 10^{34} $cm^{-2}s^{-1}$ at a collision rate of 25 ns and a maximum energy up to 7 TeV per beam. The integrated luminosity estimated for 10 years of LHC running is about 500 fb^{-1}. This will produce a very harsh radiation environment close to the interaction point for materials and equipments. The destructive environment during collisions is one of the major challenges during the design of the whole LHC project. The products of LHC collisions produces a high intensity cascade that in the end results in a large quantity of low energy particles.

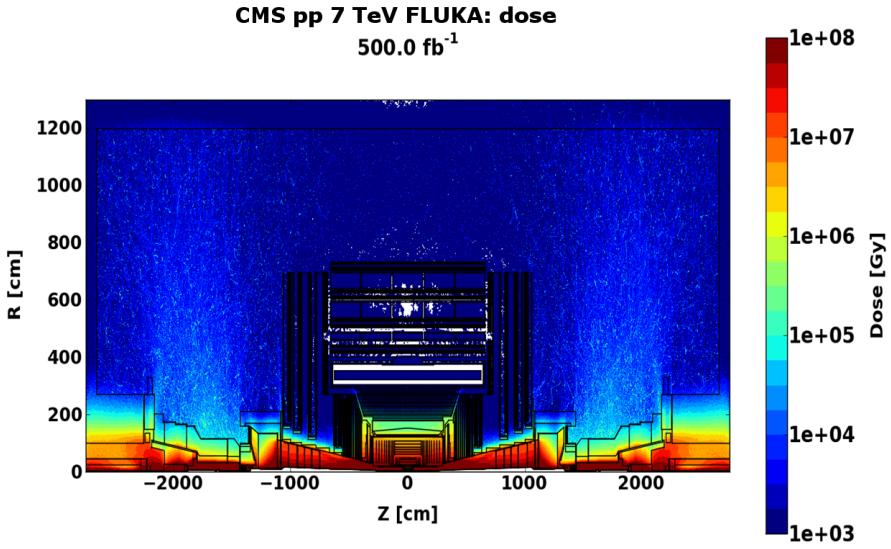

Figure 2.8: Absorbed dose in CMS after 500 fb^{-1} of integrated luminosity delivered by LHC

The absorbed dose or more commonly known as the total ionizing dose (TID) represents the energy deposited in medium by ionizing radiation per unit of mass (kilogram). Its unit is the Gray (Gy). The fluence is the total number of particles per unit area, which is expressed in (cm^{-2}). The expected absorbed dose in CMS, after 500 fb^{-1} delivered luminosity is shown in fig. 2.8. The figure shows that the volume in the proximity to the beam pipe has the highest dose levels in CMS. This is the volume where most of the CSS instrumentation is located.

During the three years of LHC running, the total luminosity recorded by CMS was 29.44 fb^{-1} (see the fig. 2.9). Fig. 2.10 shows the radiation levels on the forward region measured after the opening of CMS in 2013, after the three years of LHC running. The highest dose levels are close to the beam pipe. The CSS instrumentation will be affected by the radiation and this has been assumed in the conception and maintenance of the system. Following the market availability, as explained later, when defining the CSS components were chosen so that a relatively quick replacement is feasible.

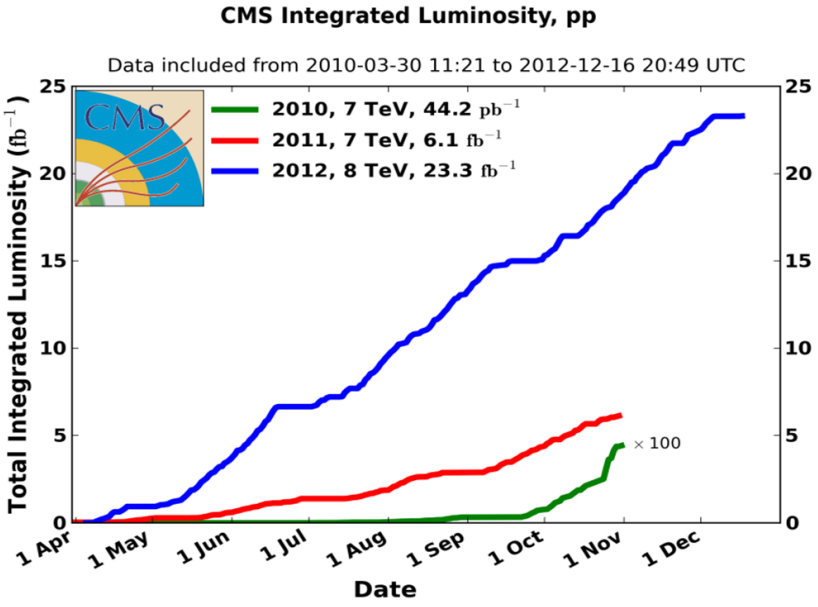

Figure 2.9: Integrated luminosity recorded by CMS over the 3 years of LHC operations.

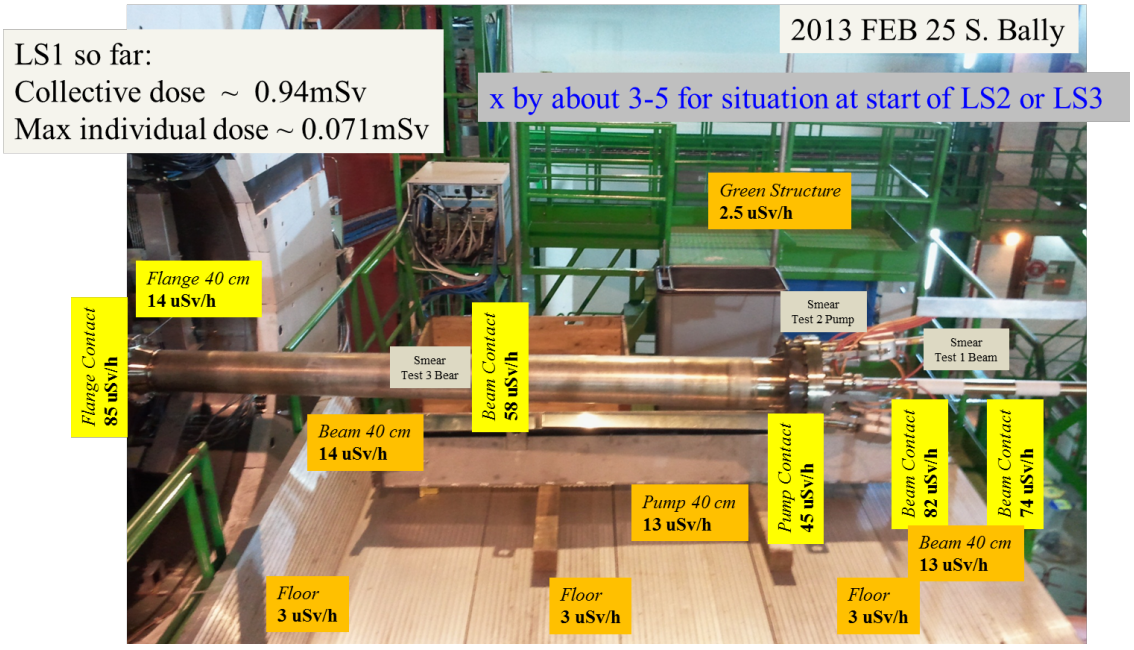

Figure 2.10: Radiation levels on the forward region as measured the 25^{th} February, 2013.

2.5 CMS Detector Control System

The Detector Control System (DCS) [19] is responsible for ensuring the safe, correct and efficient operation of the experiment. The DCS is programmed to automatically react to the LHC operational mode. CMS sub-detectors parameters are set depending on the machine mode and particle beam conditions. The control and monitoring of the CSS system is integrated in the CMS DCS in order to facilitate operations, but it maintains the flexibility to work in a stand-alone mode when needed. The DCS hardware and software follows the standards of LHC project. Its main characteristics are explained below.

The DCS is based on a commercial software PVSS recently named SIMATIC WinCC Open Architecture created by ETM. The process selection of the software was finished in 1999 with demanding criteria of selection by the Joint Controls Project (JCOP), which was a collaboration formed between the four major LHC experiments and the CERN IT/CO group. The program is a Supervisory Control And Data Acquisition (SCADA), which is one of the several types of Industrial Control System (ICS). A framework with several packages integrated as the Finite State Machine (FSM) was built in order to cover common needs of the LHC experiments. The SCADA is a system that could be centralized, or not, with the function of monitoring and controlling a remote process.

The control systems have a structure based on three layers. The first layer is the supervisory, which collects or acquires the data of the process for visualization and operating, analysis, storing, archiving data and control of the process. The second layer, is the front end that performs the readout of the sensors, converts signals into digital information, monitors the hardware status and sends data to the supervisory layer. The third, is the communication layer, which allows the flux of information between the front end layer and the supervisory layer.
SCADA monitors and controls two different types of front end systems - the Remote Terminal/Telemetry Units (RTUs) and Programmable Logic Controller (PLCs) - with the functions of data acquisition, and the capability of taking actions automatically. The RTUs and PLCs are capable of sending status reports of the hardware units to the SCADA. The Human-Machine Interface (HMI) is an important element of the supervisory layer that establishes the interface between the operator and the system. The operator will use a user-friendly Graphical User Interface (GUI) allowing a simple and efficient handling of the system. The communication layer can be used in different network protocols as TCP/IP, Object Linking and Embedding for Process Control (OPC), and other commercial protocols.

The CMS DCS makes an extensive use of the FSM and is a key package that makes possible an implementation and integration for a large-scale control system. The FSM is based on State Management Interface (SMI++) tool that provides the hierarchical

organization of the FSM objects, making possible the monitoring and control of the experiment. The toolkit provides three types of software objects to the developer:

- Control Units (CU): abstract objects corresponding to internal nodes in the hierarchical tree. CUs runs in a separate SMI domain
- Logical Units (LU): represents abstract objects, running within the CU process they are included in
- Device Units (DU): represents a device and is connected to a data point in PVSS

The FSM trees are constructed with logical FSM nodes to setup the control logic with FSM device leaf nodes linked to the hardware. Each sub-detector has its own DCS with its own FSM controlling their systems. The CMS DCS has a main tree, with its own set of rules that will integrate and manage all sub-detectors trees, forming a single tree. With this configuration it is possible to monitor and control the CMS detector, thus reducing the complexity of the system.

2.6 Sensors for CMS

A dedicated task called Sensors for CMS (S4CMS) [20] allows to display in a standardized way the most relevant sensors data, including part of the CSS information, and make it accessible to the entire CMS community through a dedicated screen at the CMS Control Room.
The S4CMS project was developed on a PVSS platform and is integrated on the DCS environment, making it possible a direct connection to the data points, allowing the access to the actual value and historical data. All the documentation of each type of sensor is available. The first version of the project has its location in the groups of sensors in 2D by geographic location and the views available are: Muon, UXC, Vac tank, Beam pipe, HF platform.

3

Sensor Technologies

Distance sensors were chosen to cover the demands of the Closing Sensor System outlined in the previous section. Depending on their location in CMS, the CSS distance sensors have to survey reliably distances ranging from few mm up to few tens of cm. These numbers give an estimate of the total sensor range needed as well as its resolution. A moderate 0.5 mm measurement precision will comply with the requirements established by CMS Technical Coordination and Integration group. Since the aim of CSS is mainly the monitoring of safety clearances rather than making precise alignment, the goal can be largely achieved with standard commercial devices, nevertheless care should be taken for critical safety regions since the "smaller" the measured distance, the bigger the danger for CMS and stronger the requirement on measurement reliability. Different sensor technologies were studied in order to efficiently cover these requirements.
However, no matter what distance should be measured the sensors in CMS will be exposed to radiation and magnetic field. The required immunity or tolerance to both effects being a function of the sensor location in the experimental apparatus. Currently no standard commercial device can fulfil the requirements imposed by the LHC and CMS environment. The scalability and maintenance scenarios drove the decision to use Commercial Off-The-Shelf (COTS) items as far as possible and whatever was available in the market. However, tests as thorough as possible were performed to have a clear idea on the expected lifetime and behaviour of the sensors with magnetic field. Degradation of performance under radiation has been followed during the runs of the LHC. To ensure a reliable operation of the system a regular replacement of sensors is performed whenever the access to them is allowed.

Several distance/proximity sensors were scrutinized in order to provide solutions

for the different ranges. Based on tests and experience, two major sensor groups were defined and used:

Non-contact sensor

- Ultrasound technology sensors
- Infrared technology sensors

Contact sensors

- Potentiometer sensors

A short presentation of the main characteristics and limitations and/or advantages for each sensor type group is given below. A detailed review of the tests done before installation, during integration and the performance of the sensors is given in the next chapters.

3.1 Non-contact sensors

Although non-contact sensors are more vulnerable to radiation, due to their more sophisticated working principle and components, for safety reasons they need to be the default option for most distance measurements in an environment like CMS where we have separate structures sliding among them, or geometrical configurations where direct contact is not allowed or recommended due to the fragility of the elements.
Moreover, non-contact sensors using as measurement variations of a pilot signal that is received back after being reflected on a surface, need an appropriate target. Unfortunately in many occasions the target is often an important source of errors in the distance measurement that must be studied carefully .
The transmitted pilot signal can be any form of electromagnetic wave or mechanical wave; in our implementation we deal with sensors in the infrared range and the ultrasound (sonic frequency 380 kHz information provided by the manufacturer[21]).
These two technologies were adopted due to their availability in the market, their small size, allowing an easy integration in the pre-existing detector structures and their performance over the range of distances to be measured.

3.1.1 Ultrasound Sensors

Ultrasound sensors are based on the principle of the emission of acoustic waves produced by a piezoelectric material, excited by a frequency and reading the echo produced by reflection in the object at the measuring distance. The mechanical waves are produced by a piezoelectric surface that can alternatively be used as an emitter or a receiver, since piezoelectricity is a reversible phenomenon. The emission frequency is that of ultrasounds.

The obvious advantage for this type of sensor within CMS is the fact that, most of the detector surfaces can be used as targets. The basic criterion for ultrasound wave reflection is that the target material cannot be soft, which is easy to be fulfilled in the detector.
In CMS, the ultrasound based sensors faces problems such as, response under specific geometries (beam pipe shape and size), size of the target, vibrations, or large angle between the sensor and target such that can reflect to a direction different from where it is the receiver. Other drawback is that ultrasound sensors do not produce a direct measurement demanding all embedded electronics to provide a linear output signal, making the ones that are commercially available non-radiation tolerant devices.
Ultrasound sensors come pre-calibrated from the manufacturer and, in general, only small corrections have to be applied to their output curves.

The selection of the sensor model (Baumer, UNDK 10U6914/S35A [22] - see fig. 3.1 -) was based on its size and dynamic range. We selected the smallest one available in the market, making possible the integration in all necessary locations in CMS. The dynamic range fulfils the requirements demanded. The performance of the sensor was satisfactory over a wide spectrum of distances and at different angle orientations needed for our application.
Ultrasound sensors of that family can operate under magnetic field with a limited degradation in performance. The price of the sensor is in the medium range, allowing a modest replacement if needed. The ultrasound sensors have been working in the CMS environment from the very first closing test in the CMS cavern up to now without major malfunctioning. Results from the performance studies done on these type of sensors is given in Section 5.2.

3.1.2 Infrared Sensors

Infrared sensing is the second non-contact sensor technology which uses a pilot signal, this time in the infrared region that is reflected and detected back by a receiver (phototransistor). In the infrared sensor case the emitter and the receiver are two separate components. The emitter is Light Emitting Diode (LED) on the infrared range spectrum and the receiver a phototransistor, sensitive to the specific wavelengths emitted by the LED.
For short measuring ranges, infrared sensors offers similar benefits as the ultrasound ones for CMS applications. They are compact and can be easily integrated in pre-existing structures. They are very cheap, such that they can be frequently replaced as needed. However, they need dedicated optical targets for the light reflection and the space for this target has to be found; the target should be radiation tolerant and easy to handle, keeping in mind, for its selection, the special care the beam pipe might require. Moreover, contrary to sound pollution, which is much more limited inside the CMS detector, there is always some “stray” light which can affect the infrared sensor measurements. The sensors can be also sensitive to the magnetic field as discussed in Section 5.1.4.

Stabilized current circuits have to be used for the LED supply in order to ensure a constant light emission. Using a current source allows to position the electronic systems away from the irradiation zones and therefore using conventional parts. In the same way a stabilized voltage source has to be provided to the receiving phototransistor for a stable polarization; this part of the conditioning electronics is positioned closer to the phototransistor itself. Regulators could also be important to protect the system against short circuits on the components exposed to the high levels of radiation. It has to be noted that, the "infrared" sensors might have individual performance curves due to the different gain on the phototransistor.

After testing several models and brands, a very cost effective sensor manufactured by Perkin Elmer (now produced by Excelitas (VTR24F1H model [23] -see fig. 3.1-) was chosen at the first stage of the project.

3.2 Contact sensors

3.2.1 Potentiometers Sensors

This electromechanical device potentiometer is made by an electrically conductive wiper that slides against a fixed resistive element, according to the position, or angle, of an external shaft. For these sensors it is important to have very stable power supply, in order not to add noise in the measurement even when the compensation is done by software. The compensation is done having the voltage with which the potentiometer was calibrated and the voltage with which the sensor is biased.
They are compact and easily available for the required measuring range. They are very robust and best suited for challenging environments as the LHC experiments. They can be easily found in the market. The chosen sensors for this application belongs to the series CLS1300 from Active Sensors [24]. This sensor has been used in a variety of harsh environments such as in the automotive industry or in the aerodynamics industry.

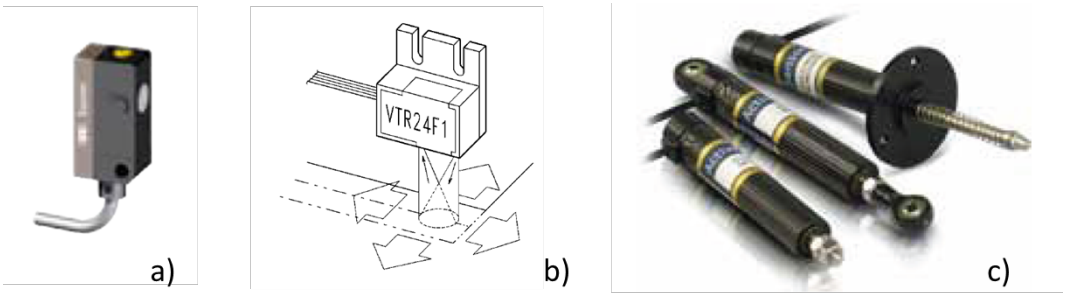

Figure 3.1: Selected CSS devices: ultrasound (left), Infrared (middle), and potentiometer sensors (right).

4

Calibration setup

The different types of sensors used by the CSS system were characterized prior to installation in the detector using a dedicated calibration stand. Given the essential differences between the three types of sensors selected and the different performance tests required for each specific location in the detector various configurations of the experimental setup and acquisition system were used during the calibration campaigns. The main characteristics of the calibration bench are given below. Whenever relevant, details related with specific tests will be given in Chapter 5.

The aim of the performance studies was different for non-contact and contact devices. Special emphasis was given to study the source of systematics uncertainties affecting the different technologies used. Contact sensors are practically immune to most of the external "disturbances" inside CMS. Non-contact sensors are essential for the CMS critical regions. For the latest, the study was mainly focused on the sensor performance for short range, 0-20 mm measurements, the angular orientation sensitivity, and the target performance and response. The calibration tried to reproduce as much as possible in all cases the real operating conditions, which strongly depend on the sensors location in the CMS detector.

4.1 Mechanical bench

To study the sensor response to relative displacements, sensor linearity, the calibration bench was equipped with a 2D motorized platform (Charlyrobot/Isel [25]) with a 0.0125 mm resolution per step. For this application a step of 0.5 mm on the X/Y table was chosen. Extra mechanical support was added to fit the different types and models of sensors. The mechanical support was designed to incorporate the possibility to test different target relative orientations for different types of sensors. The values chosen for

the test were $0\,°$, $5\,°$, $10\,°$, $15\,°$, $20\,°$ and $25\,°$. The angles were selected to understand the behaviour of non-contact sensors in the presence of an unknown angle between the target and the sensor, after its installation in the detector. If the uncertainty on the measurement introduced by angular misalignment was above 2 mm the sensor and or the target were rejected. The basic concept of the mechanical bench and its different components is illustrated in fig. 4.1. In the design, care was taken to reduce possible reflections and phantoms for each type of sensor to test. The design also allowed to study the linearity of the targets surface were tested.

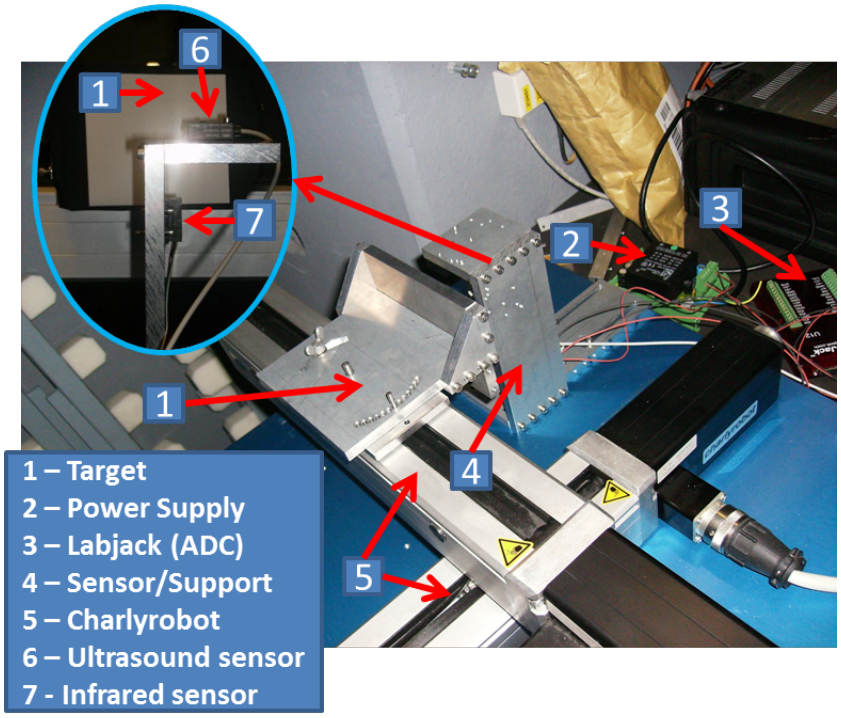

Figure 4.1: Basic design concept of the calibration setup, showing a 2D motorized platform with extra mechanical supports (left). Photograph of the implemented bench (right).

The basic setup was also adapted to test specific target shapes when needed. An example is shown in fig. 4.2, where the mockups of TOTEM (T2) detector and beam pipe were used in order to characterize the behaviour of infrared (see Sec. 5.1.2) and ultrasound sensors (see Sec. 5.2.1) with a cylindrical target as it is the beam pipe.

4.2 Readout electronics

At the early stage of the project, the readout system used for calibration was based on Labjack [26] U12 with USB communication. A diagram of the configuration is displayed in fig. 4.3. Labjack is based on a 0 to 10 V analogue input range with a resolution of 12 bits. The electronic design was optimized to use the full ADC range. The motorized 2D X/Y table was equipped with a control system consisting of a power supply card, two power motor drivers cards for the stepper motors, and a control card with RS232C

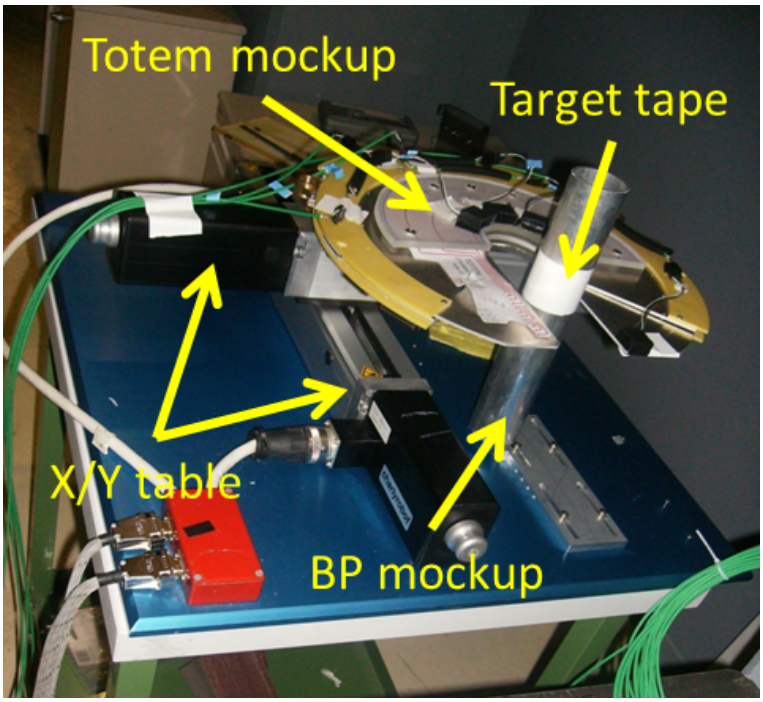

Figure 4.2: Adaptation of the calibration bench to different target shapes. The sensors were placed as required for the TOTEM (T2) detector. For the target a mock-up of beam pipe was used.

communication port to communicate with the computer. Labview [27] was chosen as control and data acquisition system. Later on, following the development of the readout system to be used in the CMS detector, the calibration system was updated, replacing Labjack readout by Beckhoff [28] modules with CANBUS as communications protocol, using a Kvaser PCIcan 4xHS [29] card. The following Beckhoff modules were used:

- "Compact" Bus Coupler BK5150 for CANopen [30], supporting up to 64 Bus Terminals. The module offers automatic baud rate detection up to 1 Mbaud and two address selection switches for address assignment.
- Voltage input modules KL3464: from 0 to 10 V with a resolution of 12 bits
- Current input modules KL3468: from 0 to 20 mA with a resolution of 12 bits
- Output current modules KL4112: from 0 to 20 mA per output channel with 15/16 bits of resolution and is electrically isolated. Ground potential for the output channels of a Bus Terminal was common with the 24 VDC supply. The output stages are powered by the 24 V supply.
- Power control modules KM2002: combines 16 digital outputs with eight channels per plug connector in a compact design that can provide a maximum current of 0.5 A with a voltage of 24 V.

- Bus end terminal modules KL9010: for data exchange between the Bus Coupler and the Bus Terminals. Each group of Beckhoff modules must be terminated at the right end with a KL9010 bus end terminal. The bus end terminal does not have any other function or connection facility.

The final version of the calibration electronics consists of two groups of Beckhoff modules and a ELMB [31] (Embedded Local Monitor Board) card, as for real operations in the detector. The arrangement of the crate front panel is shown in fig. 4.4. The calibration readout crate was used for the debugging of the hardware as well as for the calibration of the sensors. During the various calibration campaigns the readout setup was adapted to the specific demands of the different sensor configurations implemented in the detector.

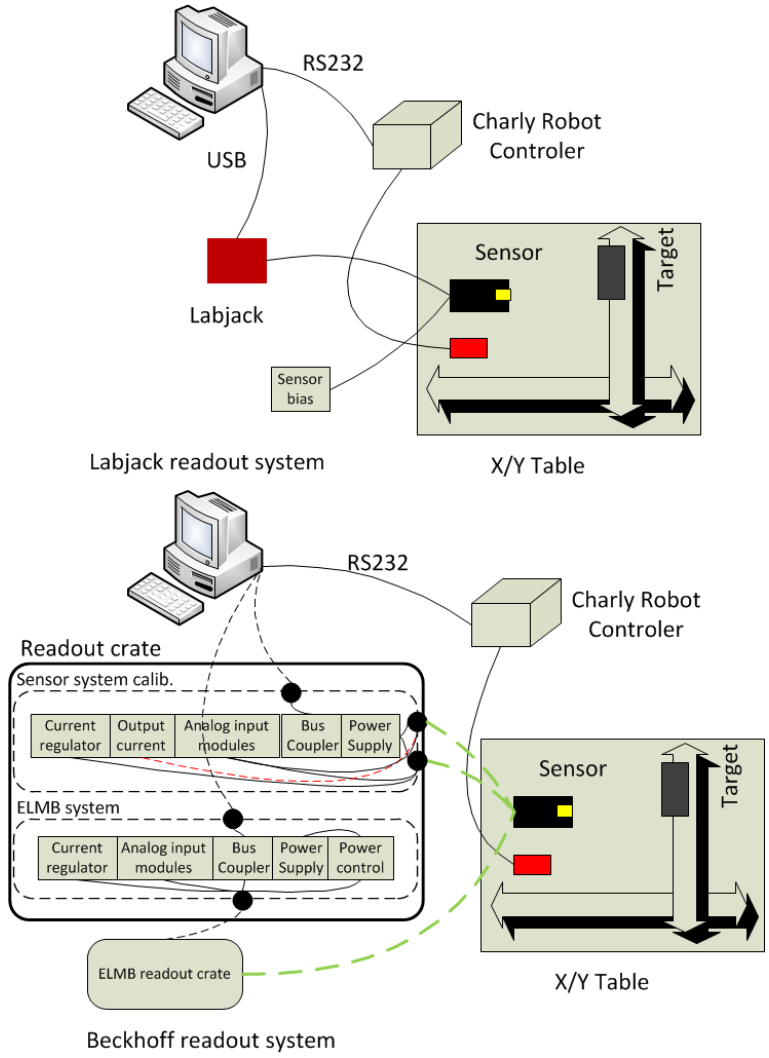

Figure 4.3: Diagram of the calibration system based on Labjack and Beckhoff modules.

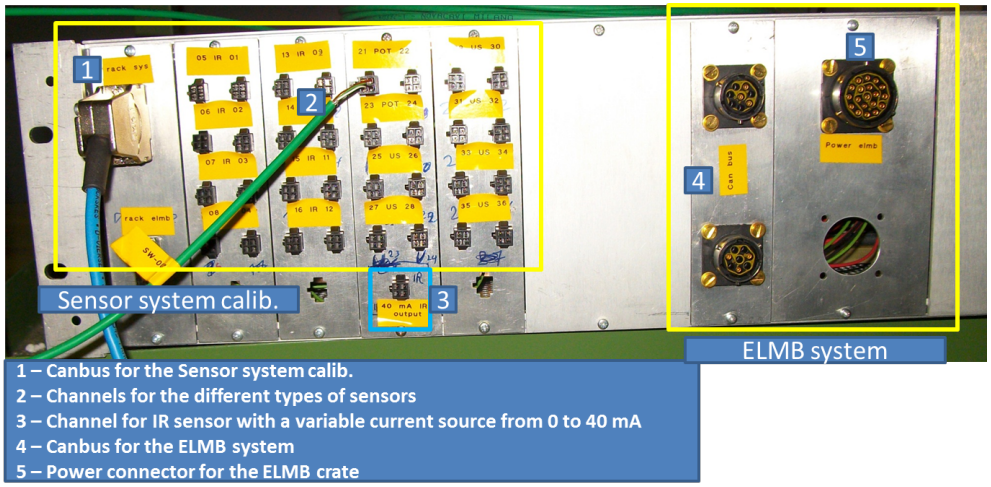

Figure 4.4: Front panel of the calibration crate.

4.3 Data acquisition and control software

The Labview platform allows an easy integration and migration between the different readout's hardware during the development period. The Labview program used was designed to allow flexibility for the different types of hardware used and different configuration tests required for the qualification of the system. The program works like a finite state machine and follows a sequence of operations as shown in fig. 4.5. Before the calibration starts a series of settings are defined: the configuration of the speed of the stepper motor; the current in the LED; the range of calibration; the number of cycles, etc. A series of buttons allows to define the reference point for the controller of the X/Y table ("Home" button), and to move the target with the defined start position ("Initial position" button). The calibration of the sensor starts when the button "Start" is selected, which initiates the sequence by setting the X/Y table in the initial position. Normally, the values recorded are the value of the position calculated by software, the output voltage from the sensor under calibration, the position provided by the controller, the number of cycles calculated, the configuration of the other peripheral hardware being used for the calibration, etc.. An additional routine was programmed to calculate the time needed for a calibration cycle. This feature allows time optimization such that several sensors can be calibrated in a short period of time. An example of the software developed is shown in fig. 4.6. Data trends were introduced to monitoring of the calibration process of the sensors.

The Labview panel shown in fig. 4.6, is identical for all types of sensors used, with the difference of the channel used for calibration. The different functions enumerated in fig. 4.6 are described below:

1. This panel displays the table with the parameters (relative position (mm), voltage (V), position provided by the controller of the X/Y table converted in (mm), value

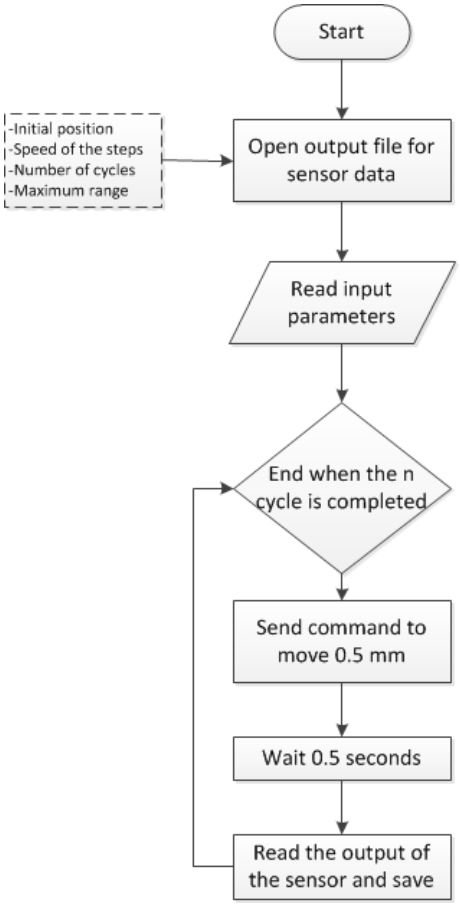

Figure 4.5: Layout of the Labview program.

of the position sent to the table, and absolute position (mm)) saved on the text file. These values allow to obtain the sensor parameters after the fit.

2. Indicates the configuration for the communication with the X/Y table, the values provided by the table during the operating period. The status of the communications with the Beckhoff modules is on the corner of the text box, it provides the counts that are converted to a voltage on the text box below.

3. Configuration of the different parameters of the X/Y table as: speed, initial position, maximum range of the sensor, and number of the cycles to be performed. The time spent for the calibration of the sensor is also available.

4. The graphics shows the displacement (mm) versus voltage (V) during the calibration period.

5. The button "Initial position" is to set the position on the X/Y table defined by the user. The button "Start" indicates the start of the calibration. The button "Home position" is to set the zero position on the X/Y table. The button "Stop" is to stop the full cycle. The date of the calibration can also be included.

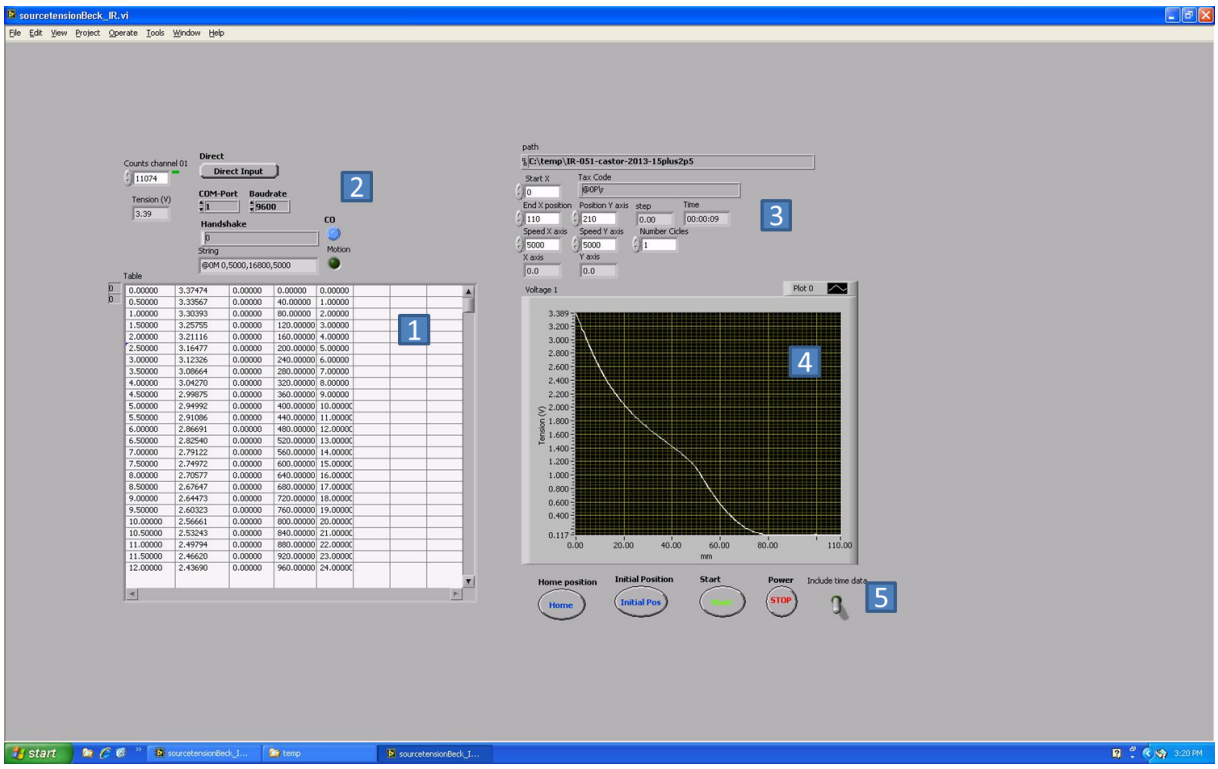

Figure 4.6: Example of the Labview panel used for the calibration of infrared sensors.

5

Sensor calibration and performance results

A summary of the most relevant aspects of the calibration process as well as the main results obtained in the different calibration campaigns are presented in this Chapter.

Optical sensors need an overall characterization to optimize its performance. Emphasis is given to the study of short distance measurements, target selection and response, and the influence of the sensor/target angular orientation on the response of the sensor. After a full characterization specific calibration functions are obtained per sensor unit allowing to unambiguously assign a distance measurement to a given output voltage. The influence of the magnetic field was understood with dedicated tests and the capability of the sensors to reliably measure under special target configurations was also established.
Ultrasound sensors present some advantage with respect to the infrared technology. They are easy to integrate and more immune to the presence of magnetic fields. Unfortunately unlike the optical models they are not suited for special target geometries as needed in the forward region of CMS.
Finally contact potentiometers are the simplest and most robust technology but unfortunately their implementation in the detector is limited since they require a direct contact with the target that is not always possible.

As a result of the calibration, the operation parameters for each type of sensor were defined, and the requirements in terms of dynamic range, reproducibility and measurement precision for all technologies was guarantee.

5.1 Optical sensors: infrared PerkinElmer VTR24F1H

Technical information for this model provided by the manufacturer is summarized in fig. 5.1. The figure shows the schematics of the sensor configuration as well as the typical response of the sensors for a given target. Note that, the target used by the manufacturer, a Kodak Card Cat# 1527795 for two reflectance values, is no longer available.

Optical sensors need an overall performance test with emphasis on small distance measurements and small misalignment between the sensor and the target that could introduce extra errors on the measurements. As they need targets to function, significant effort was dedicated finding and testing the most appropriate target for the required performance. The characteristic curves of the sensors had to be explored to obtain the optimal sensor performance reducing the effects of unknown error as most as possible. External factors like ambient light, magnetic field, possible cable/conditioning, or other target dependencies have been studied, and their impact has been estimated.

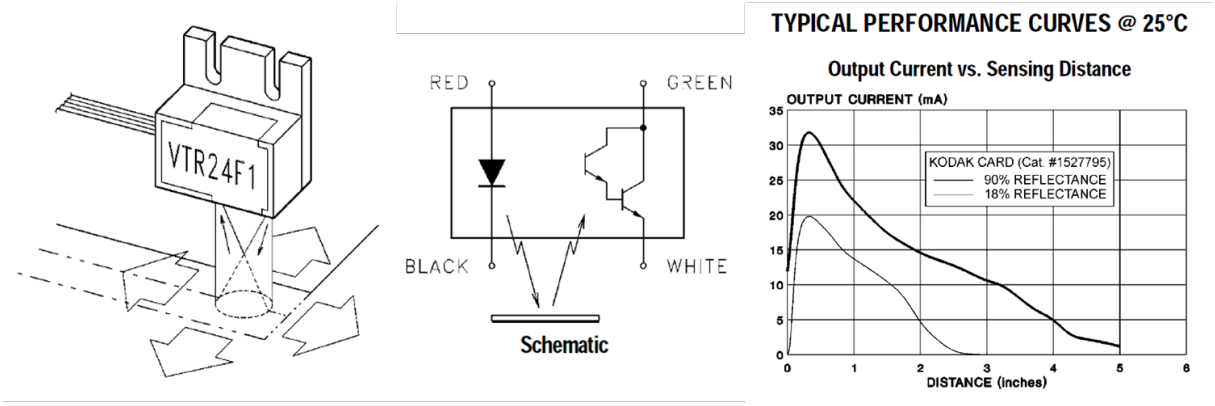

Figure 5.1: Information from the manufacturer: Drawing of the sensor shape (left); wiring connections (middle); typical calibration of the sensor (right).

$$RLed = \frac{U1 - ULed}{lLed} \tag{5.1}$$

The working parameters relevant to study the performance of sensors, are shown in fig. 5.2. The polarization of the LED (RLed); and the LED current, (ILed). The relation among them is given by Equation 5.1, where U1 is the input voltage, and ULed the voltage drop in the LED.
For the LED, the operation values selected were: U1 = 5 V, ILed = 15 mA, and assuming ULed = 1.7 V results in R1 = 220 Ω. The polarization of the phototransistor was set to R2 = 120 Ω. The relative calibration constant (relation between light intensity recorded and distance) is obtained from the study of the variation of the current in the resistor which, will produce, a variation of the voltage across the resistor, due to the change of light intensity at the base of the phototransistor.

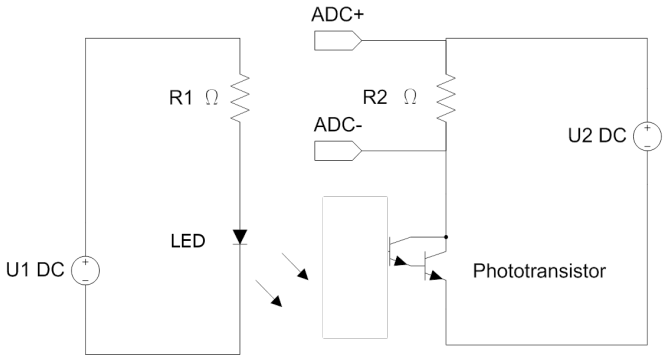

Figure 5.2: Schematics of the electronic circuit for infrared sensors.

Table 5.1 summarizes the electrical values used in the test. The listed values were obtained using always the same unit from the bunch of infrared sensors that have been purchased. The maximum range is obtained when the sensor reaches the lowest current crossing R1 that is the dark current produced internally by the phototransistor, which is different on each infrared sensors. It is also known as the dark current by the leakage current.
Although the recommended maximum LED current for a continuous emitter is ∼40 mA, to optimize the sensor's dynamic range, a test was done changing the LED resistance in order to increase the LED current. The values studied are summarized in Table 5.2 together with other relevant settings. For this test the input voltage for the LED and the phototransistor was set at 5 V. A 25 m cable (reference D 345 FRNS TP from SAB Associated Wire Products) was used to simulate real operating conditions. Although a higher value of the current than the advised by the manufacturer could have impact on the LED lifetime, no degradation in the functionality of the sensor was observed during the test period time. The result of the test is shown in fig. 5.3.

Table 5.1: Summary of the electrical values used in the LED current test (see text)

LED resistance (Ω)	**Phototransistor resistance (Ω)**	**Cable (m)**	**LED Current (mA)**	**Max Range (mm)**
120	120	25	28,9	98
120	220	25	28,9	101
85	120	25	39,6	113
65	120	25	50,0	119
50	120	25	62,6	127

In the final system, the resistors (fig. 5.2) were replaced by the respective regulators in order to provide the parameters, obtained from the different studies, which optimize the sensor performance. The current and voltage regulators, produced by the Istituto Nazionale di Fisica Nucleare (INFN) are key elements to allow a proper operation of the sensor, i.e. stable signals, when long distance are required between the sensor and the

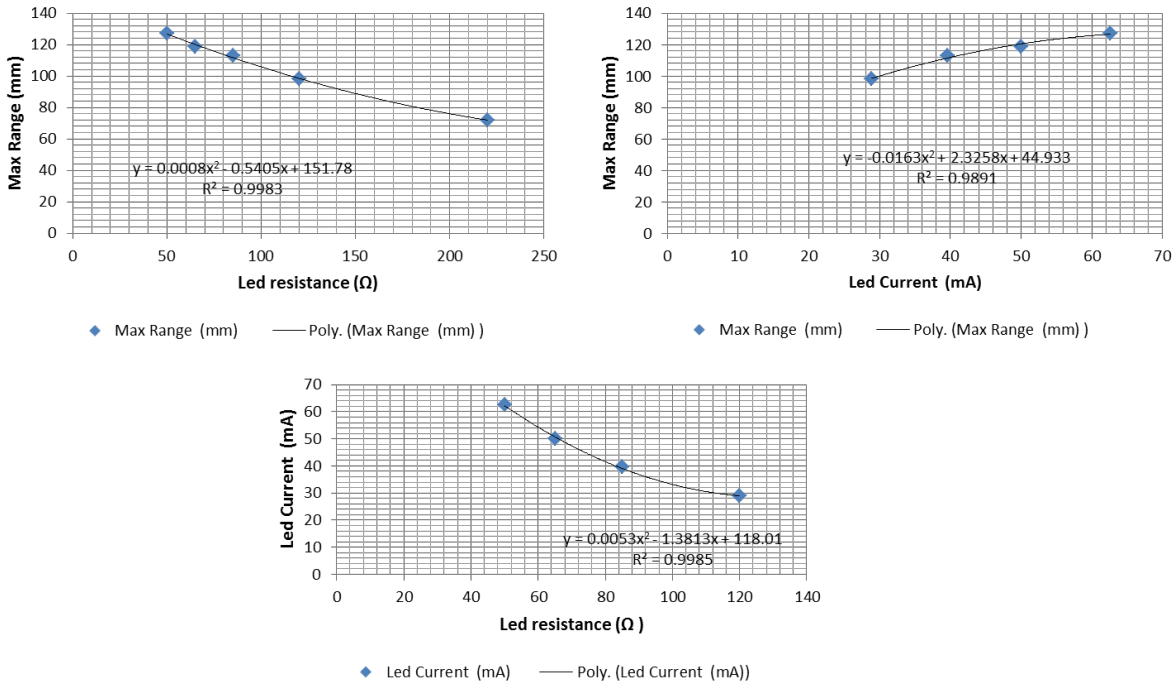

Figure 5.3: Dynamic range versus LED resistance (top-left); Dynamic range versus LED current (top-right); LED current versus LED resistance (bottom).

readout system. In the final implementation in CMS, the current source is mounted in the readout crate and the voltage source is mounted next to the sensor. The final electrical operational values are given in Table 5.2. The value of the current was selected to provide the range required.

Table 5.2: Final operational electrical values used in the system.

Current constant source	Voltage constant source
35 mA	3.33 V

Studies performed to obtain the sensors "calibration function" are described in the following sections. Calibration functions give the relation between the output sensor response and the relative distance target-sensor. To unambiguously assign a distance measurement to a given output voltage the calibration functions must be a bijective function, in other words: the voltage measured for one position plus the interval error associated. The next sections report the studies of different effects affecting the sensor measurement.

5.1.1 Sensor response *versus* target type and relative target/sensor orientation

Infrared sensors working as distance measurement devices need a surface/target that provides a diffuse reflection and constant index of reflection in the whole area being measured. When sensor and target sit in different distant structures a robust measurement also requires a small dependence as possible on the relative orientation of those elements. A study of the calibration function for infrared sensors and its dependence on target type and angular orientation was done using a generic calibration setup as shown in fig. 5.4. During the calibration process the target was kept in a fix position, while the sensor moves with constants steps of typically 0.5 mm. The target orientation can be varied from $0\,^{\circ}$ to $20\,^{\circ}$ in steps of approximately $5\,^{\circ}$.

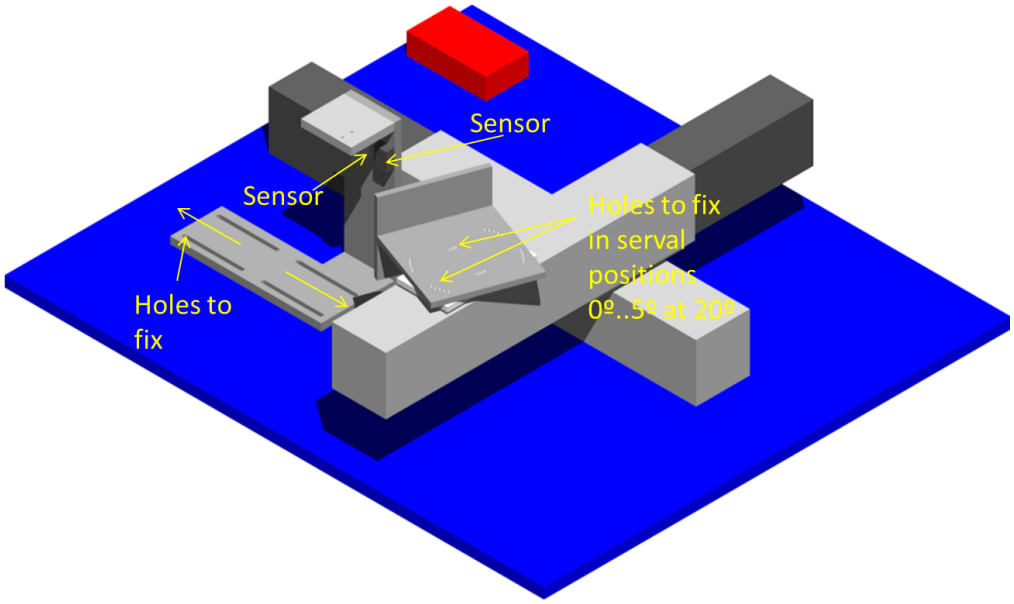

Figure 5.4: Sketch of the calibration bench

An intensive search for commercially available suitable reflective surfaces was done. The reflector must fulfil the following specifications: a) provide a large dynamic range, as much as possible; b) minimize angular dependence; and c) have a good surface homogeneity. It is worth to note that, the first requirement is somehow in contradiction with the other two. In overall, diffuse materials are more suitable to fulfil at the same time all the listed requirements. The different target types tested are listed in Table 5.3.

The targets that show better performance were anodize aluminium (TT9) and Gaffa

Table 5.3: Target Types (TT) used in the test.

Target Type	Distributer	Code Reference	Short description
TT1	CERN	44.01.30.005.6	ALUM.SH. 99,5 HF-HD EP. 0,5
TT2	FARNELL	7054981	TAPE, POLYCLOTH LAMINATE WHITE
TT3	FARNELL	8169780	WATERPROOF GAFFA TAPE WHITE
TT4	FARNELL	3069448	TESA TAPE, DS POLYPROP 38 mm
TT5	FARNELL	1676634	LEMARK - CT50050W - MAGTAPE MATT WHITE
TT6	FARNELL	1394774	GAFFA TAPE 50 mm x 50 m MATT WHITE
TT7	FARNELL	1530134	Sensor Retro reflective Tape
TT8	FARNELL	4626722	TAPE, REFLECTIVE, 5 m
TT9			Common aluminium anodize crate front panel
TT10	3M		Microspheres reflector

Tape-Matt tape (TT6). In what follow, we present test results for only these two types of targets and in particular for the type TT6. TT6 is easier to handle and therefore it was selected for the final implementation in the CMS detector. First tests were done using the Labjack readout described above and characterized by a moderated ADC resolution. The working parameters for the electronic circuit are: R1 = 220 Ω and R2 = 120 Ω. A 25 m long cable from the sensor to the readout electronics was used. Fig. 5.5 shows the sensor response to different distances between sensor and target, as measured in the motorized platform. The initial calibration position corresponds to the smallest distance target-sensor.

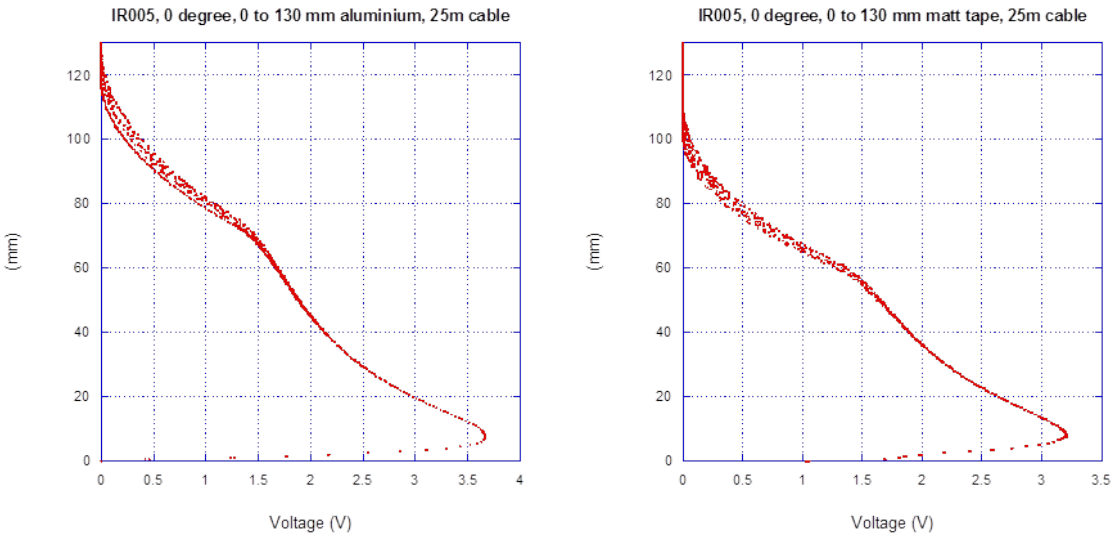

Figure 5.5: Distance (in mm) target-sensor as measured by the motorized platform versus sensor response (output voltage in V) for Target types TT9 (left) and TT6 (right).

Figure 5.5 shows for the two type of tapes that there is a zone, corresponding to the

first approx. 10 mm, where it is not possible to assign a single voltage value. This zone, commonly called "blind zone", it is not useful for distance measurement applications. In what follows, measurements and systematic studies are presented only for target-sensor distance above 10 mm. Voltage range and response shape are very similar for both types of targets as well. A dispersion of the values in the tail of the distributions is also observed, which indicates degradation in the measurement precision for large target-sensor distances. The dynamic range in both cases is comparable, although TT9 shows a slightly larger range (up to about 120 mm) compared with TT6 (up to about 100 mm).

The reproducibility of the calibration parameters was studied in a dedicated test lasting approx. 30 hours where the complete calibration cycle (scanning a relative distance target-sensor from 10 mm to 90 mm) was performed 30 times. The set of calibration parameters obtained was found to be very similar among the different cycles. The residuals, defined as the difference between the actual measurement and the fitted value, although small - in all cases within the range [-0.1, +0.1] mm - show a systematic trend due to the fixed order of the optimized calibration function used in this exercise (see fig. 5.6). Although the test was performed varying for a relative target-sensor distance from 10 mm to 90 mm, in the figure the relative distance is shown after subtracting the first 10 mm (blind zone). For this test the angular orientation target-sensor was set to 10 degrees.

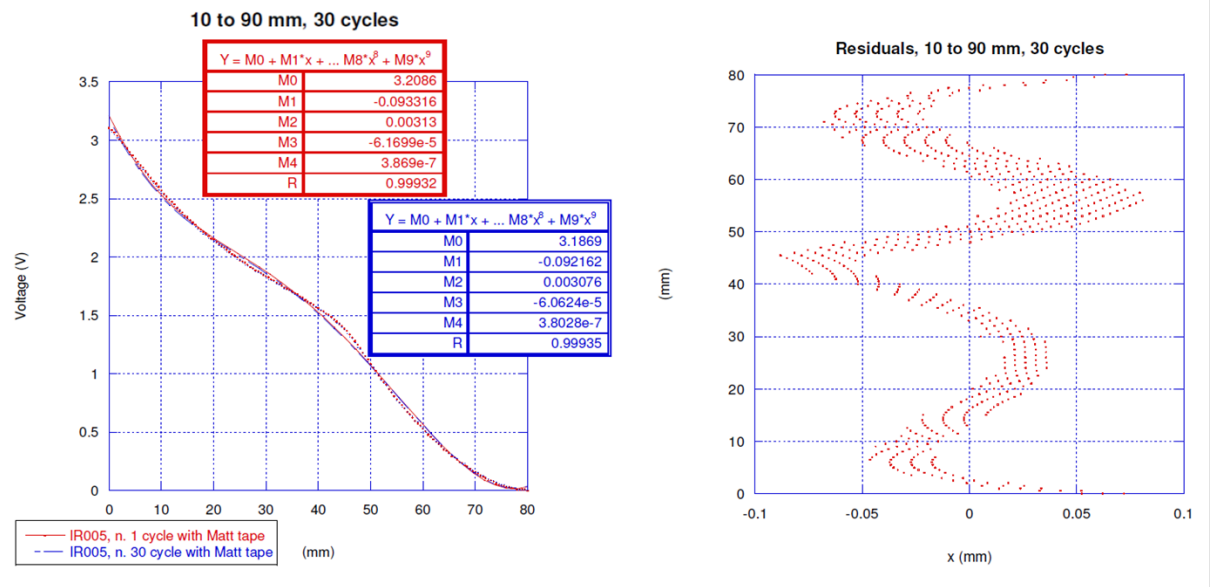

Figure 5.6: Results for 30 measurement cycles: (left) output voltage versus distance target-sensor (in mm) as measured by the motorized platform (see text). A fit to the data is superimposed. Fit results for the first and last cycle are also shown. (right) Distance target-sensor (in mm) versus residuals (in mm). The effect of the digitalization of the signal is due to the moderate resolution of the ADC used in this measurement. TT6 were used in all measurements.

To quantify the effect of the target homogeneity, in the calibration parameters, a test was performed fixing the relative target-sensor distance at a fixed value, and moving the sensor parallel to the target surface. The results are displayed in fig. 5.7 for different relative distances 10, 20, 30, 50, 70 and 100 mm. The voltage variation due to the parallel scan, although small in all cases, increases for a long relative distance target-sensor due to the shape of the response curve (see Table 5.4). This result confirms that, the quality of the target is not degrading significantly the performance of the sensor.

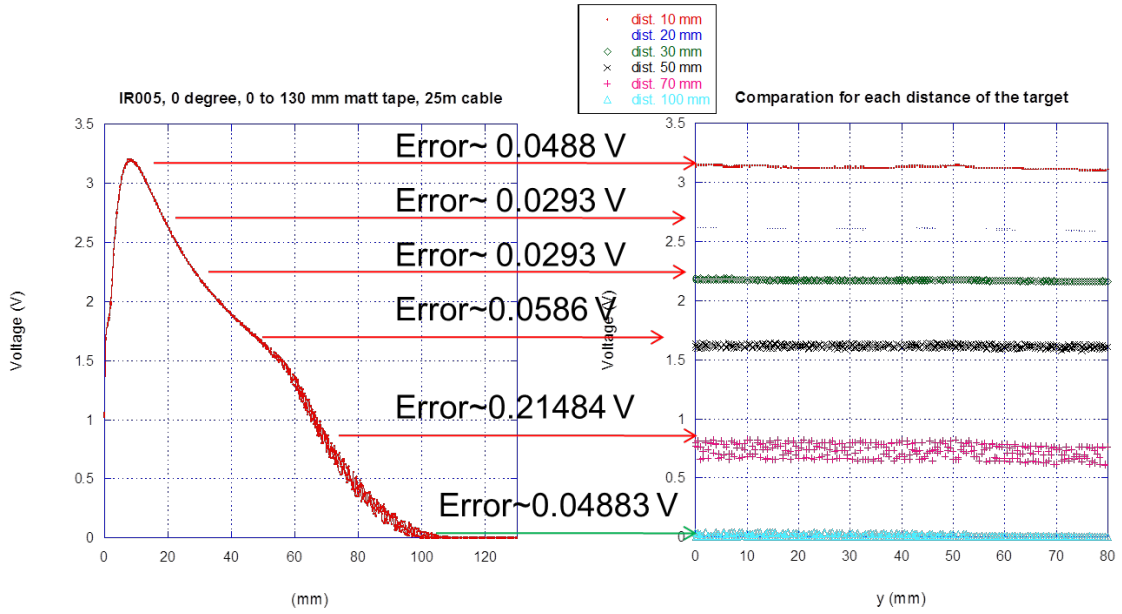

Figure 5.7: Sensor response with parallel motion target-sensor as recorded at six fixed relative distances target-sensor (10, 20, 30, 50, 70 and 100 mm). The left plot shows the calibration curve distance versus voltage, while the right plot shows the measured voltage for the five relative distances with a parallel movement. The error is represents difference between minimum and maximum.

Table 5.4: Maximum and minimum voltage recorded during the parallel scan sensor-target performed for six fixed relative distance target-sensor.

	Dist. 10 mm	Dist. 20 mm	Dist. 30 mm	Dist. 50 mm	Dist. 70 mm	Dist. 100 mm
Max.	3.15430 V	2.61719 V	2.18750 V	1.64063 V	0.82031 V	0.03906 V
Min.	3.10547 V	2.58789 V	2.15820 V	1.58203 V	0.60547 V	-0.00977 V
Error	0.04883 V	0.02930 V	0.02930 V	0.05860 V	0.21484 V	0.04883 V

The influence of the relative orientation between target and sensor was also studied. Sensors were calibrated at different relative orientations. The target was rotated at fixed angles: $0°$, $5°$, $10°$, and $15°$ and a complete calibration cycle was recorded for each orientation. The results are shown in fig. 5.8. The left plot shows the calibration curve obtained for a given sensor. A small discontinuity is observed for short range relative

distances but the dispersion increases for larger ranges. To quantify the error introduced by the lack of parallelism between the two objects, target and sensor, the $0\,^{\circ}$ calibration constants is used to analyse the data recorded for the rest of the orientations. Residuals, defined as the difference between the measurement and the fit result, are shown in the two right plots of the same figure. The upper bound of the residuals is assigned as systematic error. The middle plot shows large errors for long relative distances (larger than 40 mm) and large angular orientations. The right plot is a zoom of the same results but for short relative distance target-sensor, up to 30 mm. The errors in this case are limited to 1-2 mm for relative angles below $10\,^{\circ}$. This result is considered acceptable, since the operation conditions foreseen for these sensors are mainly in the short relative distance range. Moreover the relative orientation in real conditions is not expected to be larger than approx. $5\,^{\circ}$.

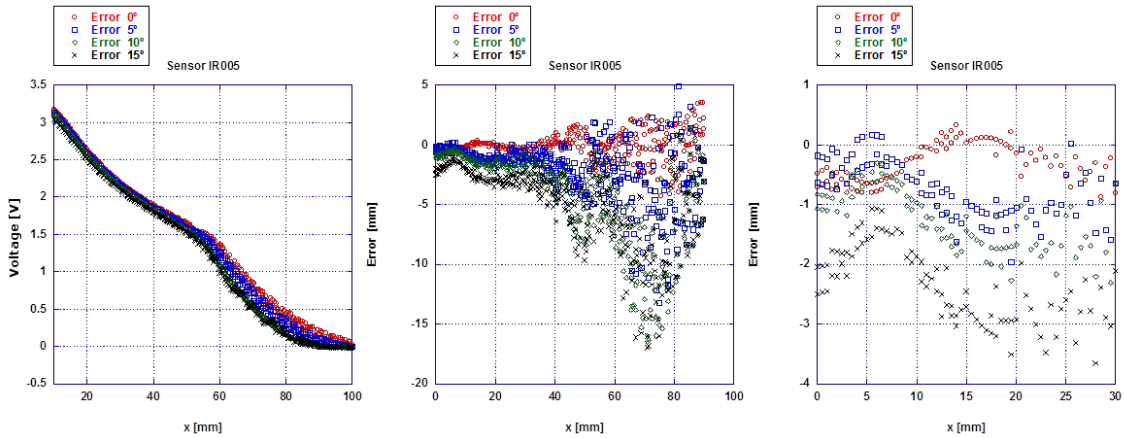

Figure 5.8: Calibration curves for the same sensor sample in different angular configuration target-sensor (left). Error (see text) for the whole relative distance target-sensor (right-top). The right-bottom plots shows the same error but zoomed in the short distance range.

The entire set of tests described above was repeated for a subsample of sensors, using the final readout configuration as implemented in the detector. All the results were found compatible. To conclude, the systematic error introduced in distance measurement using infrared sensors with the selected target TT6 are mainly due to non parallelism between target and sensor and non homogeneity of the target surface. The first will account for +/- 1 mm for short range distances, up to approx. 30 mm. The later is limited to +/-0.6 mm in the whole dynamic range of the sensor.
Finally, fig. 5.9 shows the calibration curve for a set of 16 sensors from two production batches. This set was used for the first closing of the CMS detector in April 2008. Two conclusions emerge from this figure: a) the dynamic range varies significantly from unit to unit; b) sensor units labelled as IR005 show a much shorter dynamic range. These units belong to a second purchased batch; an incorrect plastic filter was added in front of the sensor window. The problem was identified and fixed.

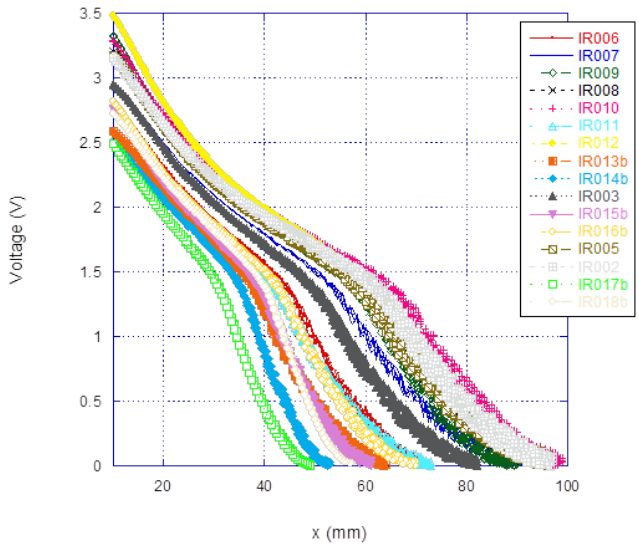

Figure 5.9: Calibration curves for a subset of 16 infrared sensors bellowing to two different production batches.

5.1.2 Sensor response with cylindrical target geometry (beam pipe geometry)

Infrared sensors are used in special critical areas of the detector, namely the forward region. Sensors are installed along the inner diameter of TOTEM T2 and CASTOR detectors in order to monitor its distance to the beam pipe, which acts as a target. Given the special cylindrical geometry of the beam pipe, and the stringent requirements in terms of measurement precision, a dedicated test was carried out to certify the functionality of the sensors under these conditions. One of the calibration setups used is shown in fig. 5.10, where a mockup of the beam pipe is placed at the target position. In the region of TOTEM T2 and CASTOR the corresponding beam pipe zone is called CT2. Mockups of CT2, as provided by the Beam Division, were tested. The mockup consists of a cylindrical stainless steel tube with two different surfaces, as used in the detector, one machined and another one non-machined. The machined side has a diameter of 59.75 mm while the non-machined side had a diameter of 60.75 mm.

Three different studies were performed: a) using a naked beam pipe as target by the machined and non-machined sides; and b) using the standard TT6 target adapted to the beam pipe shape.

The motivation for a) is to try to avoid any extra material added to the beam pipe, because its delicate nature, and also because the amount of radiation the extra material

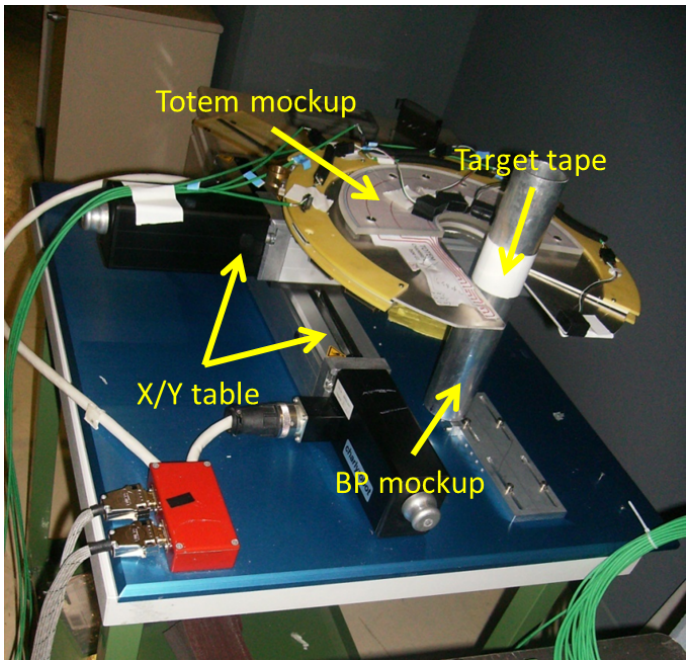

Figure 5.10: One of the calibration setups using a mockup of the CMS beam pipe, CT2, as target.

will be exposed to. To minimize systematic uncertainties in the comparison of the results the same sensor unit and same (final) readout electronics were used for tests. The three calibrations are presented in fig. 5.11. Plots on the left correspond to the corresponding calibration curve, while the right side plots are the residuals for each case. The top plots show the results using TT6 target, the middle row corresponds to the case of a naked non-machined beam pipe used as a target and finally, the bottom plots correspond to the case when the naked machined beam pipe is used as a target.

From the calibration curves (left plots of fig. 5.11) we can conclude: a) the beam pipe surface (non-machined and machined) has higher reflectivity than the TT6 target, as well as lower diffusion power. The maximum voltage recorded increases from 3.5 V, 4 V, and 5 V for TT6, non-machined beam pipe, and machined beam pipe respectively. Note that in the bottom-left plot corresponding to the beam pipe machined surface the calibration curve differs from the other cases, it does not present the typical shape (”inflexion” observed medium-long distances) thus allowing a lower order polynomial used to fit the data. For the three cases, the residuals indicate that intrinsic calibration errors are within 0.5 mm or less. The double line in the residuals is due to a known malfunctioning of the motorized calibration table.
As a result of the above comparison, one might conclude that the three targets could be suitable for the measurement. Unfortunately, the less diffuse nature of the stainless steel, together with the small radius of CT2 induce larger systematic errors as appears from angular dependence or surface homogeneity tests. Fig. 5.12, and fig. 5.13 summarize the

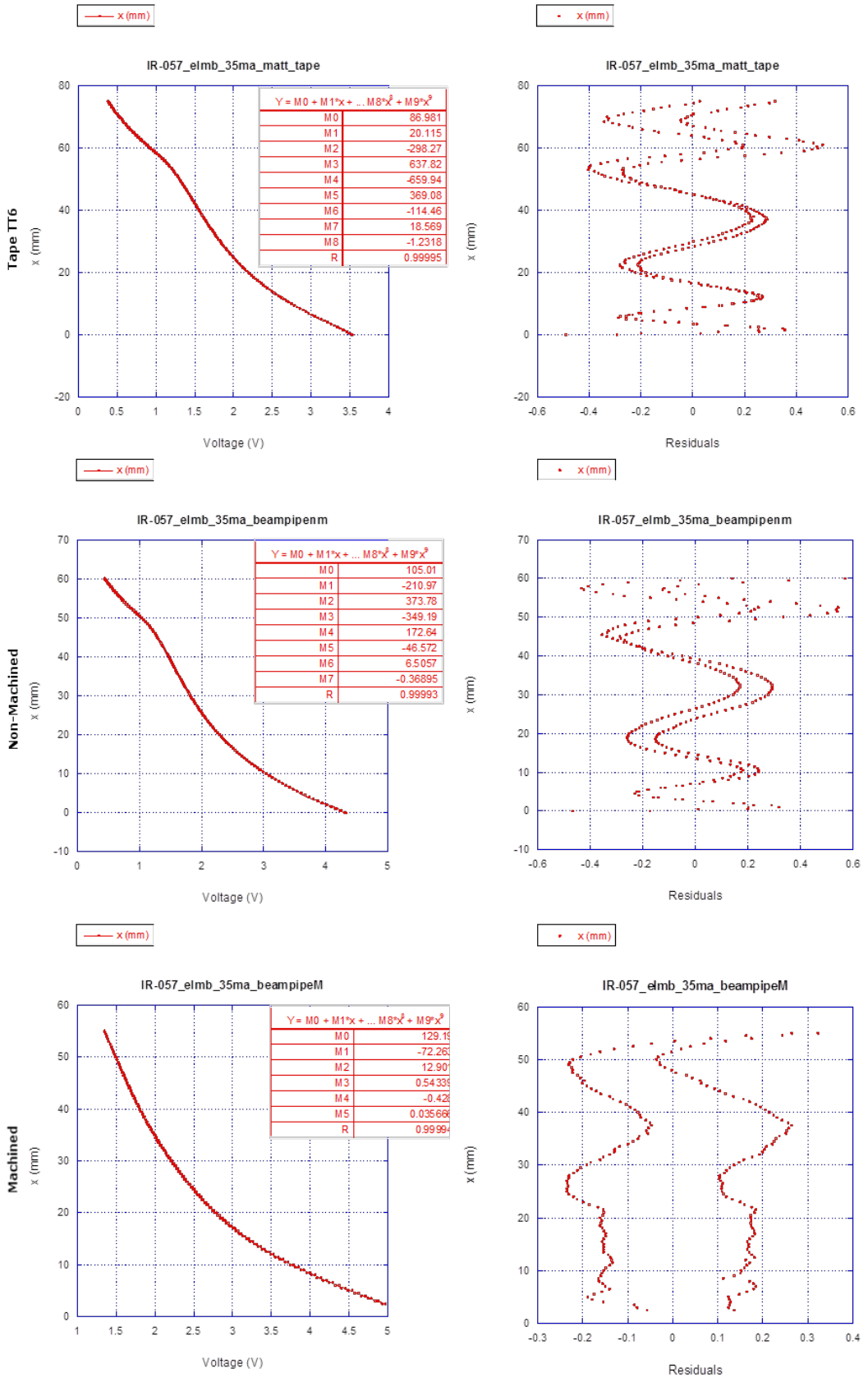

Figure 5.11: Calibration results using three target types: TT6 (top); naked beam pipe stainless steel non-machined side (middle); and naked beam pipe stainless steel machined side (bottom).

results from the angular dependence and surface homogeneity studies, respectively. From the test changing the relative target-sensor orientation, the non-machine stainless steel surface shows a rather acceptable performance. Small misalignment of angles (below $5\,^{\circ}$) will induce errors limited to +/- 1 mm. Instead, the machined stainless steel shows larger dependences, with a sizeable effect even at the shortest relative distances. In the case of the study of the parallel motion, at several constant target-sensor distances, measurements are affected by error above 1 mm in the whole dynamic range tested. Although the overall performance of the stainless steel is not too bad, it was considered safer to maintain for this application the same type of target (TT6) as for the rest of the detector. The complexity of the location and the difficult accessibility to this zone can introduce extra complications, not fully considered (or present) in the calibration laboratory.

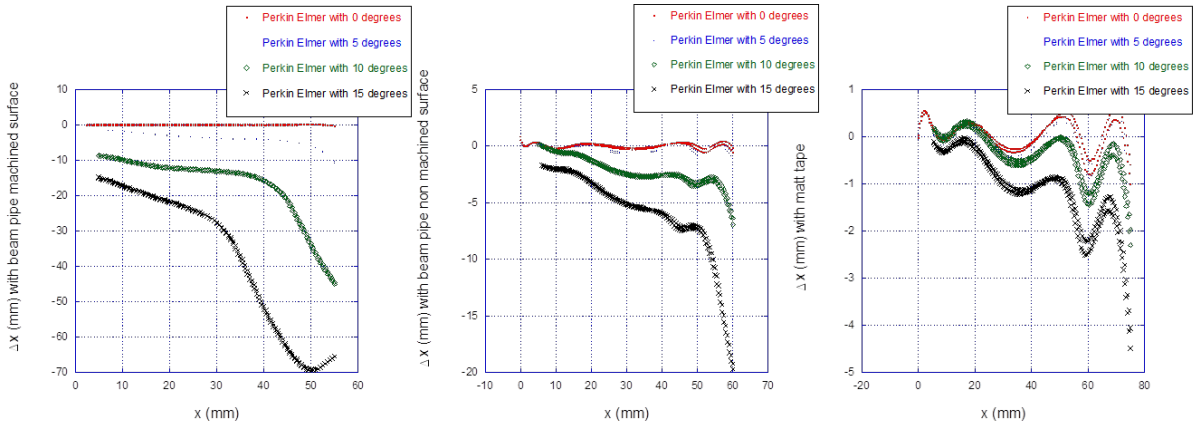

Figure 5.12: Induced error versus distance due to the relative orientation target-sensor. Using as target TT6 (left); non-machined beam pipe (middle); machined beam pipe (right).

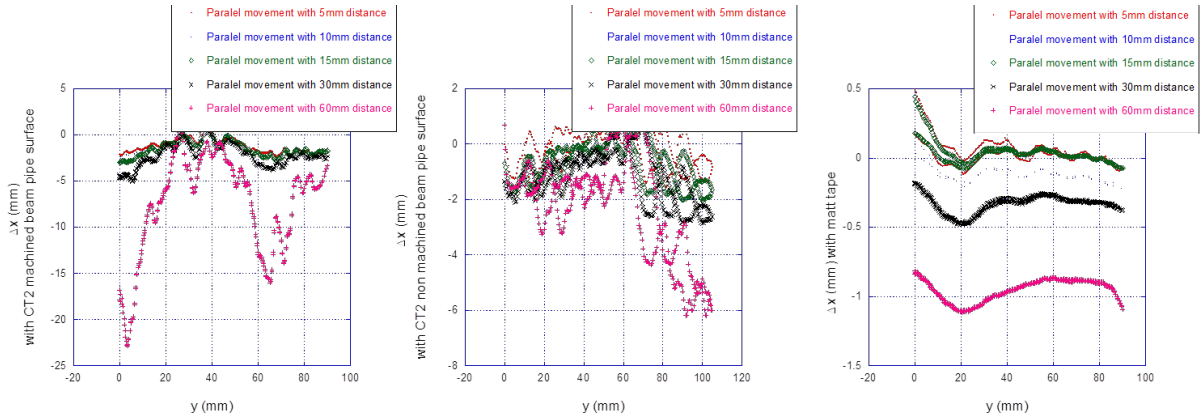

Figure 5.13: Induced error versus distance due to the surface homogeneity test (parallel scan). Using as target TT6 (right); non-machined beam pipe (middle); machined beam pipe (left).

5.1.3 Test of the sensors configuration required for TOTEM T2

In order to optimize the sensor configuration to be used for monitoring the TOTEM T2 detector, a complete test was performed using a mockup of one of the detector disks together with the mockup of the beam pipe. The final sensor layout for this detector will be further described in the next chapter.
The calibration setup for this test is illustrated in fig. 5.10. In fig. 5.14 a front view of the TOTEM T2 disk with four sensors installed in a given angular arrangement is shown. The four sensors are labelled as "Entry", "Left", "Centre", and "right" in the figure. The "Entry" sensor is meant to help a good centring of the detector during the installation process. During installation, the two independent half shells of the detector (each composed of various disks) slide, in the plane perpendicular to the beam pipe, until they join each other. Once closed, the inner diameter - formed by the two independent halves - has a nominal clearance of few mm with respect to the beam pipe. Note that the "Entry" sensor will only give a valid signal when this part of the detector crosses the beam pipe surface. The other three sensors are distributed along the inner detector boundary as shown in the figure. The goal of the test is to determine the best angular arrangement of the latter sensors as well as to understand the characteristics of the data with the selected configuration. Two main angular arrangements were tested: a) with the "right" and "left" sensors at $45\,^{\circ}$ with respect to the sensor at the centre; and b) with the "right" and "left" sensors at $30\,^{\circ}$ with respect to the sensor at the centre.

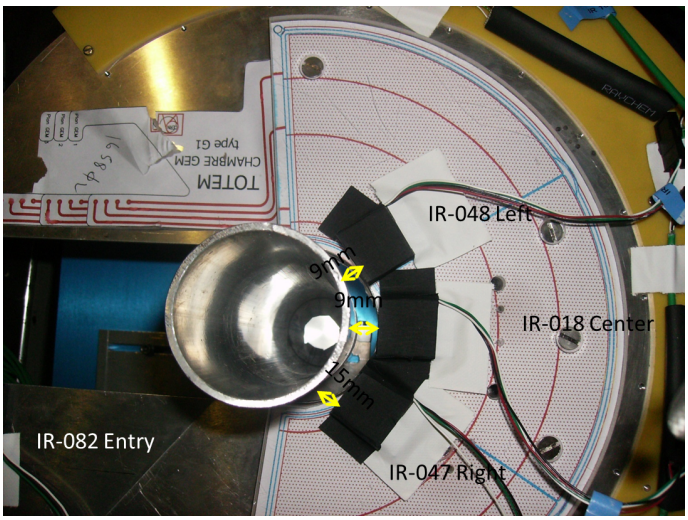

Figure 5.14: TOTEM T2 mockup instrumented with infrared sensors. The "right" and "left" sensors are located at $45\,^{\circ}$ with respect to the "Centre" sensor.

For this test a lower value of the LED current was selected (20 mA) to minimize secondary emission between the three sensors sitting in the inner boundary. This lower value fulfilled nevertheless the needed dynamic range for the measurements. Furthermore, to avoid further reflections the readout electronics was adapted to incorporate a relay

system allowing to switch on/off sequentially the four sensors under test. Labview software was also modified accordingly so that for each step of the motorized table the data from each sensor at a time as well as the corresponding position were recorded. The data acquisition speed was set to 1 measurement per sensor and second.
On top of the two main angular configurations, three different initial positions of the T2 detector with respect to the beam pipe were also tested. One position corresponding to the detector centred with respect to the beam pipe, and other two positions with the detector shifted to the right or to the left by 7 mm. A gap of 9 mm between the beam pipe and the detector was considered. These two last tests were conducted to understand the performance of the measurements under extreme initial mispositioned before the detector. Tests were performed for both "45 °", and "30 °" sensor angular arrangements.

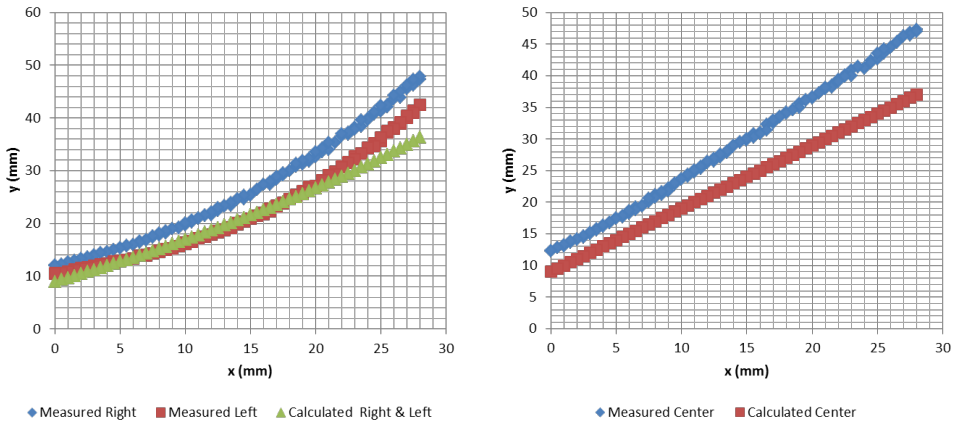

Figure 5.15: Comparison between the theoretical and the measured value of the distance (see text), and 45 ° angular sensor configuration

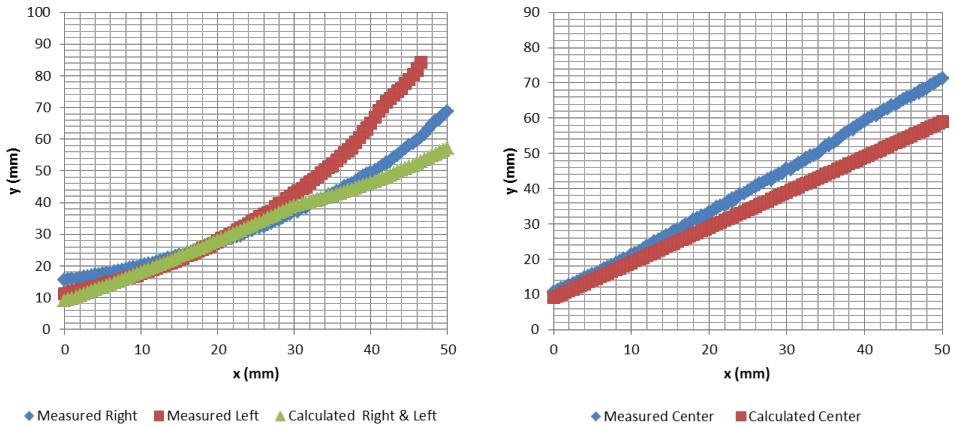

Figure 5.16: Comparison between the theoretical value and the measured of the distance (see text), and 30 ° angular sensor configuration.

The tests show that in all cases the sensors do not stop measuring due to initial

misalignment, and the safety of the beam pipe was always guaranteed. Moreover, to further understand the limitations or potential uncertainties introduced in the measurements, a calculation of the theoretical distance between the detector and the sensor was performed for each case under test and the result compared with the the measurements obtained from the tests. As an example, figs. 5.15 and 5.16 show the results obtained for the first case considered -detector centred around the beam pipe-, and the two angular configurations. The examples illustrated in the figures, show few mm of difference between the Left and Right sensor readings and the calculated values, at larger distances, 15-20 mm, the discrepancy increases. For the sensor located in the centre, the behaviour is different for the two angular configurations, but this was understood due to an initial wrong installation of the sensor in the 45° configuration. The study of the different cases allowed to establish the necessary initial conditions that should be achieved before closing the two halves of the detector and the interpretation of the results during real operations. As a result of this study, a 45° configuration was finally chosen.

5.1.4 infrared sensor characterization under magnetic field

A priori, infrared sensors can be affected by the presence of magnetic field; induced Hall Effect in the phototransistor could alter the response of the sensors. If this is the case, the sensor response can vary depending on the orientation of the sensors with respect to the field lines. To study the sensitivity of this sensor model a test was performed using a dipole magnet able to provide fields up to approx. 2.2 T. The sensor was installed, as shown in fig. 5.17, screwed to an Al plate, mounted on a sliding guide in two different orientations with respect to the field lines, at 0° and 180°. To test the mechanical stability two types of screws were used: plastic and stainless steel. A TT6 target type was used for the test. The LED current was set to 20 mA. The readout system consisted of Beckhoff modules recorded data for four configurations: a) fig. 5.17 (Left), sensor oriented in a 0° configuration, and using plastic or stainless steel screws; and b) fig. 5.17 (Right), sensor oriented in a 180° configuration, and using plastic or stainless steel screws.

The data taking consisted in recording 60 measurements, taken during one minute per each magnetic field value, during the ramp up of the magnet from 0.2 T to 2.2 T. The field values corresponding to the measurements were also stored. Results from the test reveal a sizeable dependence of the response with magnetic field. The variation of the voltage versus the field value is shown in fig. 5.18 (left) while the corresponding fake variation of distances is given in fig. 5.18 (right). This result corresponds to the "0°" configuration, and using plastic screws to support the sensor. Similarly but for the "180°" configuration is shown in fig. 5.19.

From the inspection of fig. 5.18 we conclude that relative high field values will alter

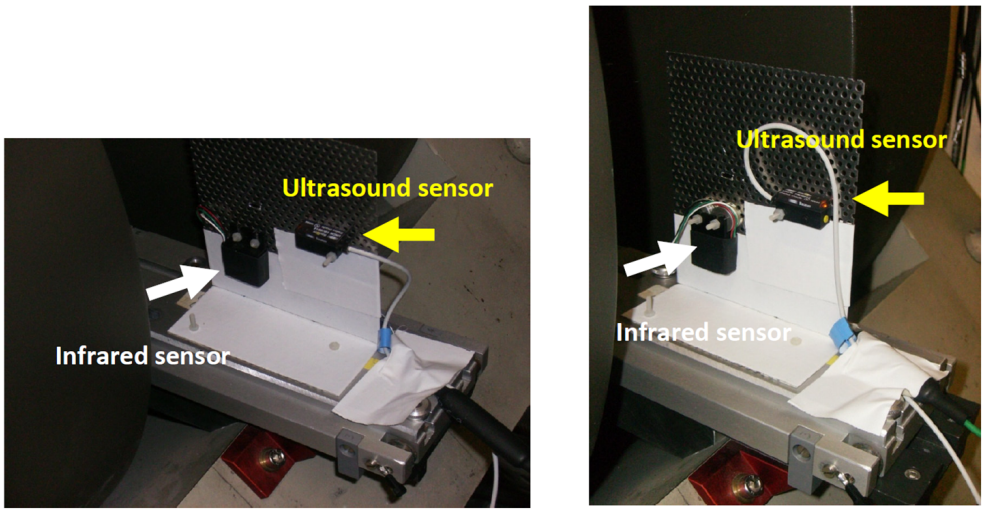

Figure 5.17: Experimental setup for the test with Al support and plastic screws. White arrow indicate the location of the infrared sensor and the yellow arrow the ultrasound sensor. The unit is oriented with respect to the field lines: at $0\,^{\circ}$ (left); and at $180\,^{\circ}$ (right).

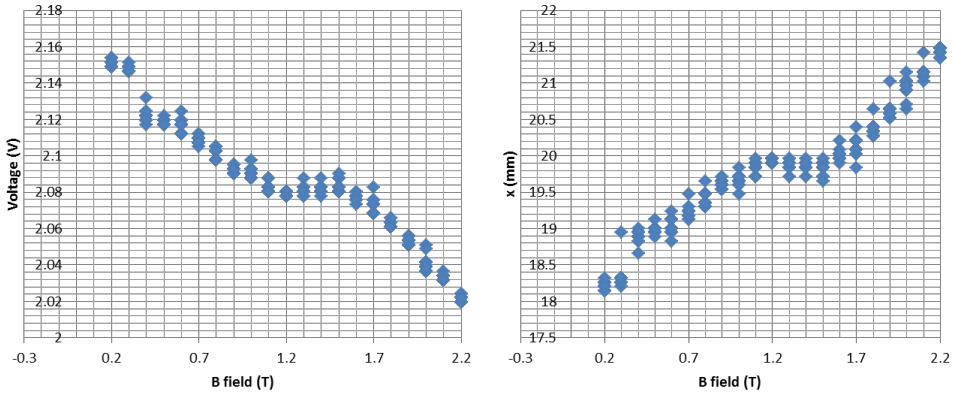

Figure 5.18: Sensor response for ”$0\,^{\circ}$” configuration. Output voltage versus the field value (left); measured distance versus field value (right).

the output voltage in approx. 4%, which translates to errors up to 3.5 mm in the measured distance. For the "180 °" data (see fig. 5.19), in the same range of field values, we observe up to a 10% variation in the output voltage that translate to an error in the measured distance of up to 5 mm. This imply that theses sensors can only be reliable when used in regions of the detector with low field, with field values below ∼0.6 T. From the test we also conclude that the sensor does not suffer a permanent damage, its nominal functionality is recovered in absence of a field.

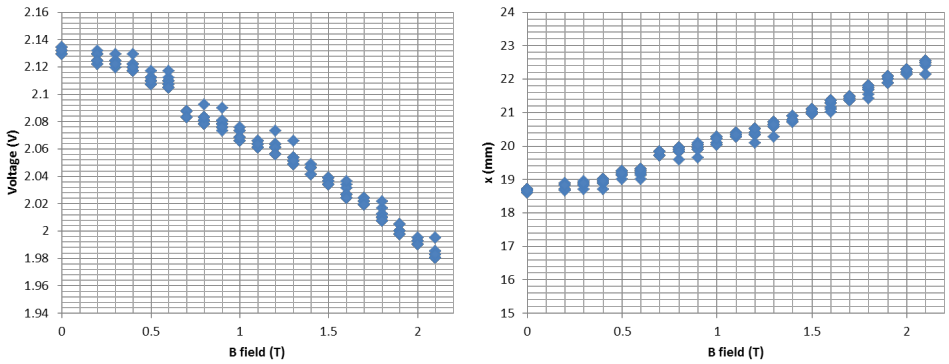

Figure 5.19: Sensor response for "180 °" configuration. Output voltage versus the field value (Left); measured distance versus field value (Right).

The impact of mechanical motions was observed, by comparing data taken when the sensor was fixed using plastic screws (fig. 5.18) with, the data collected when the sensor was fix with stainless steel screws (fig. 5.20). In the later case we observe sizeable discontinuities that are caused by a erroneous position of the sensor during the test of the sensor due to the magnetic field. Disregarding jumps, the overall conclusions are the same as in the case of plastic screws.

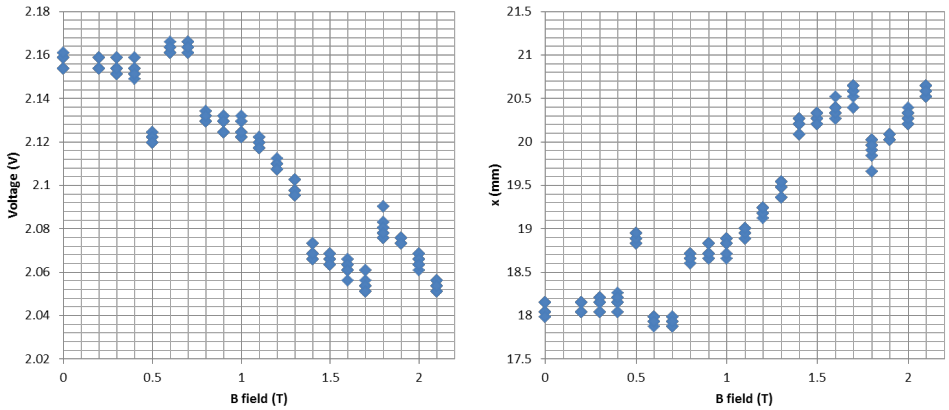

Figure 5.20: Same as fig. 5.17 but in this case using stainless steel screws instead of plastic screws to fix the sensor in the setup.

5.2 Ultrasound sensor: Baumer UNDK 10U6914

The infrared sensor discussed above as well as the ultrasound sensor chosen[1] for the system are small size sensors in order to allow easy integration. The technical information provided by the manufacturer is summarized in fig. 5.21. The figure shows the schematics of the sensor configuration as well as the typical sonic cone profile. The device has a large dynamic range suitable for this application. As shown in the figure, this model covers from 20 mm to 200 mm provided by the manufacturer, with a blind zone of 20 mm. For this application the electrical configuration was defined as follows: the +VS wire was connected to a 24 VDC; the output wire to the readout electronics (ADC of the Labjack or ELMB); and the 0 V and control/Teach-In was connected to 0 V of the power supply. Fig. 5.21 (right) shows how the sound propagates in the air. The size of the cone determines the target size that should be used, and therefore a target of 15 mm x 15 mm, positioned perpendicularly to the sensor's reference axis, is needed to cover the full dynamic range.

The acoustic sensors were bought pre-calibrated; their expected performances are known from the manufacturer. However, we always need to study possible effects, specific for our application that could modify the nominal performance. These studies are summarized below.

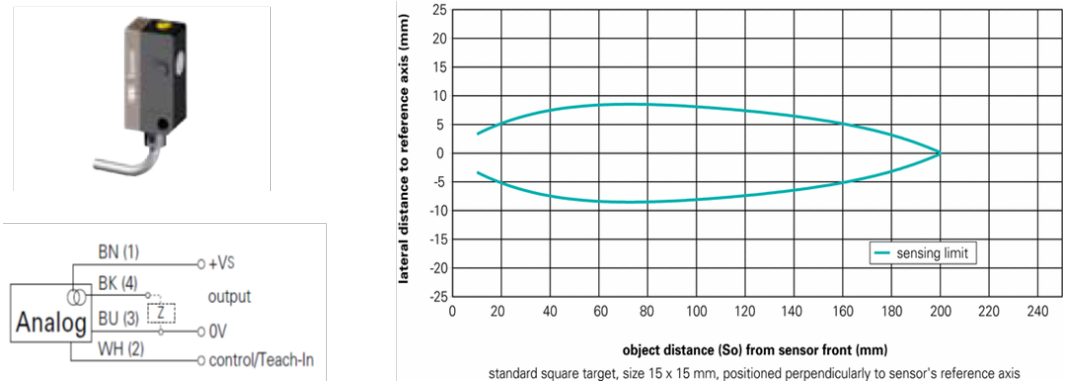

Figure 5.21: Information from the manufacturer: Sensor shape (left top); Connection diagram (left bottom); Typical sonic profile (right).

5.2.1 Study of the possible effects affecting the response of the sensor

A series of tests were performed, limited to a subset of units, prior to the installation of the sensors in the detector. We studied: a) the influence of the cable length in the sensor response; b) sensor functionality under various angular orientations target-sensor; and c)

[1] http://sensor.baumerelectric.com/productnavigator/downloads/Produkte/PDF/Datenblatt/Ultraschall_Sensoren/UNDK_10U6914_web_EN.pdf

functionally and performance of this technology for special configurations as the ones required for the forward detector TOTEM T2. The effect of the magnetic field was also studied and is reported in Sec. 5.2.2.

Two tests were carried out to quantify the influence of long cables in the response of the ultrasound sensors. The first one, used the initial calibration readout electronics (Labjack) and with 4 wires 50 m cable (Sabix D 345 FRNS TP). For the second test, the final system readout electronics (ELMB) as well as the final selected cables (4 wires custom cable from NOVACAVI) were used. A 25 m cable was tested in this case. The test consisted in comparing the response of the sensor with long cables to the one obtained when the sensor was directly connected to the readout electronics. Compatible results were obtained in both cases. The analysis of the data using a 50 m long cable shows (see fig. 5.22) a small offset of about 0.1 V in the output voltage, with respect to the output voltage obtained when using a short wire. A small degradation is observed in the measurement resolution: from 0.18 mm to 0.28 mm (for 50 m cable length). Taking into account the data provided by the manufacturer (reproducibility accuracy < 0.5 mm; resolution < 0.3 mm), we conclude that there is not significant degradation of the expected performance. The results from the test with 25 m cable are displayed in fig. 5.23. As visible in the left graph of the figure, the residuals are below 0.5 mm for the whole range of distances, and again within specifications.

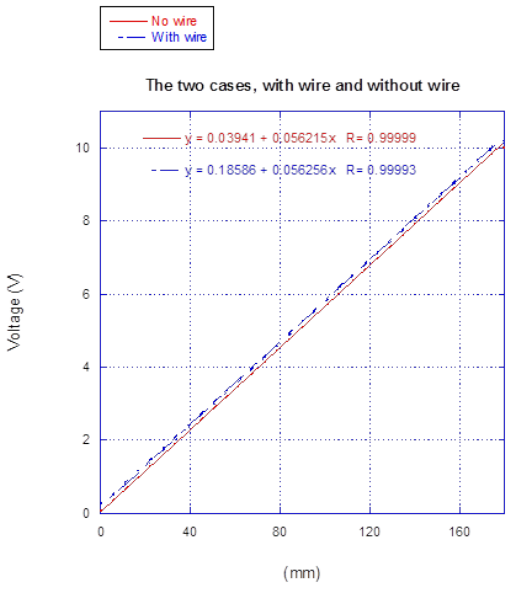

Figure 5.22: Response curve for ultrasound sensors using a 50 m cable (red) and a short (∼10 cms) cable (blue).

The influence on sensor response, due to the relative angular orientation between target-sensor was studied using three samples of sensors (units US-001, US-002 and

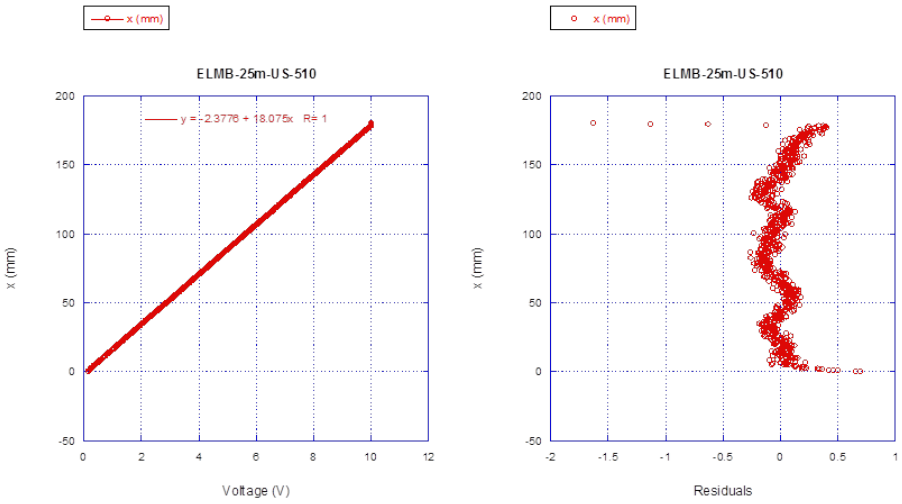

Figure 5.23: Response curve for ultrasound sensors using a 25 m cable (right). Residuals: data-fitted response (left).

US-003). The experimental setup consisted of a 1 cm thickened aluminium plate mounted on the 2D motorized table. The sensors, were at a fixed location during the test; they were connected, with a 50 m cable to the Labjack readout. Four relative orientations target-sensor were studied: $0\,^{\circ}$, $5\,^{\circ}$, $10\,^{\circ}$ and $15\,^{\circ}$. Results are shown in fig. 5.24.

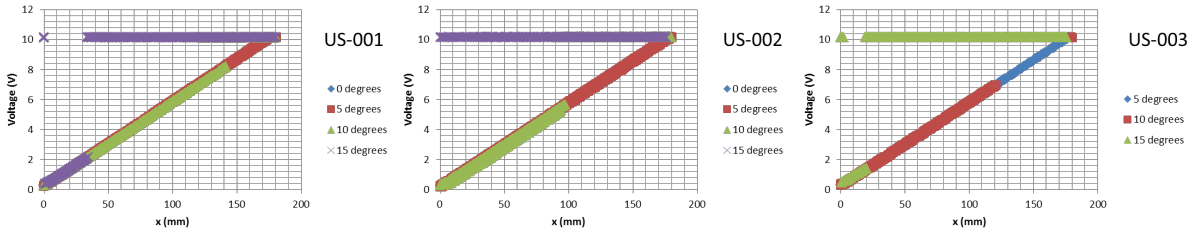

Figure 5.24: Calibration curve (output voltage versus distance) for three ultrasound sensors US-001 (left), US-002 (middle), and US-003 (right).

The sensors reveal a dependence on the angle. Note that, this fact was expected, since this dependence is inherent to this technology. Nevertheless, for angles below $10\,^{\circ}$ the sensors behave correctly although for a shorter dynamic range, up to about 100-130 mm. For a $15\,^{\circ}$ angle the sensor stops working properly. A spread in response between the different units is also observed, i.e. for the samples US-001 and US-003 and an angle of $15\,^{\circ}$ there is still a small region (range between a few mm and up to about 30 mm) where we still can observe an adequate response. We conclude from this test that measurement performances are not degraded if the relative orientation between target and sensor is kept within reasonable limits, always below $10\,^{\circ}$.

Finally we tested the functionality of this technology for the special configuration

required for the forward detectors as TOTEM T2. The experimental setup, was similar to the one used in the case of infrared sensors, as it is illustrated in fig. 5.25. The distribution of sensors is visible in the figure; the unit US-012 is located in the "Entry" position (see Sec. 5.1.3 for details). The sensors units are displaced with respect to the inner detector diameter to avoid the blind zone. Due to the sensors sensibility to the angles with polished surfaces and the small diameter of the beam pipe, that it does not allow having a minimum area for the reflective sound wave back to the sensor, we concluded that this technology is not suitable for this specific configuration.

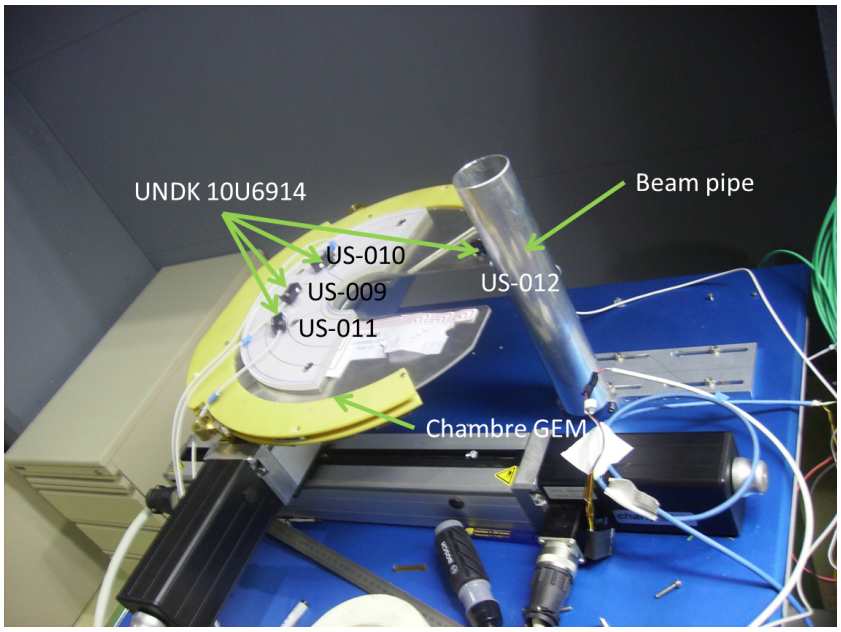

Figure 5.25: Experimental setup for the test of ultrasound sensors in a TOTEM T2 configuration.

5.2.2 Ultrasound sensor characterization under magnetic field

Using the same strategy and experimental setup as described in Sec. 5.1.4, the response of ultrasound sensors was tested for magnetic field induced effects. In this case, the observed behaviour is different as the one reported for infrared sensors. The sensor response is displayed in figs. 5.26 and 5.27 for the "$0°$" and "$180°$ " configurations respectively. The first observation is a clear stratification of data for which we do not have a clear explanation; nevertheless, the bands are easy to separate offline. The lower band is the most populated with data and in particular, the bottom line from this band is not altered with the magnetic field. Indeed, this bottom line corresponds to the real reading (voltage value without the magnetic field), and therefore, the measured distance, as obtained from this bottom line, would be the "correct" sensor response. Taking into account the (constant) dispersion observed for the bottom band we could assign a systematic uncertainty to the measured distance, which in all cases remains below +/-0.5 mm. No

significant dependence with the orientation of the sensor with respect to the field lines is observed (figs. 5.26 and 5.27).

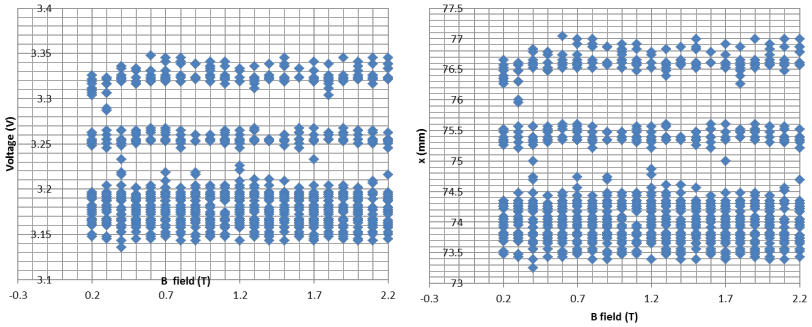

Figure 5.26: Sensor response for "0 °" configuration. Output voltage versus the field value (left); measured distance versus field value (right). Using plastic screws to fix the sensor in the setup

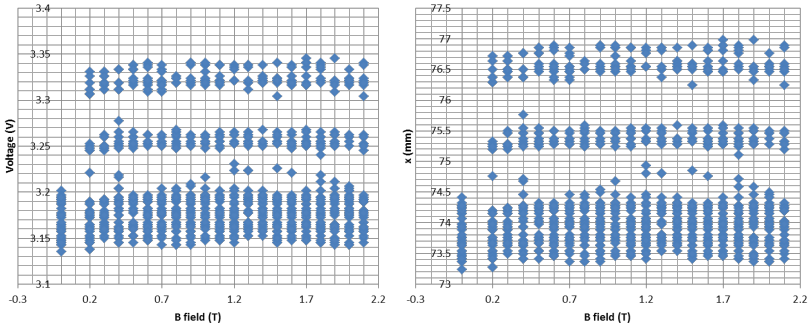

Figure 5.27: Sensor response for "180 °" configuration. Output voltage versus the field value (left); measured distance versus field value (right).

Results from the test, using stainless steel screws to fix the sensor in the setup are displayed in fig. 5.28. Although we recognize the same general features with not sizeable differences, a small change can be verified (see figs. 5.26 and 5.28), which can only be interpreted as mechanical motion of the assembly.

5.3 Potentiometer sensor: Active Sensors CLS 1313

Potentiometers are simple and robust technology. They are magnetic field insensitive and radiation resistant. Unfortunately, its implementation in the detector is limited due to the fact that they require a direct contact with the target. The characteristics, from the manufacturer, of the model selected for the system are summarized in fig. 5.29. The sensors were bought pre-calibrated such that their expected performance is known; nevertheless, using the specific systems readout, calibration curves and sensor resolution

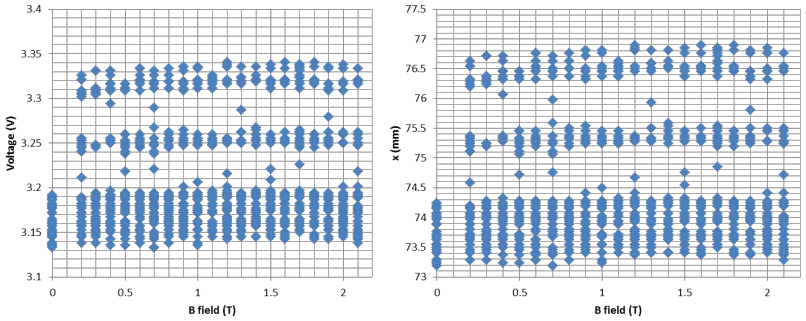

Figure 5.28: Sensor response for ”0 °” configuration. Output voltage versus the field value (Left); measured distance versus field value (right). Using stainless steel screws to fix the sensor in the setup

were studied. Magnetic field effects were also studied and results are reported in Sec. 5.3.1.

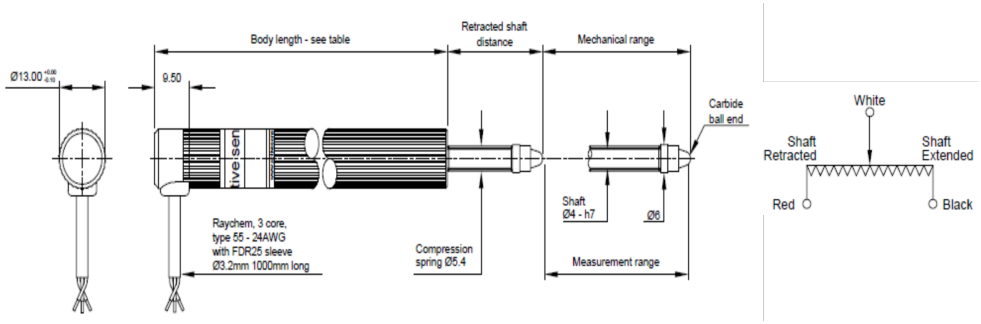

Figure 5.29: Information from the manufacturer: mechanical characteristics (left); and electrical configuration (right).

Electrical connections are as follows: the red wire is connected to +V, the back wire is connected to the common ground of the power supply, and the white wire is connected to the readout; it measures from 0 to the maximum of the power supply. The calibration function can be expressed as a function of the output voltage (Vpot) or as a function of the relative value (Vpot/Vsupply); in this context, the first is called ”absolute” calibration while the second will be the ”relative” calibration. The later has the advantage to reduce or eliminate directly the dependence on possible fluctuations of the voltage supplied.
Several calibration campaigns were done with the readout (using Beckhoff modules or ELMBs) configured as to have an analogue input 0 to 10 V with a 12 V power supply for the bias. This setup does not allow scanning the whole range of the sensor during the calibration.

To establish the measurement resolution, the ELMB was first configured with the ADC sampling rate of 30 Hz, the speed of the calibration cycle was 6 seconds per step. Results are shown in fig. 5.30. With this configuration, a measurement resolution better than 0.15 mm can be obtained. A test lowering the reading rate, setting the configuration

of the ELMB at 15 Hz with 10 seconds interval to read the value, was also performed. This result is shown in fig. 5.31. The residual distribution (right plot of the figure) shows that a factor three improvement in resolution can easily be obtained. The two lines in the (fig. 5.31-Right) are due to a mechanical fault of the calibration setup. The final operational parameters were set on the ELMB at 1 Hz.

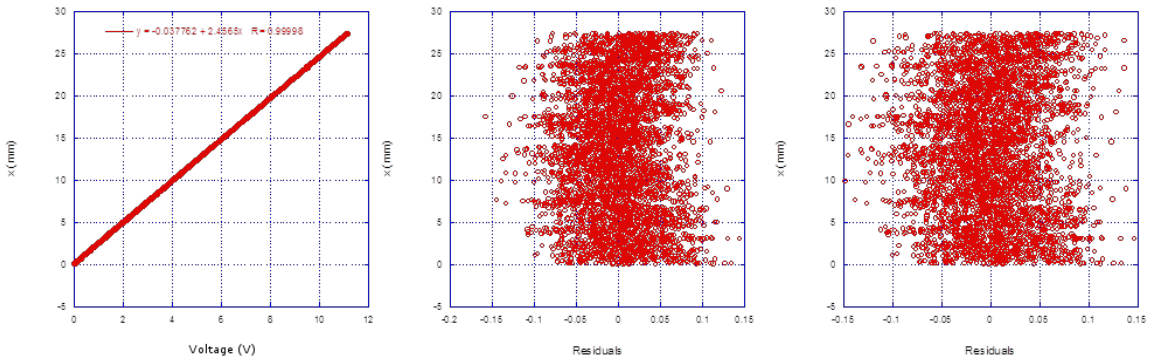

Figure 5.30: Typical calibration curve of potentiometers (left). Measured distance versus residuals: using ”absolute” (middle), and ”relative” (right) calibration functions.

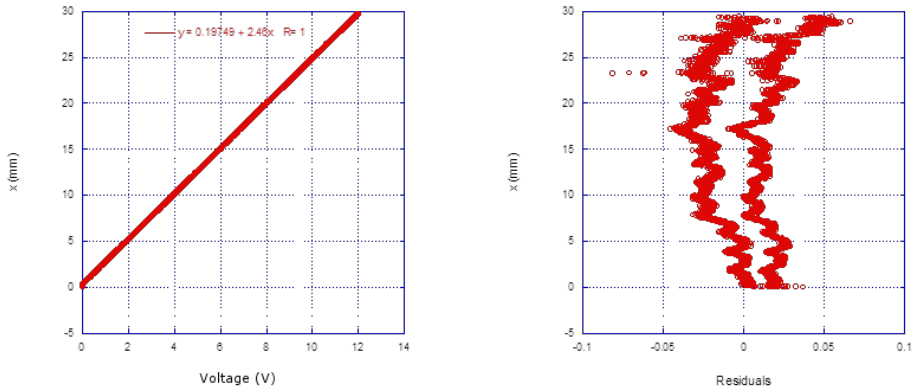

Figure 5.31: ”15Hz reading rate”: Typical calibration curve of potentiometers (left). Measured distance versus residuals (right).

5.3.1 Potentiometer sensor characterization under magnetic field

As done for the other technologies, the response of potentiometer sensors was tested under magnetic field in the range of field values from 0 to 2.2 T. The hardware setup to insert the sensor inside the magnet is shown in fig. 5.32.

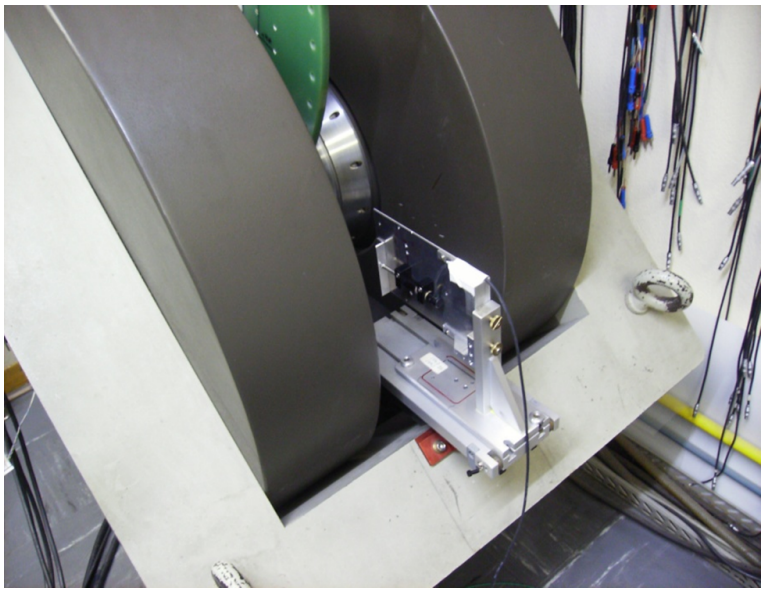

Figure 5.32: Experimental setup used to test the potentiometer response under magnetic field. The figure shows the insertion of the potentiometer into the magnet poles.

Data were recorded from 0.02 T to 2.2 T in 0.02 T steps. For each step 10 measurements were recorded with a rate of 1 per second. The output voltage is shown in fig. 5.33. No change in voltage is observed, the distribution of data is a result of noise in the ADC. The resolution of 12 bits corresponds to 4096 bins that provide a measurement of 0.0024 V per bit. The percentage of the error in output voltage is less than 0.01, for all ranges of field values, due to the ADC resolution.

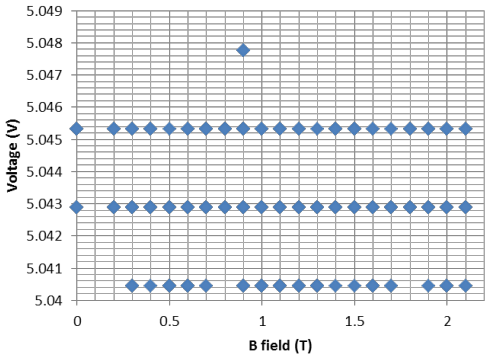

Figure 5.33: Output voltage versus magnetic field value.

6

Implementation of the sensor system in CMS

A detailed description of the implementation of the CSS sensors in the detector is given here. Details of its functionality, geometrical distribution, type of sensor technology as well as its accessibility are given. Sec. 6.1 is devoted to the CMS Central Part. The instrumentation implemented in the Forward region is described in Sec. 6.2. The naming convention for the sensors introduced here will be used in the following Chapters. Considerations on the procedure followed during the closing and opening operations of the forward detectors are discussed in Sec.6.3.

6.1 The Central region

In terms of safety and detector integrity, the most critical area in the central CMS structures is related to the "53 degrees service crack", joining the YE+/-1 nose and the Vac tank. During the closing and opening operations, because of their geometry, the YE+/-1 structures require special attention. YE+/-1 is about 14 m high and weighs approx. 1,400 tonnes. Two main issues of concern were considered when implementing the CSS system in this detector region: a) the special shape of YE+/-1, with the nose housing heavy detector components as the Endcap Hadronic and Electromagnetic calorimeters strongly shifting the centre of gravity of the disk, makes specially challenging a smooth motion of the structure during the process of closing/opening. In the path from full aperture, when the disk is at 10.65 m from the interaction point to closed position there are intermediated positions where the clearance between the inner diameter of the ES-cone and the beam

pipe becomes as small as 50 mm or less (see fig. 6.1). These locations correspond to beam pipe flanges joining the different beam pipe pieces. Once YE+/-1 enters the Vac tank the clearance in the top position is about 30 mm (see fig. 6.2). Finally at the last stage of the travel, at about 1 m from its final position, again the clearance between the inner diameter of the ES-cone and the beam pipe support, including the thermal screen at the tracker ends can be as small as 20 mm. Once in its final position, the clearance between the detectors and associated instrumentation located inside the Vac tank (53 degree crack) is again of the order of 10-15 mm in some locations.

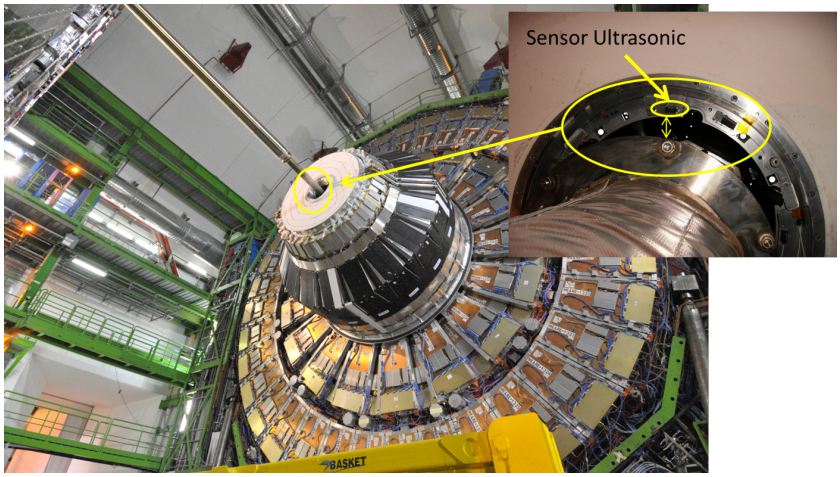

Figure 6.1: Photo of YE+1 in its travel from full aperture to detector closed position, passing the beam pipe flange. The inserts shows a zoom in of the ES-cone and associated instrumentation.

For the purpose of surveying this area, a set of sensors were installed both in the YE+/-1 nose and Vac tank. The location of the sensors, along the Z axis, is shown in fig. 6.3. Arrows in the figure indicate the direction of the measurement, pointing from the sensor device to the target. Sensors are distributed at seven locations along z:

- ES-cone: ultrasound sensors installed in the inner diameter of the ES detector, at four ϕ positions (top, bottom, far and near with the angles around $36\,^{\circ}$, $126\,^{\circ}$, $216\,^{\circ}$ and $338\,^{\circ}$ degrees) are used to survey the radial distance from ES to the external beam pipe diameter and/or other detector components.

- ES, EE and HE1: infrared sensors are distributed at three locations along the "53 degrees service crack". They monitor the distance between detectors and instrumentation (PP1 patch panels) inside the Vac tank and the conical part of the YE+/-1 nose. As before, for each location a set of 4 sensors distributed in ϕ are used.

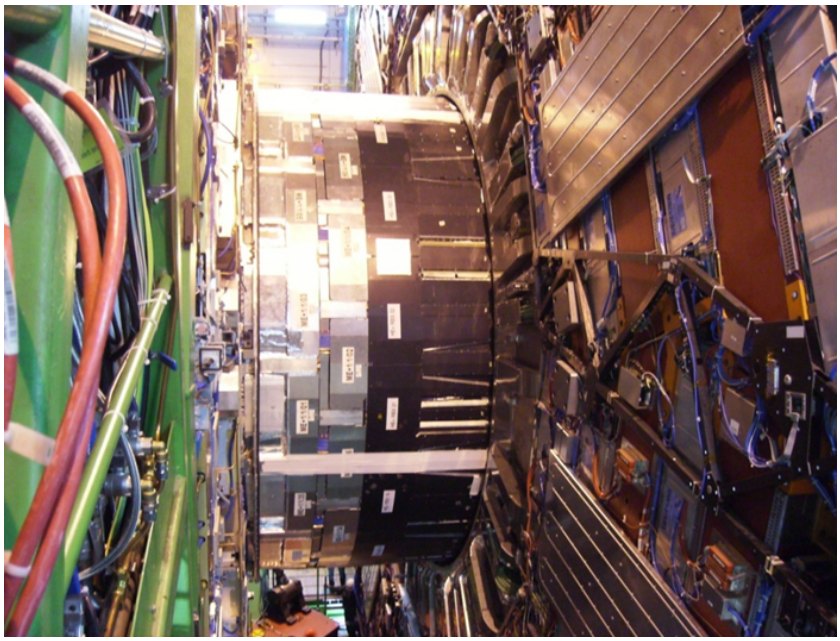

Figure 6.2: Insertion of YE+1 nose into the Vac tank.

- YE+/-1 nose, and HE2: infrared sensors located at the two ends of the cylindrical part of the nose are used to monitor the centring of the nose with respect to the Vac tank inner circle. A set of 4 sensors, for each location, distributed in ϕ are used. To allow the measurement during the insertion of the nose inside the Vac tank, the YE+/-1 nose sensor is housed in the YE+/-1 disk, as indicated in fig. 6.3.

- SR: infrared sensors are also used to measure the distance in z-coordinate between the end of the coil and the sealing ring located in YE+/-1. A set of 4 sensors distributed in ϕ are used. The main purpose of this measurement is to monitor the correct functioning of the sealing ring.

Figure 6.3 shows a detail of the location of the "53 degrees service crack" sensors for one of the ϕ positions. The yellow arrows, distributed along the Vac tank, are pointing from the sensor to the target surface. Special supports were made for each radial position, for all places. Open windows on the sensor covers were included, for services routing, when needed. The routing of the cables from the inside (ES) to the outside locations (HE1) is also indicated (see fig. 6.4 b)). For infrared sensors targets were glued over the corresponding places covering the maximum calculated area to guarantee not missing the target during the movements of the structures. The fixation of HE2 sensors at the end of the coil volume is also shown in the picture (see fig. 6.4 b)); for this sensor the corresponding target is glued along the cylindrical part of the YE+/-1 nose. The target, white band, for a couple of ϕ positions is clearly visible in fig. 6.2. The ϕ distribution of the

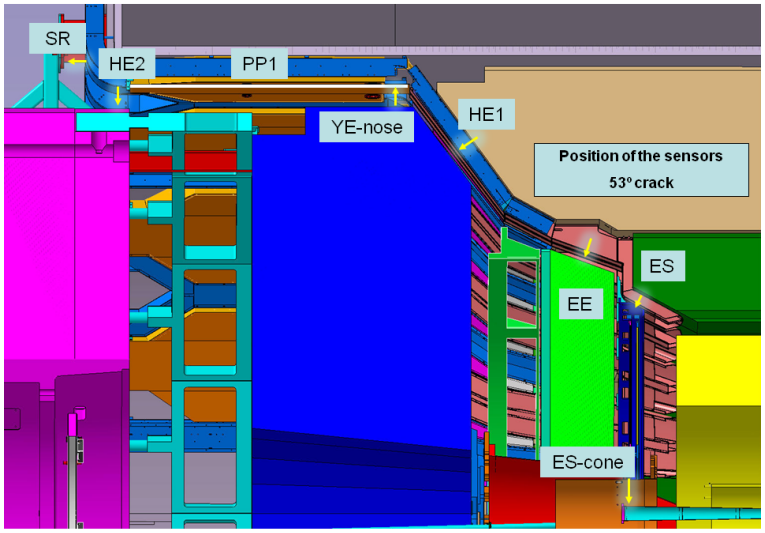

Figure 6.3: 3D drawing showing the distribution of sensors inside the Vac tank and at the end of the coil (see text).

targets glued inside the Vac tank, for the +Z detector side, serving the sensors installed on the conical part of YE+/-1 nose is shown in fig. 6.5. YE+/-1 nose sensors, not shown in these figures, are housed in the cylindrical part of the nose and the corresponding targets are glued on top of the PP1 covers. Finally, the ϕ positions of the HE2 and SR sensors are slightly displaced from those presented in fig. 6.4 b) in order to fit the available space for integration.

6.1.1 Movable barrel wheels instrumentation

The barrel yoke is composed of 5 barrel wheels; the central one, YB0, housing the magnet coil is fixed to the floor of the collision cavern at its nominal position while the other four wheels YB+2, YB+1 (at the +Z detector side) and YB-2 and YB-1 (at the –Z detector side) are movable to allow maintenance. During the assembly of the detector, the movable wheels slide over the external part of the coil travelling a distance of 5 m for YB+/-2 and 2.5 m for the YB+/-1. The wheels are moved using an air-pads system combined with a special hydraulic system. The minimum distance between elements can be as small as 30 mm. The barrel wheels are approx. 2.5 m wide and 15 m diameter. To monitor their distance to the thermal screen that cover the outer boundary of the coil and to help keeping the wheels centred with safety clearance, the wheels were instrumented with ultrasound sensors radially placed. The internal wheels (YB+/-1) are instrumented at both sides of the wheel in the Z direction, distant in z by approximately 2 m, with four sensors following the distribution in ϕ as shown in fig. 6.6 a); in total each YB1 wheel uses eight sensors. The external wheels (YB+/-2) are instrumented in a similar way to YB+/-1 but

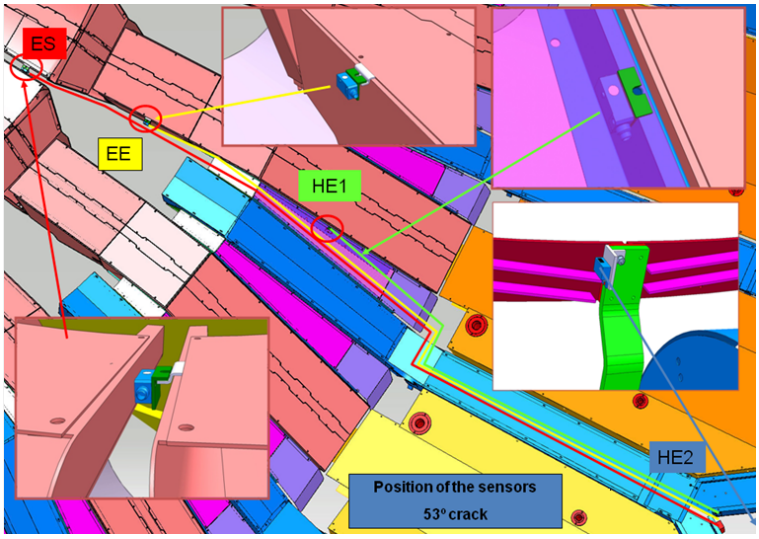

Figure 6.4: Details of the sensor fixation and cable routing for the sensors located in the "53 degrees service crack" PP1 panels are visible in the figure.

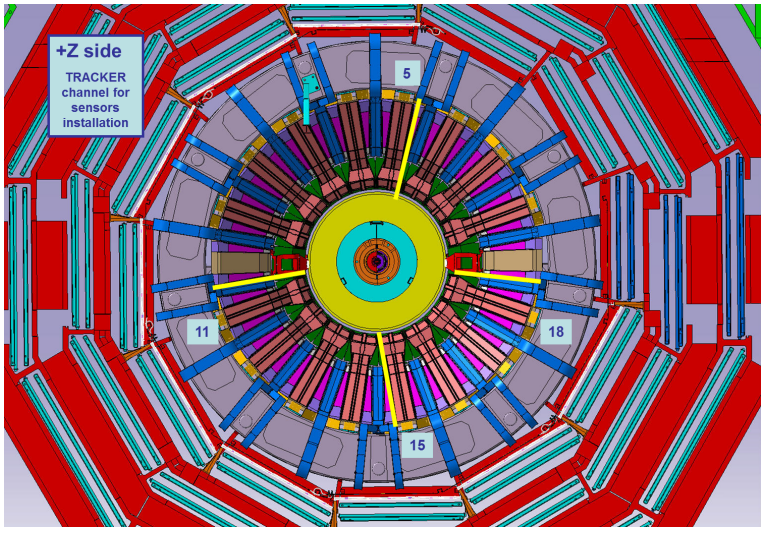

Figure 6.5: 3D drawing showing the inside of the Vac tank. Yellow lines indicate the ϕ distribution of the sensors located along the 53 degree crack; for the +Z detector side.

with a slightly different Z position. This layout allows checking possible misalignment of the wheel, in particular rotations around the CMS x or/and y axis.

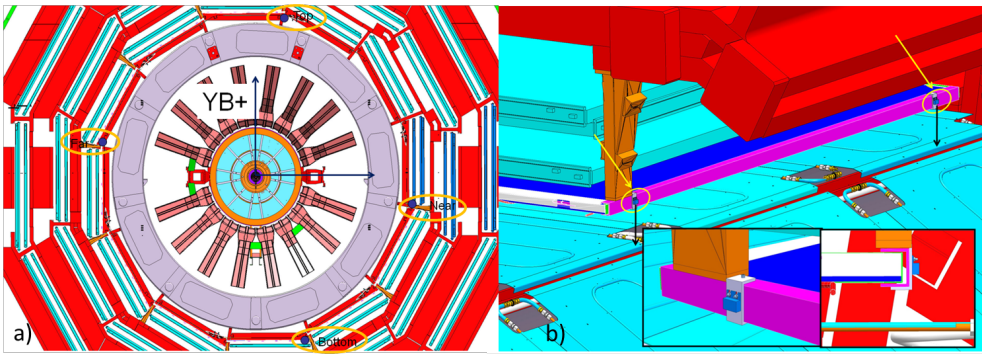

Figure 6.6: Distribution in ϕ of ultrasound sensors in the movable barrel wheels; a) the four sensors mounted on the different phi positions on all movable barrel wheels (YB+1, YB+2, YB-1 and YB-2), b) 3D drawing showing where the sensors are mounted on the YB wheels. The small box shows the mechanical support.

Sensors are mounted on the YB structures, as illustrated in fig. 6.6. They measure the radial distance to the thermal screen surrounding the coil. The use of ultrasound sensors allows avoiding specific targets. Due to the sensor technology, attention must be given that the sensors are oriented perpendicular to the measured surface. A picture of the actual sensors installed in the detector is shown in fig. 6.6 b). From the fig. 6.6 it is evident that there will be different periods during the motion of the movable barrels wheels. The most demanding in terms of survey is when the movable barrels wheels begin to enter the magnet coil volume, the CSS can only provide information when the first set of sensors on the IP side of the barrel wheel reach the thermal screen installed around the magnet coil, from that moment on the sensor will measure in continuous mode.

The total number of sensors instrumented in the central region as well as nominal clearance are summarized in Chapter 2, Table 2.1. Note that to access all those sensors a full opening of CMS is required.

6.2 The Forward region

From the CSS point of view, the Forward region of CMS is considered as the set of detectors, support mechanics, and shielding ancillary located at the two ends of CMS. Two effects motivate an extensive and dedicated survey: a) the proximity of heavy components to the beam pipe; b) the large motion the various elements suffer when the magnet is energized. Magnetic forces in this region induce large displacements and deformations of the structures, as well as displacements of detectors mainly along the z-axis. Although, this motion is mainly along the z-axis, it is specially sensitive when related to objects close

to the beam pipe or beam pipe ancillary since any radial displacement can damage them. A drawing of the complete forward region of the minus side, is shown in fig. 6.7. Instrumented with CSS sensors are the Hadronic Forward Calorimeter (HF), TOTEM and the CASTOR detectors, as well as the mechanical parts: Collar platform and shielding, CASTOR table, and Rotating Shielding.

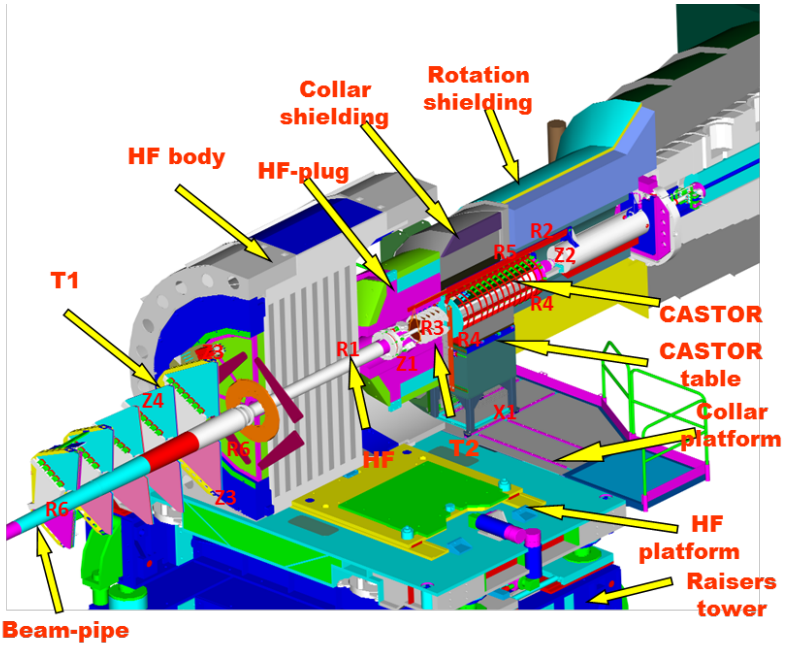

Figure 6.7: Schematics of the CMS, -Z side, forward region, showing the different components (detectors and mechanics). The location of the different CSS sensors (R1 to R5, Z1, Z2, and X1) is also shown (see text).

Sensors installed in this region are classified based on the measured coordinate. There are 5 different sets of sensors measuring the radial coordinate:

- R1: four potentiometers installed in the inner part of the HF detector, and distributed in ϕ, measure the radial distance to the beam pipe. They are located at the end-side of the detector, away from the interaction point (IP), labelled as NonIP side. Details are shown in fig. 6.8. Access to the sensors, for installation and/or maintenance, requires a configuration of the detector so that Rotating Shielding, Collar and HF are open.

- R2: 2 X- and 2 Y- measuring potentiometers installed at the beginning and the end of the CASTOR NonIP side measure the distance against the adjustable beam pipe support. The main purpose of this set of sensors is to provide information on possible tilts and rotations of the HF platform during the magnet cycles. Details

are shown in fig. 6.9. Access to the sensors requires a configuration of the detector such that the Rotating Shielding and the Collar are opened. For safety reasons these sensors must be removed, for maintenance or replacement purposes, before opening the CASTOR detector.

- R3: this set of sensors is dedicated to the survey of TOTEM T2 detector. There are two groups of six infrared sensors each located at the two ends of the detector (IP and NonIP sides). Two extra sensors help opening and closing the detector. Once T2 detector is closed and in its final position the sensors are outside of their dynamic range, and therefore not used. Details are shown in fig. 6.10. In order to access this set of sensors, for maintenance purposes, Rotating Shielding, HF, TOTEM T2 and BCM (Beam Counter Monitors) detectors should be open and if possible far from the beam pipe (i.e. in two or less raisers or in the garage position) since the sensors are glued to the detector body and its manipulation is delicate. It is recommended to do the work without both Collar's and with the CASTOR Table shifted towards the NonIP to have T2 outside HF. During technical stops or shutdown it is convenient to replace the targets mounted on the beam pipe to ensure a correct measurement.

- R4: as for TOTEM T2, two groups of 4 and 6 infrared sensors located at the ends of the CASTOR detector (IP and NonIP sides), distributed in ϕ, are used to monitor the detector. Details are shown in fig. 6.11. Access to the sensors requires an identical situation as in the case of R3. As in the case of R3 sensors, whenever access to this area is allowed the target mounted on the beam pipe should be replaced.

- R5: a set of six infrared sensors, distributed in ϕ and located at the NonIP side external diameter of the CASTOR (see fig. 6.12) are used to survey the clearance of the detector with respect to the Rotating Shielding. Access requires opening the Rotating Shielding and Collar elements. In this case the target is mounted on the Rotating Shielding and as before its replacement is recommended whenever possible.

Two sets of axial sensors, measuring along the direction of the CMS Z-axis:

- Z1: a potentiometer surveys the distance, along the CMS Z coordinate, between the beam pipe support and the beam pipe flange (see fig. 6.13)

- Z2: a potentiometer located at the near (+X) half of the CASTOR, and at the NonIP end of the detector, surveys the distance to the adjustable beam pipe support (see fig. 6.13)

Note that, the Z2 sensor must be removed before HF moves in Z, or CASTOR will have

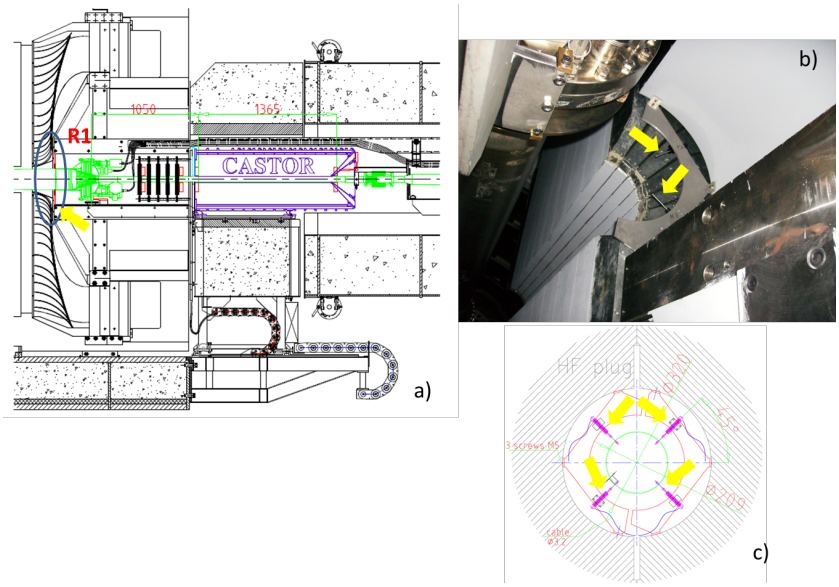

Figure 6.8: a) Longitudinal view of the HF region. Yellow arrow indicates the z position of the sensors; b) view of a half of HF (as seen away from the IP) illustrating the two sensors installed in this half; c) Rϕ view, drawing indicating the ϕ location of the four sensors.

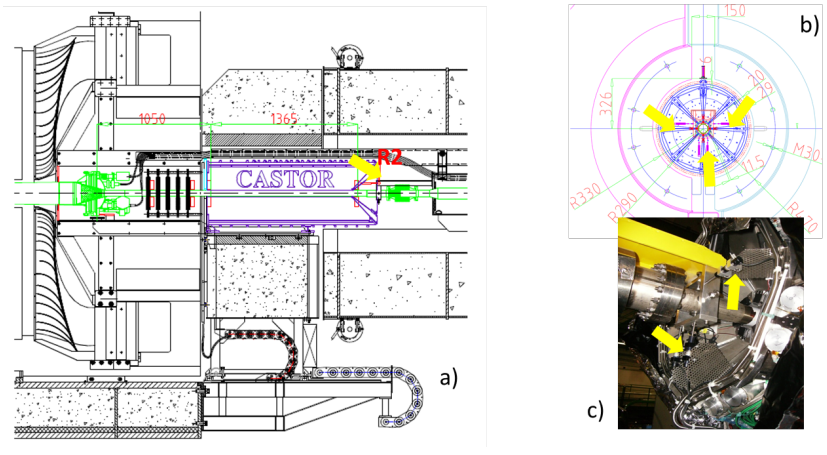

Figure 6.9: a) Longitudinal view of the HF and CASTOR region. Yellow arrow indicates the z position of the sensors; b) Rϕ view, drawing indicating the ϕ location of the four sensors; c) view of the sensors mounted onto their support once in its final position.

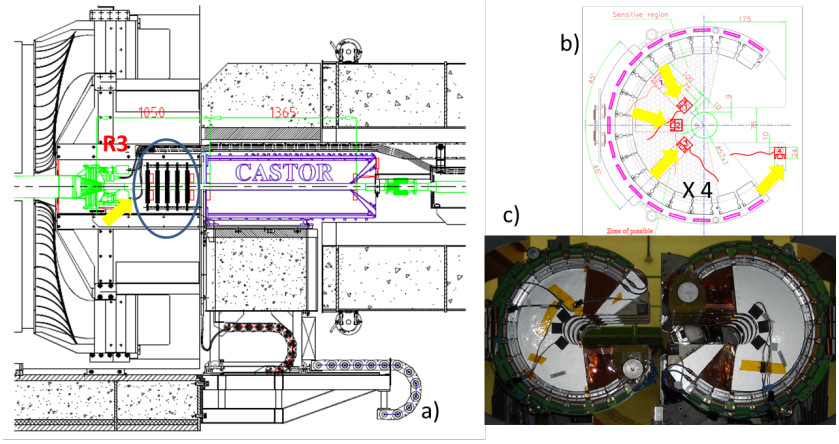

Figure 6.10: Longitudinal view of the forward region with TOTEM T2 highlighted. Yellow arrow indicates the z position of the sensors; b) Rϕ view, drawing indicating the ϕ location of the four sensors in one detector disk; c) view of the sensors mounted on the IP side of the detector. T2 is in an open position, in the picture.

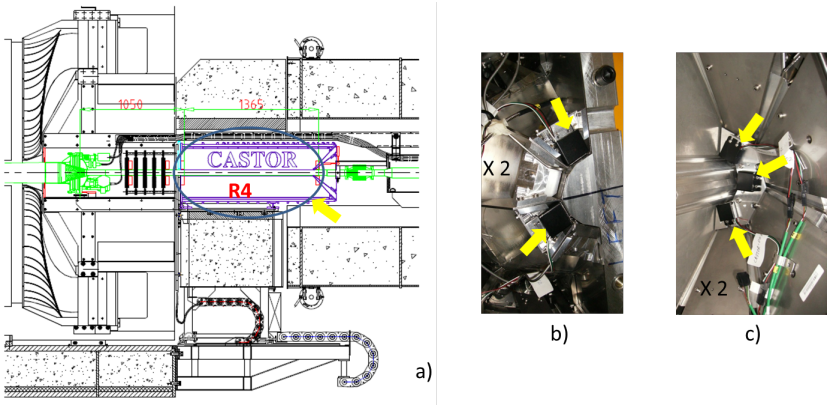

Figure 6.11: a) Longitudinal view of the forward region with the CASTOR highlighted with a blue circle and yellow arrow. Rϕ view of the detector with the sensors mounted on a half of the detector: b) for the IP side; c) for the NonIP side of CASTOR.

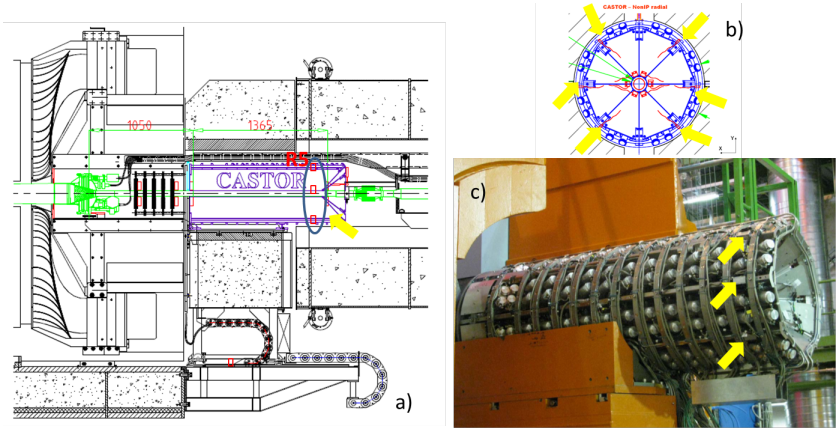

Figure 6.12: a) Longitudinal view of the forward region with the CASTOR highlighted with a blue circle and yellow arrow; b) Rϕ view, drawing indicating the ϕ location of the sensors installed in the outer perimeter of the detector; c) view of the sensors mounted on detector, yellow arrow indicates the z location of the sensors at the NonIP end.

to be opened. Similarly, the Z1 sensor must be removed when the beam pipe support is lowered in order not to damage the sensor or the beam pipe flange.

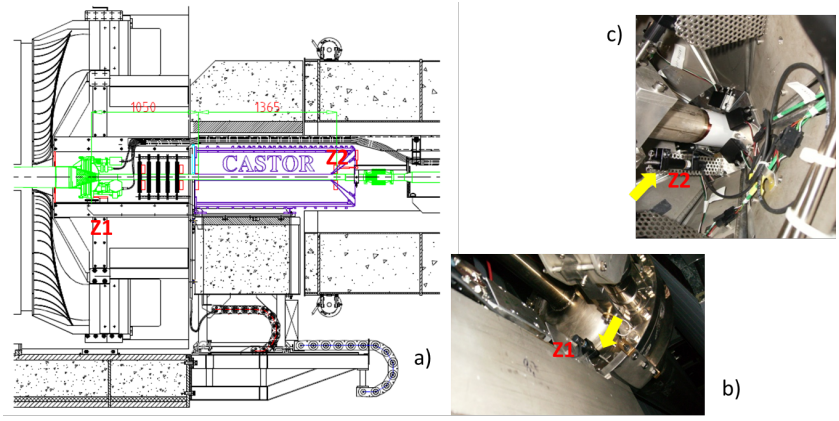

Figure 6.13: a) Longitudinal view of the forward region with the location of the Z1 and Z2 sensors; View of the potentiometers mounted in the detector and measuring: b) from the CASTOR table to the beam pipe support arm; c) same as in the NonIP CASTOR end.

Finally, there is a set of sensors measuring along the direction of the CMS X-axis:

- X1: 2 potentiometer sensors mounted one on each half of Collar are used to measure the Collar against the CASTOR table rails. See fig. 6.13 for details. These sensors need to be removed before opening the Collar.

The instrumentation described above corresponds to the -Z side of the detector. The difference between the minus and plus Z sides is due to the uncompleted assembly of forward detectors in the +Z side. At the time of this write-up, the CASTOR detector is only

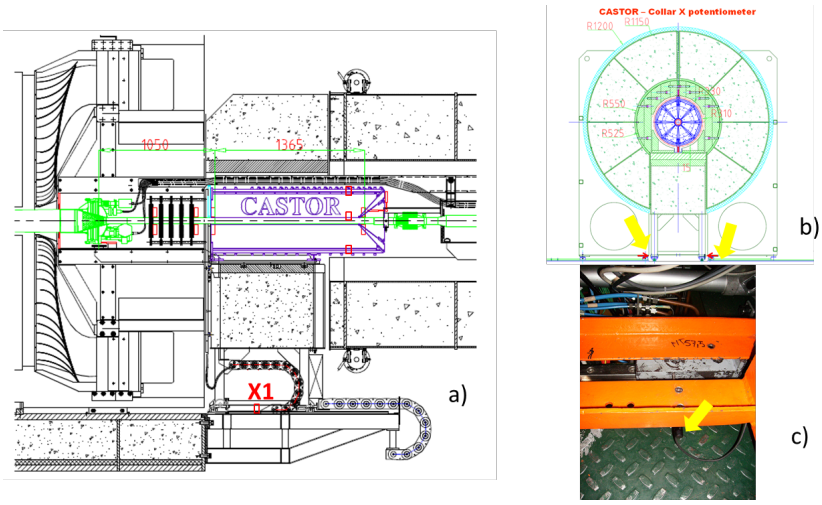

Figure 6.14: a) Longitudinal view of the forward region with the location of the X1 sensors. b) Rϕ view, drawing indicating the location of the sensors installed in the Collar measuring against the CASTOR Table rails; c) view of the sensors mounted on the detector, the yellow arrow indicates the location of the sensors.

installed in the -Z side. This difference imposes a slight different (and provisional) layout of the sensors. The present configuration (at the time of this write-up) is illustrated in fig. 6.15. The set of sensors labelled as R1, R2, Z1 and X1 are similar to the ones described for the -Z. Z2 is a potentiometer sensor installed in the CASTOR cradle to measure the distance against the back side of the HF-plug. This sensor informs on the distance, and possible deformation, due to magnetic forces, between the Collar platform and the HF structure. A couple of potentiometers, labelled as Z3, surveys the distance between, the external part of the HF and the inner part of the HF-plug. The sensors are installed at the tip of an auxiliary extension aluminium bar fixed at the external side of the HF body. Z2 sensors maintenance requires having Rotating Shielding opened. To avoid damaging the sensors, they must be removed before HF opening.

The full detector TOTEM T1 (see fig. 6.16) was installed in the winter shutdown of the 2010/2011. This detector is located inside the 3 endcaps (YE+/-1, YE+/-2 and YE+/-3) on both ends of the CMS. TOTEM T1 is subdivided in four quarters, and two quarters, per detector end, were installed.
T1 consist of five layers of chambers in each quarter plus one more layer that is used exclusively for connections of the services of the detector.
Fig. 6.16 shows all the four quarters identified with the colours. The yellow and blue quarters are the pair installed on the plus end of the CMS detector. The yellow quarter corresponds to the near side and, the blue quarter to the far side. The green and red quarters are the pair installed at the minus end of the CMS. The green quarter corresponds to the near side and the red quarter to the far side.
CSS sensors are mounted on the 1^{st} and 5^{th} layers (see fig. 6.17). The 1^{st} layer is on the

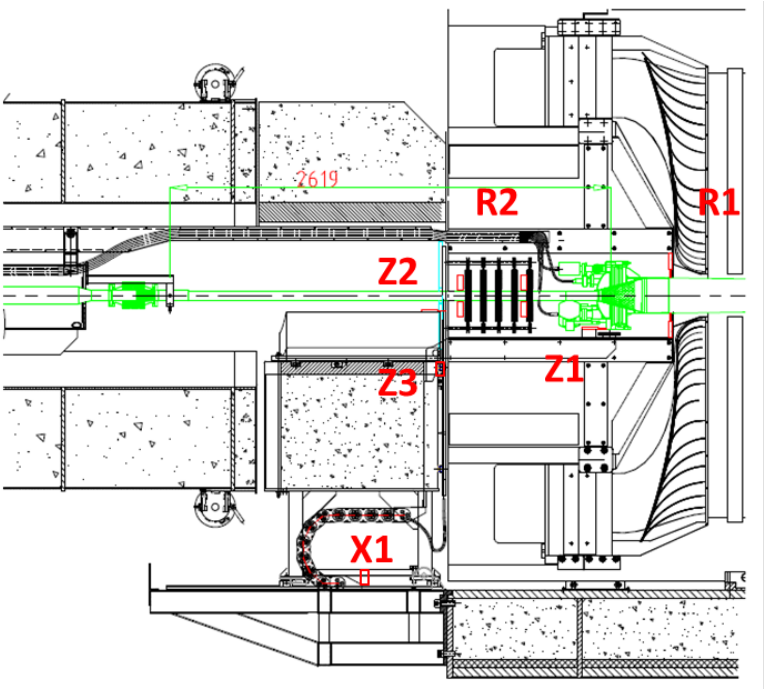

Figure 6.15: Longitudinal view of the forward region with the location of the CSS sensors for the +Z detector side.

IP side of the detector and the 5^{th} layer is the NonIP. These sensors monitor the critical process of closing T1 detector, they provide the only available measurement, able to certify that the gap between the layers and beam pipe is within the safety limits and the detector is in its nominal position. The sensor technology chosen was the ultrasound sensor thus avoiding the use of a dedicated target. Figure 6.18 shows a transverse view of the detector with the radial sensors distributed for the 5^{th} and 1^{st} chambers.

Moreover, potentiometers have been mounted to measure the Z movements during the ramp cycles of the magnet between the T1 detector and the three different endcap disks. These potentiometers, shown in fig. 6.19 are used to assist the closing, but the important application is the monitoring of T1 during the magnet ramping cycles. There are two sensors on the 5^{th} layer on each quarter installed on the top and bottom of the layer, against the YE+/-3 disk. Other two sensors monitor any movement between the detector and YE+/-2 and YE+/-1 disks. Each sensor is mounted in a different quarter. The sensor mounted between the T1 detector and YE+/-2 monitors the fixation point of the detector on the YE+/-2 disk and it should never reveal any movement.

The total number of sensors instrumented in the forward region is summarized in Chapter 2, Table 2.2. Considerations related to the required access for system maintenance are given below.

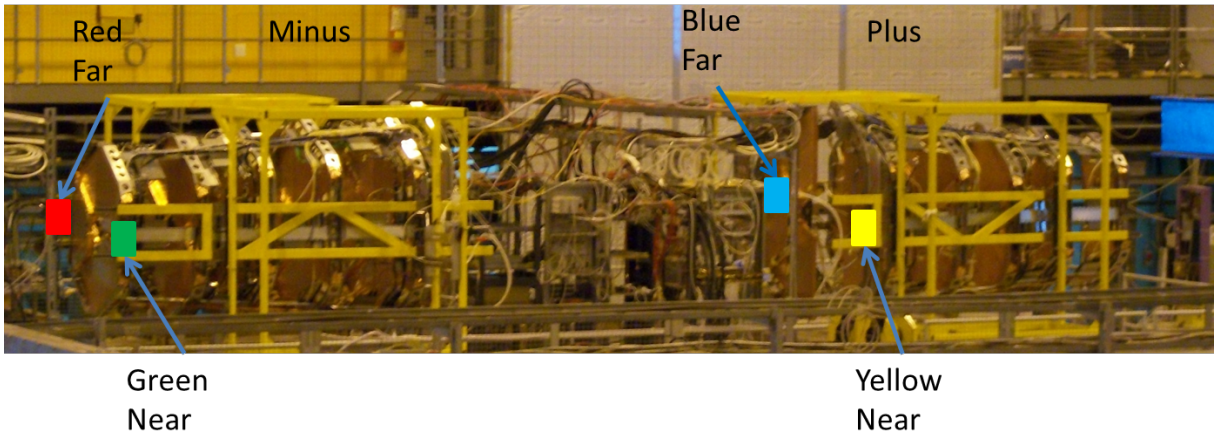

Figure 6.16: Photo of the four quarters of TOTEM T1 with the colours that identify each quarter during the assembly and commissioning of the detector.

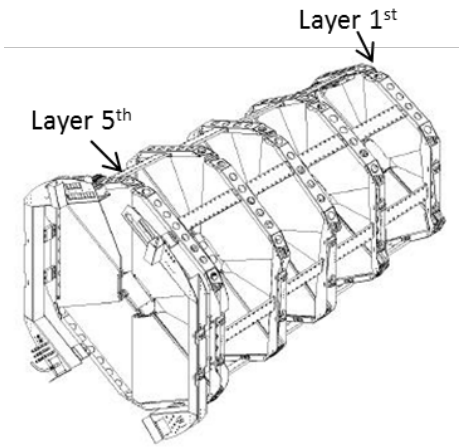

Figure 6.17: Two quarters of the T1 detector close with a 3D view.

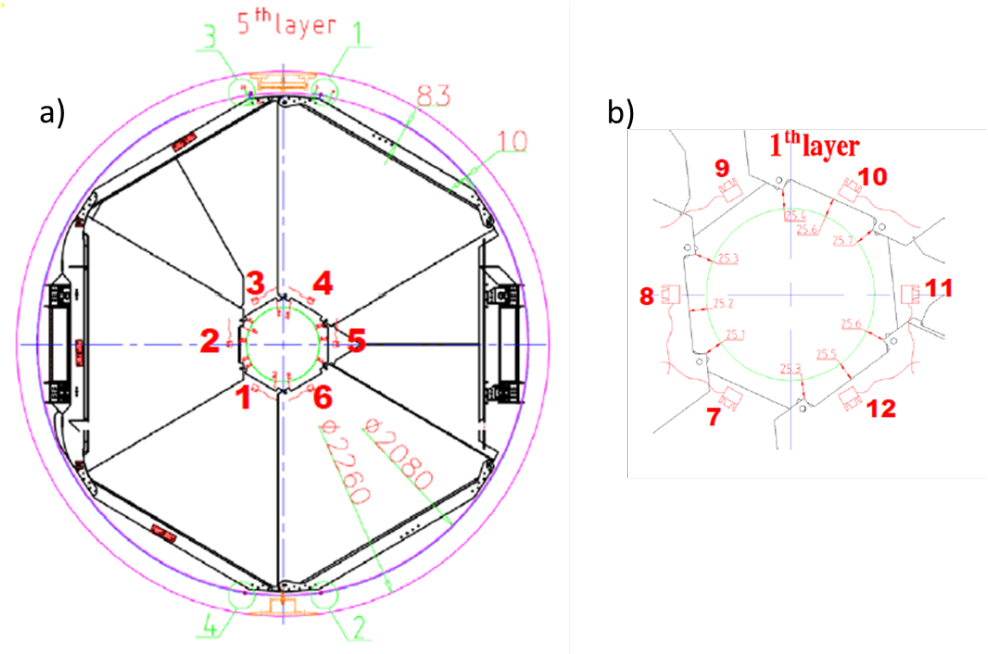

Figure 6.18: Front view drawing of the TOTEM T1 detector for the 5^{th} layer a); and the 1^{st} layer b).

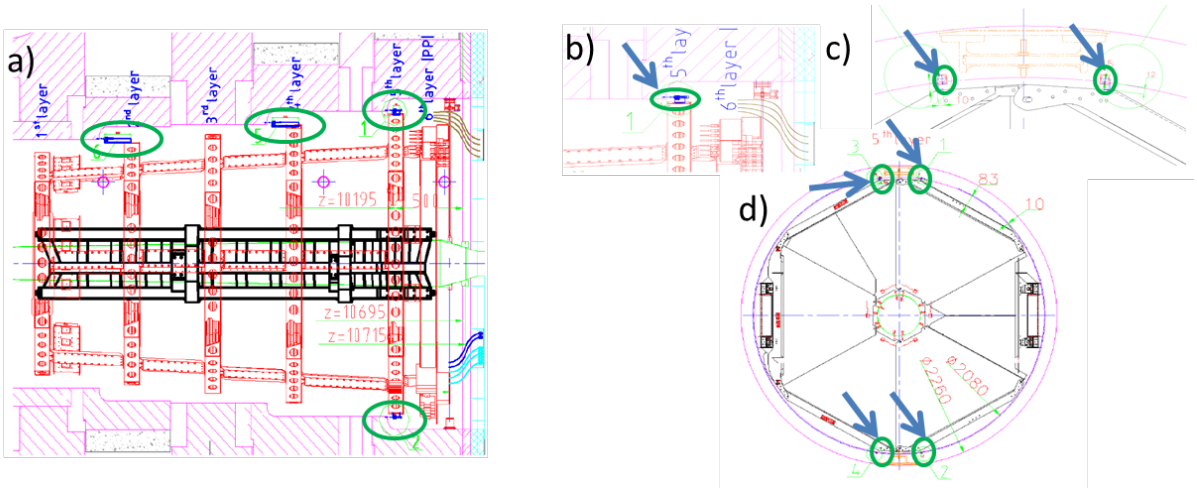

Figure 6.19: a) Drawing of TOTEM T1 inserted into the endcap disks showing the potentiometers mounted at the different disks. b) Zoom of the sensor on the top of the 5^{th} layer. c) The two sensors mounted on the top of each quarter on the 5^{th} layer; and d) the 5^{th} layer with the four sensors mounted on the top and bottom.

6.3 Forward detector closing procedures

A brief description of the procedure followed in the closing of the detector is given below. The lessons learned from the use and maintenance of the CSS during these years are also summarized.

6.3.1 TOTEM T2 Detector

The procedure of closing TOTEM T2 is a delicate operation due to the small gap with respect to the beam pipe. The detector T2 has a nominal distance of 9 mm to the beam pipe. Once LHC is in operation, the radiation levels in the area make manual interventions or visual inspections unsafe. To ensure good functionality of the monitoring system a series of actions are recommended before the closing process starts: i) to check the Z potentiometer installed in the CASTOR table support versus the flange of the beam pipe (Z1) to guarantee a starting correct position; ii) to check the correct positioning of the targets; iii) to check the distance between the high voltage connectors installed in the beam pipe flange and T2 so that, a safe closing of HF and T2 is possible and further motions along the beam pipe are also allowed.
The closing procedure starts with the closing of one half of T2, the CSS system with the entry sensors on both sides of the detector, helps to monitor the initial alignment with respect to the beam pipe. When the detector starts approaching the final position, the radial sensors, installed in the centre of the half detector, will start measuring the distance between the two objects, and this information allows a final adjustment in the detector support in order to have a good nominal safety clearance between the IP side and NonIP side of the first half. The second half of the detector needs to take into account, not only the alignment to the beam pipe but also the alignment with the first half already in its nominal closed position.
TOTEM T2 is a flexible detector made up of several disks. The gap available between the disks is small and most of the time the disks are in contact during the closing. The surfaces of the disks are now protected with kapton foil to obtain a better sliding. Once the detector is completely closed and in its final position all distances with the neighbour components are re-checked to be sure further motions due to magnetic forces are safe.

[1]This measurement is in order to have a reference to close safely and make monitoring during the ramps of the magnetic field.

6.3.2 HF Detector

This detector is the largest in the forward region. Its closing is motorized with manual controls. After the first closing, references coordinates were recorded such that can be reproduced with an average accuracy of 0.5 mm in successive operations.
As for the other forward detectors, the closing starts approaching one half of the detector towards beam pipe. When the radial CSS sensors reach the beam pipe, the measurement starts and from this point on the movement is done step by step until the correct final position is achieved. During the process, it is recommended to check if other sensors (for instance located in T2) register any change of position, sometimes a final mechanical adjustment of TOTEM T2 could be needed. The last step in the closing of HF is a movement of few millimetres in Z using the Z1 sensor to monitor the shift towards IP needed to completely close the gap between the detector and the third endcap disk, YE+/-3.

6.3.3 CASTOR Detector

The CASTOR detector is the simplest to close because it is the most external and easy to access. Although the IP side of the detector is blind for the operators, the clearance on the NonIP side is easy to check directly. The first step in the process of closing the CASTOR is to check that the targets are in the correct position to allow a continuous measurement not only during the closing but also during the cycles of the magnet. The target located at the IP side of the CASTOR is shared with T2. Before closing, it is also important to verify the values of the potentiometers installed on the NonIP side of the detector. Each half of the calorimeter is manually closed moving the detector towards the beam pipe, and as soon the beam pipe is in the range of the sensors, the distances measured should be equally distributed between sensors. If there is any misalignment, the whole process needs to be repeated until the detector is well centred and the final positioning values are close to the reference ones.

6.3.4 Collar and Rotating Shield mechanics

The closing of the Collar is assisted with motors and the CSS is used when the pieces are approaching their final position. Using the reference values, obtained by the system, the work consists mainly in avoiding possible contact between the Collar and the supports of the TOTEM T2 and BCM or the CASTOR detectors, which could induce displacements of the detectors or risk the integrity of the beam pipe. One of the major challenges of the CSS is to correctly reproduce the reference values since the sensors must be re-mounted in each operation.
The rotating shield is made of two half's with 100 tonnes weight closing towards the beam pipe. This element is the last one being closed. It is a slow process assisted by an

hydraulic system with visual checking from the operator placed where the system is commanded. The CSS provides an assistance to check if the clearance between rotating shield and CASTOR is respected during the process.

6.3.5 TOTEM T1 detector

The closing of TOTEM T1 detector, on each end of CMS, is done with a special configuration of the forward region. The HF platform on 2 raisers and with HF closed serves as support of the two cages that contain the T1 detector. T1 has been previously installed and aligned inside the cages by the survey team. Rails are embedded on the cage of the quarter T1 detector that will be used to fix the whole detector. The rails are connected to so called TRUSS rails (located inside the endcap disks) making possible to move T1 inside the endcap disks. Again, prior to installation, the TRUSS rails have been installed and aligned by the survey team. A first test, with one quarter of the T1 inserted is done to check the alignment and clearances between the quarter detector and the beam pipe.
In this step the CSS potentiometers are used to obtain the final adjustment. Then the T1 quarter detector is extracted to the cage and the process is repeated for the other quarter. These specific configurations are illustrated in fig. 6.20. From the initial to the final position the detector needs to travel a distance of approximately 3.2 m. During the simultaneous insertion of the two quarters of T1 in the endcap disks the CSS will provide the information on the clearance to the beam pipe and its final position in Z. The same fig. 6.20 shows blue dots with the red arrows pointing to the beam pipe, showing how the measurements are actually done. Axial measurements indicate if the detector has reached the final position. This operation could be simplified using a mechanical system with a stopper to make a more precise tune of the final position. The closing procedure followed with TOTEM T1 is safe and relatively fast thanks to the use of the rails system. The most risky operations are the checks with the individual quarters inside the endcap disks, when the operators need to work in this critical area, and the final operation of closing since it is done with the beam pipe suspended only on a titanium bar and any hit or push on the beam pipe can create a serious problem. To end the operation of closing the HF platform is on 3 raisers. The HF detector should be completely open to connect the services of the detector.

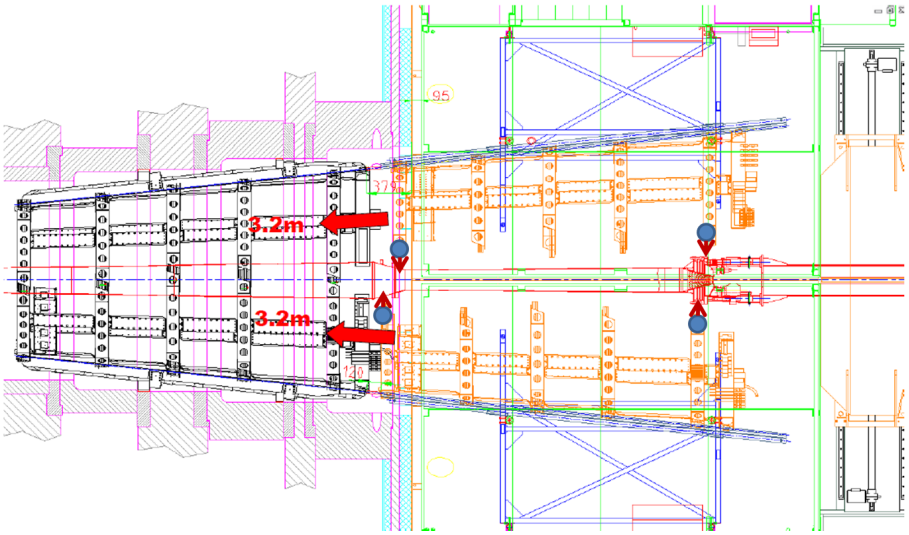

Figure 6.20: Top view for the T1 installation: the initial position of T1 (in orange) on the cages on top of the HF with 2 raisers, and at its final position inside the endcap disks (in black).

7

Readout and Control Electronics

The choice of the readout system was driven to make the best use of the CMS infrastructure and to match the performance requirements and safety restrictions of the experiment. ELMB (Embedded Local Monitor Board) cards, a radiation tolerant and immune to magnetic field electronics developed for the LHC experiments, were used to collect the signal from the CSS sensors. Ad-hoc solutions were developed to adapt the output of the different technologies used by the CSS to the ELMB cards. All components must fulfil strict LHC safety rules. The layout of the readout system was defined as modular as possible to allow easy replication as needed in the successive extensions of the system. Flexibility to allow the operation the system under CMS data-taking and maintenance conditions was also imposed. The readout of the network of sensors distributed over the detector is concentrated in few points (racks) close to the detector, in the collision cavern. Power supplies and Communication-Hub are located remotely in the underground electronics cavern to facilitate maintenance.

7.1 CSS Readout and Control

Given the CMS environment (radiation, magnetic field), most of the readout systems have to be located in the CMS electronics underground cavern which is ∼100 m away from the detector. However, some electronics in radiation tolerant format and immune to magnetic field, were developed for all LHC experiments providing a limited variety of readout/control electronics that can be used as front-end cards located in the collision caverns. They are part of a system known as ELMB.
The CSS sensor signals are collected and digitized using these ELMB cards that are

situated next to the detector. Apart from using the general ELMB development, we had to do some ad-hoc developments in order to transform the sensor signal into a signal that can be processed by the ELMB modules and to ensure the power distribution to the sensors, which also takes place close to the detector. The ELMB is configured with resistor adaptors to set the correct voltage range to its ADC. The ID number for the CANBUS is also set on the ELMB board. The power distribution was designed to allow switching on/off groups of sensors per element or detector. The DC power supplies are mainly 3 types, 24 VDC, 12 VDC and 10 VDC, each power supply is protected by a fuse. The 24 VDC serves the Beckhoff modules, relays, and ultrasound sensors. The 12 VDC serves the potentiometers, voltage regulators and current regulators. The 10 VDC is only used for the ELMB cards.
The sensors are distributed all over the detector and are connected either via concentration points or directly to the readout crates which are situated as well in the detector area, the collision cavern. The crates are organized in racks. Particular care had to be taken for specific sensors; a voltage regulator is positioned next to the infrared sensors in order to assure that there is no voltage variation and no noise pickup produced on the lengthy cables and affecting the phototransistor. They also need a constant current source which is being used by the emitter; this source had to be developed since it has to be driven over $\sim$50 m cables. To summarize, the sensors network is mounted on the detector, the concentration points are installed close to the detector and the readout is installed in the racks. The power supplies are installed outside the detector cavern; they are remotely controlled and this makes maintenance easy. The layout of the CSS readout and control system is shown in fig. 7.1. The final diagram of the CSS is drawn on the fig. 7.2.

The standard way to view any information from CSS is through the online display of the CMS experiment's control data. The system that does that, putting together the control and critical monitoring data of all CMS sub-detectors and subsystems is called DCS (Detector Control System). The DCS system was discussed in Chapter 2. The software layer used for DCS is PVSS, a commercial application chosen due to its flexibility (it can run on both Windows and Linux platforms) and its adaptability to the high energy Physics, large scale experiments. PVSS however is an HMI application used in industry.
Apart from being able to follow CSS from the detector control room, it is important that the application runs locally, on the PCs of the people who are working in the cavern, close to the detector during the periods of the detector opening/closing, at the LHC shutdown periods, when central data taking is disturbed and when the detector is open. Local instances of the display program as well as power controlling functions are available for designated operators, via remote connection.

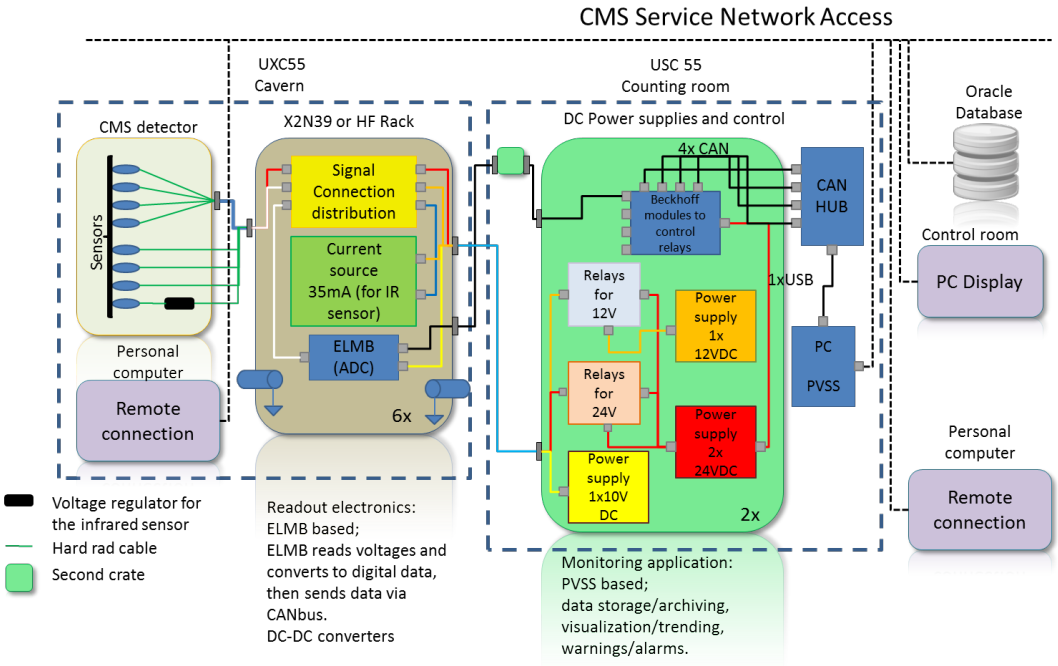

Figure 7.1: Layout of the CSS readout and control system

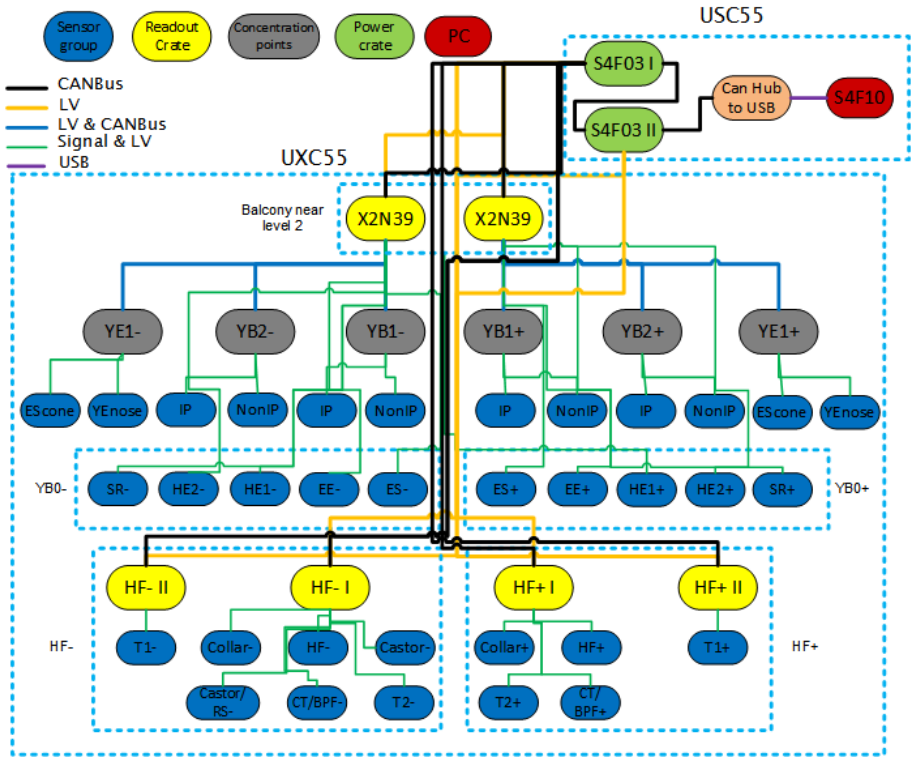

Figure 7.2: Diagram of the Readout and Control system

7.2 Layout of connections for the sensor technologies

A simplified schematics of the connections for each type of sensor used by the CSS is shown in fig. 7.3. Four wires radiation resistant cables (from Novacavi, see 7.3) were produced and used for all type of CSS sensors. AMP-Tyco "Micro Mate 'n Lok" connectors were also selected due to its small size.
The non-contact infrared sensor (fig. 7.3 a)) requires some custom made electronic devices as the voltage regulator and the current regulator. A voltage regulator located close to the sensor/phototransistor for maintaining it at a constant value. It also helps reducing electronic noise due to the high voltage cables present in the detector. Moreover, a current source located inside the readout crate, provides a constant signal to the sensor LED and allows maintaining constant emission intensity despite the use of long cables.
The connection convention used for ultrasound sensors is shown in fig. 7.3 b). The "Teach in" pin is not used in our application and it is connected to ground to avoid any undesirable reset of the sensor.
Finally, potentiometers are three wired sensor, the last pin is connected to the 0 V of the power supply. The connection scheme is shown in fig. 7.3 c).

7.3 Readout, power, and communication cables specifications and layout

As mentioned above, a small diameter and hard radiation custom made cable was used for the readout of all the sensors in the system. This cable was used in the CMS Tracker for the application in the thermal screen where the radiation level is very high. The specifications of the cable are 1 x 4 x 28 AWG AL Shielded Rad. Res. from Novacavi with a nominal overall diameter of 3.40 mm, and with green colour cover (known as "green cable"). The cable with reference 04.21.48.336.5 - CAB.SIGN. BLINDE MCA36 (available at the CERN store) was used to transport the signal/power from the detector (concentration points) to the readout crates located in racks (X2N39) arranged along the cavern walls and on the HF platform. The cable has some mechanical resistance and can be installed in hostile environments as the cable chains. The cable used for the CANBUS communication was 04.21.60.421.0 - CABLE CANBUS 2 x 2 x 1,0 mm^2 (available in the CERN store). The diameter of the wire is 1 mm^2 to allow long distances without losing the signal. HF or S2N39 and power crate. The cable selected to provide low voltage between power crate and the readout crates was 04.21.52.130.6 - CAB.SIG.BL. 9 x 2 x 0,50 mm^2 NE18 (available in the CERN Stores), the diameter was selected according to the maximum current required for the application.
3D drawings for all cable routing, inside and outside the detectors, were provided by the CMS Integration Office and are available at the central equipment database of the experiment. The CANBUS lines are serial lines according to the communication protocol

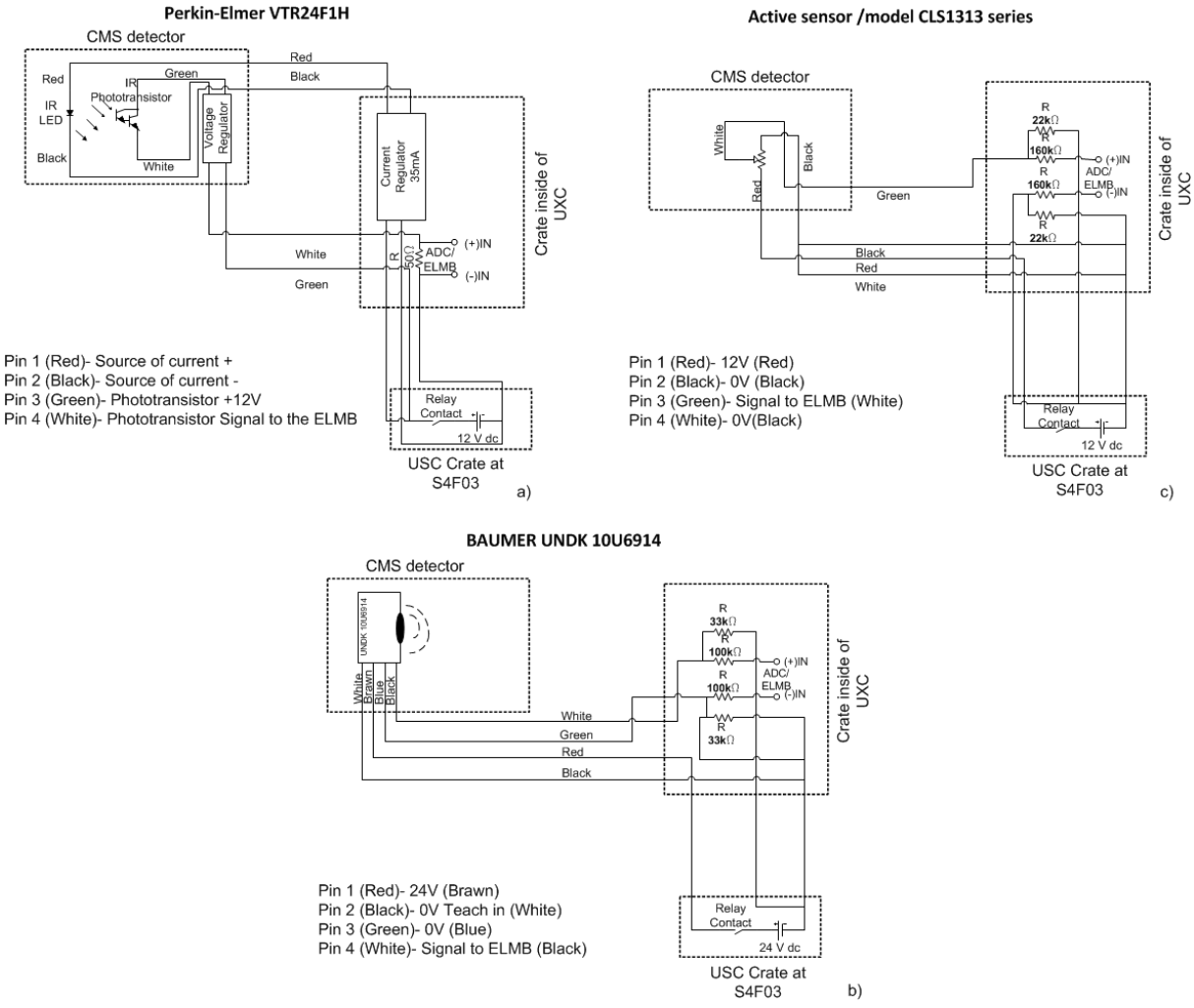

Figure 7.3: Schematics of the sensors connections: a) infrared; b) ultrasound, and c) potentiometers.

specifications of the experiment. The maximum recommended length is 500 m and is working with a speed of the CANBUS set to 125 kbit/s that are inside the specification for the length. The fig. 7.4 shows the schematics of the installed CANBUS lines.
The line can be closed between YB1 and X2N39 in case the line is cut and allows the possibility to connect this termination to the system and keep working the other half of the line. The S4F03 II and HF+/- II crates were the last additions to the system in the of 2010 winter shutdown in order to allow the installation of T1.

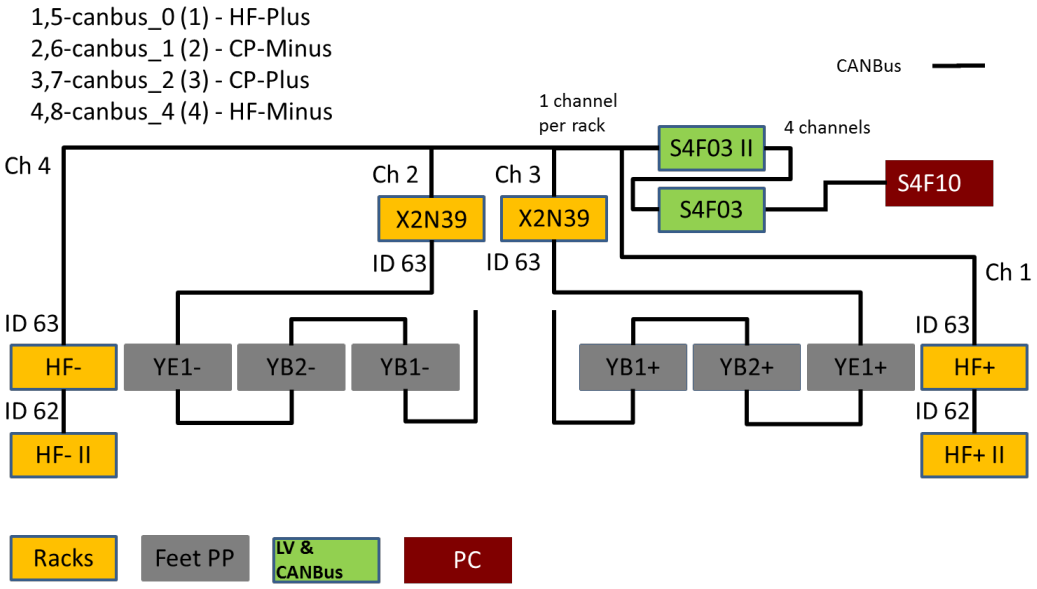

Figure 7.4: Schematic for the CANBUS lines installed

The fig. 7.5 is a simplified scheme of the CANBUS line inside all readout crates, which is connected to the ELMB through the DB9 female connector. This layout allows communication between the power crate in the service cavern (back of the rack) and a direct connection to a portable PC (front of the rack) in the experimental cavern. In the central region a long CANBUS cable is connected on the front of the rack that passes on YE+/-1, YB+/-2, YB+/-1 with a patch panel on each that allow to connect a portable PC and returning to the start point.

Figure 7.6 shows the layout for the CANBUS between the power crate S4F03 and the USB Can-Hub to connect to the server on S4F10.

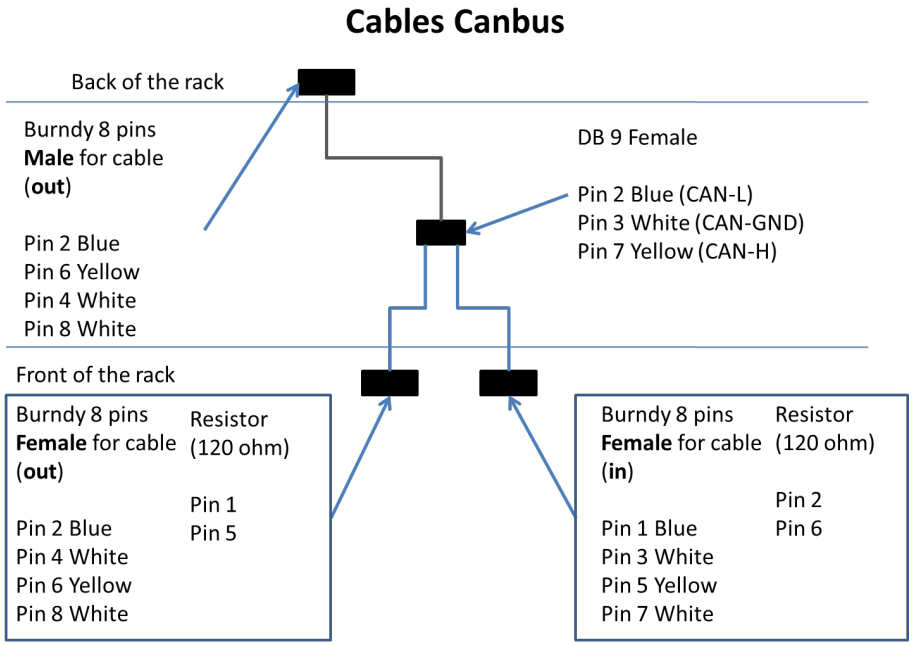

Figure 7.5: Layout for the CANBUS line inside of the readout crate

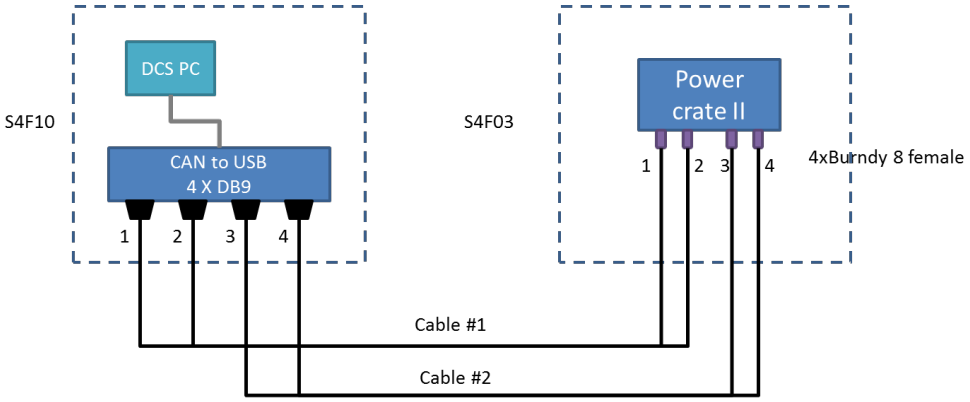

Cable #1 Label (CSS CAN1)			
Female Burndy 8#1 Label (#1)	Function	Wire Color	DB9 female #1 Label (#1)
2	CAN-L	White (pair with orange)	2
4,8	CAN-GND	White (pair with blue)	3
6	CAN-H	Orange (pair with white)	7
Female Burndy 8#2 Label (#2)			DB9 female #2 Label (#2)
2	CAN-L	White (pair with red)	2
4,8	CAN-GND	Blue (pair with white)	3
6	CAN-H	Red (pair with white)	7

Cable #2 Label (CSS CAN2)			
Female Burndy 8#3 Lab el (#3)	Functio n	Wire Color	DB9 female #3 Label (#1)
2	CAN-L	White (pair with orange)	2
4,8	CANGND	White (pair with blue)	3
6	CAN-H	Orange (pair with white)	7
Female Burndy 8#4 Label (#4)			DB9 female #4 Label (#2)
2	CAN-L	White (pair with red)	2
4,8	CANGND	Blue (pair with white)	3
6	CAN-H	Red (pair with white)	7

Figure 7.6: Layout for the CANBUS between the power crate S4F03 and the USB Can-Hub to connect to the server on S4F10

7.4 Readout and control crate

7.4.1 ELMB configuration

The ELMB device has 64 analogue to digital inputs with 16 bits. It is used by the CSS to digitalize the measurements provided by the sensors. The operational range selected for the ADC was 0 to 2.5 V (this range allows to use a simple conversion factor in the adaptors modules). The bipolar reading mode of ELMB was selected in order to optimize immunity to the external electrical fluctuations. The motherboard (fig. 7.7) contains a series of sockets for adaptors that are specific for each type of sensor.

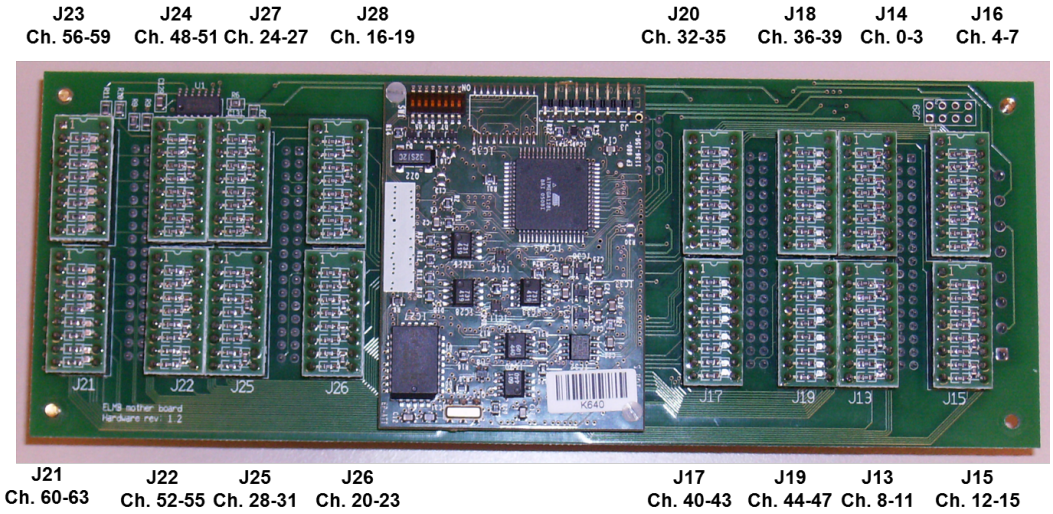

Figure 7.7: Photograph of the motherboard (bottom side) ELMB with the resistor adapters

7.4.2 Current and voltage regulators

To provide constant bias currents for the LED emitters, a 16-channel PCB (fig. 7.8) has been developed in association with INFN (Istituto Nazionale di Fisica Nucleare) Pisa. The board carries a common circuit that provides 12 VDC regulated and filtered power for the rest of the circuitry from an external, unregulated 12 VDC power supply, and sixteen individual subcircuits, each one driving LED emitter with a constant current. The current sourcing circuits have been implemented using a LM 117 regulator connected for constant current operation, and the current is set by one SMD resistor. Multiple pads allow for easier changes of the LED bias currents. This PCB is housed in a DIN rail compatible box, in the Counting Room. These boxes have an internal converter to convert from 12/24 V to 5 V to supply the sources of current for the LED. Tests have been made to ensure the compliance even over the long cables feeding the emitters.

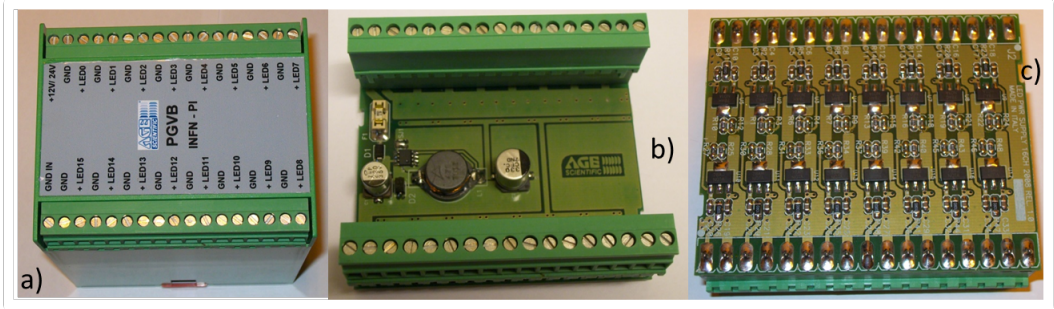

Figure 7.8: Photograph of constant bias current for the LED emitter box with 16-channel a), the top view of the board b), and the bottom view where is possible to see the components for each channel c)

In order to assure a constant collector-emitter voltage independent of the current drawn by the photo-Darlington receivers, a miniature PCB (fig. 7.9) was also developed. It carries a SMD version of the LM117 regulator, two SMD capacitors, two SMD resistors and two 4-way AMP-Tyco "Micro Mate 'n Lok" connectors and has a total footprint of 0.5" by 1.4" (12.7 mm by 35.6 mm). For convenience, the LED biasing lines are also routed through this PCB, which therefore connects to the 4-wire cable from the counting room on one side and to the 4-wire cable from the emitter/receiver pair on the other side. The receiver-driving PCB is located at a distance between 5 and 15 cm from the sensors. Only in the forward region it was not possible to mount the regulators next to the sensor because of the lack of space in the detectors T2 and CASTOR. Extensions of 2.5 m between the sensor and the regulator were used.

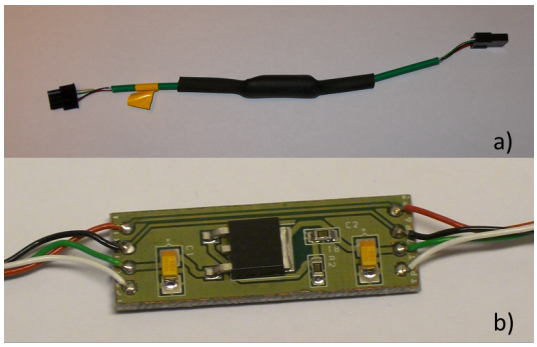

Figure 7.9: Photograph of a regulator ready to install with the connectors a), and the circuit board with the electronic components mounted b)

7.4.3 Dimensioning the power

The consumption of the IR phototransistor plus the voltage regulator ranges between ∼0 and 40 mA for most of the cases of sensors calibrated and used by the system. The average

current is 30 mA for the voltage regulator plus phototransistor in nominal position. The source of current provided to the LED is 35 mA and has a power consumption measured of ∼0.213 W on the LED. The phototransistor has a power consumption of maximum average measured of ∼0.48 W. The maximum current consumption of the ultrasound sensor is 35 mA with a voltage of 24 V and has about 0.84 W of power consumption. This information is provided by the manufacturer. For potentiometer sensors with a resistance of 1200 Ω (information provided by the manufacturer), and an applied voltage of 12 V to the terminals the current should be ∼ 0.01 A. We consider that the resistor of the ADC of the ELMB is almost infinit. A summary for all sensors and components is given in Table 7.1.

Table 7.1: Power consumption of the different types of sensors and components

Type of sensor	voltage (V)	Current (A)	Sensor consumption (W)
IR voltage regulator	12	0.04	0.48
IR current source	5	0.0426	0.213
Ultrasound	24	0.04	0.84
Potentiometer	12	0.01	0.12

In Table 7.2 to 7.5 the specifications for the different crates are given. Note that, for all the groups of sensors, all the currents are much less than 1.5 A, the maximum supported by a conductor with a section 0.5 mm^2 and a factor of safety >20%. The section of all conductors used between USC crates and UXC can be 0.5 mm^2. The system has been designed with a good margin in power management.

Table 7.2: Dimensioning of the power consumption of the central region of each crate

Central region Crate			
Group of sensors	Sensors installed	voltage of the power supply (V)	Max. Power Consumption (W)
YB0	21 x Infrared sensors	12/5	14.53
YB+/-1	8 x ultrasonics sensors	24	7.56
YB+/-2	9 x ultrasonics sensors	12	1.92
YE+/-1	4 x ultrasonics sensors	24	2.42
YE+/-1	4 x Infrared sensors	12/5	2.77
ELMB	1 ELMB motherboard	10	10.00

7.4.4 Readout and power crates

The readout crates were designed and built with some flexibility, with modular elements like the constant bias current module, to allow different configurations for the different

Table 7.3: Dimensioning of the power consumption of the HF I of each crate

HF I Crate

Group of sensors	Sensors installed	voltage of the power supply (V)	Max. Power Consumption (W)
T2	16 x Infrared sensors	12/5	11.09
CASTOR	16 x Infrared sensors	12/5	11.09
HF pots	16 x Potentiometrics sensors	12	1.92
T1	12 x Ultrasonic sensors	24	10.08
T1	12 x Potentiometrics sensors	12	1.44
ELMB	1 ELMB motherboard	10	10.00

Table 7.4: Dimensioning of the power consumption of the HF II of each crate

HF II Crate

Group of sensors	Sensors installed	voltage of the power supply (V)	Max. Power Consumption (W)
2 x Spares	16 x Infrared sensors	12/5	22.18
HF pots	4 x Potentiometrics sensors	12	0.48
T1	12 x ultrasonic sensors	24	10.08
T1	12 x Potentiometrics sensors	12	1.44
ELMB	1 ELMB motherboard	10	10.00

regions in the detector.

Figure 7.10 shows the arrangement of a readout crate (left picture) with the different elements mounted (the current bias regulators modules, ELMB, and the other modules in charge of the connections between the different elements). This layout ensures the possibility to change the configuration (install a new set of sensors or change the type of sensors) changing only a few wires, as well as allowing an easy maintenance. The right-hand photo shows a power crate built with enough space, in the interior, to have good heat dissipation and ventilation from the power supplies, relays and controllers. The low density of components allows the passage of the air flux from the bottom of the crate to other crates, when installed in a rack cabinet with a vertical cooling system. The layout of the custom made front and back panels, used for the readout crates, is shown in fig. 7.11. The back panels have two plugs, one for communications, CANBUS line, and other for the power supply. Fig. 7.11 b) shows the distribution of the connectors on the front panel

Table 7.5: Maximum rates of the devices used and maximum power rate of the power supplies

Power Crate on USC S4F03

Device	Quantity	voltage of the power supply (V)	Max. Power Consumption (W)
Beckhoff BK5150	4	24	96
Beckhoff KM2002	4	24	9.3
Beckhoff KL9010	4	-	-
Finder relay 38.51.7.024.0050	4	12	9.3

Power supplies installed

Device	Quantity	Power supply output (V)	Max. power output (W)
Siemens LOGO! 6EP1332-1SH51	2	24	192
Siemens LOGO! 6EP1322-1SH02	1	24	54
TDK Lambda DSP100-12	1	12	100

for the crate of the central region. AMP connectors are used for the cables, coming from inside the Vac tank, that connects directly to the readout. DB37 connectors come from the concentration points using the MCA36 on YB+/-1, YB+/-2 and YE+/-1 structures. The connector for the CANBUS line can be used to extend the system. This extension line can be used, as well for local operation in the collision cavern, with a computer directly connected to the crate. Fig. 7.11 c) shows the distribution of the connectors on the front panel for one of the crates of the forward region (HF I crate type), used for HF, CASTOR, and TOTEM T2 instrumentation. Fig. 7.11 d) shows the distribution of the connectors on the front panel for the second type of crates of the forward region (HF II crate type), used for the TOTEM T1 detectors.

The power is supplied to all readout crates by cables following the configuration shown in Table 7.5. For safety reasons, the power supply is outside the cavern, at the service cavern, USC at S4F03. The power is distributed by groups of sensors of the same type in most of the cases they correspond to an area/detector.

Few examples of the connections inside the readout crate, for the different types of sensors and connectors used are shown in fig. 7.12. The sequence of the colour of the wires in the different types of plugs, for the different sensors, was always the same. The FLKM 34 module can be used to connect the wires to a flat cable of 34 pin type 3M 3431 used by the ELMB for the signals coming from the sensors (grey colour in the drawings).

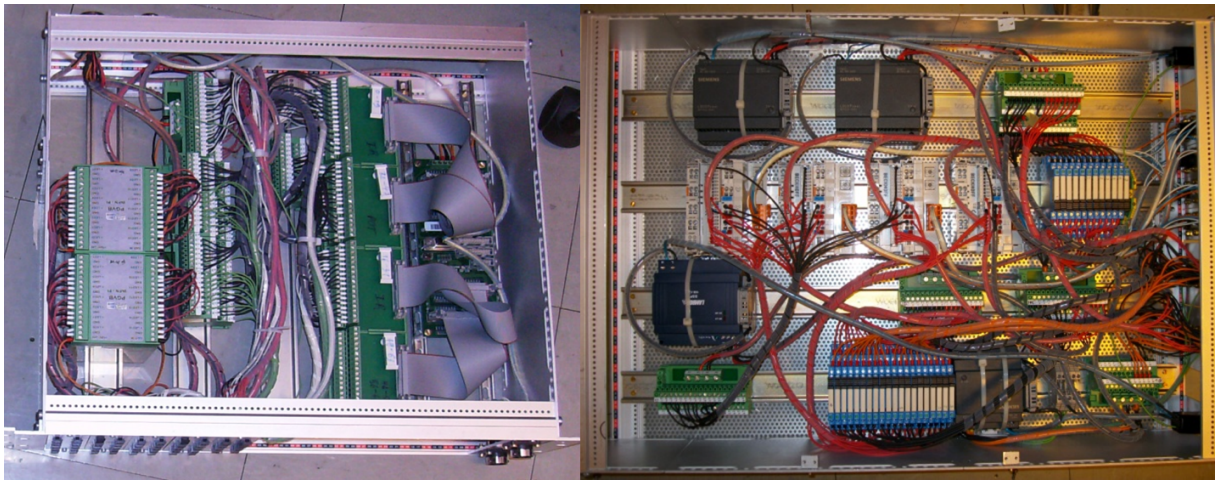

Figure 7.10: Photograph of the readout crate (top view) in the left and in the right the power crate (top view)

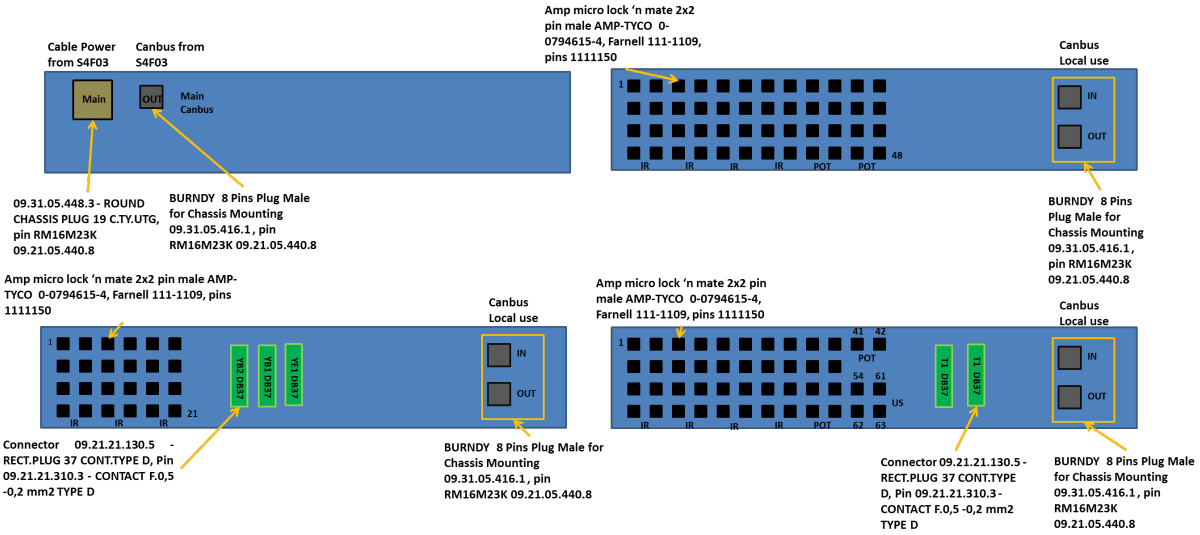

Figure 7.11: Layout of the back and front panels used in the readout crates. a) Back panels for all readout crates. Front panel for the Central region b), and forward region c) and d).

Table 7.6: Connector/wire X2N39 to S4F10 BURNDY 19 pins

Pin number	Wire number	colour of wire	voltage (V)
1	1	white	0
2	10	brown	12
3	2	white	0
4	11	brown	12
5	3	white	0
6	12	brown	12
7	4	white	0
8	13	brown	24
9	5	white	0
10	14	brown	24
11	6	white	0
12	15	brown	12
13	7	white	0
14	16	brown	12
15	8	white	0
16	17	brown	24
17	9	white	0
18	18	brown	10
19	—-	Copper	GND

The power crate was designed to support up to 4 readout crates with independent control and CANBUS line. A different ID was attributed to each Beckhoff module that has the function to control 8 relays to bias the different groups of sensors. The amount of sensors groups were determined for the cable selection used to bias the sensors. The selected cable allows to power up a maximum of 8 different groups of sensors. The voltages on the cable are distributed as shown in the Table 7.6. A simple layout of the connections distribution on the crate figures in fig. 7.13.

Relay sequence for power crate for the Central Region			
Relay number	Tension	Sector	Application
1	12V	YB0a	Orange
2	12V	YB0b	Orange
3	12V	YE1	Orange
4	24V	YB1	Red
5	24V	YB2	Red
6	24V	YE1	Red
7	12V	--	Orange
8	12V	--	Orange

a)

Relay sequence for power crate for HF I			
Relay number	Tension	Sector	Application
1	12V	T2	Orange
2	12V	T2	Orange
3	12V	HF	Orange
4	24V	--	Red
5	24V	--	Red
6	24V	--	Red
7	12V	CASTOR	Orange
8	12V	CASTOR	Orange

b)

Relay sequence for power crate for HF II			
Relay number	Tension	Sector	Application
1	12V	--	Orange
2	12V	--	Orange
3	12V	T1	Orange
4	24V	T1	Red
5	24V	--	Red
6	24V	--	Red
7	12V	--	Orange
8	12V	--	Orange

c)

Table 7.7: Sequence of the voltages for each relay

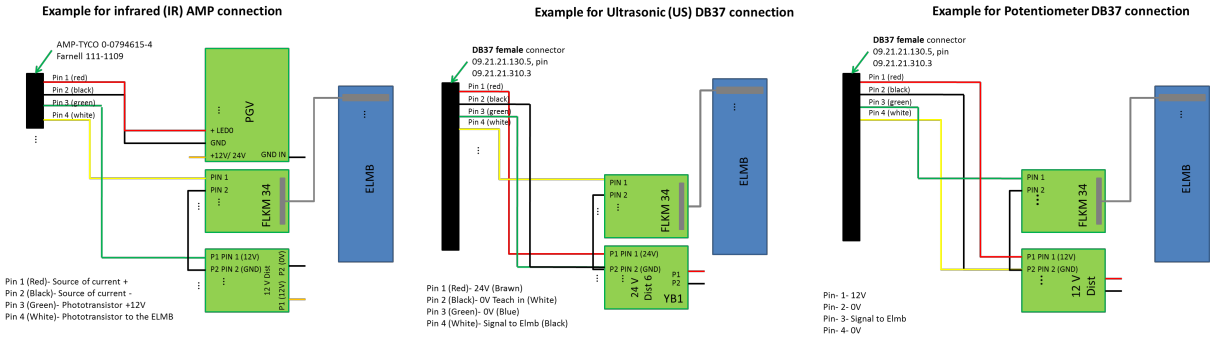

Figure 7.12: Layout of: infrared (IR) DB37 connection a); ultrasound (US) DB37 connection b), and Potentiometer AMP connection c)

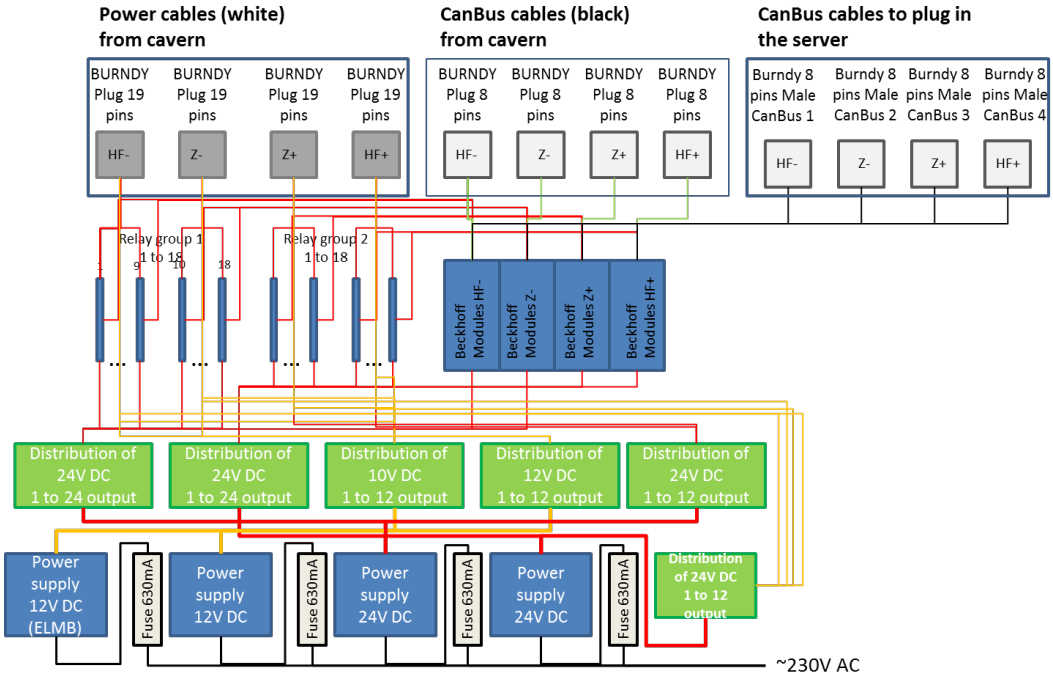

Figure 7.13: Power crate layout diagram connections

Table 7.7 shows the different voltage distribution of the different groups of sensors,for each readout crate type, installed with the corresponding relay on the Beckhoff module. The distribution of the voltages is equal on both sides of the CMS detector. The same voltage sequence was used, in order to, avoid electrical faults in case of wrong connection. The colours of the wires used were, red for 24 V and orange for 12 V. The outputs of the relays are connected to Burndy plugs with 19 pins with the sequence listed in Table 7.6. The final readout and control system was implement in July 2009. The system shows a good stability and no major problem has been encountered after more than 4 years of operation.

8

Control and Data Acquisition Software

A complete software package has been developed for the control and data acquisition of the Closing Sensor System. It uses the PVSS-SCADA framework, a software selected by the LHC experiments for detector control related tasks. In this Chapter a brief introduction to the main characteristics of PVSS is given followed by a detailed description of the structure and specific functionality of the package developed for the CSS project.
The performance of the CSS software have improved over the years with the inclusion of new features following the experience acquired from the operation of the system during the different phases of the experiment. In its development emphasis was given to incorporate easy to interpret displays to allow a quick transfer of information to the technical team in charge of the assembly of the detector or to the personnel in charge of the operation of the CMS magnet. The software pack began with simple functions, in order to assist the first closings of the detector and it is now a fully integrated system in the CMS DCS working in a continuous and autonomous mode. It is worth stressing this software has been developed to be able to work as well as a standalone system as required during the LHC maintenance periods.

8.1 Introduction

The PVSS is a SCADA (Supervisory Control And Data Acquisition) software, developed by the Austrian ETM Company. This company was established in 1985. The PVSS was selected by the LHC experiments in 2000, after 3-year evaluation phase. This type

of software allows building a standalone system that controls the hardware with the respective drivers and stores the data or retrieves it from a database. It has a HMI that allows operating the hardware system. The main feature of this type of software is the possibility of scalability and the possibility of interaction between different and distant systems, which allows the creation of large systems.
One of the most important features of PVSS is the highly distributed architecture. A PVSS application is composed of several processes, called managers. The base version of PVSS is composed of the following Managers:

- The Event Manager (EVM) – is the manager responsible for all communications. It receives data from any Drivers (D) and stores it in the database.
- The Data Base Manager (DBM) – provides a platform that manages the database.
- User Interface Managers (UIM) – can read device data from the database, or write data to the database to be sent to the devices, they can also request to keep an "open" connection to the database and be informed (for example to update the screen with the new values received and processed) when new data arrives from a device.
- Ctrl Managers (Ctrl) – is the manager that provides for any data processing as "background" processes, by running a scripting language. This language is like "C" with extensions.
- API Managers (API) – this manager allows users to produce their own code in C++ using a PVSS API (Application Programming Interface) to access the data in the database.
- Drivers (D) – the drivers manager provides the interface to the devices to be controlled. These can be PVSS provided drivers like Profibus, OPC, etc, or user-made drivers.

A PVSS System is an application containing one data base manager, one event manager and any number of drivers, user interfaces, etc. For very large applications one PVSS system could not be enough, therefore in these cases a PVSS Distributed System can be used. A distributed system is built by adding a Distribution Manager (Dist) to each system and connecting them together. Hundreds of systems can be connected in this way. The Detector Control System (DCS) of the CMS experiment controls all the experiment subsystems. It is one of the most vital parts of the CMS infrastructure and the one that combines information of all services as well as sub-detectors in order to evaluate whether the CMS is in a safe state or not and what actions are to be taken or what actions are allowed. It is a huge system whose upper software layer is being covered by PVSS. All LHC experiments as well as infrastructure services and the LHC accelerator use the very same SCADA program.
The PVSS software is used to connect all the hardware directly or indirectly involved in

the experiment to a decision taking, monitoring and data storage mechanism, providing at the same time a HMI that gives user an on-line feedback and allows the expert to drive its own system. The PVSS software has the task to monitor all sub-detector and infrastructure data and initialize, configure and operate them. It was thus developed to include different components and tools capable to manage the different problems a SCADA system of that size has to. The archiving solutions are relatively simple and robust as required for critical systems. To best serve the HEP community, a dedicated framework has been developed at CERN with different selectable components that allows the use of several electronic home made components and also to handle the different home made software components.

The Closing Sensors System (CSS) of CMS mostly uses the Ctrl Managers. The CSS software has the major challenge of running in a central system mode (during the cycles of the magnet and in normal data-taking periods) and as a standalone mobile application easy to interact with and optimized to provide online feedback to the operators to help them taking decisions in the process of opening and closing the detector.

8.2 CSS Human-Machine Interaction

The primary purpose in developing the CSS Human-Machine Interaction (HMI) was to provide a friendly user interface. As explained in previous chapters, the system is designed to be used in real time and specially during critical actions when the detector is being opened/closed. The CSS software has to be easy to handle by non-expert technical operators and by different users with different levels of knowledge of the detector.
The first item to define was the structure for the sensors, following the general layout of the hardware in the main detector regions. The regions are then divided in different groups that could be either, a detector or an infrastructure object, with a separate panel each. Particular effort was put to reflect the hardware details onto the software by means of a series of display panels. The data are organized in panels where the measured points are displayed. For sensitive variables, trends are shown as a function of time or B field, and variations with respect to a reference value are also given. All this information, filtered for suspicious sensor behaviour, is recorded in a database. Data are quickly accessible; so are the trends, etc. without the need of special offline analysis or too high memory usage.
One single summary panel, including all the necessary information was included to monitor the detector during the ramping of the magnet such that can be easily followed by the magnet operators. The panel contains the information of the relative variation ("deltas") of the measurements with respect to a reference measurement. This helps to discriminate if the current measurements are in agreement with the nominal values and gives the operator the possibility to take corrective actions as needed.

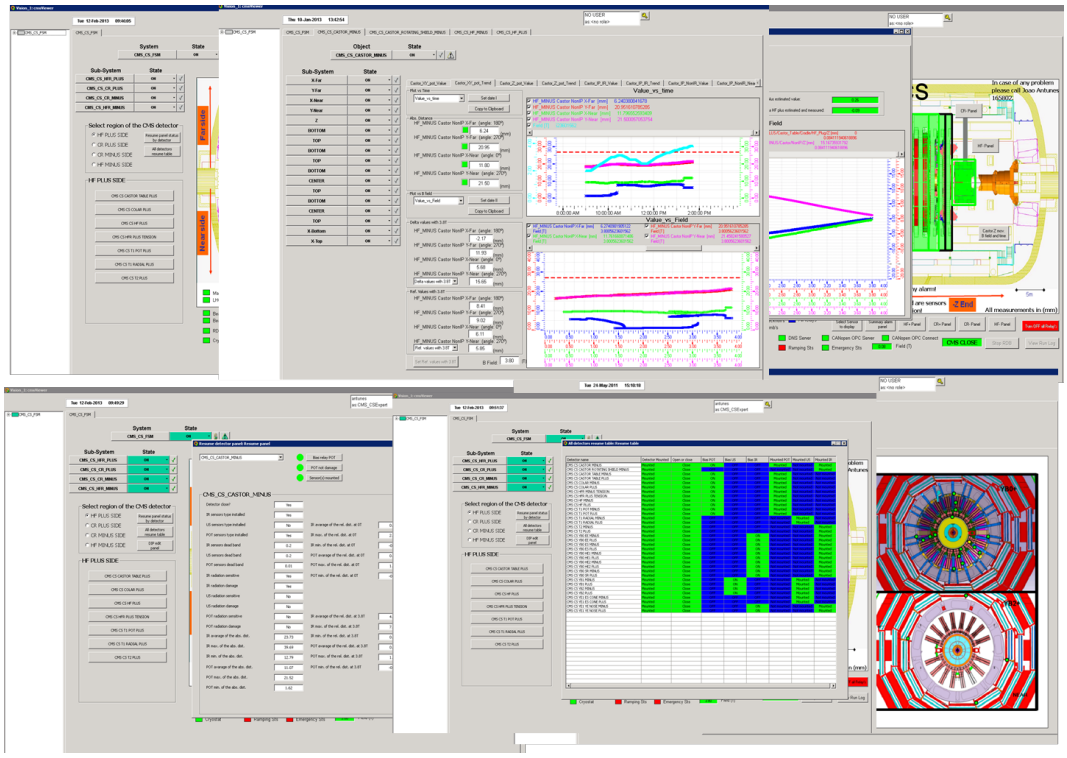

Figure 8.1: Picture of some panels developed for the CSS system

Fig. 8.1 shows different panels of the CSS that allows navigating through the different areas of the detector. Reference values, for comparison purpose, were created for critical sensors as explained before. The panels displayed in the figure show some of the functionality developed in the software. The software went through continuous improvements to incorporate new features of the hardware or more functionalities to increase the performance for the requested needs. A software able to operate a large detector as CMS -with many different elements, high level of complexity, and specific conditions- is not available in the market. It is a complex unique tool that combines know how acquired during the years.

8.3 Configuration panel and Finite State Machine

The software that controls the CSS hardware was developed under FSM (Finite State Machine) that allows the control of the hardware in a logical way with defined rules for the different states of the hardware and it could provide warnings to the operator in case of any malfunction.

The Finite State Machine is a tool of the JCOP framework consisting of two nodes: Control Units (CU) and Device Units (DU). The CU node is an user interface able to

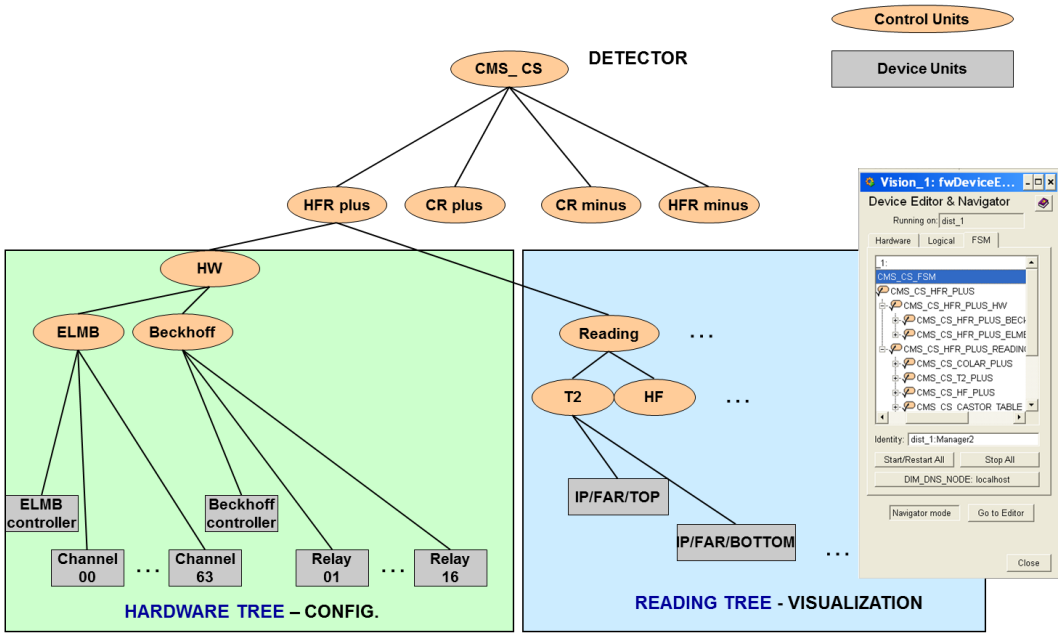

Figure 8.2: The FSM structure of the CSS

summarize information from the above levels and "set" actions through the lower levels. It is capable to implement specific behaviour, taking local decisions with sequence and automated operations and it is also capable to recover from errors. The DU node provides an interface to the real devices as electronic, algorithms, etc. As represented in fig. 8.2, four branches exit from the top Control Unit. They correspond to the four CANBUS nodes of the different areas of the detector. The areas are defined as "HF plus" "HF minus", "CR plus" and "CR minus" corresponding to the Forward (called here HF) and the Central Region (CR) of the detector, with the subsequent division on plus and minus side. This structure follows the actual geometry of the detector and allows local connections providing a more robust and reliable layout.

The Hardware branch is again divided in two branches, one for the ELMBs and the second one for the Beckhoff modules (see Chap. 7). The ELMB branch contains an ELMB controller that gives informations on the status of the ELMB, and all the channels used by the system. Similarly, the Beckhoff branch contains the control module and the relays positions. Each branch, of a given region, is again divided in two parts, one for the hardware signals that controls and make the reading of the voltages of the channels of the ELMB or the relay's that provides the bias to the sensors.

The Logical or Reading branch informs about the sensor being biased or not and allow to check all parameters of the sensor. It contains branches for the different CMS sub-detectors or infrastructure surveyed by the CSS. Three main Control Units corresponding to the CMS_CS_Supervisor_Node (fig. 8.3), the CMS_CS_Hardware_Node (fig. 8.4) and the CMS_CS_Sensor_Node (fig. 8.5) were created.

CMS CS Supervisor Node

STATE	ACTION -> STATE	WHEN condition
OFF	OFF-> ON OFF -> OFF	ALL children ON -> ON ANY CHILDREN STANDBY and ALL CHILDREN not in state ERROR -> STANDBY ANY children ERROR -> ERROR
STANDBY	STANDBY -> ON STANDBY -> OFF	ALL children ON -> ON ALL children OFF -> OFF ANY children ERROR -> ERROR
ON	ON -> OFF ON -> ON	ALL children OFF->OFF ANY CHILDREN STANDBY and ALL CHILDREN not in state ERROR -> STANDBY ANY children ERROR -> ERROR
ERROR	ERROR -> OFF	ALL children ON -> ON ALL children OFF -> OFF ANY CHILDREN STANDBY and ALL CHILDREN not in state ERROR -> STANDBY

Figure 8.3: FSM Control Unit CMS_CS_Supervisor_Node

The control unit CMS_CS_Supervisor_Node has the task to operate the children nodes and to check their status. Fig. 8.3 shows the defined states as well as the possible actions for each state. The "WHEN condition" is also defined with the transitions for the different states. The main purpose is to have all children OFF when everything is on state OFF and ON when all children's are ON. The ERROR state indicates error on any children. For safety reasons if any children are in ERROR the system will change to ERROR the possible action is to turn OFF the system. The STANDBY state is possible only for the Beckhoff controller or for the ELMB when any of them are on and all the relays (Do) off.

CMS CS

Hardware node

STATE	ACTION -> STATE	WHEN condition
OFF	OFF-> ON OFF -> OFF OFF -> RESET	ANY Beckhoffnode in state ERROR or ANY ElmbNode ERROR -> ERROR ALL Beckhoffnode ON and ANY Do ON or ALL ElmbNode ON -> ON ALL Beckhoffnode ON and ALL Do OFF and ANY Beckhoffnode STANDBY and ANY ElmbNode STANDBY and ANY CHILDREN not_in_state ERROR -> STANDBY
STANDBY	STANBY -> ON STANBY -> OFF STANBY -> RESET	ALL Beckhoffnode OFF and ALL Do OFF or ALL ElmbNode OFF -> OFF ALL Beckhoffnode ON and ANY Do ON or ALL ElmbNode ON -> ON ANY Beckhoffnode ERROR or ANY ElmbNode ERROR -> ERROR
ON	ON -> OFF ON -> ON ON -> RESET	ANY Beckhoffnode ERROR or ANY ElmbNode ERROR -> ERROR ALL Beckhoffnode OFF and ALL Do OFF or ALL ElmbNode OFF -> OFF ALL Beckhoffnode ON and ALL Do OFF and ANY Beckhoffnode STANDBY and ANY FwElmbNode STANDBY and ANY CHILDREN not in state ERROR ->STANDBY
ERROR	ERROR-> OFF ERROR-> RESET	ALL Beckhoffnode ON and ANY Do ON or ALL ElmbNode ON -> ON ALL Beckhoffnode OFF and ALL Do OFF or ALL ElmbNode OFF -> OFF

Figure 8.4: FSM Control Unit CMS_CS_Hardware_Node

The function of the Control Unit CMS_CS_Hardware_Node is to control the hardware units, the Beckhoff modules (Beckhoffnode) status and relays (Do) states as well the ELMB's (ElmbNode) status. There are four possible states OFF, RESET, ON, ERROR and STANDBY. In addition a RESET action allows resetting the hardware in order to recover the hardware from an error state or to (re) initialize the system. The STANDBY state indicates that the hardware is in a pre-operational state and could be turned ON or OFF.

CMS CS

Sensors Node

STATE	ACTIONS->STATE	WHEN condition
ON		ANY children ON -> ON
OFF		ALL children ON -> ON

Figure 8.5: FSM Control Unit CMS_CS_Sensor_Node

The control unit CMS_CS_Sensor_Node is used to display the state of the sensors depending on the bias of the sensors provided by the relays or if the Beckhoff modules or the ELMB loose the communication.

8.4 Logical view and hardware view

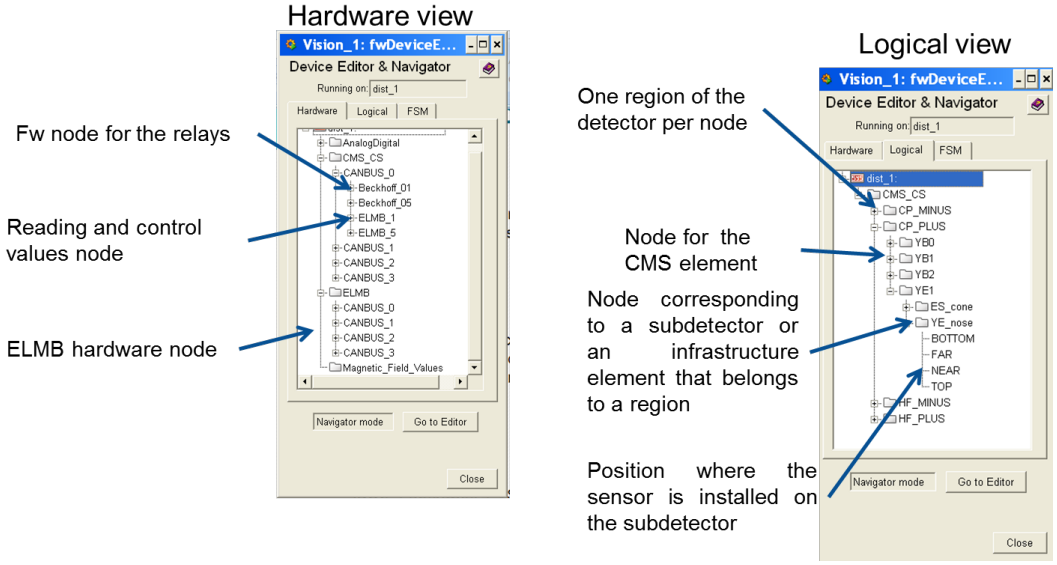

Figure 8.6: The panel on the left shows the “Hardware view”, and the panel on the right shows the “Logical view”.

One of the main tasks when building the CSS software pack was to organize the information from the more of 200 CSS sensors. This was done by creating a “data point” for each type of sensor (the “Hardware View”) and a conversion of the read value into an object that can easily be identified by the user (the “Logical View”). This structure of “data points” includes the constants from the calibration of the sensors that allows calculating from the sensor response distances (in units of mm) automatically. This conversion allows an easy checking of the performance of the hardware.

The Hardware View is where the hardware tree of the “data points” of the system are structured and displayed. They follow the number of the channel or the number of

the relay as well as the CANBUS nodes number. The Logical View is the tree of the data points organized in a way closer to the user. The hardware names are replaced by the names of the detectors or infrastructure objects, where the sensors are installed. Panels for both views are shown in fig. 8.6.

Table 8.1: List of sensors per subdetector or infrastructure element included in the software.

CMS_CS Hardware:			
6 readout crates 2 power crates			
HFR plus:	CR plus:	CR minus:	HFR minus:
1 POT-CASTOR Table vs BP Flange	20 IR-YB0+ (HE2,HE1,ES,EE,SR) +1 TS	20 IR-YB0- (HE2,HE1,ES,EE,SR) +1 TS	1 POT-CASTOR Table vs BP Flange
1 POT-CASTOR Cradle vs HF plug	8 US-YB+1 Interior	8 US-YB-1 Interior	5 POT-CASTOR vs BP support
2 POT-External HF vs HF plug	8 US-YB+2 Interior +1 TS	8 US-YB-2 Interior +1 TS	2 POT-Colar vs CASTOR rails
2 POT-Colar vs CASTOR rails	4 US-YE+1 ES-cone +1 TS	4 US-YE-1 ES-cone +1 TS	4 POT-HF vs BP
4 POT-HF vs BP	4 IR-YE+1 YE-nose	4 IR-YE-1 YE-nose	16 IR-T2 vs BP
16 IR-T2 vs BP			10 IR-CASTOR vs BP
6 POT-T1 vs YE+/-1, YE+/-2 and YE+/-3			6 IR-CASTOR vs RS
12 US-T1 vs BP			6 POT-T1 vs YE+/-1, YE+/-2 and YE+/-3
			12 US-T1 vs BP

Table 8.1 shows the list of sensors per type and infrastructure element, and the quantity. Adding the different types of sensors, to the different elements, we have the list of elements of the CMS detector per surveyed region. The software description follows the same structure: first the 4 regions are described and then the different elements surveyed. The first item listed in the table refers to a test sensor installed in the corresponding area. This is also present on the Logical view and in the FSM structure. The number of the power crates and readout crates are also available in Table 8.1.

8.5 Graphical user interface

The Main panel of the CSS Graphical User Interface (GUI) monitors the functioning of the system. It is shown in fig. 8.7. The system allows two levels of users, the “expert” and

the "user" levels. The expert level has the possibility to take actions on the hardware and define the reference for the measurements. The user level allows navigation through the different levels of the system that give access to the results of the measurements.

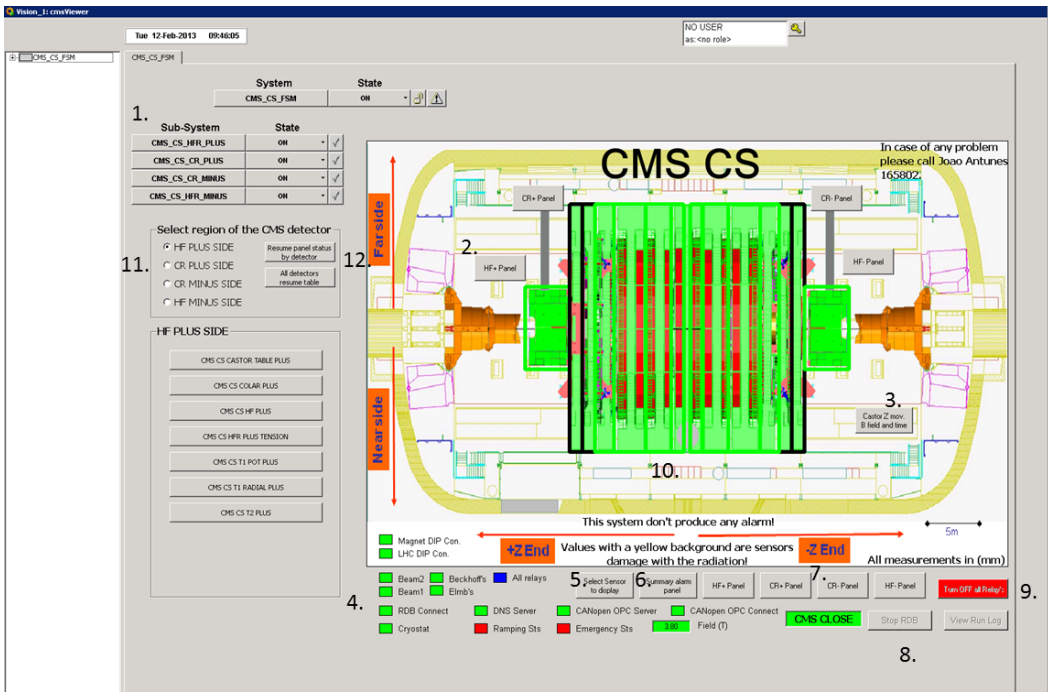

Figure 8.7: The CSS main panel on PVSS integrated in DCS.

The background selected for the Main panel represents the CMS cavern with all its elements. In green the main 11 structures YB0, YB+/-1, YB+/-2, and YE+/-1 are displayed together with the forward/backward (HF) instrumentation. This representation is used by Technical Coordination to schedule the maintenance/upgrade tasks. It is therefore a very common representation to the people directly involved in the manipulation of the CMS infrastructure. The panel also has complementary information that could be relevant to the measurements (e.g. the magnetic field status, etc.). By double click on the elements YB0, YB+/-1, YB+/-2, and YE+/-1 a tab will open displaying the location of the sensors installed in a given element as well as the plots for each group of sensors with the most important information (reference values, difference between measurements and reference (deltas), the value of the magnetic field, etc.). There are two plots per panel and group, showing the actual measurement versus time and versus the magnetic field value. They are useful to monitor any (expected or unexpected) discontinuity in the movement being monitored. The different groups of buttons and actions shown in fig. 8.7 are as follows:

1. Buttons of the FSM structure that, with the name of the CMS region, allows navigating through the different instrumented regions of the detector and control the system.

2. Compact summary panels for each region. They inform on the measurements, references, and magnetic field value for all the sensors in a given region. They include the possibility to (re) set the references when needed.

3. Due to its criticality, there is a special panel that summarize the measurements of the most important sensors placed on the CASTOR detector. This panel gives the possibility to follow the movements in the whole Forward region of the detector that becomes critical when the magnet is energized.

4. A series of buttons provide extra information of the CSS system, the CMS detector and on LHC conditions. As for the CSS, they give information about the status of the database, the status of the relays that bias the sensors, the ELMB and Beckhoff status, and the communications.

5. This button allows to select and display (trends) the desired sensor per sub-detector.

6. Panel showing the list of sensors with "warning" status.

7. There are four buttons one for each region providing the resume on the safety states, indicating if a given measurement is inside the allowed values. They also allow navigating through the different elements and sensors. The corresponding panel could display full information to the expert, including status of the hardware.

8. Buttons to control the data base functions. They are only accessible at expert level.

9. A single button that allows turning off all relays. It is only accessible at the expert level.

10. The different elements located at the central region (the 7 main CMS structures) are accessible by double clicking the corresponding structure.

11. Button that allows the selection of a region without the need to navigate through the FSM tree. It updates the list of buttons above to access the different sub-detectors.

12. These two buttons give access to the status and management of the sensors on each sub-detector (see fig. 8.12 and fig. 8.13)

Navigating through the system one can find a graphical representation of the different instrumented elements of CMS. An example of these graphical panels is shown in figs. 8.8 and 8.9. Graphical panels allows having a visual memory of the position of the sensors installed, and a simple and quick understanding of the measurements provided by the system. Complementing this type of panels, and as shown in fig. 8.9, trends with the result of the measurements are also available.

In the following paragraphs a detailed description of fig. 8.8 and fig. 8.9 is given. The left panel in fig. 8.8 displays the status of the sensors at a given moment in time. The other

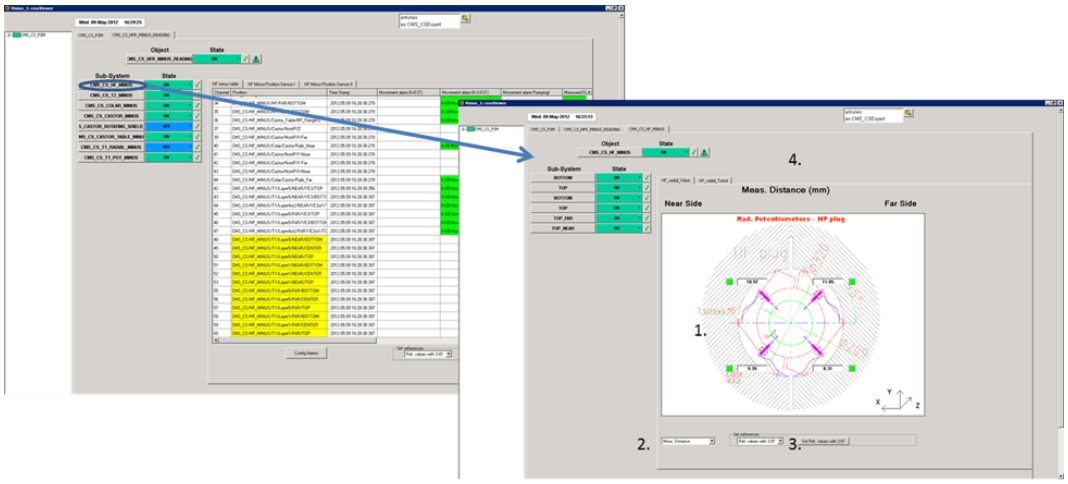

Figure 8.8: (left) Panel displays (HF minus) per sensor the measurement, parameters and alarms as identified by the system. (right) The panel shows the instrumentation on the HF sub-detector.

tabs available on the panel give a picture of the region, with the location of the sensors and the information of the sensors status. Different colours are used to indicate the status of the measurement with respect to the allowed limits: “green” indicates that the actual measurement is within the allowed limits; “yellow” when the measurement is close to the safety limits; and “red” when the measurement is outside the defined safety limits; and finally “blue” when the sensor is out of range or the bias is off. The right panel in the same figure shows an engineering drawing of the inner part of HF calorimeter instrumented. Several functions available on the panel and indicated in the figure which are:

1. The actual readings from the sensors. Note that the values are displayed as close as possible to the actual location of the sensor in the detector. The sensor is indicated with a small coloured box following the convention explained above.

2. A function to allow the selection of absolute or relative measurements (in mm) from each sensor.

3. Two expert buttons allow to set new references to all sensors related with the status of the magnetic field (ON or OFF).

4. The tab allows accessing the trends over time or over B field. Other information on the sensors is also available.

Following from the right panel in fig. 8.8 and selecting the next tab of the panel the trends of the measurements are displayed (as shown in Fig 8.9). Trends can be displayed versus time or versus the magnetic field value, thus allowing a fast online analysis of the detector movements. In case of an expected behaviour there is an option to combine more information to obtain a more complete interpretation of the origin of the measurement.

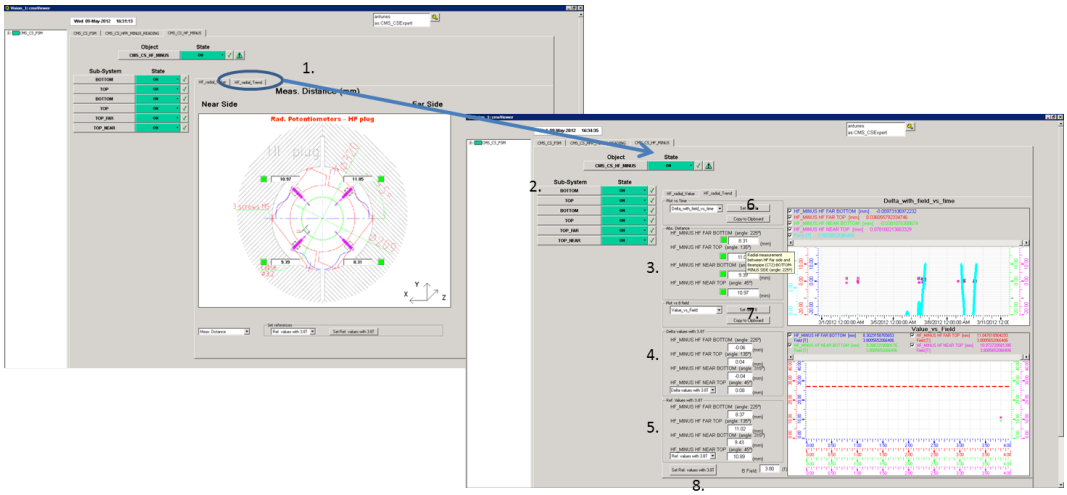

Figure 8.9: The left panel shows where the sensors are located, while the right panel displays specific trends.

On the display of the trends two dashed lines (yellow and red) across the graph are visible on the screen. The yellow lines define the range of safety measurements. Measurements falling within the red lines are considered risky. The numbers in fig. 8.9 correspond to the following functions:

1. Selects the display with trends and measurements.
2. The different buttons give access to all the information of the sensor (fig. 8.10).
3. Gives the actual absolute value measured by the sensors (in millimetres).
4. Gives the difference in millimetres, between the actual measured values and the reference (for the closing position, and for two values of the magnetic field, 0 T or at 3.8 T.
5. The reference values for the closed position: the nominal value, and the measured values at 0 T, at 3.8 T.
6. Selects displaying the measurements versus time. It allows to define the correct settings on the graphics.
7. Same as 6 but displaying the measurements versus the magnetic field value.
8. A series of expert buttons to set new references for the sensors that are selected on the panel.

Figure 8.10 shows the displays of the sensor parameters, measurement, references and alarms status. Different types of trends are also available to visualize the behaviour versus time and with the magnetic field. The information if the sensor is biased is presented in

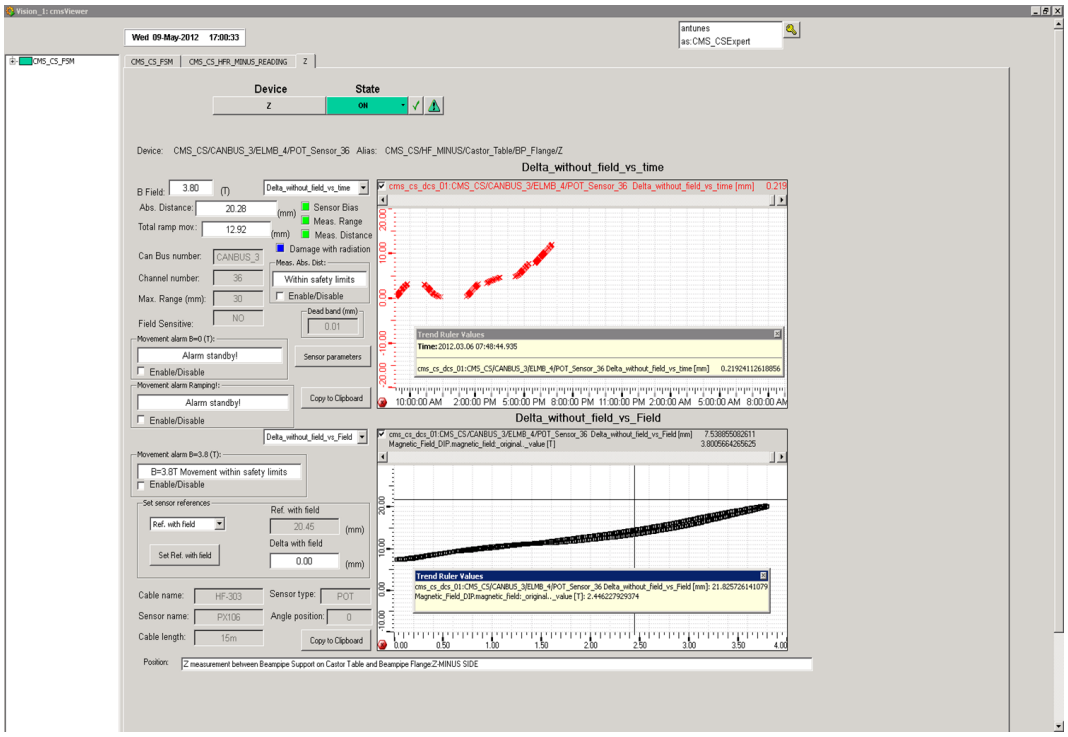

Figure 8.10: Panel on PVSS of the CSS for a single sensor that show all the information.

green colour.

Fig. 8.11 corresponds to the panel displaying the "sensor parameters". This panel allows to visualize the different parameters of the sensor, at the user level and to update the values on the sensor at the expert level.

CSS sensors are distributed over the whole CMS detector. Navigating through the FSM hierarchy allows to reach the panels in order to visualize and control (expert access) the different regions. The control actions with the expert access are: turning ON, OFF or reset a given element of the system, which includes electronic modules, sensor relays, etc. The FSM structure already provides most of the control and management of the hardware system. Nevertheless, in the last version of the CSS a new data point structure was included that gathers all the information per sub-detector unit. This allows to do a fast management of the all data in a given sub-detector. The panel shown in fig. 8.12, working at the expert level, allows setting different states and parameters of the sensors installed in the CASTOR sub-detector. We can now know which sensors -of each type- are installed on the detector and set the sensors damage by radiation if any. All the information of the detector is accessible by scrolling the list of sub-detectors available and selecting them. This organization provides a full map (see fig. 8.13) of the different status and parameters of all the detectors recorded in a database. It helps following the installation or removal of a given sub-detector during the LHC runs, and to keep a better

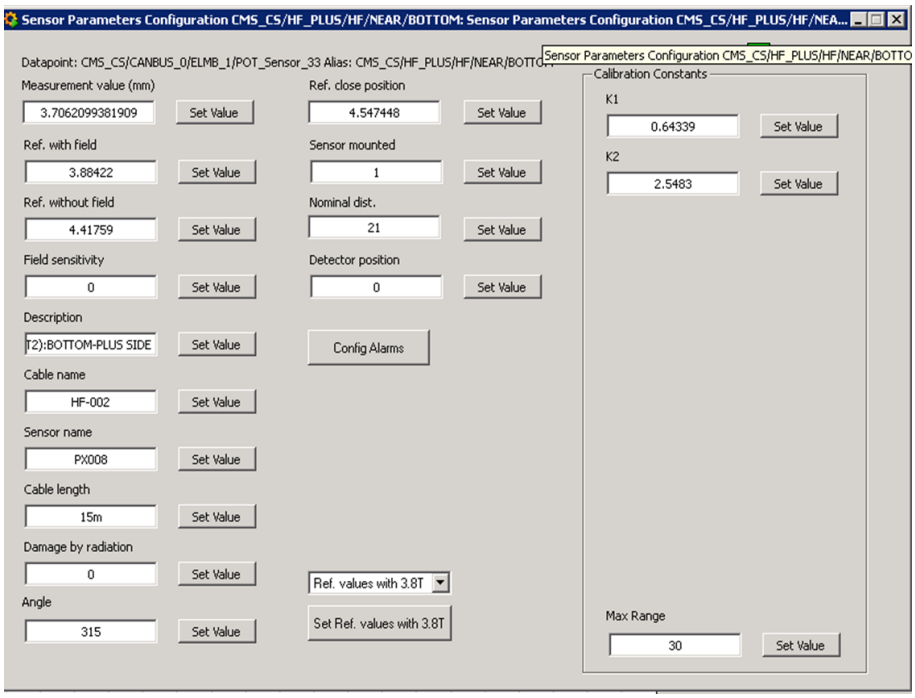

Figure 8.11: PVSS panel to display and update the sensor parameters.

history log of the operations done over the LHC maintenance period.

8.6 Warnings and alarms

Warnings and alarms are created to inform if the measurements recorded by the system are within the allowed and safe limits as determined for each part of the detector. Although the different regions of CMS could accept different safety criteria, a general rule has been following up to now. A warning is defined if the measurement indicates that the relative distance between objects is between 5 and 10 mm. An alarm is considered if the distance measured is below 5 mm.
Simple alarms are also defined if the measurements following a given movement vary suddenly by more that a given value, thus indicating a possible misbehaviour of the sensor or of the detector element. The choice on the settings depend on the type of sensor, based on the reliability of the different sensor technologies working under specific operational conditions. For instance, since ultrasound and infrared sensors become more unstable in the presence of magnetic fields a safety margin of 5 mm was defined, while 2.5 mm was chosen for the potentiometers since they are more robust against external conditions.

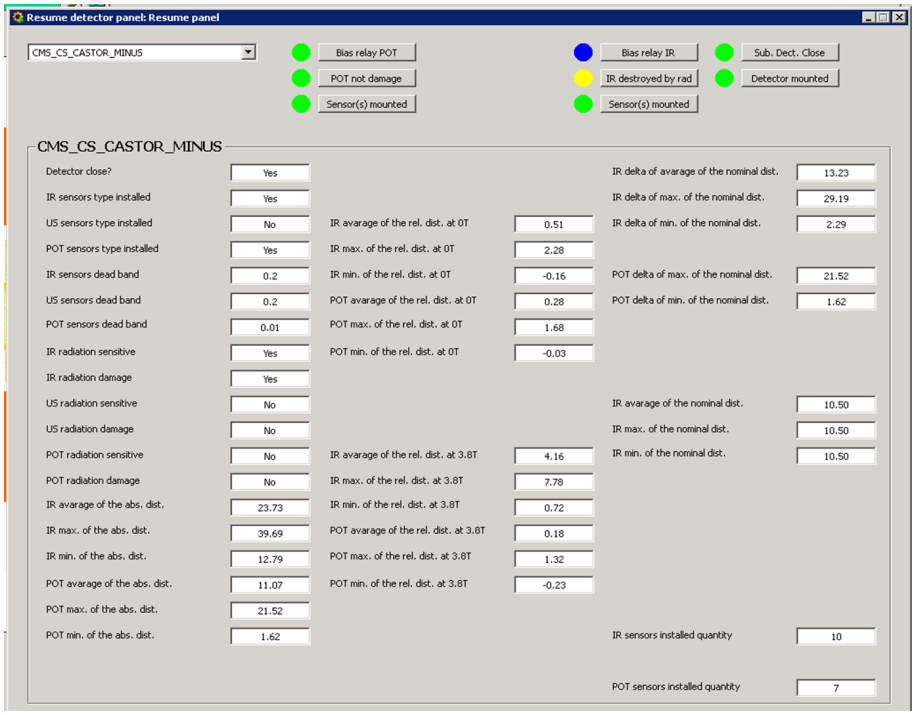

Figure 8.12: Panel with sensors status resume and management organized by sub-detector

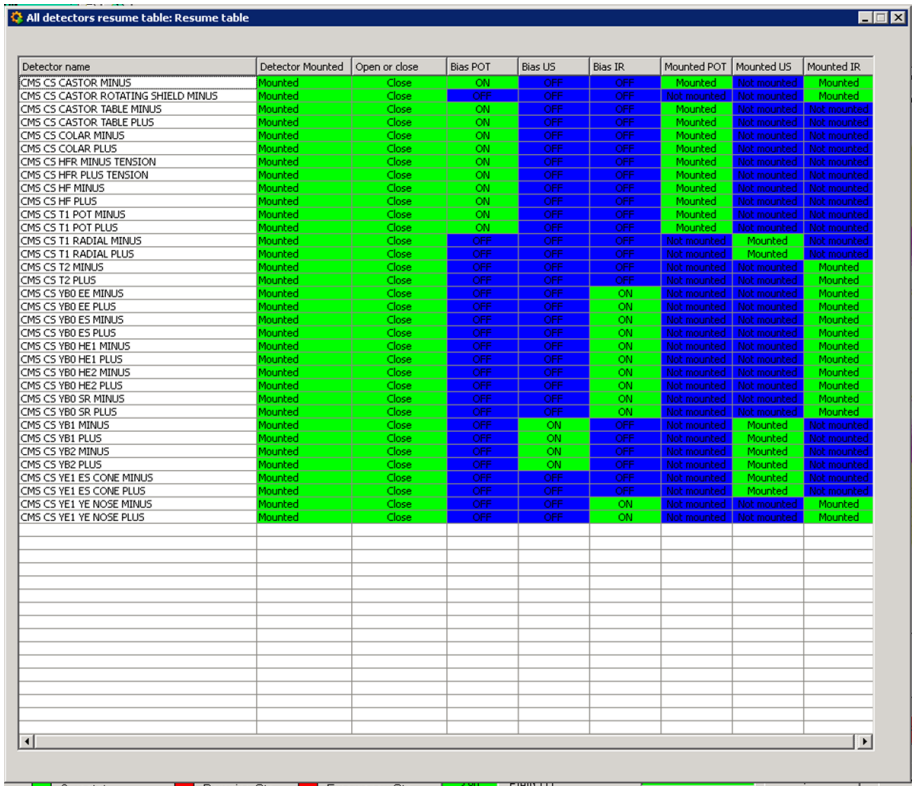

Figure 8.13: Sub detectors status panel

8.7 Summary

The performance of the CSS software has been improved over the years with the inclusion of new features following the experience acquired from the operation of the system during the different phases of the experiment. The software pack began with simple functions, in order to assist the first closings of the detector, and it is now fully integrated system in the CMS DCS, working in a continuous and autonomous mode.
The data provided by the system is published (via DIP) on the CMS technical network and it is being used by sub-detectors in their own detector control systems, as for instance in the case of the TOTEM experiment. It runs online and the collected data is stored in a database accessible to all users in the experiment. The data is also accessible on the webpage of the experiment to do simple analysis (trends) or to allow downloading the stored data. All the sensors data points have an intuitive alias that helps to access the information in any available application. The last version of the software includes a script that warns via SMS the status of the CSS, the magnet field status and DIP communications status.
It is worth to stress that this software has been developed to be able to work in an autonomous mode integrated into DCS but also as a standalone system during the LHC maintenance periods. Some of the described features, as for example the alarms, are not yet fully functional since the criteria are still not uniform.

9

Opening and Closing of the CMS Structures

Chapters 9 and 10 report on the analysis of the data collected by the Closing Sensor System. The data, collected during a long period of time, are grouped into three categories: measurements related with the closing and opening of the detector structures, measurements monitoring the powering cycles of the magnet, and finally the data collected during the ordinary operation of the detector.
The two first sets of measurements are critical for the integrity of the detector. Care must be taken by the online monitoring to ensure that the needed safety clearances between elements and structures of the detector are respected and stay within the safety limits defined in the CSS data acquisition and control system. The final detector parameters after each closing are obtained allowing to study of reproducibility achieved in the assembly process.
The set of data collected during the normal operation of the detector informs on the mechanical stability of the whole detector. Any unknown instability could influence the quality of the data obtained by CMS and therefore its subsequent scientific production.

9.1 Operations with the movable barrel wheels

As described in Chap. 2, CMS is made of 11 main structures that slide along the beam pipe during the opening or closing of the detector. The central structure, the barrel central wheel housing the Vac tank, called YB0 (YB stands for Yoke of the Barrel), is fixed to the geometrical centre of the cavern and is the only non-movable structure. YB0 is the heaviest

structure; it weighs about 3,000 tonnes. The other wheels, that forms the CMS barrel are all movable structures and are symmetrically placed at the positive and negative sides of YB0, their names are YB+/-1, and YB+/-2. The weight of each movable wheel is around 1,000 tonnes (see fig. 9.1). When closing CMS, the movable wheels are the first structure to move. They slide along the Z-axis, are inserted around the Vac tank of the CMS magnet until they reach their final position adjacent to YB0. This operation is considered non critical and because of time constraints the wheels were only instrumented with CSS sensors during 2009; therefore in what follows, data will be presented from that year onwards. The barrel instrumentation described in Chapter 6, consists of 8 ultrasound detectors per structure as shown in fig. 6.6.

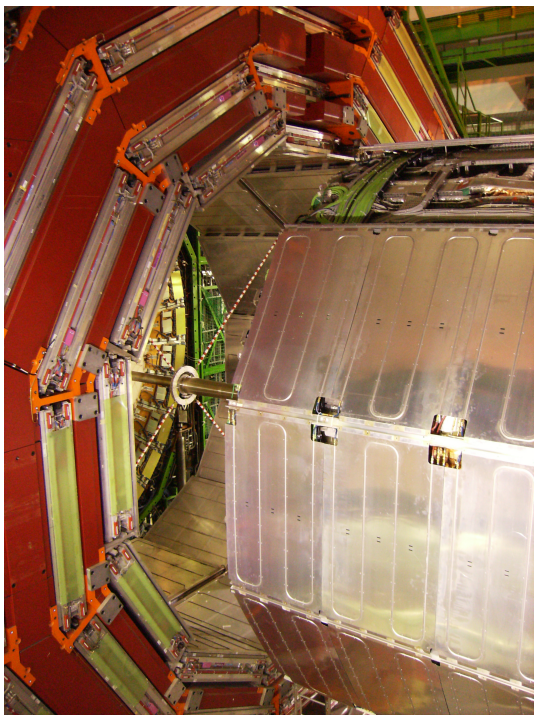

Figure 9.1: Photograph of a movable wheel on the left (with the support for the beam pipe installed), on the right the cover of the Vac tank is displayed.

Figure 9.2 shows the reading of all the sensors located on YB+1. The distance between the inner boundary of the wheel and the outer part of the Vac tank, as measured by the sensors, is displayed versus time, for the sensors in IP side of the wheels (top right) and the NonIP side (top left). CSS measurements are done in a continuous way, and as the horizontal axis of the figures shows, the time needed to close the structure can take up to 2 hours. This is the time spent by the operators to slide the wheel about 5 m once it is inserted around the Vac tank. Note that it is only when the wheel reaches the Vac tank that the CSS start to work. The last part of the measurements shown in the figures present a rather constant reading of the sensors indicating that the wheel has reached its final position.

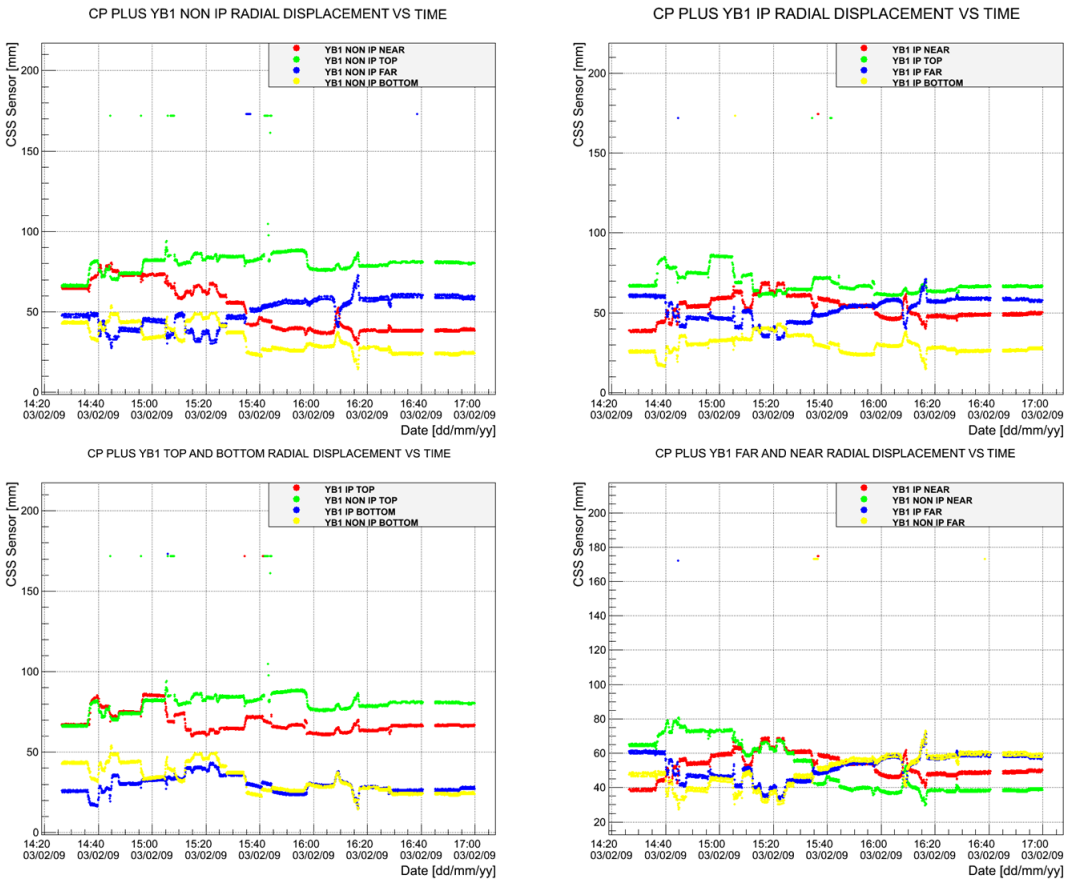

Figure 9.2: Distance between the inner circle of YB+1 and the outer boundary of the Vac tank versus time, during the closing of the YB+1 wheel. Top left: for the sensors placed in the NonIP side of the wheel; top-right: for the IP side sensors. The bottom plots show the same measurements combined as indicated in the graphic (see text).

The top plots show that during the process the distance between the two objects has always been above 20 mm, except in two cases: at about 14h35 (for the IP side bottom sensor) and at 16h15 (for both sides, IP and NonIP, bottom sensors) when the measurement gets closer to 10 mm. For these sensors the tolerance was set to 50 mm (this was the initial nominal distance defined, without taking into account the thermal screen located around the magnet coil). Towards the end of the motion IP and NonIP sensors suffer a correlated jump in the reading associated to the transition from the air-pads system used during the motion to a fixed support, once the wheel is in its final position. In both plots, we can see some data out of range indicating that the sensor is giving faulty readings due to undesired angle sensor/target or wheel vibration. In the bottom plots the sensor readings are grouped as follows: on the left, top and bottom sensors from both sides of YB+1 are shown; on the right plots, the two pairs of near and far sensors are displayed. The correlation among them indicates the changes in the wheel orientation during its motion. The information is mainly used in a qualitative way

since the inhomogeneities inherent on the sensor target structure prevent us to obtain an accurate quantitative interpretation. One can note as well that when the operation started both top sensors were measuring similar distances but the bottom sensors were given different readings of about 20 mm difference between them. Along the process the position reverses indicating a rotation of the wheel around the global CMS X-axis and a possible alignment on both sides of the barrel. Furthermore, the difference between both top and bottom sensors readings are considerably large, more than 20 mm, indicating that the two cylinders -inner boundary of the wheel and outside of the Vac tank boundaries- are not exactly concentric. Similar correlations are observed between the behaviour of the far and near sensors as displayed in the bottom right plots. Table 9.1 shows the clearance reached in the final position of YB+1 at this closing. All clearances are above 20 mm. Very similar values were obtained for the far and bottom measurements in the IP and NonIP side, showing the wheel is well centred. The top and near sensors show a significant difference on their values on both sides. In this case, this is interpreted as being due to a possible deformation on the thermal screen used as target (i.e. the presence of a cooling pipe).

Table 9.1: Clearances of the final position of YB+1 when closed.

Sensor position at: 2009.02.03 16:59:44	Dist. (mm)
YB1 IP NEAR	50.2
YB1 IP TOP	65.9
YB1 IP FAR	57.8
YB1 IP BOTTOM	28.3
YB1 NON IP NEAR	39.4
YB1 NON IP TOP	80.3
YB1 NON IP FAR	57.6
YB1 NON IP BOTTOM	24.7

Similar measurements are available for the closing of the most external barrel wheel, YB+2. Fig. 9.3 shows the reading of the sensors during the process of closing the wheel. The representation and ordering of the sensors is the same as in fig. 9.2. For the correct description of the figures, note that ultrasound sensors can only give meaningful reading when a given wheel enters into the external surface of the Vac tank.
The top plots in the figure show the distance between the inner boundary of YB+2 and the outer boundary of the Vac tank versus time. For this set of data, data taking started before the wheel overlapped the Vac tank and therefore the reading of the sensors were out of range. This is represented in the figures by straight lines with a fix and arbitrary value. After about 30 minutes, the readings fall within the sensor dynamic range. The NonIP near side sensor did not record data due to a faulty connection. The clearance for all the other sensors and during the whole operation was above 20 mm in all monitored

positions. Note that as in the case of YB+1 (fig. 9.2) the IP side sensors starts the reading before the NonIP ones. The difference in time corresponds to the travel time of the wheel on top of the Vac tank. Finally, the bottom plots show clear correlation among the symmetrically placed sensors. This is more evident in the bottom right plot, where we observe two distinguished patterns, one for the top sensors and a different one for the bottom sensors placed on the two sides of the wheel. The amplitude of the readings is in general very small along the whole closing process.
Table 9.2 shows the clearance obtained at the final position of the YB+2 wheel during this closing. All clearances are well above 20 mm. While the pair of top, and far sensors give similar values once the operation of positioning the wheel is concluded, the bottom and near sensors show a significant difference in the values between both sides, as before this is interpreted as possible deformations on the thermal screen used a sensor target.

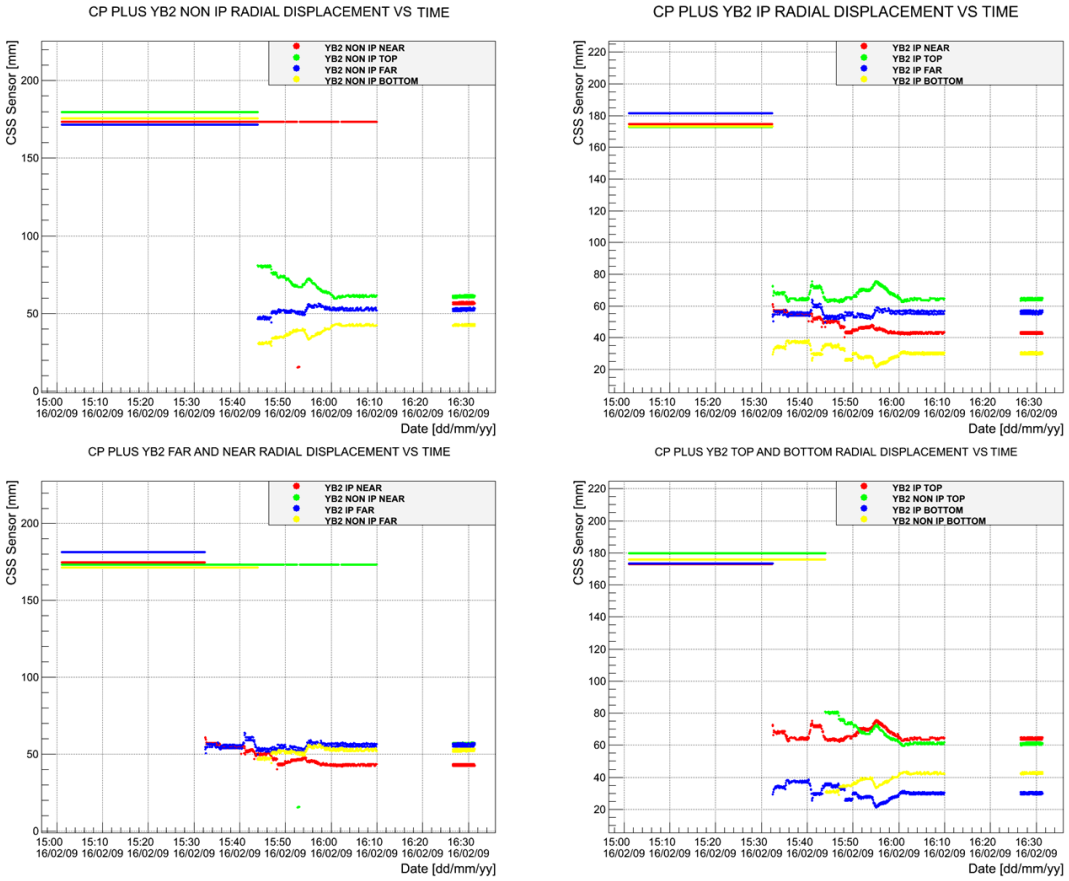

Figure 9.3: Distance between the inner circle of YB+2 and the outer boundary of the Vac tank versus time, during the closing of the YB+2 wheel. Top left: for the sensors placed in the NonIP side of the wheel; top-right: for the IP side sensors. The bottom plots show the same measurements combined in the way indicated in the graphic (see text).

In 2009, right after the closing of the negative barrel wheels, the closing of the positive ones took place. The positive wheels were instrumented in an identical way and the

Table 9.2: Clearances of the final position of YB+2 when closed.

Sensor position at: 2009.02.16 16:31:16	Dist. (mm)
YB2 IP NEAR	42.2
YB2 IP TOP	64.7
YB2 IP FAR	56.8
YB2 IP BOTTOM	30.4
YB2 NON IP NEAR	56.1
YB2 NON IP TOP	61.3
YB2 NON IP FAR	52.9
YB2 NON IP BOTTOM	42.4

CSS was fully operational to monitor the process. The data recorded by the system is displayed in figs. 9.4 and 9.5. The data shows an even smoother behaviour during the closing operations than in the previous case. Correlation in the patterns drawn by the related sensors is also visible. The final values, obtained when the wheels were at their final positions are reported in Tables 9.3 and 9.4.

Table 9.3: Clearances of the final position of YB-1 when closed.

Sensor position at: 2009.02.18 16:07:30	Dist. (mm)
YB1 IP NEAR	51
YB1 IP TOP	77.2
YB1 IP FAR	47.9
YB1 IP BOTTOM	30.1
YB1 NON IP NEAR	48.4
YB1 NON IP TOP	67.3
YB1 NON IP FAR	45.4
YB1 NON IP BOTTOM	32.8

Note that every operation (closing of a given wheel) is a unique event and although the trends are similar, one cannot expect to reproduce the exact values. Given the complexity of the structures and the limited accuracy of the target used by CSS in this region, the results obtained are considered to be in reasonable agreement and within expectations. The active monitoring provided by the system allows supervising and correcting, the positioning of the wheels when needed during their motion.

Due to a technical problem, two months later the YB+2 wheel was disassembled and closed again. The repetition of the process, within a short period of time, allows to study the level of reproducibility obtained in short term intervals. The final position obtained in this second closing is listed in Table 9.5. The first column in the table corresponds to the final positioning after the first closing, from Table 9.2, and the second column

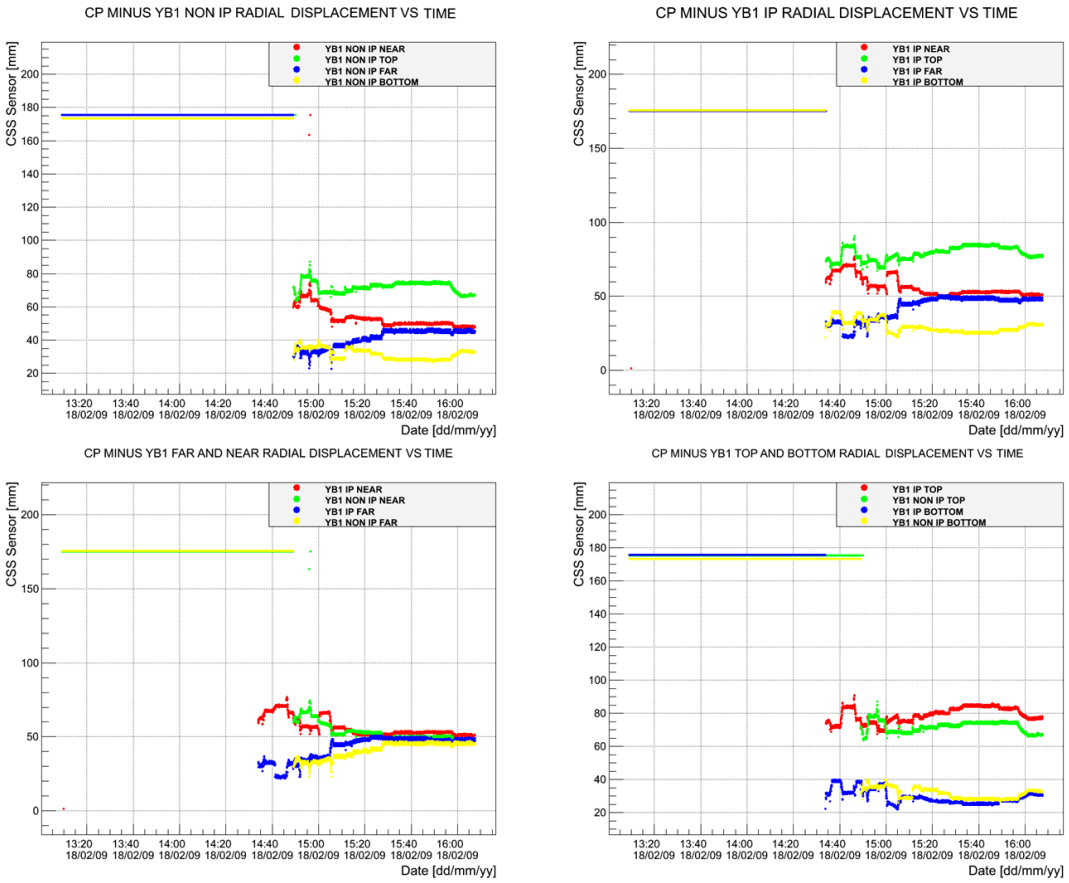

Figure 9.4: Distance between the inner circle of YB-1 and the outer boundary of the Vac tank versus time, during the closing of the YB-1 wheel. Top left: for the sensors placed in the NonIP side of the wheel; top-right: for the IP side sensors. The bottom plots show the same measurements combined as indicated in the graphic (see text).

Table 9.4: Clearances of the final position of YB-2 when closed.

Sensor position at: 2009.03.03 15:37:40	Dist. (mm)
YB2 IP NEAR	52.7
YB2 IP TOP	71.9
YB2 IP FAR	42.2
YB2 IP BOTTOM	27.0
YB2 NON IP NEAR	56.9
YB2 NON IP TOP	70.9
YB2 NON IP FAR	43.2
YB2 NON IP BOTTOM	28.9

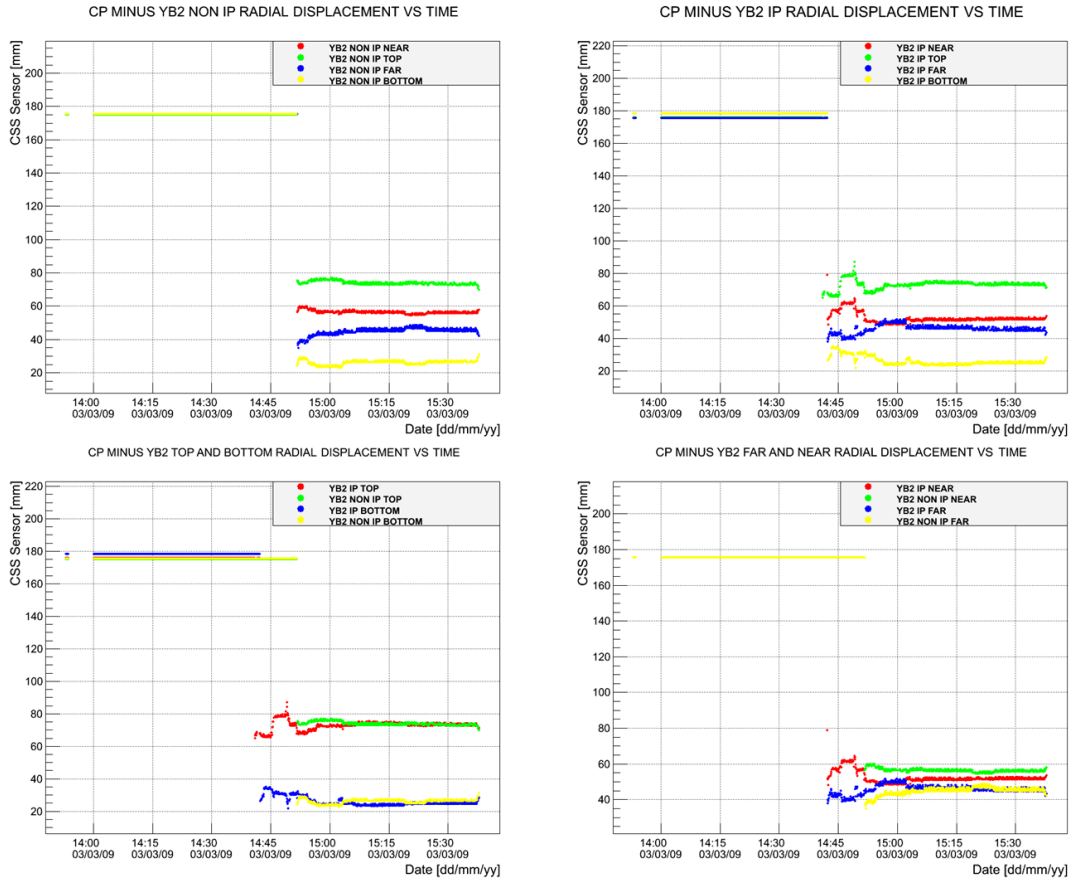

Figure 9.5: Distance between the inner circle of YB-2 and the outer boundary of the Vac tank versus time, during the closing of the YB-2 wheel. Top left: for the sensors placed in the NonIP side of the wheel; top-right: for the IP side sensors. The bottom plots show the same measurements combined as indicated in the graphic (see text).

corresponds to the values obtained after the second closing. The difference between both (third column) indicates the level of reproducibility achieved in this operation. A very good reproducibility, of few mm, can be achieved thanks to the help provided by the monitoring system.

Table 9.5: Clearances of the final position of YB+2 when closed and the variations between closing

Sensor position	Dist. 2009.02.16 16:31:16 (mm)	Dist. 2009.05.04 17:14:46 (mm)	Delta (mm)	Delta between sides (IP-Non IP)
YB2 IP NEAR	42.2	45.9	3.7	0.4 (near)
YB2 IP TOP	64.7	65.4	0.7	-1.7 (top)
YB2 IP FAR	56.8	55.6	-1.3	-2.5 (far)
YB2 IP BOTTOM	30.4	32	1.6	-0.6 (bottom)
YB2 NON IP NEAR	56.1	59.4	3.3	
YB2 NON IP TOP	61.3	63.6	2.3	
YB2 NON IP FAR	52.9	54.1	1.2	
YB2 NON IP BOTTOM	42.4	44.7	2.2	

A summary of the results for all movable wheels, during the different operations performed in 2009 is given in Table 9.6. The values are given as the sum of the final clearance recorded by the symmetrically opposite sensors (far + near, and top + bottom). The difference between IP and NonIP sensors is also shown. In this way the eccentricity of the different structures -removable wheels versus Vac tank- once the barrel detector is assembled can be easily visualized.

In an ideal situation, when the elements of the CMS detector are placed at their final positions, they should give a, as much as possible, concentric assembly. Nevertheless, due to imperfections of the mechanics and uncertainties on the target we expect to obtain a certain degree of eccentricity. This is reflected in the table, for instance, by the difference between IP and NonIP (Deltas) displayed in the third row of the second and third columns. Nevertheless this difference is in all cases not exceeding 13 mm, which given the dimensions and weight of the structures is well within the expected tolerances. Another way to evaluate the correct final positioning is by comparing the values obtained by the sensors placed at the NonIP side and the IP side of the wheels. This informs on the orientation of the wheel, with respect to Vac tank, and it is shown in the fourth column where the total sum of distances, as measured by the four sensors, is displayed. Only two movable wheels YB+1 and YB-2 showed a difference of less than 10 mm. The other two movable wheels had higher values.

Table 9.6: Summary table of the closing operations performed with the movable barrel wheels during 2009.

Sensor position at: 2009.02.03 16:59:44	Far + Near (mm)	Top + Bottom (mm)	Sum (mm)
YB1 IP	109.0	94.3	202.3
YB1 NON IP	97.0	105.0	202.0
Delta (IP-Non IP)	11.0	-10.7	0.3
Sensor position at: 2009.02.16 16:31:16	Far + Near (mm)	Top + Bottom (mm)	(mm)
YB2 IP	99.0	95.0	194.0
YB2 NON IP	109.0	103.7	212.7
Delta (IP-Non IP)	-10.0	-8.7	-18.6
Sensor position at: 2009.05.04 17:14:46	Far + Near (mm)	Top + Bottom (mm)	(mm)
YB2 IP	101.5	97.4	198.9
YB2 NON IP	113.6	108.3	221.9
Delta (IP-Non IP)	-12.1	-10.9	-23.0
Sensor position at: 2009.02.18 16:07:30	Far + Near (mm)	Top + Bottom (mm)	(mm)
YB-1 IP	99.0	107.3	206.2
YB-1 NON IP	93.8	100.0	193.9
Delta (IP-Non IP)	5.1	7.3	12.4
Sensor position at: 2009.03.03 15:37:40	Far + Near (mm)	Top + Bottom (mm)	(mm)
YB-2 IP	94.8	98.9	193.7
YB-2 NON IP	100.1	99.8	199.9
Delta (IP-Non IP)	-5.3	-1.0	-6.3

9.2 Closing and opening operations of the first endcap disks

The next step in the assembly of the CMS detector is the closing of the endcap disks and the most critical operation in terms of mechanical tolerances is indeed the closing of the first YE+/-1 disks. Due to its complexity, the whole assembly procedure was tested at different occasions, and the first disks were closed and opened several times and under various conditions during the years 2008 and 2009, before the actual closing of the detector prior to the first LHC data-taking phase. During that period, the monitoring of the process with CSS sensors varied from one try to the next, depending on the availability of the CMS sub-detectors housed by the disks, as well as on the availability of the CSS parts, sensors and readout electronics. The CSS instrumentation of the YE+/-1 disks is described in Sec. 6.1, fig. 6.3 and 6.4 show schematic views of the location of the sensors.
The list of operations monitored by CSS during the years 2008 to 2010 is as follows:

- First test of YE-1 closing performed on April 11^{th} 2008. The process took 2 days and the main purpose was to establish the procedure in a practical manner.
- Closing of YE-1 on May 23^{rd} 2008, using only ES-cone sensors to monitor the most critical safety clearance between the disk and the beam-pipe.
- Closing of YE+1 on August 18^{th} 2008, with most of the CSS instrumentation already in place. Missing parts were the Pre-shower (ES) detector and the associated CSS sensors.
- Adjustment of YE+1 on August 20^{th} 2008. (Short term reproducibility)
- Closing of YE-1 on August 23^{rd} 2008. Under the same conditions as for YE+1.
- Opening of YE+1 on December 1^{st} 2008. This operation belongs to the partial re-opening of the detector after the November 19^{th} LHC incident.
- Closing of YE-1 on June 4^{th} 2009. This is the last assembly prior to the first data-taking period of the LHC. The disk was now fully instrumented with sub-detectors and with the complete CSS.
- Closing of YE+1 on June 8^{th} 2009. Under the same conditions as for YE-1.
- Closing of YE-1 on January 21^{st} 2010. The endcap disks were disassembled during the regular end of the year short maintenance period set for the machine and experiments.
- Closing of YE+1 on January 26^{th} 2010, this was a 3 days process that included a re-adjustment of YE+1 after the endcap closing. YE disk were pushed back and closed again due to a failure of the locking system.

In what follows we describe in detail the results of the closing of the disks when the complete instrumentation of the CSS was available, which corresponds for instance to the operations carried out in June 2009. The rest of the data, whenever relevant, are used for comparisons.
The behaviour of the sensors during the closing of the negative side, YE-1 disk, is discussed first. Due to its shape the YE+/-1 disks are one of the most complicated structures of the detector from a mechanical point of view. During the closing of the structure, the disk should slide along the beam-pipe, and one of the most critical safety clearances to be monitored is the distance between the beam-pipe and the inner part of the ES detector, known as the ES-cone. This is shown in the fig. 6.1. Four ultrasound sensors are placed onto the cone as illustrated in fig. 9.6 a). In its slide along the Z-axis the point of closest approach of YE-1 and the beam-pipe arrives when YE-1 crosses the beam-pipe flange, which is illustrated in fig. 9.6 b).

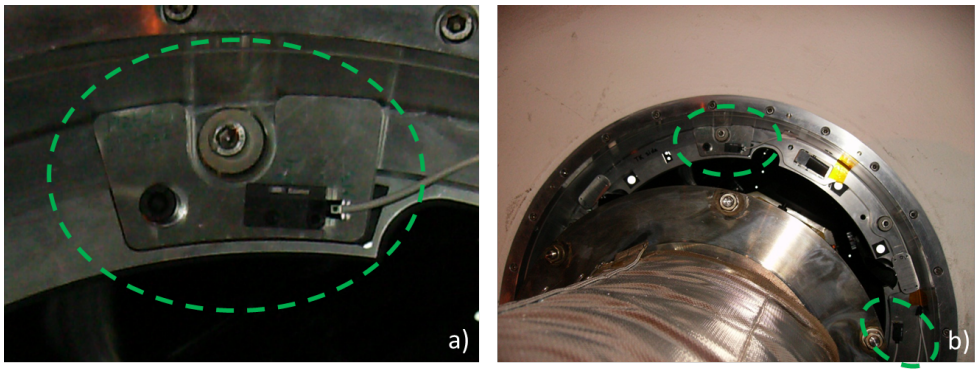

Figure 9.6: a) Picture of the ultrasound sensor installed in the ES-cone mechanics. b). Space between the inner part of the ES-cone structure and the beam-pipe flange.

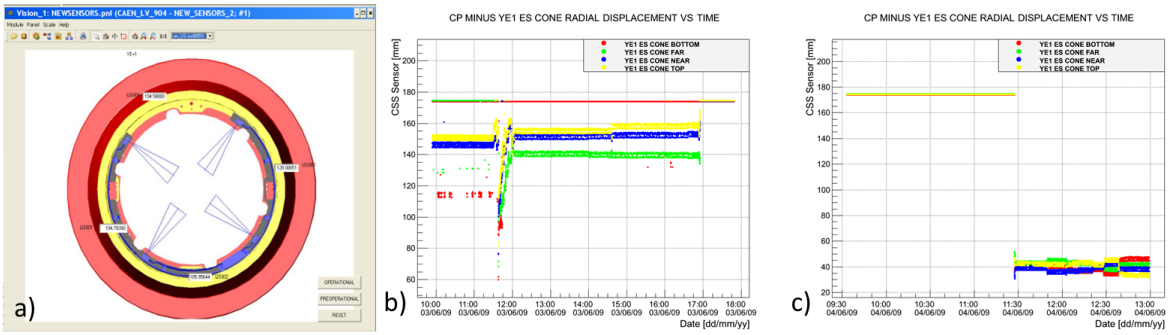

Figure 9.7: a) Graphical display of this group of sensors as implemented in the readout package. b) and c) Distance (in mm) between the inner surface of the ES and the beam-pipe surface as recorded by the ultrasound sensors during the two days of the YE-1 closing.

The location of the sensors and its field of measurement is graphically implemented in the readout software program as shown in fig. 9.7 a). The actual measurements versus time are shown in fig. 9.7 b) and c). Fig. 9.7 b) shows the distance between the inner surface of ES and the beam pipe is always maintained above 50 mm as required in the

specifications. The minimum value measured by the sensors is registered when YE-1 passes the beam-pipe large flange closer to the IP. Data from the ES-cone bottom sensor show that most of the time the sensor was out of range during this run. This could be due to the dynamic range and/or to a possible misorientation of the structure with respect to the beam-pipe. For all other sensors we observe transitions between two values that are due to some vibration of the structure when it is moving on the air pads system. Fig. 9.7 c) shows a step function in the measurements, with the sensors having almost an identical reading, this step occurs when the ES-cone enters the thermal screen of the tracker/pixel detectors. In general, the sensors show a good correlation among them.
Following the sequence of sensors in the YE-1 structure, and going from the inner to the outer part, as displayed in figs. 6.3 to 6.5, the behaviour of the group of sensors ES, EE, and HE1 is shown in fig. 9.8. Fig. 9.8 a) shows the ES group. Around 11h50 am, on the 4^{th} June, the sensors started measuring the distance between the inner parts of the Vac tank to the Preshower detector (ES). All sensors reading reach very close values, indicating a good centring of the nose inside the central tank. At about 12h40 am, when YE-1 is completely inserted, the endcap disk is adjusted (lowered) to its final position and the readings of top and bottom sensors indicate a good correlation between them, while the far and near readings are practically unchanged. Fig. 9.8 b) shows the EE sensor group during the same interval of time. This group of sensors measure the distance between the conical part of the electromagnetic calorimeter (EE) and the surface inside the Vac tank. Their behaviour is very similar to the ES group of sensors. We observe a large difference of almost 40 mm, between the top and bottom sensors corresponding to a possible tilt of the nose. During the whole closing period the minimum clearance, corresponding to the bottom sensor, was about 35 mm. Finally, fig. 9.8 c) shows the HE1 group of sensors. This set measures the distance between the endcap of hadronic calorimeters (HE) placed in YE+/-1 and the Vac tank respectively. The first recorded measurement occurs at about 12h00 am. One can observe that three of the four sensors have very similar values, but the bottom sensor indicates a difference of almost 20 mm. The near and far sensors are measuring similar values towards the end of the process. The top and bottom sensors show (anti)symmetrical excursions, as observed in the previous sets of measurements. The minimum clearance is small, but always above to 20 mm.

The last set of monitored positions corresponds to the ones instrumented with the groups of sensors YE-nose, HE2 and SR (see Sec. 6.1, figs. 6.3 to 6.5). While YE-nose and HE2 groups provide information on the radial distance, between the cylindrical part of the nose and the Vac tank, the SR group measures, in the Z-axis direction, the distance between the end of the coil and the sealing ring located in YE-1. Their measurements are displayed in fig. 9.9. The fig. 9.9 a) shows the HE2 set of measurements. Note that this is the first group measuring the clearance between the nose and Vac tank and the only group with all the sensors inside their dynamic range during the whole period of measurements. The graphic shows that between 11h00 am and 11h30 am the orientation,

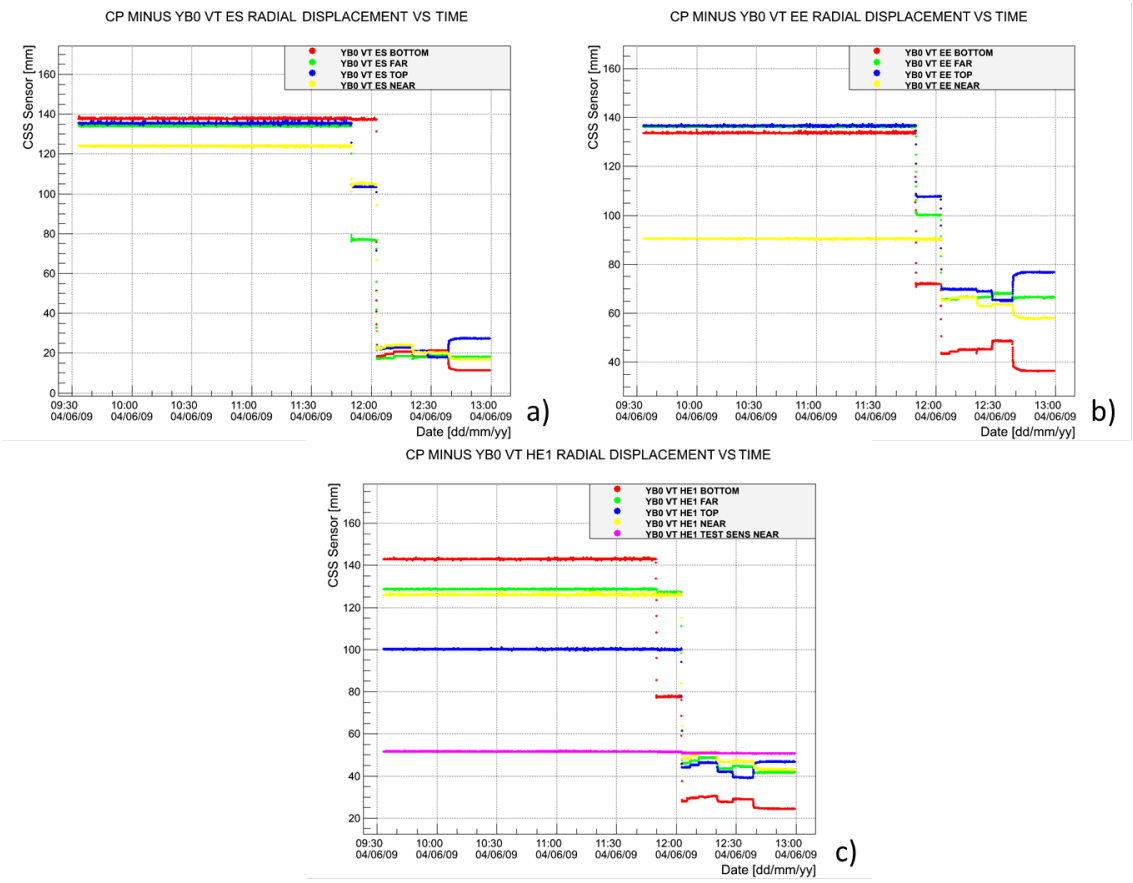

Figure 9.8: Reading of the sensors placed along the 53º crack. a) Distance between the Pre-shower detector and the inner part of the Vac tank. b) Distance between the conical part of the electromagnetic calorimeter (EE) and the surface inside the Vac tank. c) Distance between the conical part of the hadronic calorimeter (HE) and the surface inside the Vac tank.

of the structure, was corrected resulting in a change on the readings of the top and bottom sensors. The readings for the far and near sensors were not significantly affected. At about 12h00 am we observe a big jump on the measurement of the bottom sensor, which is due to a transition between the standard tape target and an aluminium cover. The jump is caused by the high reflection index of the cover. The final position achieved is given by the last part of the graph, at about 12h45 pm the YE-1 disk was lowered from the moving air path system and a last adjustment of the position was performed; we observe a clearly different reading, for top and bottom sensors, informing the centring of the structure in the vertical direction. The fig. 9.9 b) shows the reading of the YE-nose group of sensors. The overall behaviour is similar to the previously discussed HE2 group. The response of the SR group is displayed in fig. 9.9 c). Note that with these sensors we are monitoring the movement along the Z-axis of YE-1. The pattern of movements during the closing is similar for all the group. The differences observed between sensors is understood as due to the support mechanics and the placement of the target and as well as the Seal Ring.

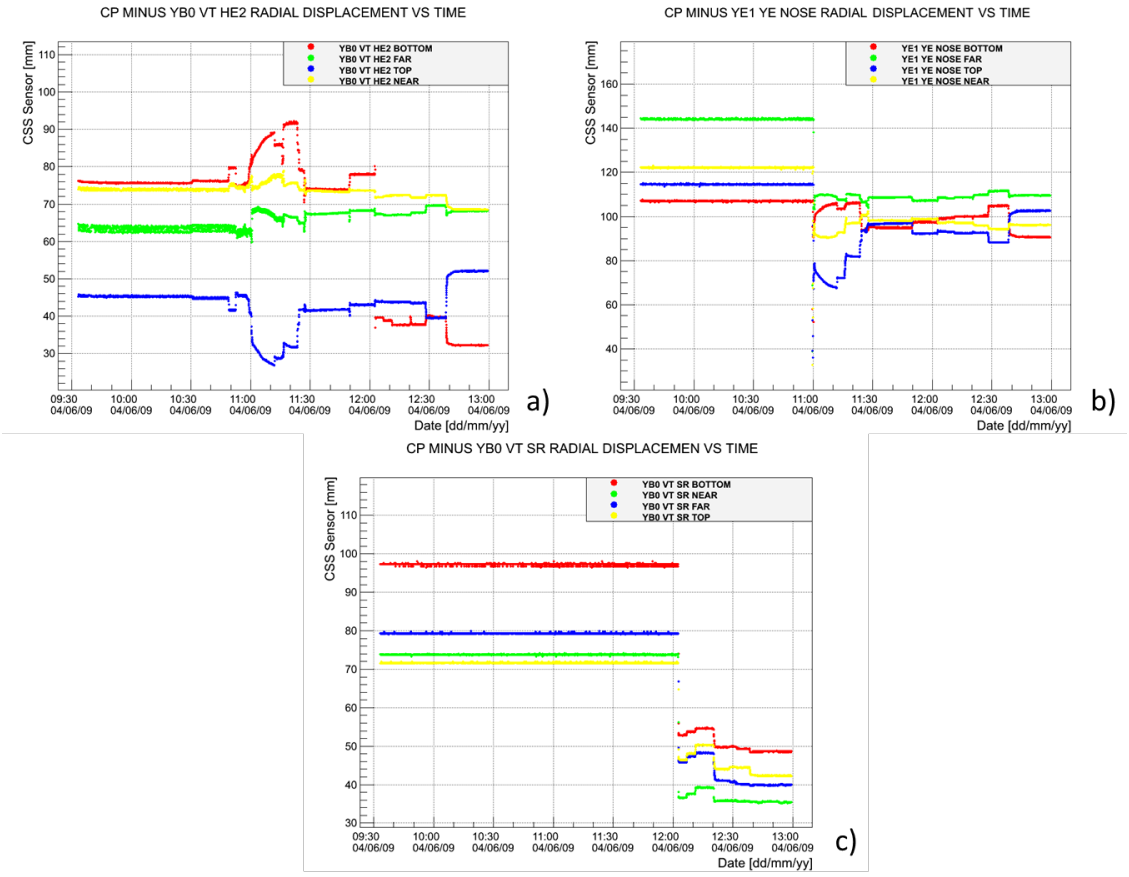

Figure 9.9: Reading of the sensors placed on the cylindrical part of the YE-1 nose. a) and b) Distance between the cylindrical part (two ends) of the YE-1 nose and the inner part of the Vac tank as measured by the YE-nose and HE2 set of sensors. c) Distance in the Z direction between the end of the coil and the sealing ring placed on YE-1.

Three groups of sensors, the ES-cone, the YE-nose, and the HE2 perform a pure radial measurement between detector elements. We can make a direct comparison of their readings, grouping the sensors in base on their position in the detector (top, bottom, near or far). Fig. 9.10 shows the absolute readings of the sensors, grouped by sensor position. We should expect to find a clear correlation on their behaviour as it is in this case. Fig. 9.10 c) shows the already discussed target problem for the HE2 bottom sensor.

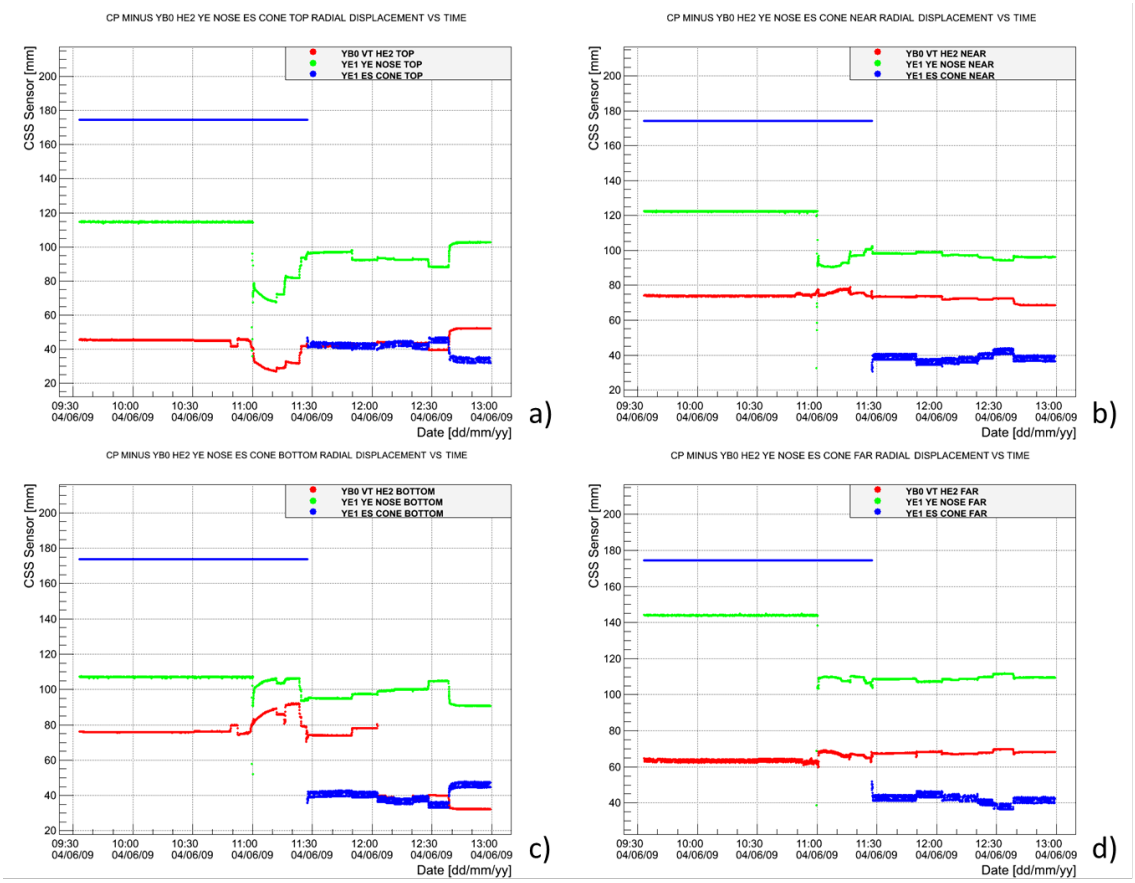

Figure 9.10: Absolute radial distance measured by the ES-cone, YE-nose, and HE2 set of sensors: a) for top, b) near, c) bottom, and d) far sensors.

Similar information was recorded for the closing of the other endcap disk, YE+1, located at the positive side of the detector. Although the actual measured values are very much dependent on the specific operation and structure, the graphics and features of the process, the amplitude of the measurements, and the main clearance are comparable to the discussion made above for the YE-1 disk. For completeness fig. 9.11 and 9.12 show the response of the different group of sensors located in YE+1.

Tables 9.7 to 9.10 summarize the final closing values obtained in the different operations performed during 2008, 2009 and 2010. In general one can conclude that the final positions of the detector structures are reasonably well reproduced, within few mm

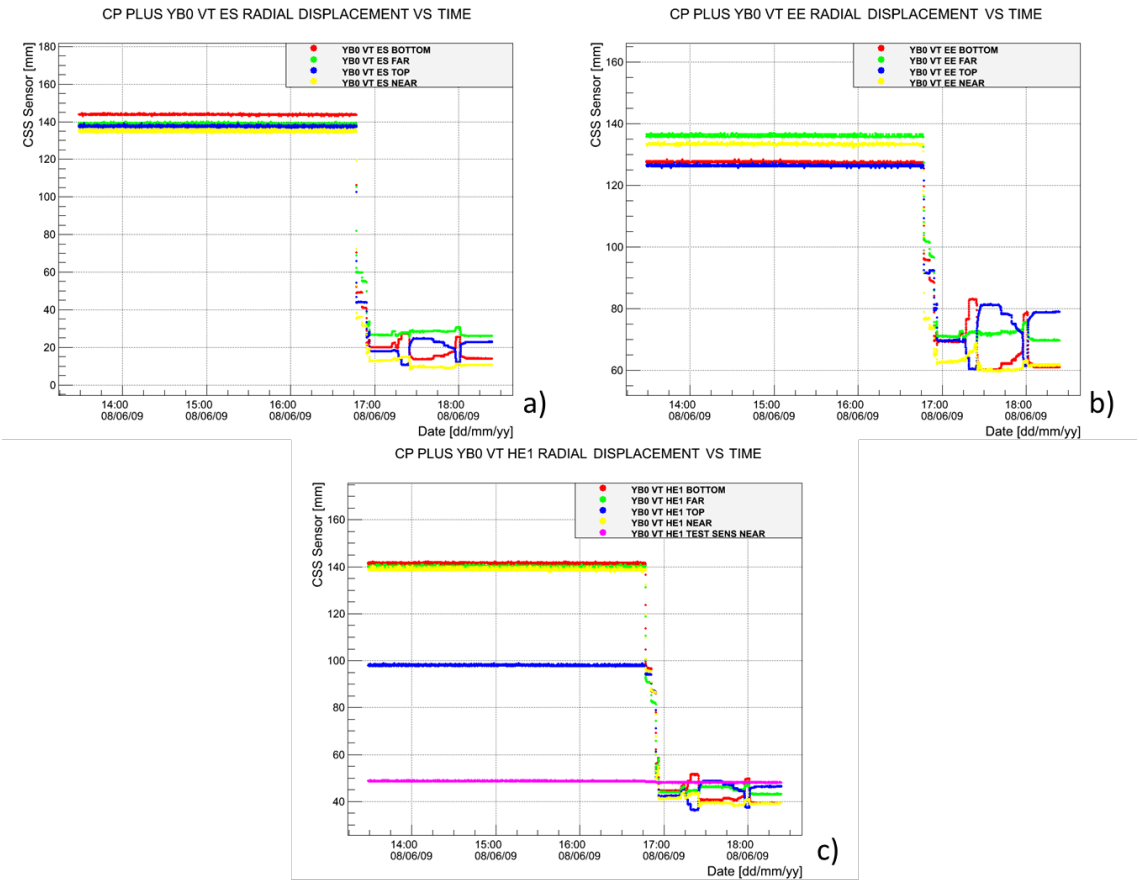

Figure 9.11: Positive side of the detector. Reading of the sensors placed along the 53º crack. a) Distance between the Pre-shower detector and the inner part of the Vac tank. b) Distance between the conical part of the electromagnetic calorimeter (EE) and the surface inside the Vac tank. c) Distance between the conical part of the hadronic calorimeter (HE) and the surface inside the Vac tank.

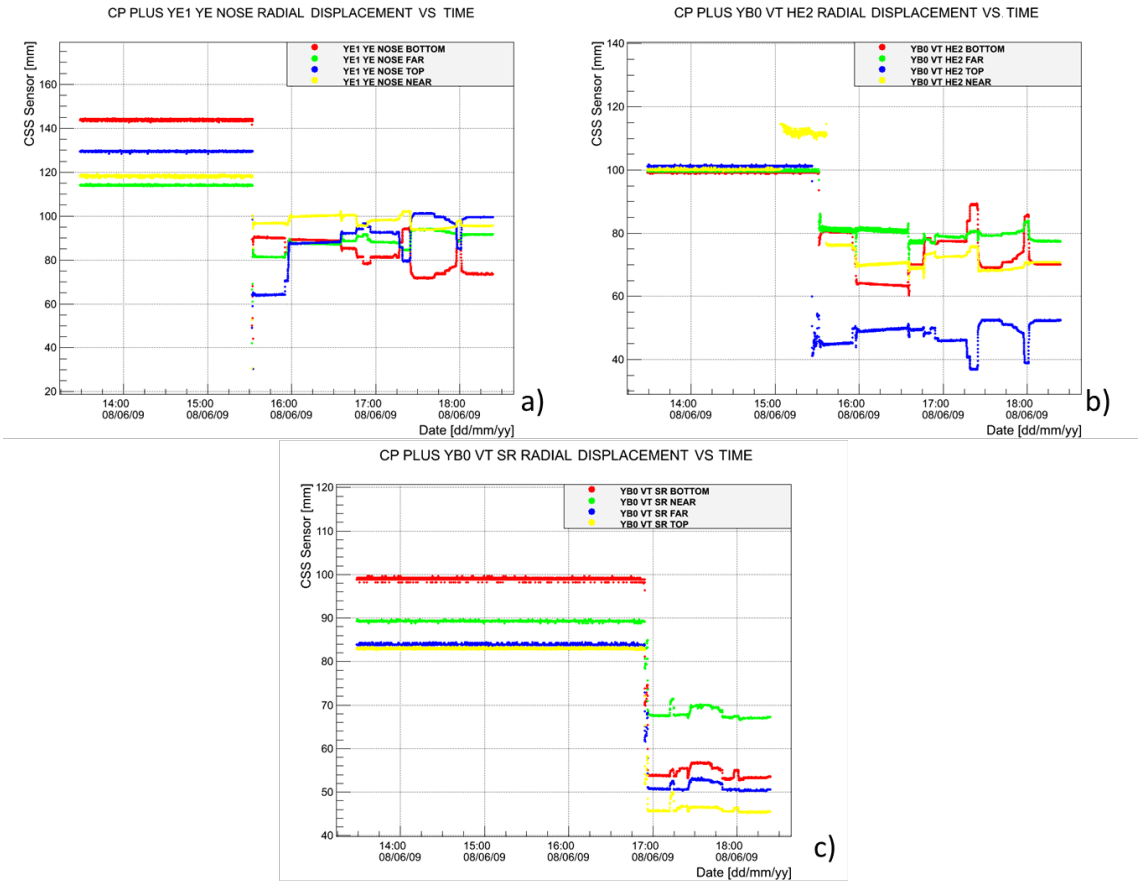

Figure 9.12: Reading of the sensors placed on the cylindrical part of the YE+1 nose. a) and b) Distance between the cylindrical part (two ends) of the YE+1 nose and the inner part of the Vac tank as measured by the YE-nose and HE2 set of sensors. c) Distance in the Z direction between the end of the coil and the sealing ring placed on YE+1.

Table 9.7: Summary of the final sensor readings for the different closings of the YE-1 structure done during the years 2008, 2009 and 2010.

Sensor position at:	Close Dist. 2008.08.30 16:16:14 (mm)	Close Dist. 2009.06.04 12:59:12 (mm)	Close Dist. 2009.07.22 09:51:08 (mm)	Close Dist. (mm) 2010.01.21 19:59:06 (mm)
HE2 BOTTOM	64.8	32.2	31.8	35.0
HE2 FAR	75.7	68.1	69.4	67.8
HE2 TOP	51.8	52.0	52.1	52.7
HE2 NEAR	74.7	68.4	68.6	72.1
ES BOTTOM		11.2	11.3	11.3
ES FAR		18.0	19.1	19.3
ES TOP		27.2	26.9	29.2
ES NEAR		16.7	15.7	18.9
EE BOTTOM	31.3	36.4	37.4	37.2
EE FAR	65.0	66.5	68.8	67.5
EE TOP	80.7	76.6	74.2	79.5
EE NEAR	63.5	57.9	56.9	61.1
HE1 BOTTOM	20.2	24.4	22.7	24.7
HE1 FAR		41.6	41.2	43.7
HE1 TOP	47.6	46.7	45.2	48.5
HE1 NEAR	37.5	42.9	42.4	48.4
HE1 TEST SENS NEAR	47.9	50.6	49.7	49.8
SR BOTTOM		48.6	49.9	58.2
SR NEAR		35.4	36.9	49.9
SR FAR		39.9	40.6	48.7
SR TOP		42.2	44.5	55.1
YE NOSE BOTTOM	79.4	90.6	92.9	85.9
YE NOSE FAR	95.5	109.5	110.4	111.1
YE NOSE TOP	91.6	102.5	103.2	109.1
YE NOSE NEAR	88.3	96.0	96.2	100.5
ES CONE BOTTOM	77.0	44.5	44.8	45.7
ES CONE FAR	64.5	42.3	37.8	35.6
ES CONE NEAR	83.8	36.5	32.9	32.1
ES CONE TOP	69.1	31.9	40.1	42.5
ES CONE TS		—	35.2	35.1

Table 9.8: Deltas in 2008, 2009 and 2010 for minus side

Sensor position at:	Delta (2009.07.22 - 2008.08.30) (mm)	Delta (2009.07.22 - 2009.06.04) (mm)	Delta (2010.01.21 - 2009.07.22) (mm)
HE2 BOTTOM	-33.0	-0.4	3.1
HE2 FAR	-6.3	1.3	-1.6
HE2 TOP	0.3	0.1	0.7
HE2 NEAR	-5.1	0.2	3.5
ES BOTTOM		0.1	0.0
ES FAR		1.1	0.2
ES TOP		-0.3	2.3
ES NEAR		-1.1	3.2
EE BOTTOM	6.1	1.0	-0.2
EE FAR	3.9	2.4	-1.3
EE TOP	-6.5	-2.4	5.3
EE NEAR	-6.6	-1.0	4.2
HE1 BOTTOM	2.5	-1.7	2.0
HE1 FAR		-0.4	2.6
HE1 TOP	-2.4	-1.5	3.3
HE1 NEAR	4.8	-0.6	6.0
SR BOTTOM		1.3	8.2
SR NEAR		1.5	12.9
SR FAR		0.7	8.1
SR TOP		2.3	10.5
YE NOSE BOTTOM	13.5	2.2	-7.0
YE NOSE FAR	14.9	0.9	0.7
YE NOSE TOP	11.6	0.7	5.9
YE NOSE NEAR	8.0	0.2	4.3
ES CONE BOTTOM	-32.2	0.3	0.9
ES CONE FAR	-26.7	-4.5	-2.2
ES CONE NEAR	-50.9	-3.6	-0.8
ES CONE TOP	-29.0	8.2	2.4

in position.
Table 9.7 shows the reading of the sensors once the structures located in the minus detector side are set to their final position, for the operations done from 2008 to 2010. Table 9.8 shows the relative variations observed between the different set of data. The reference used for the deltas was chosen as the values recorded on 2009.07.22 (only in 2009 CMS and the CSS system were fully instrumented).
The HE2 group of sensors show a rather good reproducibility over the years, taking into account among others the structural mechanical stability of these large structures, and the possible residual deformations due to magnetic forces. The large difference observed in the case of HE2- bottom sensor is due to the faulty measurements due to the change in the target, as already mentioned. As for the ES group of sensors note that there are no measurements during 2008, since the detector itself was not yet installed in CMS. For the rest of the data we observe a good reproducibility. The same is valid for the next groups of sensors listed in the tables, the EE and HE1 sensors. The Seal Ring was installed in 2009, and only from 2009 onwards data are available for this group of sensors. A more spread range of variations is observed due to the non-perfect behaviour of the sealing system at that time. For the last two sets of sensors YE-nose and ES-cone groups we observe a large difference between the data recorded in 2008 and those obtained in 2009 or 2010. This is understood as due to the adaptation of the sensor mechanical supports. All the values of the different sensor groups are at nominal safety distances.
Tables 9.9 and 9.10 list the corresponding data for the positive endcap disk YE+1. As before the reference values for comparison are those from July 22, 2009. As shown in Table 9.9, all the values of the different sensors are close to the nominal distances. Once the detector and the CSS system are fully instrumented the reproducibility is in most of the cases very good, at the level of few mm; for the other cases similar comments as given in the case of YE-1 apply. The differences observed in the ES, EE and HE1 are due, in part, to slight difference (in angle) on the location of the sensors between the two detector sides, being the nominal angles: 53° for HE1, 19° for EE, and 34° for ES.

During all the closings assisted by the CSS safety clearances have been respected without compromising or damaging any equipment, as well as the safety of the operators involved in the process. Moreover the efficiency and reliability of the system improved over the years.

9.3 Closing and opening operations of the forward region of the CMS detector

The forward detectors of CMS were the last to arrive. In 2008 when the first closing of the detector took place, the two forward hadron calorimeters (HF) were present,

Table 9.9: Summary of the final sensor readings for the different closings of the YE+1 structure done during the years 2008, 2009 and 2010.

Sensor	Close Dist.	Close Dist.	Close Dist.	Close Dist.	New system Dist.	Dist.	Dist.	Dist.
position at:	2008.04.11 15:30:20 (mm)	2008.08.19 19:13:55 (mm)	2008.08.20 15:50:51 (mm)	2009.06.08 18:23:37 (mm)	2009.07.22 09:51:08 (mm)	2010.01.26 17:41:59 (mm)	2010.01.29 01:00:02 (mm)	2010.01.29 13:35:03 (mm)
HE2 BOTTOM		49.7	59.3	70.0	69.9	72.9	71.9	72.7
HE2 FAR		18.9	16.5	77.4	77.2	79.8	80.3	79.6
HE2 TOP		23.0	21.4	52.3	52.1	48.5	50.0	48.8
HE2 NEAR		23.7	26.8	70.7	71.3	72.1	71.6	72.2
ES BOTTOM				13.9	12.7	14.5	13.4	14.2
ES FAR				25.9	24.9	28.4	30.9	28.5
ES TOP				22.8	21.3	22.1	27.4	22.3
ES NEAR				10.6	11.4	11.7	13.9	12.2
EE BOTTOM		47.5	52.6	60.9	60.8	64.4	62.4	64.4
EE FAR		74.3	72.7	69.5	68.1	72.0	72.8	71.6
EE TOP		81.4	75.9	78.9	76.9	79.1	87.2	79.2
EE NEAR		57.6	59.8	61.8	61.3	59.4	61.1	61.6
HE1 BOTTOM	38.7	34.8	38.3	39.1	36.9	40.3	44.5	39.8
HE1 FAR	40.9	42.4	41.5	42.9	41.2	47.0	51.9	47.0
HE1 TOP	42.7	48.9	46.3	46.4	44.7	46.9	51.5	46.8
HE1 NEAR	48.3	28.2	32.8	39.2	37.1	39.5	43.4	39.3
HE1 TEST SENS NEAR		48.8	48.2	48.0	47.9	49.3	48.7	49.6
SR BOTTOM				53.4	51.9	62.5	71.6	63.5
SR NEAR				67.2	65.1	72.1	76.1	71.2
SR FAR				50.5	50.2	57.1	63.4	57.4
SR TOP				45.4	44.9	57.6	58.9	57.6
YE NOSE BOTTOM	74.0	70.4	75.8	73.5	74.5	81.8	79.4	82.9
YE NOSE FAR	42.3	88.6	85.2	91.3	92.0	96.0	98.0	95.5
YE NOSE TOP		94.7	89.6	99.5	100.6	102.9	106.3	102.9
YE NOSE NEAR	81.0	80.7	86.6	95.5	96.0	97.6	97.1	97.9
ES CONE NEAR		68.5	70.4	41.8	39.1	40.2	37.9	39.7
ES CONE TOP		57.7	62.4	28.5	28.7	28.3	25.0	28.7
ES CONE FAR		74.0	72.4	38.9	37.2	36.2	39.4	36.7
ES CONE BOTTOM		83.6	77.7	46.7	46.5	46.9	50.7	46.5

Table 9.10: Deltas in 2008, 2009 and 2010 for plus side

Sensor position at:	Delta (2009.07.22 - 2008.04.11) (mm)	Delta (2009.07.22 - 2008.08.19) (mm)	Delta (2009.07.22 - 2008.08.20) (mm)	Delta (2009.07.22 - 2009.06.08) (mm)	Delta (2010.01.26 - 2009.07.22) (mm)	Delta (2010.01.29 - 2009.07.22) (mm)	Delta (2010.01.29 - 2009.07.22) (mm)
HE2 BOTTOM		20.1	10.5	-0.1	3.0	2.0	2.9
HE2 FAR		58.3	60.7	-0.2	2.6	3.2	2.4
HE2 TOP		29.1	30.7	-0.2	-3.6	-2.1	-3.3
HE2 NEAR		47.6	44.5	0.6	0.8	0.3	1.0
ES BOTTOM				-1.2	1.8	0.7	1.5
ES FAR				-1.0	3.5	6.0	3.6
ES TOP				-1.4	0.7	6.1	0.9
ES NEAR				0.7	0.3	2.6	0.9
EE BOTTOM		13.3	8.2	-0.0	3.6	1.6	3.6
EE FAR		-6.3	-4.7	-1.5	3.9	4.7	3.5
EE TOP		-4.5	0.9	-2.1	2.2	10.3	2.4
EE NEAR		3.7	1.5	-0.5	-1.9	-0.2	0.3
HE1 BOTTOM	-1.8	2.1	-1.3	-2.2	3.4	7.6	2.9
HE1 FAR	0.3	-1.2	-0.3	-1.7	5.8	10.7	5.8
HE1 TOP	2.1	-4.2	-1.5	-1.7	2.1	6.7	2.1
HE1 NEAR	-11.2	8.9	4.3	-2.1	2.4	6.3	2.3
HE1 TEST SENS NEAR		-0.8	-0.3	-0.0	1.4	0.8	1.7
SR BOTTOM				-1.6	10.7	19.8	11.7
SR NEAR				-2.0	6.9	11.0	6.0
SR FAR				-0.3	6.9	13.1	7.2
SR TOP				-0.5	12.7	14.0	12.7
YE NOSE BOTTOM	0.5	4.1	-1.3	1.0	7.3	4.9	8.3
YE NOSE FAR	49.7	3.5	6.8	0.7	4.0	6.0	3.5
YE NOSE TOP		5.9	11.0	1.1	2.3	5.7	2.3
YE NOSE NEAR	15.0	15.3	9.4	0.5	1.6	1.1	1.9
ES CONE NEAR		-29.5	-31.3	-2.8	1.2	-1.2	0.7
ES CONE TOP		-29.0	-33.7	0.2	-0.4	-3.6	0.0
ES CONE FAR		-36.8	-35.2	-1.7	-1.0	2.2	-0.5
ES CONE BOTTOM		-37.2	-31.2	-0.3	0.4	4.2	0.1

while CASTOR calorimeter and the TOTEM experiment were not completed. Only half of CASTOR and TOTEM T2 were installed in the minus detector side, the rest of the sub-detectors were installed over the following years. The different elements of the CSS instrumentation (sensors and readout electronics) were implemented following the pace of the detectors. This instrumentation is described in section Sec. 6.2. Forward detectors, because of their specific location, have a common geometry consisting of two halves, called far and near parts, which are closed around the beam-pipe. Due to the fact that they are delicate heavy structures, designed to be as close as possible to the beam-pipe, with very tight tolerances, the closing of these units is considered a risky and delicate operation. Furthermore, this forward region is one of the most irradiated areas of the cavern and special and more stringent working restrictions apply. Moreover, during the closing process, before proceeding to the final adjustment of the detectors around the beam pipe, the survey team as well as the vacuum team need to obtain the best and final adjustment of the vacuum pipe position that should not be altered. The results from the measurements of the forward sub-detectors (Forward Hadron Calorimeter, TOTEM and CASTOR) are discussed in the following sections.

9.3.1 Measurements of the Forward Hadron Calorimeter

The first test of closing the Forward Hadron Calorimeter (HF) took place in September 2008; several iterations were needed to obtain the right positioning of the two parts of the detector as well as the correct adjustment of the initial position of the potentiometers placed on the inner surface of HF and in contact with the beam pipe. The potentiometers (R1 sensors, described in Sec. 6.2) were placed such that the measurements at the nominal closed position should be in the middle range of the sensors; with a readout value close to 15 mm. Fig. 9.13 shows the different cycles of measurements during the test of closing the two halves of HF-. Note that the far half was closed first. As shown in the figure when one half is being closed the sensors placed on the other half are out of range and no measurement is registered for them. The graphics show as well that the final reading of the far sensors is shifted with respect the design values (for both far sensors the measured distance should have been closer to 15 mm) indicating that the far half of the detector remained slightly more open than foreseen by the design specifications. A similar effect was also observed in the closing of the positive detector side, HF+. Following these results the position of the sensors was adjusted to work with safer reference starting values.

Figure 9.14 summarises the evolution of the final closed positions achieved for HF-, as recorded by the CSS in the 6 operations that took place during the years 2008 to 2012. Following the experience, and including the observed deformation induced by magnetic forces, the potentiometers were adjusted on their support in order to work with a safe range during the closing process. Once the system instrumentation was stabilized, we

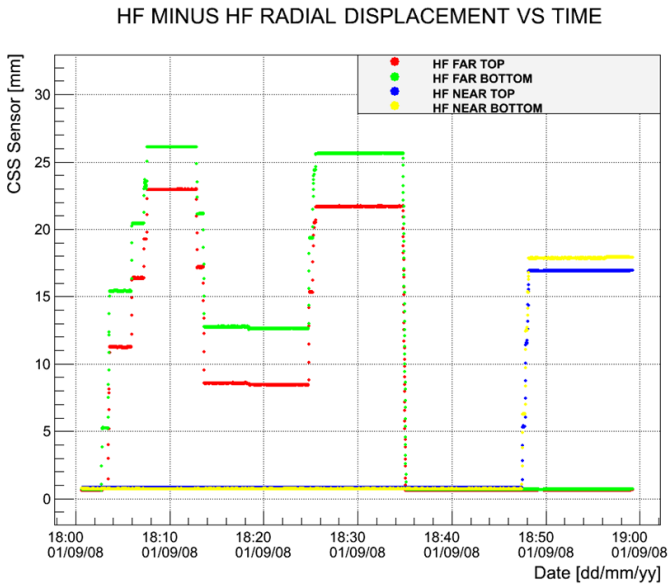

Figure 9.13: Reading of the sensors placed on the inner boundary of HF- during the first tests of closing performed in 2008. (see text)

observe a small variation in the measured values for the different sensors. The legend of the figure shows the date when the operations took place. Note that the final clearance achieved is on the order of 10 mm for all sensors in the four measured locations.

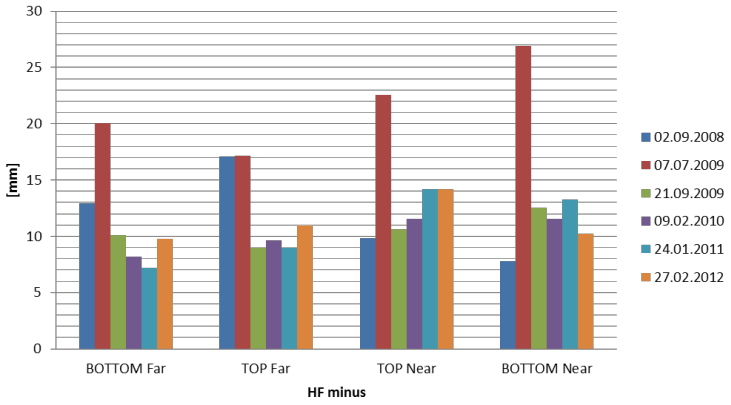

Figure 9.14: Reading of the sensors placed on the inner boundary of HF- during the different closings performed from 2008 to 2012.

Similarly, fig. 9.15 summarise the variation of the final position measured by the radial sensors on HF+. As before, during the first two years the sensors were re-adjusted in their support as needed. Note that during the first closing in 2008 the sensors located on the top far side were almost out of range. Also the near side sensors were adjusted accordingly but they were too much compressed, and only at the second closing in 2009 the sensors reached a final positioning. A good reproducibility of the measurements is observed.

Contrary to HF-, in this case top-bottom and near-far sensors differ on their readings by almost 5 mm, indicating an asymmetric positioning of the detector with respect to the beam pipe.

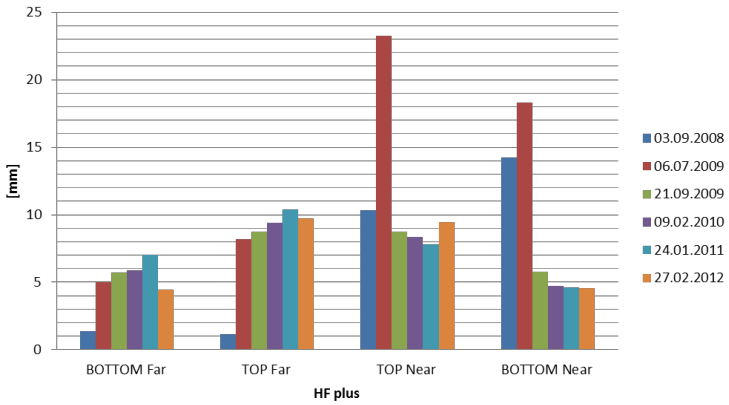

Figure 9.15: Reading of the sensors placed on the inner boundary of HF+ during the different closings performed from 2008 to 2012.

Finally, it is worth mentioning the effect of the beam pipe pumping as observed by the HF radial potentiometers. The relative variation of the distance HF/beam-pipe was monitored by the sensors when the beam pipe was pumped to reach the ultra high vacuum conditions required for the LHC operation. Figs. 9.16 and 9.17 show the recorded variations as measured in the positive and negative side of the detector, respectively. The pumping system is located on the positive side of the cavern and this explains the difference observed between the two figures, the evolution of the measurements is smoother on the negative side. In both figures, together with the radial measurements (R1 type of sensors), the axial measurement along the Z-axis (called Z1 sensors in Sec. 6.2) as performed by the potentiometer measuring the distance between the CASTOR Table (CASTOR TB) and the beam pipe flange (BP HF(Z)) is also displayed. We observe that the pumping affects the axial measurement up to about -0.4 mm, which translate to a radial variation up to 0.1 mm, indicating that the beam pipe is shrinking in the Z-axis. During the analysed period, the measurements presented several steps corresponding to the different vacuum stages. The same behaviour is observed on the negative side of the detector, fig. 9.17. As expected, here the amplitude of the variation is smaller and the movements are smoother when compared to the plus side.

9.3.2 Measurements of the TOTEM detectors

TOTEM is composed of two tracking detectors, T1 and T2, located at low polar angles, in the most inner part of the CMS. As described in Chap. 6, T1 is located in the inner free space left by the endcap muon detectors, while T2 is located behind T1 and inside the

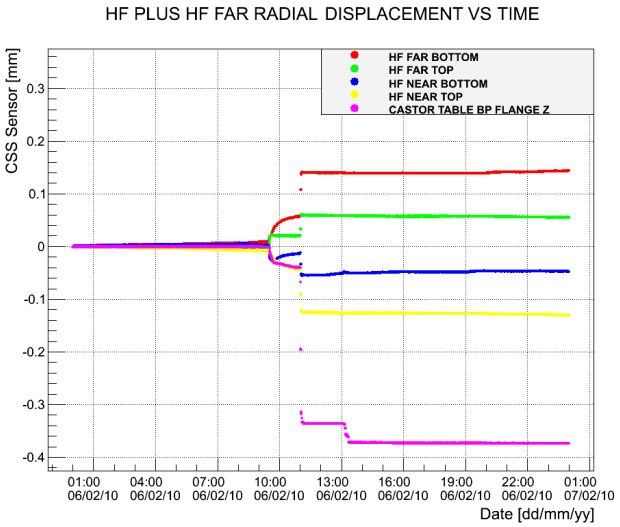

Figure 9.16: Relative variation of the HF+ radial sensors reading with respect to the final closed position recorded during the pumping of the beam pipe. The measurement was performed in 2010.

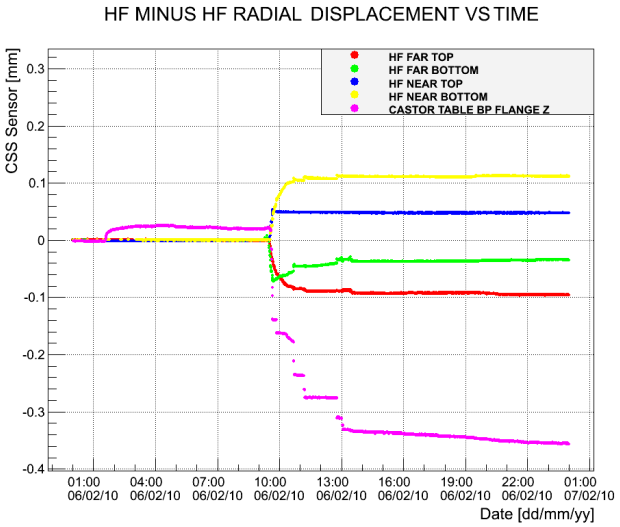

Figure 9.17: Relative variation of the HF- radial sensors reading with respect to the final closed position recorded during the pumping of the beam pipe. The measurement was performed in 2010.

inner part of HF-plug. The CSS instrumentation for these detectors is also described in Sec. 6.2. These two detectors were installed in CMS along the years 2008 and 2011. T1 was installed for the first time inside the endcap muon structures, fixed to YE2 disk, in 2011. At the time of this write up we have only one measurement related to this detector, since after its installation it has never been removed for maintenance. T1 consist of 6 layers of detectors (see Sec. 6.3.5), Tables 9.11 and 9.12 show the values recorded by the CSS sensors once the detectors (T1+ and T1-) are in their final position. These values are kept as reference for future operations. Similar patterns are observed in the two tables. The near and far side sensors have similar behaviour, and the sensors on the 5^{th} layer looks more open when compared with the 1^{st} layer indicating a slight difference on the location of the sensors.

Table 9.11: Final position of T1+ (values mm)

Sensor position at:	24.01.2011
Near side of T1 plus	
5^{th} layer BOTTOM	33.0
5^{th} layer CENTRE	34.5
5^{th} layer TOP	23.5
1^{st} layer BOTTOM	29.1
1^{st} layer CENTRE	25.6
1^{st} layer TOP	23.0
Far side of T1 plus	
5^{th} layer BOTTOM	28.6
5^{th} layer CENTRE	31.5
5^{th} layer TOP	28.2
1^{st} layer BOTTOM	27.4
1^{st} layer CENTRE	29.4
1^{st} layer TOP	26.1
Near side of T1 plus of the potentiometers	
5^{th} layer YE3 TOP Z	5.9
5^{th} layer YE3 BOTTOM Z	6.8
2^{nd} layer YE1 TOP Z	5.9
Far side of T1 plus of the potentiometers	
5^{th} layer YE3 TOP Z	11.1
5^{th} layer YE3 BOTTOM Z	11.7
2^{nd} layer YE4 TOP Z	10.9

The T2 detector was installed for first time in 2008 on the negative detector side. Due to the tight tolerances the most delicate and risky operation is the insertion of the detector around the beam pipe. Far and near halves slide along the beam pipe until the detectors are well centred around the beam pipe. During the first closing in 2008, the

Table 9.12: Final position of T1- (values mm)

Sensor position at:	24.01.2011
Near side of T1 minus	
5^{th} layer BOTTOM	30.0
5^{th} layer CENTRE	28.4
5^{th} layer TOP	26.4
1^{st} layer BOTTOM	25.2
1^{st} layer CENTRE	31.1
1^{st} layer TOP	29.0
Far side of T1 minus	
5^{th} layer BOTTOM	31.8
5^{th} layer CENTRE	34.0
5^{th} layer TOP	28.0
1^{st} layer BOTTOM	21.9
1^{st} layer CENTRE	24.2
1^{st} layer TOP	28.4
Near side of T1 minus of the potentiometers	
5^{th} layer YE3 TOP Z	13.6
5^{th} layer YE3 BOTTOM Z	11.9
Layer4 YE2 TOP Z	14.5
Far side of T1 minus of the potentiometers	
5^{th} layer YE3 TOP Z	7.8
5^{th} layer YE3 BOTTOM Z	8.6
2^{nd} layer YE1 TOP Z	9.1

detector was first aligned with respect to the beam pipe and later on the beam pipe was re-aligned producing a misalignment of the detector of around 2 mm in the Y direction. This procedure was corrected in subsequent operations. The operation is monitored using a special configuration of sensors. Fig. 9.18 shows the distribution of the R3 set of sensors. The sensor located at the outer boundary of T2 (ENTRY sensor) gives a readable signal, only during the insertion of the half, but once the detector is in place, only the three sensors sited in the inner boundary are inside the measurable range. Given the proximity of the optical sensors and the cylindrical shape of the beam pipe the sensors do not operate in continuous mode, instead, they are powered sequentially at the rate of 1 Hz to avoid possible cross talk between the measurements originated by unwanted reflection of the light on the beam pipe surface.

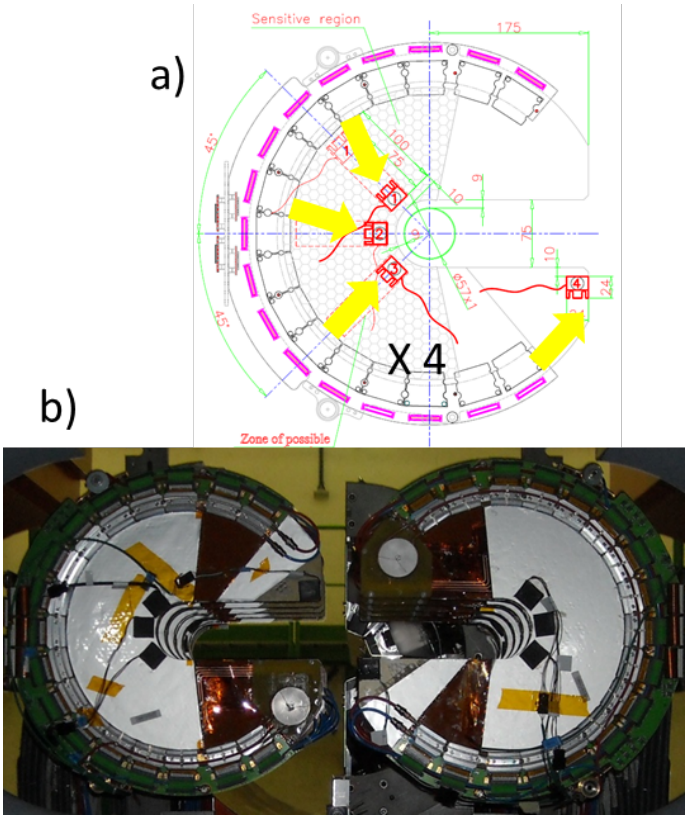

Figure 9.18: T2 detector instrumentation. Location of sensors in the disk and picture of the two detector halves.

In 2012 all sensors of the T2 detectors (on both sides of the CMS) were replaced due to the fact that they were exposed to an irradiation environment much higher than the one in 2011. This time a 0.2 mm thick fibreglass sheet (see fig. 9.19) was used as support of the sensors. The sensors were glued on the fibreglass sheet which was also glued to the detector. The new support helps reducing the replacement time of the sensors and increase the repositioning accuracy and therefore their reliability in operation.

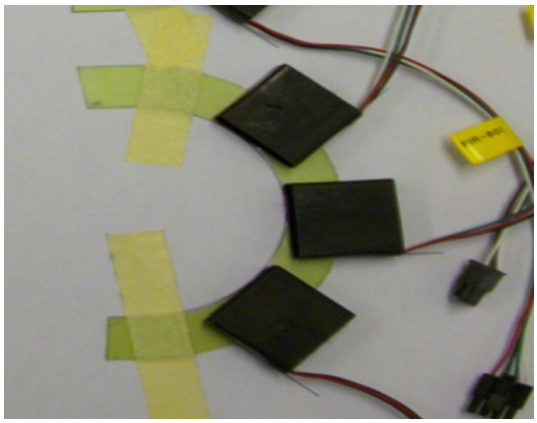

Figure 9.19: Sensors support installed in 2012 on T2 detectors.

Figures 9.20 and 9.21 summarise the readings of the sensors -or clearance reached- after the final closing of the T2 detectors, over the years. Fig. 9.20 (left) shows the measurements from the far side sensors of T2-. Only one measurement is close to 5 mm (the sensor bottom far NonIP in 2012) due to a malfunction of the sensor. In 2012 the measurements were more homogeneous when compared to the previous years. Fig. 9.20 (right) shows the near side sensors. Low values can be observed in 2009, due to the fact that the sensor plastic covers were cut during the installation, thus given faulty measurements during this run. With the exception of 2009 all other measurements are close to the 10 mm clearance, well above specifications.

Figure 9.21 (left) shows all the measurements from the far side of T2+. In all cases this half detector was close to the nominal distance. The measurements on 2012 were more homogeneous when compared to the previous years. Fig. 9.21 (right) shows the near side of T2+, again all measurements are close to the nominal value with the exception of one sensor (top NonIP sensor) in 2009 and 2010.

CSS measurements of T2 have improved over the years, achieving an excellent performance when the additional support was implemented. Overall a good reproducibility is achieved in the final position of the detectors over the years.

9.3.3 Measurements of the CASTOR detector and shielding mechanics

CASTOR sits on top a cradle located on a support called CASTOR table fixed to the HF platform. From the monitoring point of view, this detector is critical in two aspects: a) due to the tight tolerances of the detector with the beam pipe, as is the case for TOTEM detectors; and b) due to the strong and complex forces that all the elements (detector, supports, ancillary, etc.) will experience when the solenoid magnet is switched on. CASTOR installation is mainly monitored by the set of R4 sensors (see Sec. 6.3.3). On top of this basic instrumentation, there are other sets of sensors to monitor the positioning

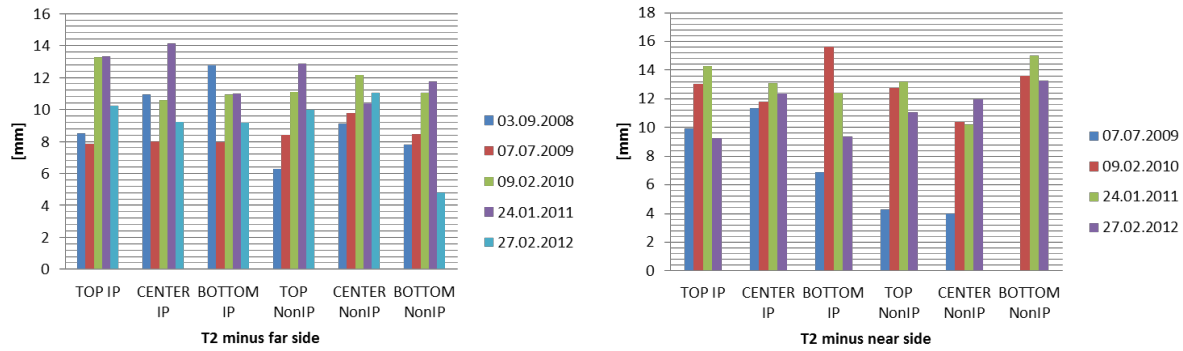

Figure 9.20: T2 detector on the minus detector side, far (left) and near (right) side half. Distance between the inner bound of the detector and the beam pipe surface as measured by the sensors after the different closings of the detector.

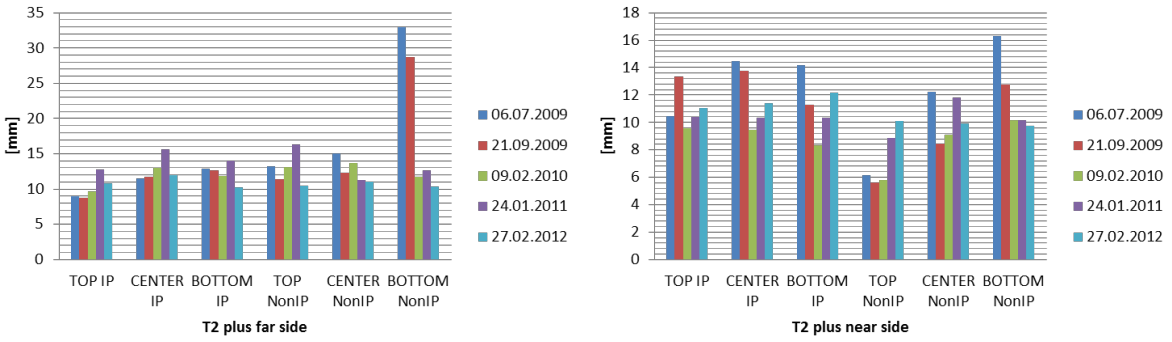

Figure 9.21: T2 detector on the plus detector side, far (left) and near (right) side half. Distance between the inner bound of the detector and the beam pipe surface as measured by the sensors after the different closings of the detector.

and possible motion of other heavy mechanical structures present in the area. This extra instrumentation (R5, Z1, Z2, and X1 set of sensors) uses CASTOR as reference for the measurements. The CASTOR detector is composed of two units located on the positive and negative ends of CMS. Each unit consist of two halves (as HF and TOTEM) surrounding the beam pipe at a distance of the interaction point of 14.37 m in Z direction. Up to now, only one end of the CMS has been instrumented, the negative end. Therefore, in what follows we will present results only for CASTOR minus side detector.
In 2008 half of the CASTOR minus, the far side, was completed and ready for installation (the second half was available in 2009, on time for the first run of LHC). The final tolerances achieved in the closing of the first half of the CASTOR are reported in Table 9.13. Given the fact that the beam pipe was visible to the operators the closing of this half detector unit was not considered critical, but was helpful to establish the procedure and understand the reference values measured by the CSS sensors. Being around 9 mm the designed tolerances between the edge of CASTOR and the beam pipe, we observe a large dispersion of values. CASTOR has a mechanical support for the sensors on the NonIP side, which prevent the correct alignment between the edge of the sensor and the edge of CASTOR; instead on the IP side a first bunch of sensors using rubber covers facilitated a reasonable alignment.

Table 9.13: Closing clearances (in mm) achieved during the first closing of CASTOR half side, in 2008.

Sensor position at:	TOP IP	BOTTOM IP	TOP NonIP	centre NonIP	BOTTOM NonIP
02.09.2008 5:58 PM	26.3	28.0	8.4	6.9	17.7

Figure 9.22 summarise the clearance achieved in the assembly of the CASTOR detector as provided by the monitoring system. Fig. 9.22 (left) shows the far side measurements, and fig. 9.22 (right) shows the near side measurements from 2009 onwards. The first installation (in 2009) shows tighter clearance in most of the sensors when compared to the results from the following years. On the contrary, in 2013 the clearance measured by most of the sensors was the largest. For the other three closings a maximum variation below 5 mm was achieved, indicating a reasonable reproducibility. The variations on the clearances between CASTOR IP and NonIP values are influenced by the difficulty to achieve a good reproducibility in the re-installation of the sensors over the years due to the lack of a good mechanical support referencing.

The clearance between the forward shielding and CASTOR is monitored using the R5 set of sensors, which provide radial measurements between the outer boundary of CASTOR and the Rotating Shield (RS) inner surface. Although the tolerances expected here are high (around 50-100 mm), its monitoring is important to ensure no contact

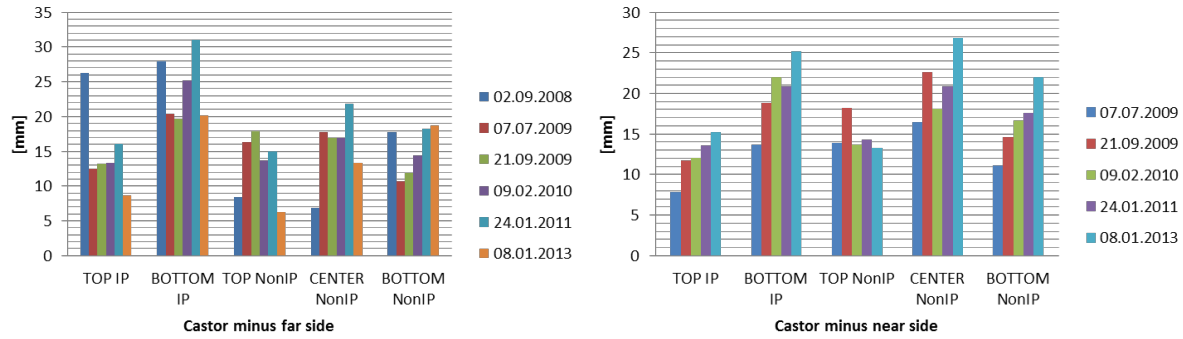

Figure 9.22: The CASTOR detector on the minus detector side, far (left) and near (right) side half. Distance between the inner bound of the detector and the beam pipe surface as measured by the sensors after the different closings of the detector.

between the heavy RS element and the light and fragile CASTOR detector. The monitoring of this clearance is not only important during the final closing of the forward shielding but also during the powering of the solenoid, again, due to the large magnetic forces acting on the forward structures. Fig. 9.23 shows the variation of the clearance for the different closings. The first closing shows, for all the sensors, the larger clearance measured. In the following years a reasonable good reproducibility of the measurements (although towards lower values) is observed. Note that these measurements should be correlated with the measured position of CASTOR with respect to the beam pipe. We observe a systematic difference between the near and far side. From this we conclude the CASTOR detector is closer to the far side of the RS; the difference being between 15 and 20 mm. Finally, the lowest value measured (by the bottom far sensor, in 2010) in all these campaigns is due to a sensor malfunction.

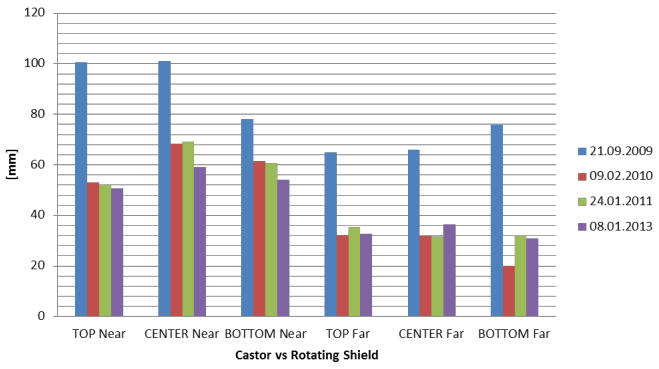

Figure 9.23: Clearance between the CASTOR outer boundary and the Rotating Shielding as measured by the R5 sensors over the years.

The X1 group of sensors, with 2 potentiometer sensors mounted one on each half of the Collar, are used to measure the Collar against the CASTOR table rails. See fig. 6.14 for details. Closing the Collar has a small but measurable effect on the CASTOR positioning.

Fig. 9.24 shows the variation, as recorded online with the PVSS software, during the closing of the Collar. The distance between CASTOR and beam pipe (as measured by the R4 sensors) is shown during the closing of both halves of the Collar. The changes are due to the contact between the Collar and the CASTOR cradle that has the effect to pull CASTOR towards the beam pipe. Collar can touch different detectors during its closing: CASTOR, BCM and T2 (if the support bars of T2 are touched), and therefore its monitoring is important. A drawback has been detected due to the fact that the potentiometers mounted on the Collar are always dismounted when the detector is open, thus losing the reference for future measurements. An adequate protection in order to have them permanently installed should be foreseen.

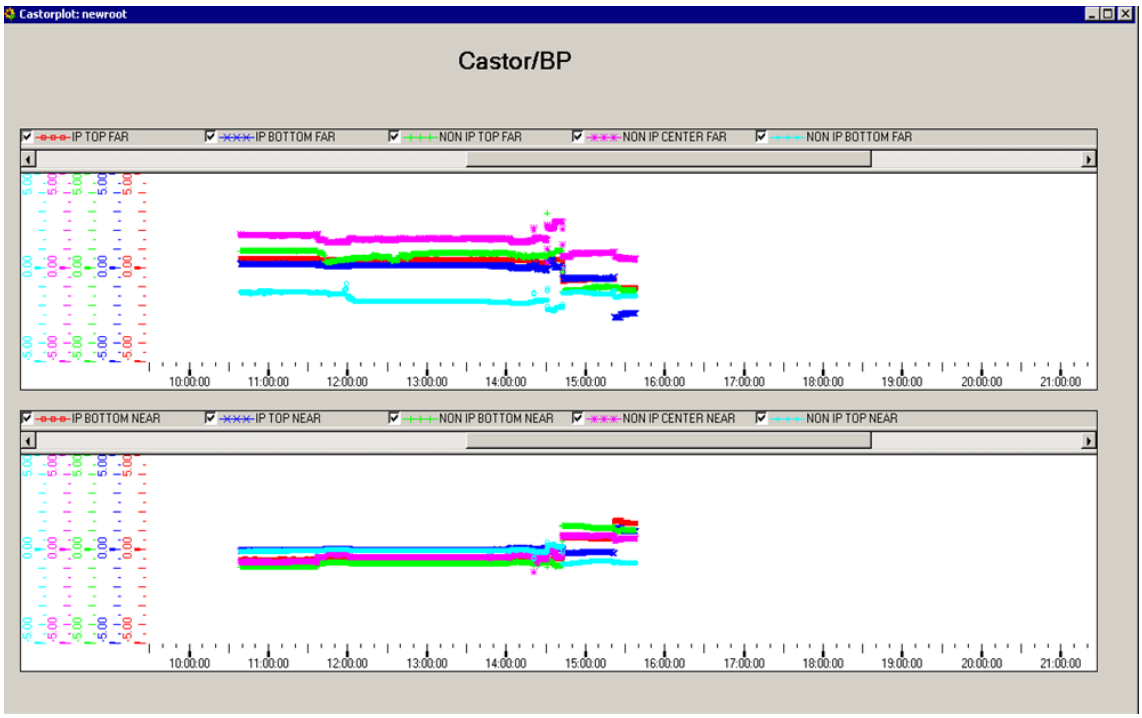

Figure 9.24: Variation of the clearance between CASTOR and beam pipe as read by the R4 sensors, during the closing of the Collar.

Other instrumentation was installed and used mainly to monitor the relative motion of forward elements as result of the magnetic field forces. Two sets of axial sensors, measuring along the direction of the CMS Z-axis, are used: a potentiometer (Z1) surveys the distance, along the CMS Z coordinate, between the beam pipe support and the beam pipe flange (see fig. 6.13); a second potentiometer (Z2) located at the near (+X) half of CASTOR, and at the NonIP end of the detector, surveys the distance to the adjustable beam pipe support (see fig. 6.13).

10

Short- and Long-term detector motion

CMS structures experience strong magnetic forces and sizeable deformations when the 4 T solenoid magnet is powered on. During the design phase finite element analyses were performed to evaluate the field map and the forces generated on the ferromagnetic elements of the detector. As described in Sec. 2.3 the magnetic forces generated in the magnet are very large compared to the gravitational forces, so that the latter can be neglected. The forces generated in the barrel layers, transmitted from ring to ring are quite substantial and the main component present is in the axial direction and pointing inward. They result in compressive axial forces of about 2,800 tonnes in the second layer, 3,000 tonnes in the third layer, and this requires care to ensure stability of the barrel ring construction in the Z direction. The forces developed in the endcap disks are also substantial. They run from 4,915 tonnes in the first disk YE1 to 153 tonnes in the third, YE3, disk. The effect of the forces in the yoke were fully analysed and considered in their construction specifications. The measurements performed on the real detector confirmed the available studies.

Although, the behaviour of the Central region of the detector –barrel and endcap- in the presence of magnetic forces was rather well known, the field map and magnetic forces in the forward detectors, ancillary components and support structures, were more difficult to simulate correctly and only rude estimations of possible deformations were available. Precise measurements of this region performed during the powering of the solenoid were therefore critical to understand the mechanical behaviour of the elements and to preserve their integrity. CSS was intensively used during the different occasions the CMS solenoid

was powered on or off. First measurements were performed in the year 2008, when only partial instrumentation of the forward region was available, and regular monitoring is being done of the magnet cycles performed in the following years. In the 2008 campaign independent measurements were performed by the CERN Metrology Group [32] using standard survey and/or photogrammetry techniques. The comparison between the two sets of data allows us to further validate the CSS output, and this is one of the main results reported in this chapter. Long-term reproducibility and mechanical stability of the different parts of CMS is also discussed based on the data recorded by the system during the normal periods of LHC and CMS operation .

10.1 Extra instrumentation used during the initial magnet tests

First tests of powering the solenoid were performed during the months of October and November of 2008. As detailed in Table 10.1 four-measurement campaigns took place.

Table 10.1: Magnet cycles done during the period from 09-10-2008 to 17-11-2008

Date:	Ramp up/down	Steps and max. B Field	Obs.
First tests cycles			
09/10/2008	Ramp up	2.0, 2.5 T	
10/10/2008	Ramp up	3.0, 3.5 T	
Second tests cycles			
16/10/2008	Ramp up	1.0, 2.0, 2.5, 3.0, 3.5, 3.8 T	
21/10/2008	Ramp down	0.0 T	
Third tests cycles			
22/10/2008	Ramp up	3.8 T	
29/10/2008	Ramp down	0.0 T	
Fourth tests cycles			
12/11/2008	Ramp up	3.8 T	
13/11/2008	Ramp down	0.0 T	
14/11/2008	Ramp up	4.0 T	
17/11/2008	Ramp down	0.0 T	

At that time, the status of the CMS forward detectors was as follows: HF was in place in both, plus Z and minus Z detector sides, and only one half of the CASTOR and TOTEM T2 detectors (the far side) were installed in the –Z side of CMS. The forward shielding was basically completed but for the so called ”cheese edges“. These pieces are located at the end of the Rotating Shielding giving continuity to the forward

shielding configuration, and closing the magnetic field lines in the forward region. The three detectors were instrumented with their corresponding CSS sensors, but only T2 and HF sensors were readout during the test. To further understand the motions of detectors and mechanics, additional monitoring sensors were temporally added. They were mainly located at the passive mechanical structures supporting the forward detectors (raisers) or attached to the heavy shielding parts. The complex HF support platform composed of modules known as "raisers" (shown in fig. 10.1), was instrumented with potentiometers. The description of these extra sensors is as follows:

a) Potentiometer sensors installed on the Raiser number 1 (bottom module) to survey movements along the Y (vertical) and Z (axial) axis. Six sensors were installed as indicated in fig. 10.2.

b) A potentiometer sensor located between the HF base structure, known as "Orange platform", and the top Raiser module, Raiser number 4, measuring in the Y direction. This sensor was mounted on the far side of the structure.

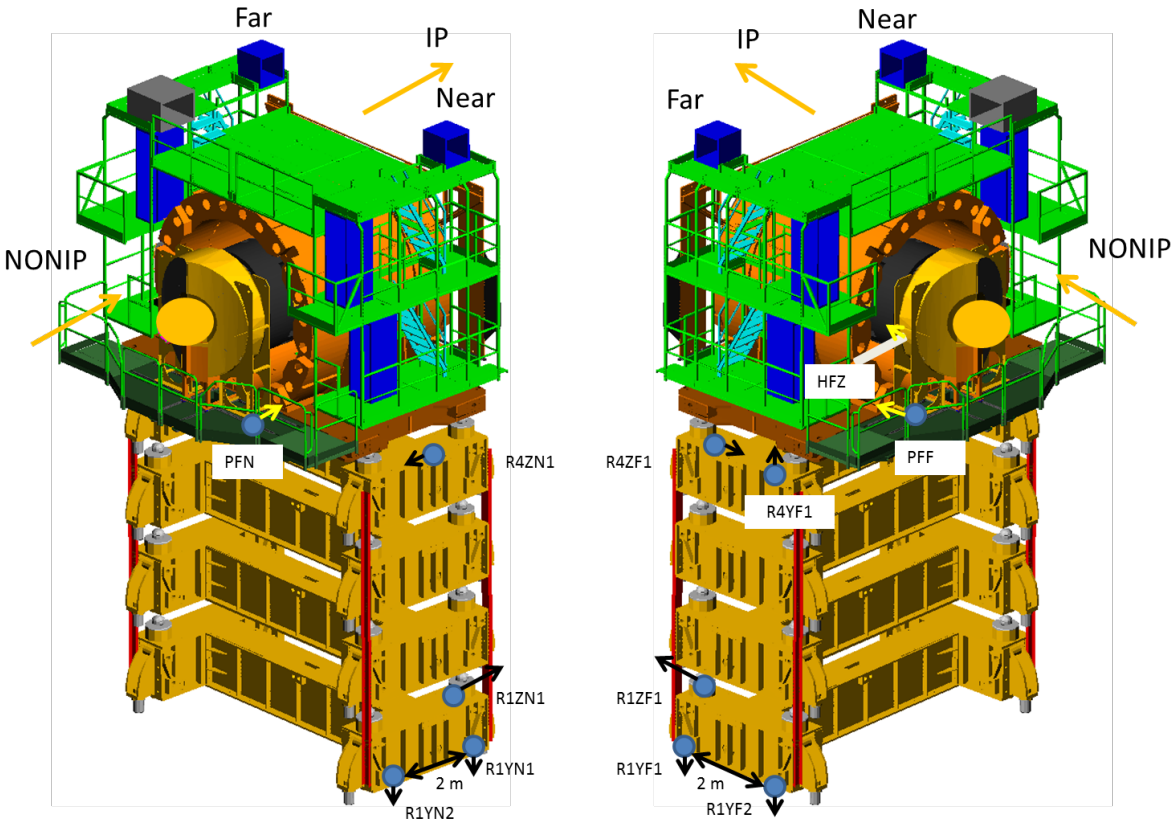

Figure 10.1: 3D drawing of the HF platforms, "raisers". Back arrows indicate the location of the CSS temporarily instrumentation.

Four more additional potentiometer sensors were also installed around the HF detector. Three of them are displayed in fig. 10.3: a) a sensor measuring HF with respect

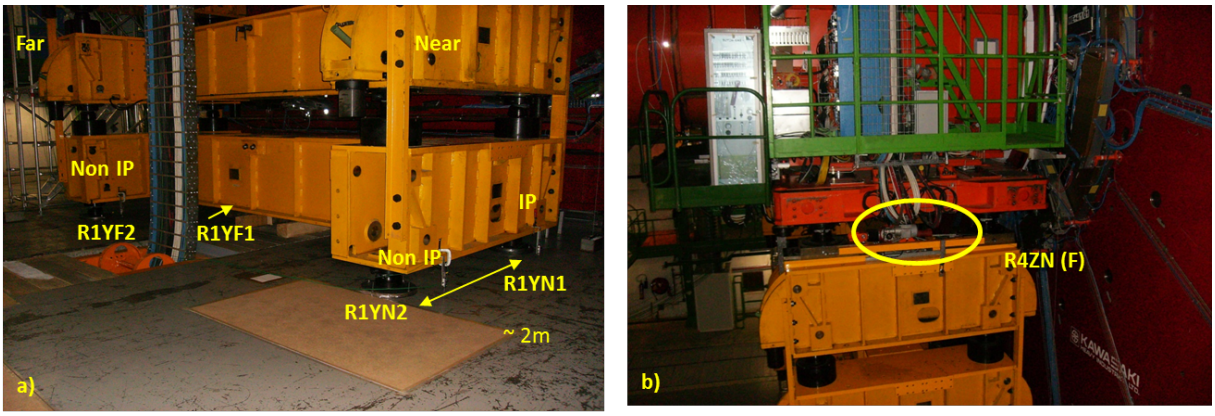

Figure 10.2: Detail of the sensors installed on the raisers at the +Z side of the detector (see text).

to the HF-Plug (PHZ or HFZ as in fig. 10.1); b) a sensor measuring displacements between the Collar Platform and HF far side along the Z-axis (PFF) (Same disposition was used in the near side.); and c) a sensor measuring the distance along the Y-axis between the top Raiser, number 4, and HF. This sensor was mounted only on the far side.

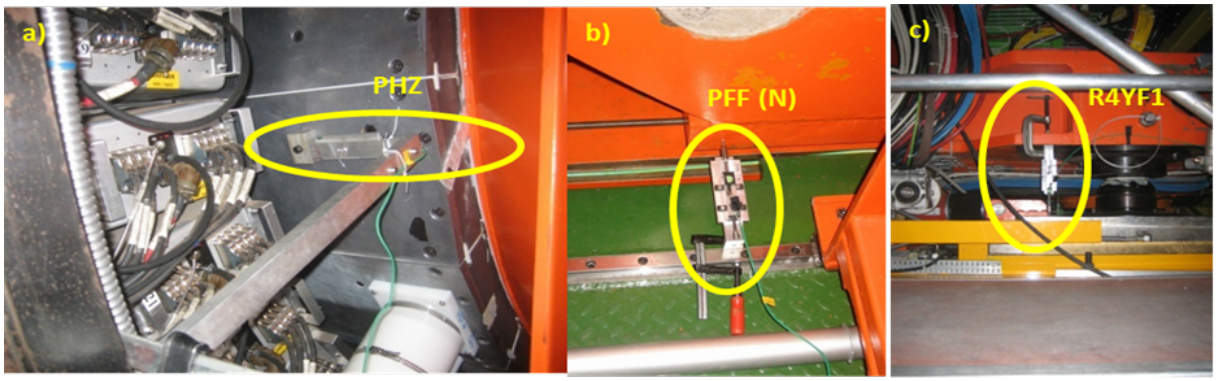

Figure 10.3: The set of sensors installed around the HF, volume. (see text)

Table 10.2 summarises the additional instrumentation described, and indicates the time when it was installed and used by the monitoring system. An additional sensor "US-test", not listed in the table, was also installed to be used as in-situ test sensor.

In parallel, measurements using standard survey techniques and photogrammetry were performed. For convenience, in what follows, we will call these results as "survey" measurements. The surveyed areas are summarized in Table 10.3. Fig. 10.4 shows some points surveyed on the HF platforms (raisers). A detailed description of the instrumentation and results can be found in [17]. Dots in fig. 10.4 indicate the location of the photogrammetry targets, on the raisers and the HF area, used during these campaigns. Survey results are expressed in the global CMS coordinate system and the accuracy of

Table 10.2: List of additional sensors mounted on HF plus detector and mechanical structures for the different measuring campaigns.

Sensor place description	Ref.	Third Test	Fourth Test
HF plus side			
RAISER1 FLOOR NEAR FRONT Y	R1YN2	X	X
RAISER1 FLOOR FAR FRONT Y	R1YF2	X	X
ORANGE PLATFORM RAISER4 FAR Y	R4YF1	X	X
COLLAR PLATFORM HF FAR Z	PFF	X	X
COLLAR PLATFORM HF NEAR Z	PFN	X	X
HF HFPLUG FAR Z	HFZ	X	X
RAISER1 BACK FAR Z	R1ZF1		X
RAISER1 BACK NEAR Z	R1ZN1		X
RAISER1 FLOOR BACK NEAR Y	R1YN1		X
RAISER1 FLOOR BACK FAR Y	R1YF1		X
RAISER4 GREASE PAD FAR Z	R4ZF1		X
RAISER4 GREASE PAD NEAR Z	R4ZN1		X
HF minus side			
Ultrasound	US-Test		X

the measurements in the three coordinates, X, Y and Z, is estimated [17] to be 0.5 mm. Although not exactly the same points were measured by the two systems, survey and CSS, the inferred motion of the structures can be reasonably compared. The result of this comparison, discussed in the next section, served as additional validation of the reliability of the CSS output.

Table 10.3: Areas surveyed by the survey team during the different magnet cycles

First Test	Second Test	Third Test	Fourth Test
YE-3 NonIP	CASTOR Table	CASTOR Table	Orange Platform
RS near side	HF- both sides	Beam Pipe at 15.50 m	HF- both sides
CASTOR Cradle		Orange Platform	2 targets on each raiser minus side far side
Green Balcony		2 targets on each raiser minus side far side	
Collar		HF- both sides	
HF- near side			

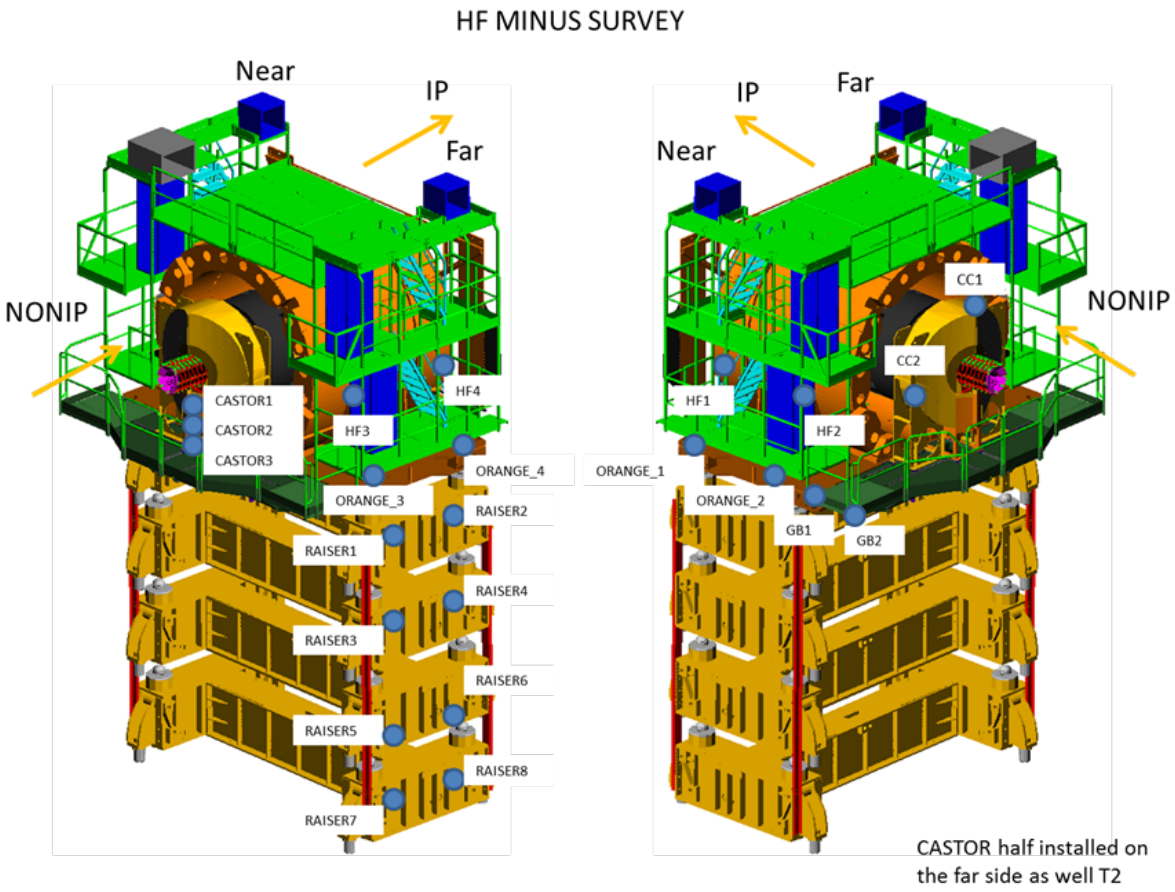

Figure 10.4: 3D drawing of the raisers and HF minus are with the survey targets.

10.2 Interpretation and comparison of CSS and Survey data

CSS is designed to provide information on relative distances between objects. In order to compare with results provided by other systems, survey in this case, CSS data need to be appropriately treated and the measurement re-interpreted in the common global CMS coordinate system. While most of the additional sensors installed for the tests, already measure in a well defined axis of the CMS coordinate system (X, Y or Z), other sensors i.e. in HF, T2 or CASTOR detectors, provide radial measurements. In most of the cases the measurement corresponds to a distance relative to the beam-pipe. To transform this relative value to an absolute distance, in what follows we will consider the beam-pipe as fixed during the magnet cycles. In fact, the beam-pipe is one of the most stable objects in CMS, which makes this assumption reasonable for the purpose of this study. Radial sensors in HF and T2 are placed in every detector quarter at approximately $45\,^{\circ}$, the exact angle can not be defined precisely due to the difficult access to the different areas. We will use $45\,^{\circ}$ to decompose the radial measurement into the two X and Y components. Moreover, contact and non-contact sensors provide different signals for the same direction of the movement, this is also taken into account in the treatment of the CSS data.
The raw data recorded by the CSS sensors during the first magnet cycle (on October 9^{th} 2008), for different field values, are listed in Tables 10.4 and 10.5, for the –Z and +Z detector sides, respectively. Note that Table 10.4 includes the HF radial sensors and the axial measurement (along the Z-axis) performed by the Z1 sensor located on the HF plus side. Table 10.5 includes all raw radial measurements between the inner surface of the HF and T2 detectors and the beam-pipe.

Table 10.4: Relative distance (in mm) as measured by the sensors installed on the +Z side of the detector for different magnetic field values. (See text)

B [T]	Date:	HF FAR BOTTOM	HF FAR TOP	HF NEAR TOP	HF NEAR BOTTOM	CASTOR TABLE BP FLANGE Z (Z1)
0.0	2008.10.09					
2.0	2008.10.09	-0.3	0.0		0.4	4.4
2.5	2008.10.09	-0.3	0.0		0.5	6.3
3.0	2008.10.10	-0.4	0.0	0.0	0.5	8.6
3.5	2008.10.10	-0.4	0.0	0.0	0.5	12.3
3.8	2008.10.10	-0.4	0.0	0.7	1.3	15.9

The motion of the HF detectors (HF+ and HF-) with respect to the beam-pipe, decomposed in X and Y components is shown in fig. 10.5 (for HF+) and 10.6 (for HF-). A common uncertainty not included in the graph) affects all the entries. The estimated uncertainty, 0.2 mm, takes into account the intrinsic uncertainty from the

Table 10.5: Relative distance (in mm) as measured by the sensors installed on the -Z side of the detector for different magnetic field values. (See text)

B [T]	Date:	HF NEAR BOTTOM	HF NEAR TOP	HF FAR TOP	HF FAR BOTTOM	T2 NonIP FAR BOTTOM	T2 NonIP FAR TOP	T2 NonIP FAR centre
0.0	2008.10.09							
2.0	2008.10.09	0.0	-0.1	-0.1	0.0	-0.4	0.3	-0.4
2.5	2008.10.09	-0.1	-0.1	-0.1	0.0	-0.6	0.5	-0.6
3.0	2008.10.10	0.0	0.0	-0.2	-0.2	-0.6	0.9	0.5
3.5	2008.10.10	0.1	0.2	-0.3	-0.4	-0.5	1.4	0.4
3.8	2008.10.10	0.1	0.3	-0.4	-0.5	-0.5	1.6	0.4

potentiometer and the uncertainty introduced by the approximate knowledge on the location and orientation of the sensor in the detector. Note that the observed motion of the HF calorimeters on both ends is limited to less than 0.5 mm, with only two points approaching 1 mm displacement.

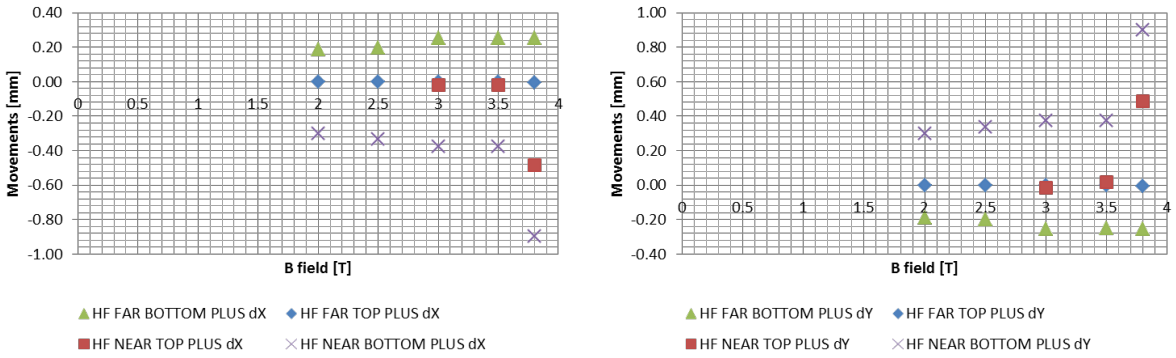

Figure 10.5: Motion of HF+, along the Y-axis (right), and along the X-axis (left) for different values of the magnetic field.

In fig. 10.7 the relative displacement in the Y coordinate relative to the value at B = 0 T, for the near side of HF- is presented. Together with the CSS results, the measurements from survey are included. HF1 and HF2 measured points are located on the outside surface of HF on the near side, approximately at a Y corresponding with Y = 0, and at the two ends (in the Z direction) of the HF calorimeter volume. As shown in the figure, while CSS does not see any significant motion of HF in this coordinate, survey measured points shows how HF1 fluctuates to values close to -2 mm (between -1.5 and 2.5 mm) for B values above 2.0 T, and HF2 has a clear increase correlated with the magnetic field. This different behaviour of the front and back part of the HF volume is interpreted as corresponding to a tilt around the CMS X-axis. This tilt, if real, will not be perceived by the CSS sensors, since they are at a unique location (in Z) and also, placed at the inner part

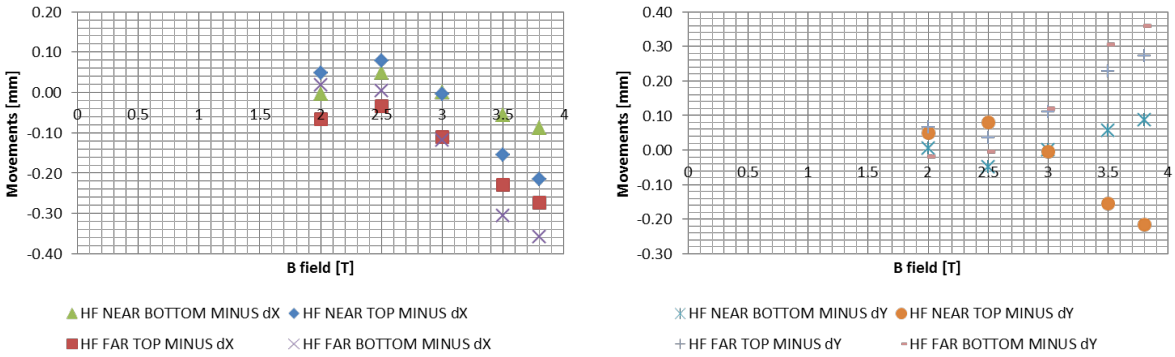

Figure 10.6: Motion of HF-, along the Y-axis (right), and along the X-axis (left) for different values of the magnetic field.

of the detector where any tilt will have very small amplitude. Survey measurements also show that the rotation should be around the mid point between HF1 and HF2, since both measurements present similar amplitude but different signs.

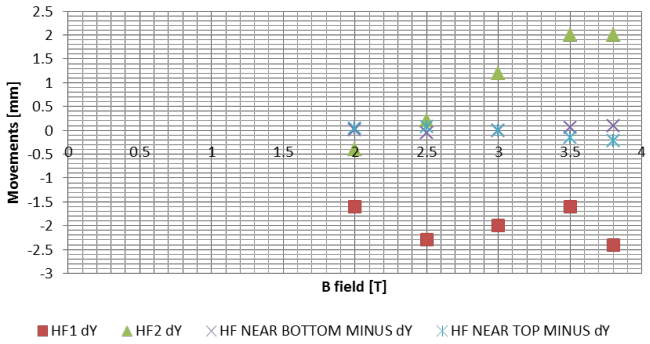

Figure 10.7: Relative movements (in mm) in the Y direction versus the magnetic field value. Survey measurements on the HF- and YE3 disk are displayed together with the results form the CSS sensors.

More conclusive results are obtained when comparing the motion in the Z-axis direction where both systems have comparable sensitivity. Fig. 10.8 shows the displacement in Z, versus the B value, obtained by the CSS Z1 sensor and the reading from survey. Measurements from both systems follow the same pattern, being a compression of the detector along the Z-axis, and with the quantitative values also in agreement within 1-2 standard deviations.

In summary, from the first powering of the CMS solenoid magnet, we observed a rather dramatic motion of the Forward region of the CMS, mainly related with the compression along the Z-axis. Survey and CSS results are in a reasonable agreement within the uncertainties introduced in the comparison. Small displacements in X and Y as measured by the CSS are difficult to interpret and a more robust understanding is

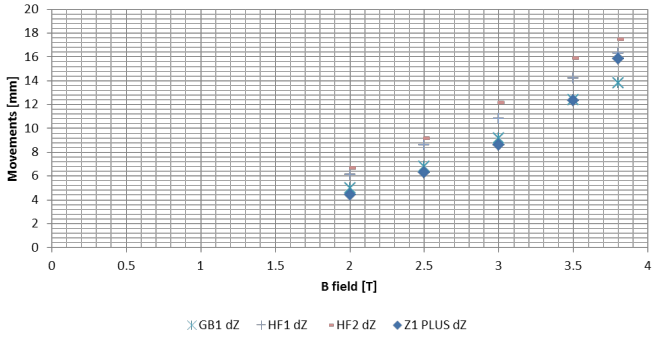

Figure 10.8: Relative movements along the Z-axis as measured by survey and CSS sensors.

obtained when we join CSS results with those obtained by survey that are obtained with similar resolution but larger lever-arms.
A second magnet cycle was performed in mid October 2008. For this campaign the survey team added some photogrametry targets to the far side of HF and in the support structure of the CASTOR detector (CASTOR table). The new points are called CASTOR_1, CASTOR_2, and CASTOR_3. The compression in the Z-direction measured in this second magnet ramp up is shown in fig. 10.9. The graphs show the results obtained from the different sensors and survey targets. These measurements confirm a very good agreement between CSS and survey. Note that the CSS measurement is done on the Z+ side of the detector, while survey measures only on the negative detector side. The agreement between both measurements confirms a good forward-backward symmetry in the field lines and induced magnetic forces. Some remaining differences in the auxiliary mechanics at the two ends of the CMS explain the small differences observed in the measurements. With this second test, the small motion (negligible within resolution) observed with the HF radial potentiometers was also confirmed.

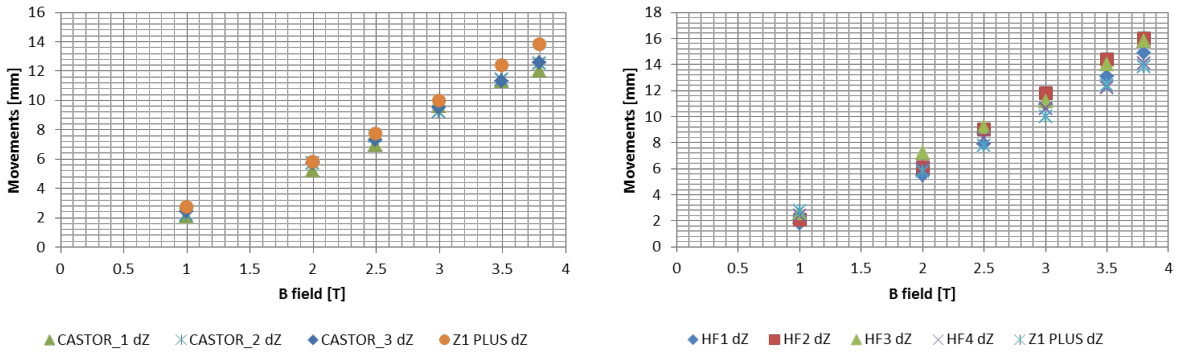

Figure 10.9: Compression in Z direction versus B field value. The CSS Z1 sensor and survey measurements performed on the CASTOR support table (left) and the CSS Z1 sensor and survey measurements performed on the HF detector outer surface (right). (See text)

The stability of the mechanics when the solenoid magnet is at 3.8 T is also an important information to be extracted from these tests. After the third magnet cycle measurements were performed at a stable 3.8 T field, in a two weeks period during three days (22^{nd}, 29^{th} October and 5^{th} November). In general, data showed a reasonable stability, at the level of 1 mm or better, as it is shown in figs. 10.10, 10.11 and 10.12 with a set of selected results. Later on, with the completed CMS and auxiliary mechanics the stability of the detector was greatly improved, reaching the sub-millimetre level.
Fig. 10.10 shows relative movements surveyed by the CSS and survey team on HF far minus after finishing the magnet ramp up, and the stability over time for the X and Y components. The measurements done by the CSS, at the inner part of the detector, were perfectly stable during the 15 days period. During the same period of time, the survey team observed a variation of about 1 mm amplitude in the Y coordinate, on both surveyed points and in opposite directions, that could indicate a further shift up of the detector. The X coordinate was stable in the same period.
The stability along Z is shown in fig. 10.11. All measurements done by survey on the HF and Orange platform are shown. The CSS Z1 sensor on the plus side is also displayed. Again, stabilities are within 1 mm, with no clear trend.

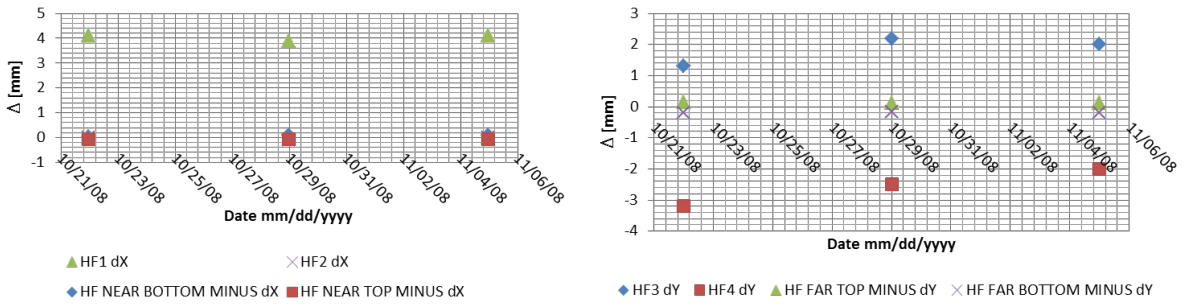

Figure 10.10: Relative movements of the HF along X-axis (left) and Y-axis (right), at 3.8 T, as measured by survey and the CSS over a period of 15 days.

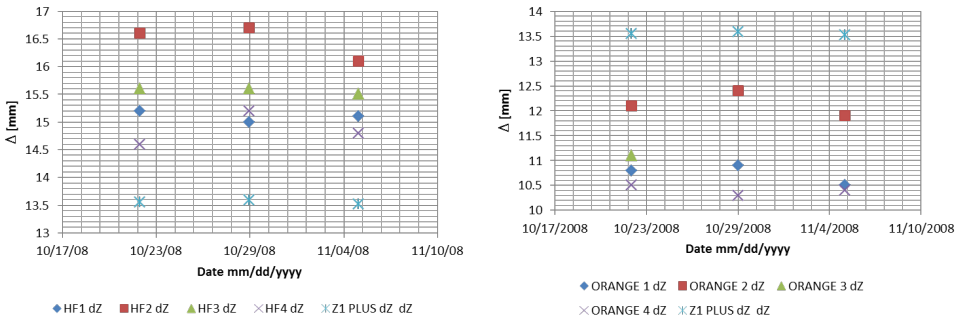

Figure 10.11: Relative movements of HF along Z, at 3.8 T, as measured by survey and the CSS over a period of 15 days.

Endcap shielding structures and forward support platforms (raiser) were instrumented

with a large set of photogrammetry targets as well as by few potentiometers. Later were used mainly as cross-check. The deformations of the structures, turned out to be rather complicated, suggesting the convenience of further reinforcements that have been already implemented. The mapping of the deformations obtained by survey is displayed in fig. 10.12 [17].
Finally, fig. 10.13 shows a subset of results on the stability of the raisers from the measurements taken by survey and the CSS at 3.8 T. The data on Raiser 1 are from the CSS while the ones on Raiser 7 and 8 comes from survey. They all show good stability within the measurement accuracy.

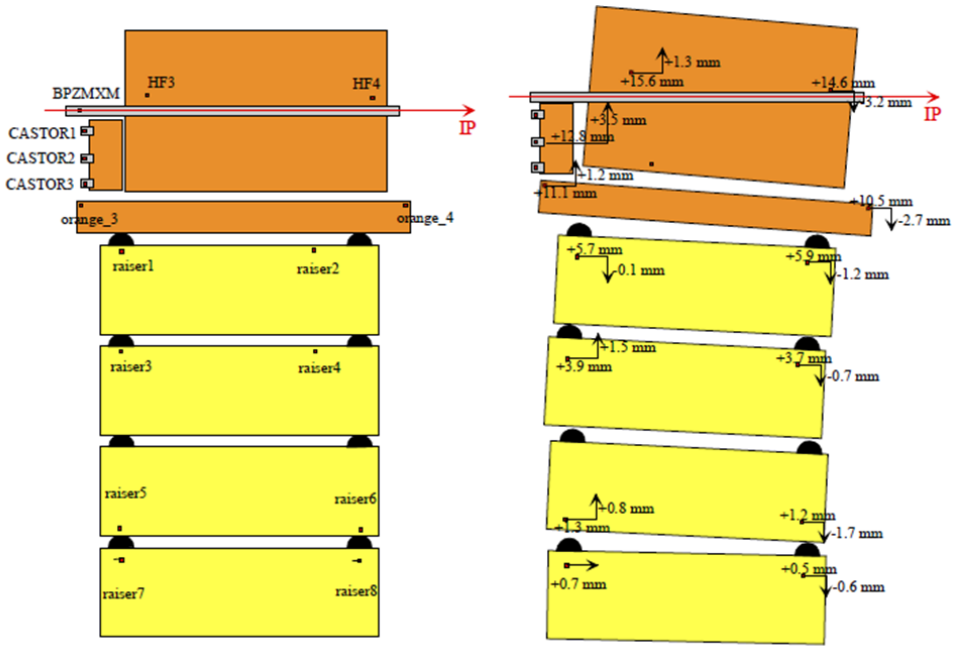

Figure 10.12: Motions between 0 T and 3.8 T as measured by survey. A side view from the minus far side of the detector is displayed.

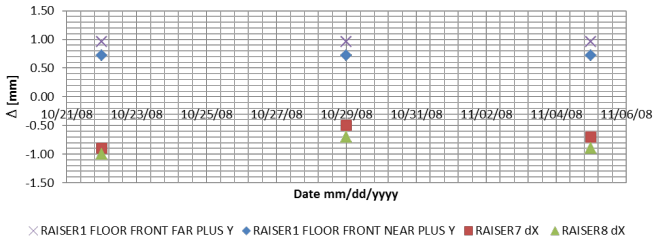

Figure 10.13: Relative movements of the Raiser along Y, at 3.8 T, as measured by survey and the CSS over a period of 15 days.

At the last magnet cycle performed in 2008 the field reached 4 T. As expected, an increase on the displacement along the Z-axis for most of the mechanical elements was observed. The effect on the other coordinates was not significant. Fig. 10.14 summarizes

the Z-compression with all data recorded during the 4 magnet cycles performed in 2008. Note that, at the beginning of the magnet tests and at the end, we obtain different behaviours, which is reflected on both HF sides and by the two different systems used to monitor the movements. During the first magnet cycle the structures suffer a initial pre-compression that explains the larger values recorded. Note as well that, as already mentioned, the values recorded on the plus side (by the Z1 sensor) are always lower when compared to the minus detector side. The last measurement was done at 4 T, even with higher magnetic field we observe in general lower values in all the measurements. This behaviour is further studied in the next paragraphs.

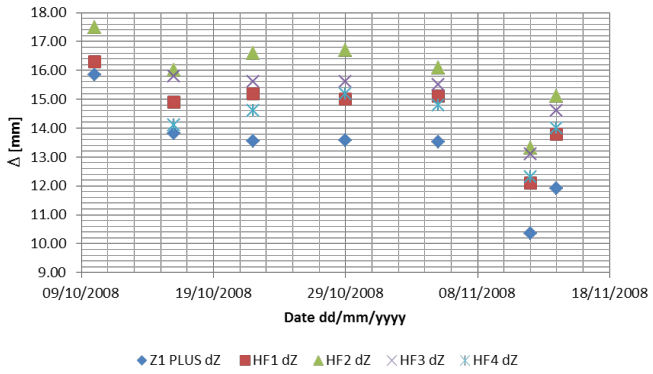

Figure 10.14: Relative movements along the Z axis performed by survey and the CSS on the HF points

The fourth magnet test consisted of a magnet cycle of up to 3.8 T with a slow discharge followed by another magnet ramp up to 4 T ending by a fast discharge. Fig. 10.15 shows the motion during the two cycles as recorded by potentiometer sensors belowing to the CSS and measuring along the Z-axis. Data from a similar measurement performed by the Muon Alignment System [12] at a different location in the detector is also shown. The left plot shows the movements (in mm) recorded by the two sensors as well as the different intensities of the magnetic field. A different sign convention between the two monitoring systems explains the shape (mirror image) of the figures. The plot also shows the different patterns observed when the magnet is powered off following a slow or a fast discharge. We see a discontinuity (with some non-linearity) between 4 T and 3 T. Note that the Muon Alignment System has a lower rate of data stored and this is reflected in the display by isolated dots.
The right plot shows the same data versus the magnetic field value. The plot shows some hysteresis during the two magnet cycles. The shapes measured by CSS for the two ramps up shows two different paths with no significant discontinuities. Instead the measurements from the Muon Alignment System does not show any change of paths. The measurements recorded by the sensors during the ramp down with slow discharge, follow a curved path, while for the second ramp down, through fast discharge, the shape

changes to almost a straight line. For both cycles the initial position is well restored.

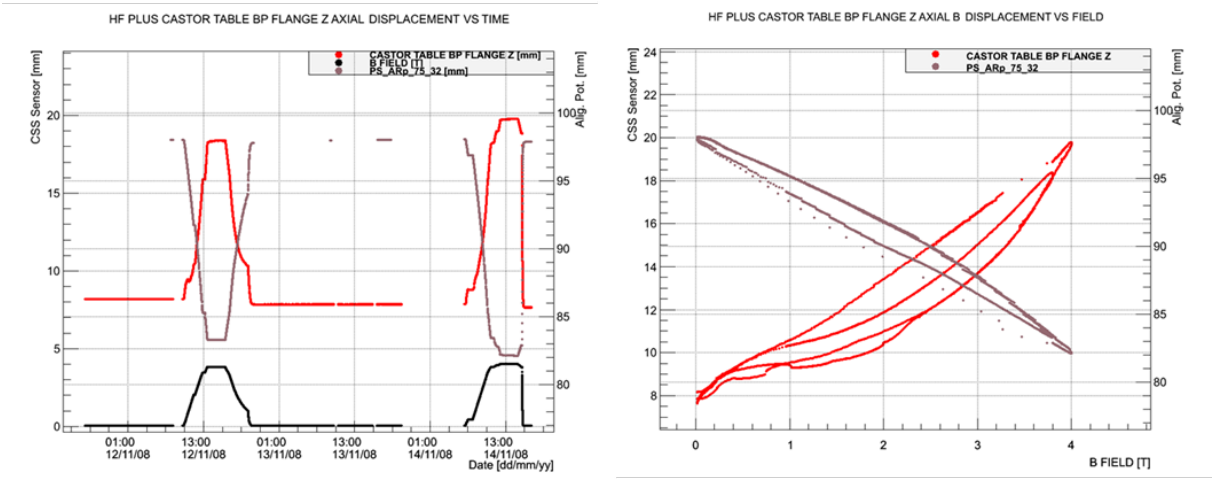

Figure 10.15: Absolute measurement done by the CSS -with the axial potentiometer on Z between CASTOR beam pipe support vs beam pipe- (red) and the Alignment System potentiometer -Arp 75- (brown). The same measurements are displayed versus time (left) and versus magnetic field (left)

Finally, the motion of both HF's (HF+ and the HF-) as seen by the radial sensors is in general very small during the two magnet cycles.

10.3 Reproducibility and long-term stability

Figure 10.16 shows the magnet cycles performed in CMS during the first operation period of LHC (Run I), from mid 2008 to February 2013. CSS recorded data for all the magnet cycles. A very good reproducibility (at the submillimeter level) in the behaviour of the different parts of the detector is observed by the different CSS sensors.

As already discussed in Chap. 5, among the three CSS technologies potentiometer sensors are the most robust, instead ultrasound sensors exhibited a small dependence in the presence of magnetic fields. Fig 10.17 shows the behaviour of a test sensor installed in the Central region (YE1 ES cone). The data corresponds to the various magnet cycles performed in 2009. From the figure we conclude the uncertainty in the response of the sensor, introduced by the presence of a magnetic field, is limited to about 0.5 mm. The sensor response is linear with the field during the fast discharge of the magnet. The dispersion observed in the data for a given field value is interpreted as the noise introduced by the field. This test sensor allows to make an in-situ study and the result obtained confirm the conclusions reached during the characterization of the sensors in the laboratory (Chap. 5).

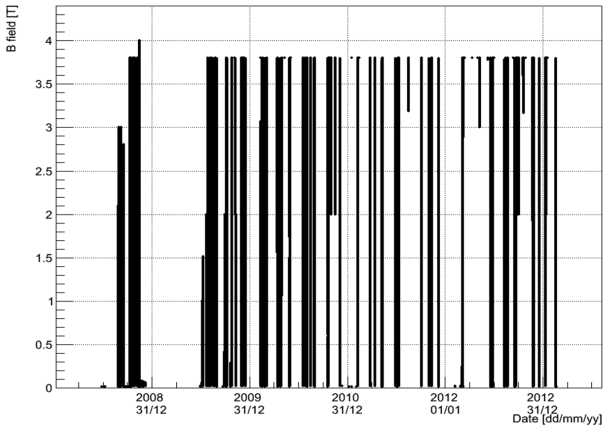

Figure 10.16: Magnet Cycles done in CMS during the first operational period of the LHC.

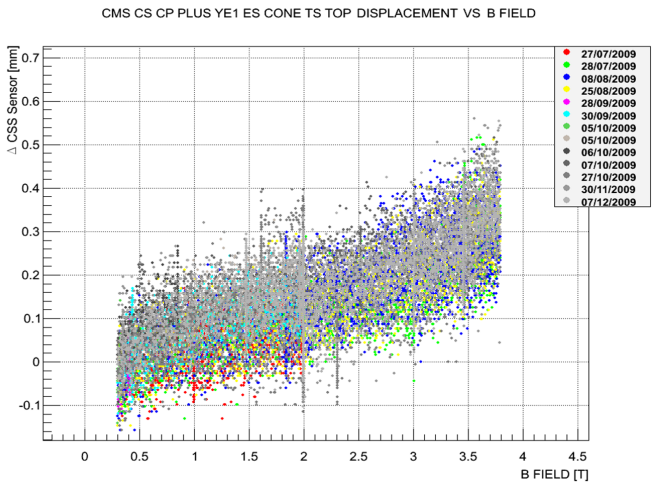

Figure 10.17: Response of a ultrasound test sensor, located in YE1 ES Cone, versus the magnetic field value. The data correspond to the various magnet cycles performed in 2009.

The reproducibility of the motion of the different parts of the CMS under magnetic forces is represented in Fig 10.18 for some selected measurements. The four plots represent variation in the measurements between ES cone and the beam pipe, as recorded by the YE1 ES cone sensors during the various magnet cycles performed during 2009. The pattern, different for each sensor, is very well reproduced in the different measuring campaigns. Although the amplitude of the motion is small in the four cases, it is interpreted as a real motion or deformation of the nose under magnetic forces. Same conclusions are obtained from other CSS sensors monitoring different parts of CMS, as Fig 10.19 shows. In this case, the data recorded by the group of sensors on YB0 and YE1, sited at the minus detector side, are displayed.

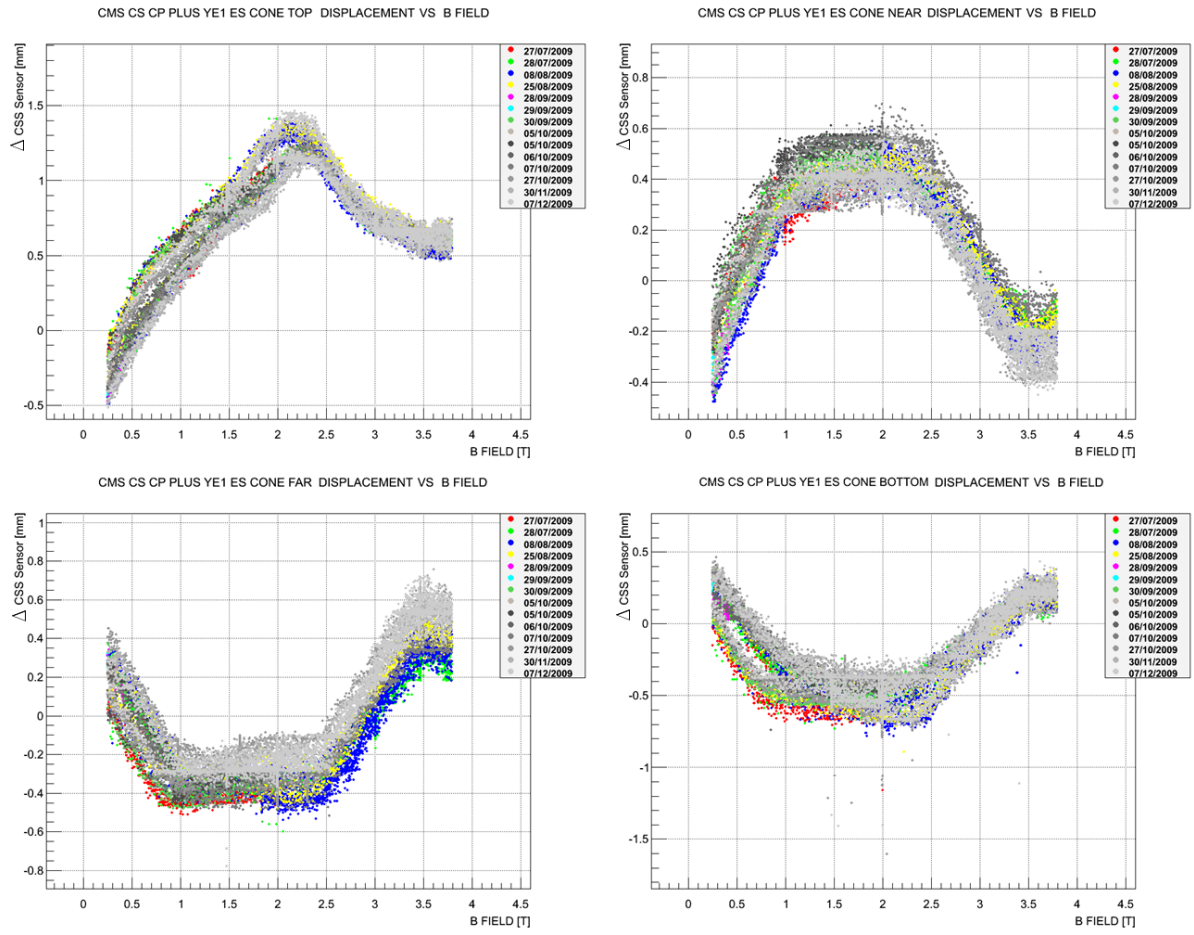

Figure 10.18: Relative clearance with respect to the beam-pipe versus the magnetic field value, as recorded by the ultrasound sensors YE1 ES Cone. The data correspond to the various magnet cycles performed in 2009.

CSS has been operating in a continuous mode during the whole running period of LHC and CMS. Using the data collected until 2013, reproducibility of the movements and stability of positions are also studied. The mechanical stability of the detector has been proved to be very good (within the CSS measurement uncertainties) for both magnetic

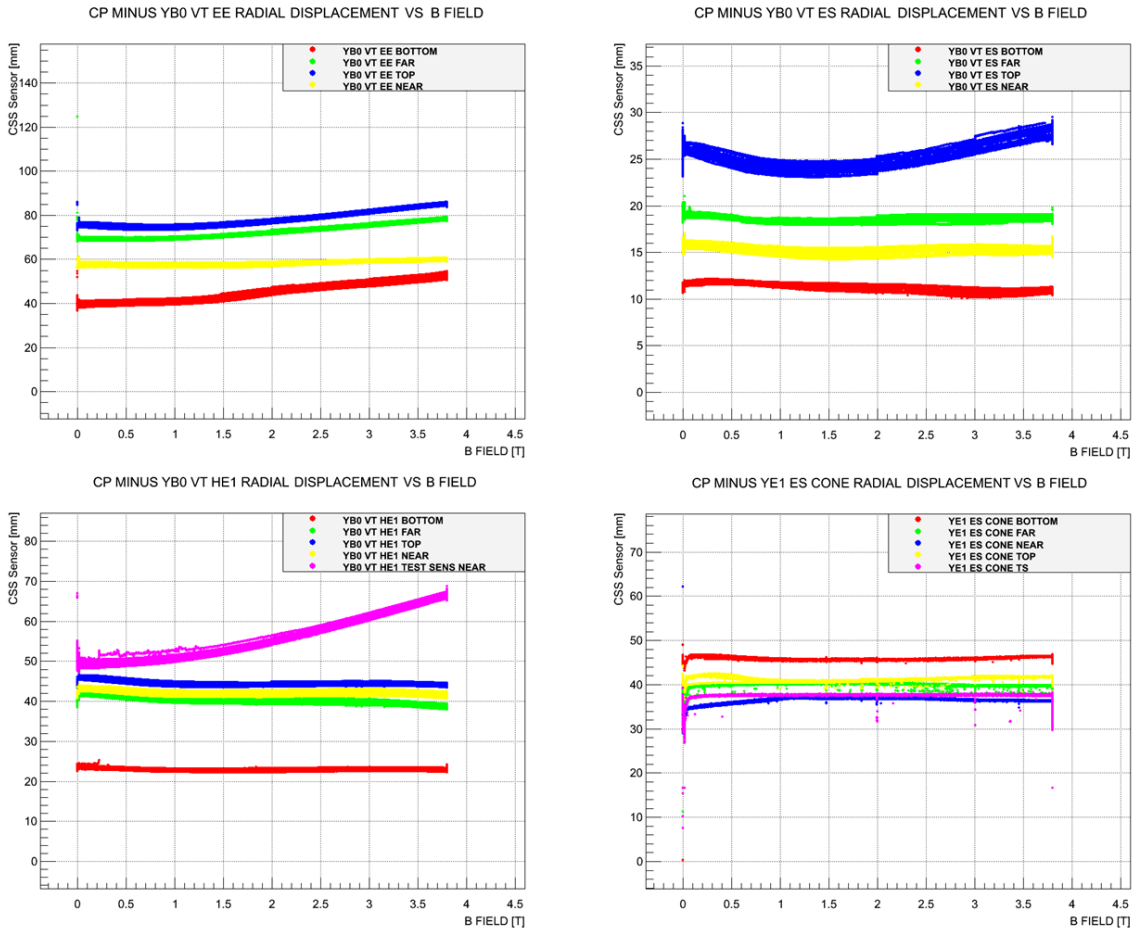

Figure 10.19: Absolute measurements versus the magnetic field value, as recorded by the group of sensors on YB0 (EE, ES, and HE1) and on YE1 (ES-cone). The data correspond to the various magnet cycles performed in 2009.

field values at 0 T and 3.8 T. The results obtained at 3.8 T corresponding to the CMS data-taking conditions show the correct behaviour of the detector and could inform on any unforeseen motion if occurs. If a problem occurs during data taking CSS could help identify and possibly provide a way to correct the data in accordance. This has proven to be specially relevant for forward detectors where no other means of monitoring is available.

Figs. 10.20 and 10.21 illustrate two cases of interest, when the monitored detector parts are not disturbed by the opening-closing of the detector (fig. 10.20), and when the monitored detector parts are altered by the operations (fig. 10.21). In the first case, fig. 10.20, we observe a very good stability of the data along the whole period. The data are represented versus time. The figure includes three sets of information: the black histogram gives the value of the magnetic field; in red the actual data recorded by the corresponding CSS sensor is shown; and in brown, and using the right hand vertical scale, the total integrated luminosity as delivered by the accelerator is displayed. The same convention is used for the data shown in fig. 10.21. Contrary to the previous figure, here we observe some discontinuities in the data (red points) corresponding to (slightly) different positioning of the detectors as result of opening-closing operations. The observed discontinuities are at the mm level indicating again the level of reproducibility achieved during these assembly operations. Both figures also inform on the reliability of CSS monitoring, the system has been running in a continuous mode during several years providing very valuable information on the behaviour of the CMS detector under different operational conditions.

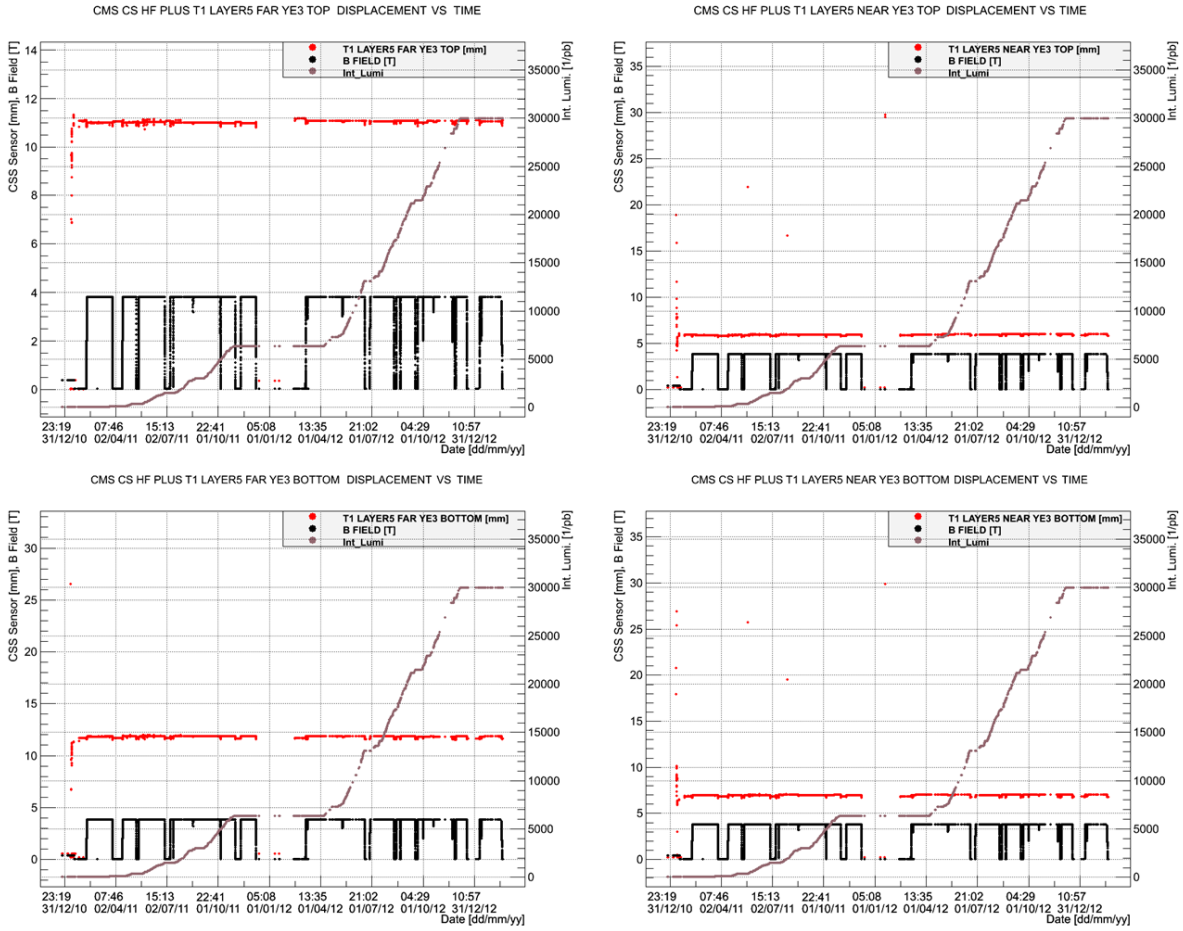

Figure 10.20: Absolute measurement between T1 TOTEM detector and YE3 endcap ring as recorded by the axial sensors housed in the 5^{th} layer of the T1 TOTEM. Data are represented versus time. The data were recorded since middle 2009 until the end of the LHC run in 2013. Top left (right) plot corresponds to the Top far (near) sensor. Bottom left (right) plot corresponds to the Bottom far (near) sensor. (see text)

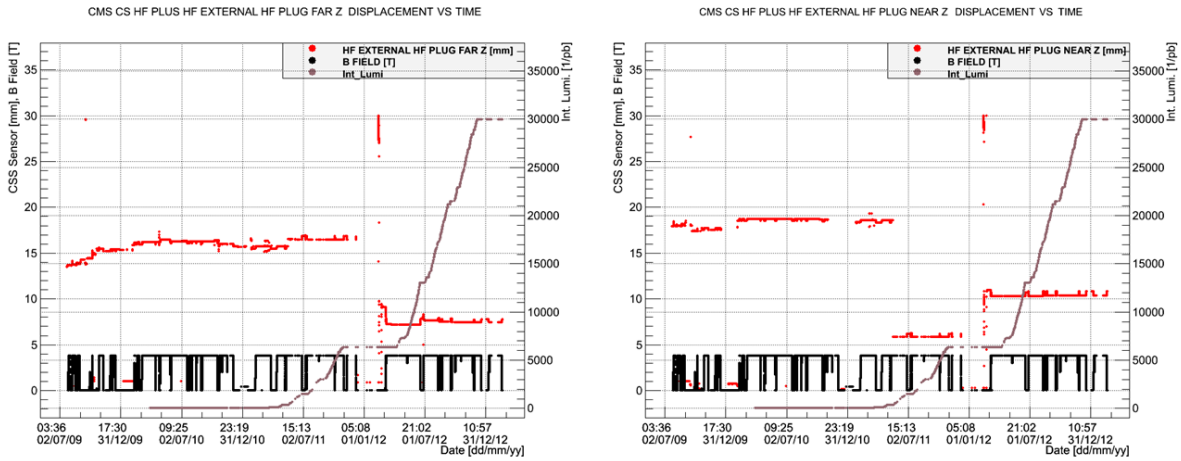

Figure 10.21: Absolute distance between HF and HF-plug detectors as recorded by the axial sensors housed in the HF region. Data are represented versus time. The data were recorded since middle 2009 until the end of the LHC run in 2013. Left (right) plot corresponds to the far (near) sensor. (see text)

Summary and Conclusion

The Large Hadron Collider (LHC) is a proton-proton (p-p) and ion-ion collider built at CERN. The protons can reach an energy up to 7 TeV, giving a total energy at the centre of mass of 14 TeV. The particles collide in bunches, at four nominal interaction points, where two general purpose detectors: CMS and ATLAS, and other dedicated detectors (LHCb, ALICE, TOTEM and LHCf) will detect the product of the collisions.
CMS is one of the two general purpose detectors at the LHC. It has a cylindrical symmetry around the collision point, a diameter of 14.6 m and it is 21.6 m long. The detector consists of different sub-detectors, each with a well defined characteristics to measure a given physical property of the particles emerging from the collision. The work presented in this thesis has been developed within the CMS experiment and consist on the development of a monitoring system to assist the complex assembly operations of the detector.

The Closing Sensors System

From the mechanical and integration point of view CMS is characterized by its modularity and compactness. Once the detector is fully assembled the nominal distance between the different structures - and from them to the beam pipe tube - is optimized to preserve as much as possible an hermetic detector. A Closing Sensors System (CSS) composed of more than 200 sensors distributed all over CMS, has been designed and implemented. The system has the task to monitor the nominal clearance between elements, provide relative positioning precision at the level of mm, thus allowing guarantee the integrity of the sub-detectors and other elements during the assembly processes that take place regularly for the maintenance or upgrade of CMS. Critical safety areas are well identified at different parts of the detector where tight tolerances should be satisfied at assembly phase. Given the size and weight of the detector elements, critical safety regions are defined mainly when heavy structures are positioned close to the beam-pipe or when the handling of delicate and fragile elements is involved. CSS instrumentation is distributed along the “central” and “forward” CMS regions.

For the purpose of this project, the central part is defined as consisting of the mechanical structures, services, and sub-detectors systems integrated into the barrel and endcap structures. While, the central barrel wheel, is located at a fixed position at the centre of the collision cavern, YB+/-1,2 and YE+/-1,2,3 are movable structures. The most critical area in this region the so called "53 degrees service crack", characterized by very tight clearance once the detector is closed, runs along the end flange boundaries of the Tracker, Electromagnetic Barrel calorimeter (EB) and Hadronic Barrel calorimeter (HB). The forward region houses several sub-detectors: the Hadronic Forward calorimeter (HF), the CASTOR calorimeter, and the TOTEM experiment composed of modules T1 and T2 detectors. There are also dedicated mechanical structures holding the sub-detectors (as the raiser system for HF, or the extension platform where the CASTOR support sits), heavy mechanics shielding the detector from machine background (as Collar and Rotating shielding pieces), etc. The forward area corresponds as well to the most fragile part of the beam pipe, the entry point of the beam pipe to the CMS collision cavern, making this area the most critical in terms of mechanical tolerance and safety related issues. The CSS is intensively used in this region during the processes of sub-detector installation and assembly, as well as to control detector motions during the powering of the CMS 4 T magnet. The strong magnetic forces induce large motion or deformations on the detectors and the associated structures that have to be precisely monitored.

Selection and calibration of CSS sensors

LHC and CMS environment impose stringent constraints in the selection of the instrumentation. The system components will be exposed to high radiation doses during the operation of the LHC, and should be able to operate under strong magnetic fields. There is no technology available in the market able to cope with these requirements. Nevertheless the scalability and maintenance scenarios of the future, drove the decision to use Commercial Off-The-Shelf items as far as possible. Tests as thorough as possible were performed to understand the expected lifetime and behaviour under magnetic field. The behaviour of the sensors under radiation is followed during the runs of the LHC and a regular replacement of sensors is done following their degradation.

Depending on their location in CMS, CSS's sensors have to survey reliably distances ranging from few mm to several tens of cm. A moderate requirement of 0.5 mm complies with the measurement precision requested for this task. Different sensor technologies were selected able to efficiently cover these requirements. Moreover, when available, compact and miniature models were selected to fulfil the restrictions imposed by the limited space available for the integration of the sensors on already built CMS structures. Several distance/proximity sensors technologies were studied in order to provide

solutions for the different ranges. Based on tests and experience, two major sensor groups were defined and used: non-contact and contact sensors. For the first category Ultrasound and infrared technologies were chosen, while for the latter more robust Potentiometer sensors were selected.
The three types of sensors were characterized using dedicated calibration stands. Given the essential differences between the three technologies and the different performance tests required for each specific location in the detector, various experimental setups and acquisition systems were built and used for calibration. In all cases, the calibration tried to reproduce as much as possible the real operating conditions, which strongly depend on the location of the sensor in the detector.
A full characterization of optical infrared sensors was carried out in the laboratory. After defining the working operational parameters (LED current and voltage) relevant for the performance of the sensors, calibration functions were obtained and the dependence with the target was studied, emphasis on small distance measurements was given. After calibration an intrinsic resolution below 0.5 mm was obtained for all units. The effect of the sensor-target orientation was evaluated for several configurations. Optical sensors are sensitive to large sensor-target angles, the sensor response was evaluated for fixed angles up to 20°. A misalignment up to 10° would increase the measurement uncertainty by 1-2 mm. This result is considered acceptable since much smaller angles are expected in the detector. Special target geometry configurations (especially those required for TOTEM T2 detectors) were studied and the working conditions of the sensors were conveniently adapted. Some sensors will be exposed to significant values of magnetic field, Hall effects in the phototransistors can be expected for these type of sensors and therefore a full characterization was also done for field values up to 2.2 T. A sizeable effect (up to 5 mm variation in the sensor response) was observed for high field values. As a conclusion, the response from these sensors would be considered reliable only for field values below approx. 0.6 T.
Acoustic sensors are characterized by a large dynamic range. An intrinsic resolution below 0.5 mm was always obtained. They were bought pre-calibrated, and therefore their expected performance were known a priori from the manufacturer. However, a series of tests were performed to a subset of units prior the installation of the sensors in the detector. As with the infrared sensors, we studied possible effects specific for our application that could modify the nominal performance: a) the influence of the cable length in the sensor response; b) sensor functionality under various angular orientations target-sensor; c) functionality and performance of this technology under special target geometries; and d) the effect of the magnetic field in the sensor response. No degradation of the intrinsic performance was found for the standard cable lengths used in this application. The sensitivity to angular orientation target-sensor is small and no degradation in performance was observed for misalignment target-sensor below 10°. Instead, the tests performed with special target geometries (as those required for TOTEM T2 detector) revealed that this technology is not suitable for some specific configurations.

An effect in the response of the sensor (stratification of the sensor output) not yet fully understood was observed in presence of magnetic fields, nevertheless the degradation of the sensor response is limited to 0.5 mm.
Potentiometers are simple and robust technology. They are magnetic field insensitive and radiation resistant. Unfortunately its implementation in the detector is limited, since they require a direct contact with the target. The series of test performed with these sensors confirmed their robustness under the expected operational conditions. After fixing the final operation parameters, the sensor resolution was measured to be at the level of 0.1 mm. In this case, uncertainties related with possible imprecisions in their installation largely determine the final uncertainty in the sensor measurement.

Readout electronics and Control system

The choice of the readout system was mainly driven to make the best use of the CMS infrastructure and to match the performance requirements and safety restrictions of the experiment. ELMB (Embedded Local Monitor Board) cards, a radiation tolerant and immune to magnetic field electronics developed for the LHC experiments are used to collect the signal from the CSS sensors. Ad-hoc solutions have been developed to adapt the output of the three types of sensors to the ELMB cards. The layout of the readout system was defined as modular as possible to allow easy replication, as needed in the successive extensions of the system. Flexibility to allow the operation of the system under CMS data-taking and maintenance conditions was also imposed. The readout of the network of sensors distributed over the detector is concentrated in few points (racks) close to the detector in the collision cavern. Power supplies and communication-hub are located remotely, in the underground electronics cavern, to facilitate maintenance.

The Data Acquisition Software was defined following the standards for the LHC experiments. SCADA PVSS II with the JCOP framework developed at CERN was the software platform used by the CSS. The DAQ program performs the control of the readout sequence, provides the display of the information, and allows the storage of the data. Different panels were defined to allow a quick and easy representation of data needed for an interactive response with the technical team conducting mechanical operations. The software has been continuously developed in order to provide sufficient support on field and in real time. On top of the standalone operations during the maintenance periods, the system can run in a centralized manner fully integrated in the CMS Detector Control System. The initial mission of CSS, consisting on the supervision of the CMS closing and opening operations has been extended and the system is also useful during the commissioning of the CMS detector, helping to understand the behaviour of the complex structures in the forward region during the powering of the solenoid magnet. Special software features were introduce to monitor detector motions due to magnetic forces.

CSS hardware, readout electronics, and the data acquisition and control system have shown excellent performance during all these years. The simple design has shown to be a robust solution under the severe LHC working conditions. During this time and following the experience the system has benefited of several updates that has increased the robustness of the system.

CSS data analysis and results

A first version of the CSS was extensively used during the first complete closing of the CMS detector that took place in the summer of 2008, and enable CMS to be ready for the first circulation of beams in the LHC. Since then, CSS has been constantly adapted to cope with the needs of the different phases that CMS went through. The data recorded by the system are grouped into three categories: measurements related with the closing and opening of the detector structures, measurements monitoring the powering cycles of the magnet, and finally the data collected during the ordinary operation of the detector. The two first sets of measurements are critical to ensure the integrity of the detector. Special care has to be taken by the online monitoring during the complex assembly processes. Safety clearance between elements are defined in the CSS control system, and a set of warnings and alarms guide the actions to be taken by the operators in charge of the different assembly tasks. Finally, the set of data collected during the regular operation of CMS informs on the mechanical stability of the detector and reproducibility of the motions. Any unknown instability could influence the quality of the data taken by CMS and therefore the subsequent scientific production. If unexpected motions occur CSS can help to understand the problem and to identify possible solutions. This is specially relevant to ensure the correct operation of the forward detectors.

The results obtained by CSS during the closing and opening operations of CMS have been discussed in Chapter 9. Data related to operations performed with the barrel movable wheels are only available since 2009. Each movable wheel (YB-2, YB-1, YB+1, and YB+2) is instrumented with eight ultrasound sensors measuring the distance between the inner wheel boundary and the external surface of the Vac tank. The comparison between the measurement recorded by the different sensors in a given wheel, informs on the final centring of the structures both in position and orientation. Centring within few mm in position and few mrad in orientation was achieved in all cases. As for the endcap structures, data from the operations performed with the YE+1 endcap disks extend from 2008 to 2010, and include closing and opening operations. In all cases, the defined safety clearance was respected thanks to the information provided by the CSS. Special care was taken in the monitoring of the safety clearance related with the beam pipe and between the elements along the “53 degrees service crack”. Although, each operation must be

considered as unique, the reproducibility of the values achieved at the various assembly campaigns is considered very good.
Probably the most critical safety area is the CMS forward region. CSS has been intensively used in this region. Data are available since 2008 up to 2013. In 2008 when the first closing of the detector took place the two forward hadron calorimeters (HF) were present but CASTOR and TOTEM sub-detectors were not yet completed. The monitoring system helped to define and consolidate the installation procedures to be followed with these detectors. Data from HF, CASTOR and TOTEM detectors are available; the final positioning achieved at the different assemblies shows a reasonable reproducibility. Within the measurement uncertainties, safety clearances have been respected in all cases. Measurements done with the infrared sensors installed in CASTOR and TOTEM detectors provide important information necessary for the understanding of the data recorded by these detectors. Note that safety clearances are stricter in this forward region and demands much care during assembly operations, which enters in conflict with the reduced time available (following the ALARA protocol) to perform the operations due to the high radiation levels reached over the years of LHC operation. The working conditions demand very robust and reliable measurements. Faulty measurements or wrong interpretations could induce human risk or accidents with fragile detector components.

CMS structures experience strong magnetic forces when the 4 T solenoid magnet is powered on. They induce large displacements and sizeable deformations in the detector. During the design phase finite element analyses were performed to evaluate the field map as well as the forces generated on the ferromagnetic elements of the detector. Forces generated in the barrel layers and endcap disks are quite substantial, the main component being in the axial direction and pointing inward. They result in substantial axial compression requiring attention in the construction to ensure stability in the Z direction. The effect of the forces in the return yoke were fully analysed and considered in their construction specifications. The measurements performed on the real detector confirmed the available studies. Although the behaviour of the central part of the detector –barrel and endcap- was rather well known in the presence of magnetic forces, the field map and magnetic forces in the forward detectors, ancillary components and support structures in the forward regions were much more difficult to simulate correctly and only crude estimations of possible deformations were available. Precise measurements of the region, during the powering of the solenoid, were therefore critical to understand the mechanical behaviour of the elements and to preserve detector integrity. CSS was intensively used when the CMS solenoid was powered on or off. First measurements were performed during the year of 2008, when only partial instrumentation of the forward region was available, and later on, during the regular magnet cycles performed in the the years 2009 to 2011. This is reported in Chapter 10. The main results extracted from the CSS data are: a) the measurement of an axial displacement of HF of approx. 13 mm,

towards the interaction point; b) the mapping of deformations and understanding of the global motion of the forward support platforms; and c) the good reproducibility of mechanical deformations induced in the forward detectors due to magnetic forces. In 2008 independent measurements were simultaneously performed using standard survey and/or photogrammetry techniques. The comparison between the two sets of data provides an extra validation of the CSS output.

CSS has run in a continuous mode during the whole period of the first LHC operations, from 2009 to 2013. Within the measurement uncertainties, the mechanical stability of the detector has been proved to be very good, for both magnetic field configurations: at 0 T and 3.8 T. The results observed at 3.8 T corresponding to CMS data-taking conditions show the correct behaviour of the detector elements and also inform about of any unforeseen motion that could occur. Long-term reproducibility of the movements have been also observed.

Outlook

Up to now the CSS has shown a very good performance over the years. Nevertheless, the challenges are increasing, due to the increased irradiation of the materials and the reduced available time for the maintenance operations. The monitoring system could be improved mainly in the critical areas at the forward region. For the forward detectors a specific challenge is the geometry of the target. The target is a small radius circumference, which, in general introduces extra uncertainty in the measurements. A possible improvement could be the implementation of an optical fibres system combined with interferometry. Initial studies on new technologies have been done by the author and are described in reference [33]. One can also envisage to replace the current sensors setup with the new optical fibre system since infrared and ultrasound sensors are not radiation resistant and therefore need to be replaced during the shutdown periods of the LHC.
A complementary system also considered in [33] is based on a laser scan. The main characteristic of a laser scan are its long range, high sampling rate and precision. The intersections between the different elements during the closing operations of the main region could be assisted with such an online scan system.

Bibliography

[1] P. Lefèvre T. S. Pettersson. The Large Hadron Collider: conceptual design. *CERN-AC-95-05 LHC*, 1995.

[2] C. G. Committee. Guidelines for the ALICE technical proposal. *CERN-LHCC-94-021-Rev*, 1994.

[3] C. G. Committee. Review of the ATLAS Technical coordination TDR. *CERN-LHCC-99-018*, 1999.

[4] C. Collaboration. CMS Physics TDR: Volume I and II. *CERN-LHCC-2006-001 & CERN-LHCC-2006-021*, 2006.

[5] L. Collaboration. LHCb reoptimized detector design and performance TDR. *CERN-LHCC-2003-030*, 2003.

[6] M. Bongi R. D'ALessandro O. Adriani, L. Bonechi. LHCf experiment TDR. *CERN-LHCC-2006-004*, 2006.

[7] P. A. G. Antchev. The TOTEM Detector at LHC (pp. 449-455). *CERN-LHCC-2003-030*, 2003.

[8] V. Karimäki. The CMS tracker system project TDR. *CERN-LHCC-98-006 ; CMS-TDR-5*, 1998.

[9] C. G. Committee and LHCC. The CMS electromagnetic calorimeter project TDR. *CERN-LHCC-97-033 and CMS-TDR-4*, 1998.

[10] C. G. Committee and LHCC. The CMS hadron calorimeter project TDR. *CERN-LHCC-97-031 ; CMS-TDR-2*, 1997.

[11] C. G. Committee and LHCC. The CMS muon project TDR. *CERN-LHCC-97-032 ; CMS-TDR-3*, 1997.

[12] Mar Sobrón Sañudo. CMS detector geometry reconstructed with the Link alignment system. *CERN-THESIS-2009-155, CMS-TS-2010-001*, 2009. http://inspirehep.net/record/894164/.

[13] E. N. collaboration. CMS (LHC) Measurements and Unusual Cosmic Ray Events. *XVI International Symposium on Very High Energy Cosmic Ray Interactions, ISVHECRI 2010, Batavia, IL, USA (28 June – 2 July 2010)*, 2010.

[14] C. collaboration. STUDY OF THE UNDERLYING EVENT AT FORWARD RAPIDITY IN PP COLLISIONS AT SQRT(S). *JHEP; CERN-PH-EP-2013-012; CMS-FWD-11-003*, 2013.

[15] E. Radicioni R. Herzog R. Rudischer E. Wobst V. Berardi, M. G. Catanesi. Total cross-section, elastic scattering and diffraction dissociation at the Large Hadron Collider at CERN TDR. *CERN-LHCC-2004-002 ; TOTEM-TDR-001*, 2004.

[16] CMS Collaboration. CMS Magnet Project Technical Design Report. *CERN/LHCC 97-10*, 02 May 1997.

[17] Aurelie MAURISSET Jean-David MAILLEFAUD. CMS-CRAFT, Deformation measurements during the CRAFT Test. October and November 2008. *CMS-SG-UR-0118. EDMS document ref.:979062*, 2008. https://edms.cern.ch/document/979062/1.

[18] U. K Vector Fields Ltd, Oxford. TOSCA/OPERA-3D Software. http://www.cobham.com/about-cobham/aerospace-and-security/about-us/antenna-systems/specialist-technical-services-and-software/products-and-services/design-simulation-software.aspx.

[19] V. B.-R. R. Arcidiacono. CMS DCS DESIGN CONCEPTS. *10th ICALEPCS Int. Conf. on Accelerator & Large Expt. Physics Control Systems. Geneva, 10 - 14 Oct 2005, PO1.062-6 (2005)*, 2005.

[20] N. Beni. S4CMS: A combined monitoring of sensors in CMS experimental site. *Nuclear Physics B (Proc. Suppl.) 215 (2011) 359–361*, 2011.

[21] Baumer. SONUS The smallest and lightest ultrasonic sensors worldwide. 2008. http://www.baumer.cn/fileadmin/user_upload/media/Baumer_China/Downloads/SONUS_EN.pdf/.

[22] Baumer. Ultrasonic distance measuring sensors UNDK 10U6914/S35A. 2012. http://baumer.amirada.net/pfinder_sensor/downloads/Produkte/PDF/Datenblatt/Ultraschall_Sensoren/UNDK_10U6914_S35A_web_EN.pdf/.

[23] Excelitas. Reflective Optoswitch - Long Range VTR24F1H . 2012. http://www.excelitas.com/downloads/DTS_vtr24f1.pdf/.

[24] Active Sensors. Linear Potentiometer CLS1313. 2012. http://www.activesensors.com/pdf/linear-potentiometer/cls1310/cls1313.pdf/.

[25] CharlyRobot and ISEL. http://www.charlyrobot.com/ and http://www.cnc-machines.isel.com/.

[26] Labjack Measurements and Automation. http://labjack.com/.

[27] LabVIEW homepage. http://www.ni.com/labview/.

[28] Beckhoff New Automation technology. http://www.beckhoff.com/.

[29] Kvaser. http://www.kvaser.com/datasheets/kvaser_datasheet.php?ean=73-30130-00084-1.

[30] CiA, CANopen. http://www.can-cia.org/index.php?id=171.

[31] Home Page Embedded Local Monitor Board. http://elmb.web.cern.ch/ELMB/ELMBhome.html.

[32] CERN Metrology Group. Large-Scale Metrology and Experimental Metrology. *CERN/LHCC 97-10*, 02 May 1997. https://espace.cern.ch/be-dep-ABP-SU/default.aspx.

[33] J. Rodrigues Antunes. Closing sensors system of cms. combining high energy physics experiments apparatus safety and permanent distance monitoring. *CMS Detector Note: CMD DN-2014-/021*, 2014.